IECO

Volume 8 No 3 Year 2025

■ Volume 8

■ No 3

■ Year 2025

University of Sistan and Baluchestan

Iranian Association of Electrical and Electronics Engineers

International Journal Of

Industrial Electronics Control and Optimization

In This Issue:

Research Artivles:

IECO

International Journal Of
Industrial Electronics Control and Optimization

About Journal

The University of Sistan and Baluchestan entered into strategic partnership with Iranian Association of Electrical and Electronic Engineers (IAEEE) to publish the International Journal of Industrial Electronics Control and Optimization (IECO). The IECO is a refereed international journal which presents to the international scientific community important results of work in these fields, whether in the form of modeling simulation, analysis, fundamental research, development, application, design or real-time implementation. The scope of IECO is broad, encompassing all aspects of Industrial Electronics, Control and Optimization..

Note: International Journal of Industrial Electronics, Control and Optimization (IECO) has qualified to **ACADEMIC RESEARCH JOURNAL (ELMI-PAJOHESHI)** status certified by the ministry of Science, Research and Technology of Iran (No. 231566/3/18 dated 1396/10/09), and is published by the University of Sistan and Baluchestan through a formal partnership (No. 952/2/1500 dated 1395/11/04) with Iranian Association of Electrical and electronic Engineers (IAEEE) in order to develop scientific and research cooperation.

Aims and Scope

International Journal of Industrial Electronics, Control and Optimization (IECO) is a Peer reviewed journal of advanced and state-of-the-art in the science and engineering of Industrial Electronics, Control and Optimization. Its Scope encompasses the applications of Industrial Electronics, power systems, control, optimization and computational intelligence for the enhancement of industrial and manufacturing system and processes. The scope of the journal include the following:

I. Industrial Electronics

- Low and high-power converters
- Renewable energy
- Drive control techniques
- Techniques for advanced power semiconductor devices
- Power quality and utility applications
- Communications
- Flexible AC Transmission Systems (FACTS)
- Control in power electronics
- Electromagnetic and thermal performance of electronic power converters
- Motion control, robotics, sensors and actuators
- Fault detection and diagnosis
- Power systems
- Factory automation, communication, and computer networks

II. Control

- Adaptive control
- Control of process systems
- Control theory
- Data processing
- Design of control systems
- Hybrid systems
- Identification and observation
- Intelligent systems
- Model-predictive control
- Optimal control
- Robust control
- Fractional order systems

III. Optimization

- Ant Colony
- Chaos Theory
- Evolutionary Computing
- Fuzzy Computing
- Hybrid Methods
- Immunological Computing
- Neuro Computing
- Particle Swarm
- Probabilistic Computing
- Rough Sets
- Wavelet

Director-in-Charge:

Dr. S. Masoud Barakati

Editor-in-Chief

Dr. S. Masoud Barakati

Editorial Board

Dr. Gevork B. Gharehpetian- University of Technology (Tehran Polytechnic)
Dr. Ebrahim Babaei-University of Tabriz & Near East University
Dr. Seyyed Hossein Hosseini-University of Tabriz
Dr. Hasan Bevrani-University of Kordestan
Dr. Amirnaser Yazdani-Toronto Metropolitan University
Dr. Mehrdad Kazerani-Ryerson University
Dr. Hasan Monsef-University of Tehran
Dr. Massoud Rashidi Nejad-University of Shahid Bahonar Kerman
Dr. Hossein Askarian-Abyaneh-Amirkabir University of Technology (Tehran Polytechnic)
Dr. Mohammad Monfared- Ferdowsi University of Mashhad
Dr. Saeed Tavakoli-University of Sistan and Baluchestan
Dr. Mahmood Joorabian-Shahid Chamran University of Ahvaz
Dr. Reza Ghazi-Ferdowsi University of Mashhad
Dr. Mehri Mehrjoo-University of Sistan and Baluchestan
Dr. Mohammad Reza Aghaebrahimi- University of Birjand
Dr. Bin Wu- Toronto Metropolitan University
Dr. Mahmoud Okati Sadegh-University of Sistan and Baluchestan
Dr. Tahere Fanaei Sheikhosleslami-University of Sistan and Baluchestan

Assistant Editors

Dr. Sobhan Dorahaki- Qatar University
Dr. Abbas-Ali Zamani-Technical and vocational University
Dr. Mojgan MollahassaniPour-University of Sistan and Baluchestan
Dr. Samaned Soradi-zeid-Industry and Mining (Khash)
Dr. Majid Ghadrdan- University of Sistan and Baluchestan

Dr. Alireza HosseinPur-University of Zabol
Dr. Ahmad khajeh-University of Sistan and Baluchestan
Dr. Hamde Torabi-University of Sistan and Baluchestan
Dr. Mahdi Kazeminia- Velayat University
Dr. Masoumeh Rezaei- University of Sistan and Baluchestan
Dr. Poria Jafari-University of Sistan and Baluchestan
Dr. Amin Zarei -University of Sistan and Baluchistan
Dr. Saeed Yousefi-Darmian-University of Sistan and Baluchestan
Dr. Maryam Khamar- University of Isfahan
Dr. Mohammad Ali Azghandi-University of Sistan and Baluchistan
Dr. Ali Hassannia -University of Sistan and Baluchistan
Dr. Ehsan Adibnia- University of Sistan and Baluchestan

Executive Manager

Kazem Piran

Page Designer

Dr. Ali Hassannia

International Journal Of
Industrial Electronics Control and Optimization
Print ISSN: 3517-2645
Online ISSN: 3568-2645
Homepage: https://ieco.usb.ac.ir/

Optimizing the Design of a Hydrogen Refueling Station Integrating Renewable Energy and Seawater Desalination: A Case Study in Southern Iran

H. Maleki[1] | M.S. Spasian[2] | M.R. Aghamohammadi[3] | M. Marzband[4,5]

Electrical Engineering Department, Shahid Beheshti University, Tehran, Iran[1,2,3]
Department of Electrical and Computer Engineering, Faculty of Engineering, King Abdulaziz University, Jeddah 21589, Saudi Arabia[4]
Center of Research Excellence in Renewable Energy and Power Systems, Department of Electrical and Computer Engineering, King Abdulaziz University, Jeddah 21589, Saudi Arabia[5]
Corresponding author's email: m_sepasian@sbu.ac.ir

Article Info

Article type:
Research Article

Article history:
Received: 31-December-2024
Received in revised form: 12-March-2025
Accepted: 30-March-2025
Published online: 23-Sep-2025

Keywords:
Hydrogen refueling station,
Photovoltaic,
Optimization,
Water desalination.

ABSTRACT

This study investigates the optimal design configuration of a hydrogen refueling station located in southern Iran, focusing on the integration of renewable energy sources and seawater desalination technology to achieve self-sufficiency. The station integrates various components, including photovoltaic panels, fuel cells, desalination units, natural gas and power-to-hydrogen conversion systems, and storage facilities for water and hydrogen. The primary goals are to achieve an independent power supply from renewable sources and an autonomous water supply through seawater desalination. To determine the most cost-effective configuration, a Mixed Integer Linear Programming (MILP) model is developed, taking into account the water and power consumption of each component. The objective is to minimize the Net Present Cost (NPC) of investment, maintenance, and operation. The model is implemented and solved using the CBC solver within the PYOMO environment. The study's findings reveal that converting natural gas to hydrogen is more economically viable than power-to-hydrogen conversion, with the former accounting for more than 95% of the hydrogen produced. The power demand is effectively met by combining photovoltaic systems, fuel cells, and hydrogen storage. Moreover, the study highlights the benefits of integrating water and hydrogen storage systems, which optimizes the utilization of photovoltaic energy. Excess energy generated by the photovoltaic panels is utilized for seawater desalination and the production of green hydrogen.

NOMENCLATURE

Sets

y	Index of years in the project's lifetime horizon
h	Index of hours in the time horizon
n	Index of typical day types
C	Set of HRS components

Variables

C^{IN}	Investment cost of the HRS ($)
C_y^M	Annual operation cost of the HRS ($)
C_y^R	Annual replacement cost of the HRS ($)
E_{in}^{H2T}	The initial value of H2T(MWh)
$Q_{y,n,h}^{H2T-}$	The Charging value of H2T (MW)
$Q_{y,n,h}^{H2T+}$	The Charging value of hydrogen to H2T (MW)
$I_{y,n,h}^{H2T}$	Binary variable for the charging mode of H2T
κ_P^{P2H}	Power consumption factor for P2H (MWh/ton H2)
$V_{y,n,h}^{WT}$	The charge value of WT(m3)
$W_{y,n,h}^{WT+}$	The charging value of hydrogen to WT (m3/h)
$W_{y,n,h}^{WT-}$	The charging value (m3/h)
$I_{y,n,h}^{WT}$	Binary variable for the charging mode of WT

Copyright © M.S. Spasian (s).
Publisher: University of Sistan and Baluchestan

$C_{y,n,h}^{NG}$	Total natural gas cost of the HRS ($)	**Parameters**	
$W_{y,n,h}^{RO}$	The water generation of the RO(m3)	K_P^{RO}	RO power consumption factor (MWh/m3 H2O)
$Q_{y,n,h}^{SMR\_CCS}$	The hydrogen generation of SMR_CCS (MW)	η^{FC}	Efficiency of FC
$P_{y,n,h}^{SMR\_CCS}$	The power consumption of the SMR_CCS(MW)	$\kappa_P^{SMR\_CCS}$	SMR power consumption factor (MWh/ ton H2)
$G_{y,n,h}^{SMR\_CCS}$	The natural gas consumption of the SMR_CCS (m3)	$\kappa_G^{SMR\_CCS}$	SMR natural gas feeding factor (m3/ ton H2)
$P_{y,n,h}^{FC}$	The electrical power generation from the FC (MW)	W_{in}^{WT}	The initial value of WST(m3)
$Q_{y,n,h}^{FC}$	The H2 power consumption of the FC (MW)	$\kappa_{CO2}^{SMR\_CCS}$	CO2 emission factor for SMR (m3/ton H2)
$G_{y,n,h}$	The amount of gas consumed in the HRS(m3)	κ_{LHV}^{H2}	Lower heat value of hydrogen (MWh/ton H2)
$Q_{y,n,h}^{P2H}$	The hydrogen power generation of P2H (MW)	η^{H2ST}	H2 tank efficiency
$P_{y,n,h}^{P2H}$	The electrical power consumption of the P2H (MW)	$\overline{Q}^{H2T}$	Charging /discharging range of the H2T
S_c	The optimized size of the HRS components.	$\overline{W}^{WT}$	Charging /discharging range of the WT
$\overline{S}^c$	Maximum capacity of the HRS components	$R_{y,n,h}^{PV}$	The solar radiation (W/m2)

I. Introduction

According to the International Energy Agency (IEA), the transportation sector is responsible for approximately 8 Gt CO_2 emissions, making it the third-largest carbon emitter globally [1]. Coupled with accelerated urbanization, the sector is projected to further escalate energy demand and CO_2 emissions. In 2022, global CO_2 emissions from transportation increased by over 250 Mt, reaching nearly 8 Gt CO_2. At the sector level, transportation witnessed the most significant rise in emissions, with an increase of nearly 240 Mt globally between 2022 and 2023 [2]. Thus, reducing carbon emissions from the transportation sector is an urgent challenge that must be addressed immediately. Conversely, clean hydrogen offers a promising solution for mitigating climate change and could be pivotal in the decarbonizing of transportation. Fuel cells will enable hydrogen-powered transportation to cut emissions, offering superior efficiency versus conventional engines [3]. Hydrogen production can be categorized into three primary types: gray, blue, and green hydrogen. Gray hydrogen, produced from fossil fuels without carbon capture, produces substantial carbon emissions. Carbon capture, utilization, and storage technologies are critical components in global climate change mitigation strategies, providing an effective method to substantially decrease carbon dioxide emissions from both industrial operations and energy production[4]. Blue hydrogen incorporates carbon capture and storage (CCS), which reduces its carbon footprint significantly [5]. Finally, green hydrogen is produced using renewable energy sources [6]. Grey hydrogen is currently the most economical and preferred pathway for commercial hydrogen generation [7], and green hydrogen represents only about 4% of global industrial hydrogen production [8]. Due to cost and CO_2 emission challenges, blue hydrogen is seen as a transitional solution, facilitating immediate reductions in carbon emissions [9]. Currently, blue hydrogen serves as an essential bridge between high-emission grey hydrogen and zero-emission green hydrogen, which remains limited in scale. While the ultimate goal of the transition is prioritizing green hydrogen through electrolysis, this shift depends significantly on technological advancements in electrolysis methods. Until such breakthroughs occur, blue hydrogen provides a practical intermediate solution on the pathway to a low-carbon hydrogen economy[10] To facilitate the broader adoption of hydrogen fuel, it is essential to plan the development of hydrogen refueling stations(HRSs) and the development of hydrogen fuel in transportation and meeting various sector demands requires long-term planning for optimal production and operation of hydrogen refueling stations. A techno-economic comparison shows wind-based systems are more cost-effective than solar for green hydrogen production in Riyadh, Saudi Arabia[11]. Analysis of five European hydrogen stations shows buses average 14.62 kg per fill with 10-minute refueling times, consuming 7 kg/100 km while operating 10 hours daily with 80% availability[12]. A model for optimal siting and sizing of hydrogen refueling stations is presented to minimize consumer costs through life-cycle cost analysis and supply chain optimization[13]. In Ref. [14], a technical analysis comparing hydrogen refueling stations in Turkey and Spain demonstrates that solar systems work best for Turkey, in contrast, combined solar-wind systems are more efficient in Spain. An optimization study for Al-Kharj examines combined solar and wind technologies with storage systems, achieving efficient hydrogen production at $9.34/kg LCOH[15]. A novel optimization study in Datong analyzes hybrid renewable systems with hydrogen refueling, demonstrating the effective integration of solar power and storage solutions[16]. A techno-economic analysis of a wind-PV hybrid hydrogen station in Çeşme, Turkey demonstrates the feasibility of fueling 25 vehicles daily, with hydrogen production costs ranging from $7.53-7.87/kg using HOMER software[17]. A comparative analysis of three PV-based hydrogen production methods reveals that grid-

connected systems achieve the lowest costs (5.5 €/kg), outperforming standalone systems with batteries (5.74 €/kg) and fuel cells (7.38 €/kg)[18]. This study optimizes a hydrogen refueling station combining PV and electrolyzer, showing trade-offs between CO2 reduction and system capacity utilization while maintaining high operational efficiency[19]. According to research [20], a Moroccan study evaluates solar-powered hydrogen stations for taxis, showing cost reductions with increased capacity.

This study reveals renewable facilities combining photovoltaic storage deliver optimal economics, achieving production expenses of 4.78-5.55 €/kg for clean vehicle support[21]. In Ref.[22], a study on 1GW agrivoltaic systems across five countries demonstrated the feasibility of combining solar power with agriculture for hydrogen production. Their analysis showed that such systems could support millions of hydrogen vehicle refueling annually while maintaining agricultural productivity, with hydrogen production costs ranging from £3.06 to £6.38/kg depending on location. The integrated energy approach can optimize hydrogen production while supporting the simultaneous generation of clean electricity, heat, and cooling which is essential for decarbonizing the energy sector [23].

Discovering enhanced methods to utilize eco-friendly renewable energy sources has become highly significant, as these approaches can mitigate the detrimental impacts of carbon dioxide emissions that threaten our ecosystem, which is already facing concerning levels of climate change[24]. The rise of Power-to-Gas technology signals an innovative breakthrough in energy conversion and storage systems, presenting a hopeful solution for managing renewable energy inconsistency while advancing decarbonization efforts throughout the energy landscape. P2G functions by transforming surplus electricity production into hydrogen-based fuels through electrolytic processes[25]. According to Ref. [26], Research shows that among integrated renewable systems, biomass achieves the highest exergy efficiency while geothermal offers the best economic performance for hydrogen production via electrolysis.

Ref. [27] presents a comprehensive methodology for dimensioning components of an on-site hydrogen refueling station. The system's electrical requirements are fulfilled through a grid-connected photovoltaic array. Considering the intermittent nature of solar resources, the conventional electrical grid provides supplementary power during periods of insufficient generation while also accommodating the export of excess production. Ref. [28] illuminates the prospects for green hydrogen development in Tunisia through a rigorous economic analysis. The study presents a comprehensive assessment of the levelized hydrogen cost and net profit metrics for a photovoltaic-powered hydrogen refueling station, offering a detailed evaluation and discussion of the financial implications. In [29] a novel off-grid integrated energy system structure was proposed to address both market hydrogen demands and the electrical, heating, and cooling requirements of the HRS support building. Through a cost-minimizing mixed integer quadratic constrained programming model, researchers solved optimal sizing and scheduling challenges, with results demonstrating the structure's effectiveness and advantages, as documented.

In [30], an integrated energy system combining wind turbines with an on-site hydrogen refueling station is proposed that can simultaneously satisfy cooling, heating, power, and hydrogen demands. The system determines equipment capacity while optimizing total annual costs. Configurations with varying numbers of wind turbines were analyzed. When equipped with 5 turbines, the system achieves 91% hydrogen self-production with minimal energy redundancy. Ref. [31] analyzes three system configurations: standalone wind park hydrogen refueling stations with battery backup, fuel cell backup, and grid connection. The analysis considers local wind potential, equipment costs, and hydrogen demand. The research aims to determine the optimal sizing for wind turbines, electrolyzers, power converters, and storage tanks. Ref. [32] introduces an off-grid integrated electricity-hydrogen system that incorporates solar and hydroelectric renewable energy sources, serves both industrial and residential loads, and includes electric vehicle charging infrastructure, hydrogen refueling for fuel cell vehicles, natural gas pipeline integration, and seasonal hydrogen storage capabilities.

According to [33], an optimized hybrid renewable energy system with a vanadium redox flow battery for on-site hydrogen production was evaluated for serving 20 fuel cell vehicles across seven South Korean locations. Their analysis reveals levelized hydrogen costs ranging from 8.77-19.1 $/kg and energy costs between 2.1-4.58 $/kWh. The global community faces a crisis as water resources become increasingly scarce and water stress intensifies, necessitating the development of innovative and environmentally friendly technologies to ensure a reliable and sustainable water supply for future generations. The nexus of water and energy systems means that water scarcity can significantly impact the efficiency and reliability of power generation[34]. Moreover, hydrogen production through both natural gas reforming and electricity-to-hydrogen conversion needs substantial water consumption as a feedstock, and expanding these facilities without considering water supply could further intensify water stress. On the one hand, reverse osmosis technology for seawater desalination has proven to be a promising solution to water scarcity. However, one of the key challenges in implementing desalination is public concern over energy consumption[35] and its expansion requires the development of electrical energy production to meet the significant power demands of these facilities.

TABLE 1 provides a summary of recent scientific research related to previous perspectives on hydrogen refueling

stations. Additionally, this table highlights the unique aspects of the present study in comparison to previous research. After reviewing the literature on hydrogen refueling stations, several advantages and limitations become apparent. Most studies [21, 27-33] successfully integrate renewable energy sources with hydrogen production for transportation, demonstrating technical feasibility across different geographical contexts.

TABLE 1 COMPARISON OF THIS STUDY WITH THE LITERATURE REVIEW

Ref.	Year	RES	FC	P2H	H2T	SMR-CCS	RO- WT	HRS Water usage
[27]	2020	✓	×	✓	✓	×	×	×
[28]	2022	✓	×	✓	✓	×	×	×
[29]	2022	✓	×	✓	✓	×	×	×
[21]	2023	✓	✓	✓	✓	×	×	×
[30]	2023	✓	×	✓	✓	×	×	×
[31]	2023	✓	✓	✓	✓	×	×	×
[32]	2024	✓	✓	✓	✓	×	×	×
[33]	2024	✓	×	✓	✓	×	×	×
This paper	2025	✓	✓	✓	✓	✓	✓	✓

However, these works primarily focus on green hydrogen production through electrolysis without considering blue hydrogen alternatives.

A significant limitation in the existing literature is the lack of attention to water requirements for hydrogen production. None of the reviewed studies [21, 27-33] address water usage or incorporate water desalination in HRS, which is crucial for sustainable operation, especially in water-scarce regions. Additionally, while some studies incorporate energy storage solutions and fuel cells, they typically don't optimize for multiple energy carriers simultaneously.

The current paper addresses these gaps by integrating both blue hydrogen and green hydrogen production pathways, incorporating water desalination technology, explicitly accounting for water consumption in hydrogen production, and representing a more comprehensive approach to hydrogen refueling station design and optimization. In summary, the innovations of this paper include the following:

A. Renewable Power and Water Supply for HRS: Providing an optimal solution for the power and water supply of HRS in remote and water-stressed areas, integrating photovoltaic energy, seawater desalination, fuel cell, and storage technologies.

B. Optimal Hydrogen Production Method for HRS: Analyzing the economics of green hydrogen production through water electrolysis and blue hydrogen through methane reforming with carbon capture technology, considering investment costs, natural gas, electricity, and water consumption.

C. Maximization of Photovoltaic Energy Usage: Optimizing surplus photovoltaic energy utilization for green hydrogen production and seawater desalination and storage systems.

This study addresses the optimal design of a hydrogen refueling station by integrating photovoltaic (PV) as a renewable energy source, power to hydrogen(P2H), steam methane reformer equipped by carbon capture (SMR-CCS), fuel cell (FC), seawater desalination (RO), and water and hydrogen storage units (WT & H2T), with focusing on meeting the power and water requirement for hydrogen production in a self-sufficient manner through photovoltaic and seawater desalination. The mathematical model is formulated based on Mixed-Integer Linear Programming (MILP). By selecting a suitable geographical area in southern Iran for station development, historical radiation and temperature data have been examined. Finally, the optimization problem was solved in the PYOMO environment using the CBC solver.

II. The structure of the proposed HRS

The Fig.1, illustrates the schematic diagram of the integrated on-site Hydrogen Refueling Station. The system consists of several components: PV, FC, P2H, SMR-CCS, RO, WT, and H2T. The HRS is connected to the natural gas network. This configuration efficiently integrates diverse energy conversion and storage elements to meet hydrogen demand. Hydrogen is produced through the P2H and SMR-CCS, while the PV and FC provide the necessary power for the HRS. The RO desalinates seawater to supply fresh water for hydrogen production. The sizing and operation of all components are optimized to minimize the net present cost (NPC) of the project.

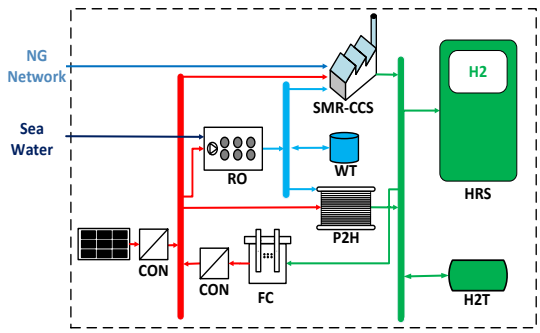

Fig. 1. The schematic of the proposed HRS

III. Mathematical formulation

This paper determines the optimal capacity of the HRS by minimizing the overall project cost, as presented in Eq. (1). In this context, Lf refers to the project's lifetime, and Nn indicates the number of representative days considered. To make the problem more manageable and solvable, the typical days (Nd) are selected according to seasonal periods. The real interest rate (r) is defined in equation (2), where Z and I correspond to the nominal interest rate and annual inflation, respectively.

$$Minimise: \quad (1)$$

$$NPC = (C^{IN} + \sum_{y=1}^{Lf}(C_y^M + C_y^R)/(1+r)^y + \sum_{y=1}^{Lf}\sum_{n=1}^{Nd}\sum_{h=1}^{24} N_n C_{y,n,h}^{NG}/(1+r)^y)$$

$$r = \frac{Z-I}{1+I} \quad (2)$$

The investment, operational, and replacement costs of the HRS components are calculated based on their optimal capacities, as defined in equations (3) to (5).

$$C^{IN} = \sum_{c\in C} \lambda_c^I S_c \quad (3)$$

$$C_y^M = \sum_{c\in C} \lambda_c^M S_c \ \forall\, 1 \le y \le Lf \quad (4)$$

$$C_y^R = \sum_{c\in C} \lambda_{c,y}^R S_c \ \forall\, 1 \le y \le Lf \quad (5)$$

The variable S is associated with the optimal size of the energy HRS components. The parameters $\lambda_c^I, \lambda_c^M \text{ and } \lambda_{c,y}^R$ correspond to the unit costs for investment, operation, and replacement of the HRS components. The replacement factor is only applied to equipment with a shorter useful life than the project's duration, and its value remains zero throughout the equipment's lifespan. When the equipment reaches the end of its useful life, the replacement cost is incurred in the relevant year. The set C refers to the HRS components. Natural gas sourced from the network is utilized in the steam methane reformers to generate hydrogen. The hourly cost of purchasing gas from the network is calculated in equation (6). The parameter $G_{y,n,h}$ represents the quantity of gas purchased per hour, while the other parameter λ^G is associated with the gas price.

$$C_{y,n,h}^{NG} = \lambda^{NG} G_{y,n,h} \quad (6)$$

A. P2H model

The P2H is capable of converting electricity into hydrogen. The mathematical model for the P2H system is formulated based on the relationship between the electricity input and hydrogen output, as shown in Eq. (7). The electrolyzer consumes approximately 55 kW of electrical energy to produce one kilogram of hydrogen at 60% efficiency[36, 37]. Furthermore, Eq. (8) determines the water consumption of the P2H, which is based on the volume of hydrogen produced

$$P_{y,n,h}^{P2H} = k_P^{P2H} Q_{y,n,h}^{P2H} \quad (7)$$

$$W_{y,n,h}^{P2H} = \kappa_W^{P2H} Q_{y,n,h}^{P2H} \quad (8)$$

B. RO model

At present, reverse osmosis using membrane technology is the most widely employed method for seawater desalination. This process requires electrical energy for desalination and is more energy-efficient compared to other methods [38]. In [39], A review of data from over 70 seawater desalination plants reveals that the lowest specific energy consumption for reverse osmosis (RO), considering the plant's additional electrical consumption, is 3.1 kWh/m³.

$$P_{y,n,h}^{RO} = SEC^{RO} W_{y,n,h}^{RO} \quad (9)$$

The parameters $P_{y,n,h}^{RO}, SEC^{RO} \text{ and } W_{y,n,h}^{RO}$ represent, in order, the electrical energy usage in kWh, the volume of freshwater produced in cubic meters, and the specific energy consumption coefficient of the RO plant.

C. FC model

The proposed HRS focuses on utilizing carbon-free power generation systems. Considering the unavailability of the PV at night and its reliance on weather conditions, the FC serves as a controllable energy source. Thus, since electricity can be generated from hydrogen via an FC, this unit is included in the study as described in equation (10).

$$P_{y,n,h}^{FC} = \eta^{FC} Q_{y,n,h}^{FC} \quad (10)$$

D. SMR-CCS

The SMR is a widely used method for hydrogen production, accounting for approximately 76% of global hydrogen production. It is also important to note that hydrogen production from coal gasification represents 22%, while only 2% of global hydrogen production comes from electrolysis[40].

Hydrogen production from natural gas requires the consumption of natural gas, electricity, and water, and results in CO2 emissions. The necessary heat is produced by burning natural gas, while electrical energy is used to set up the required process conditions. In this study, the mathematical model for this unit is developed using equations (11) to (13).

$$P_{y,n,h}^{SMR-CCS} = \kappa_P^{SMR-CCS} Q_{y,n,h}^{SMR-CCS} \quad (11)$$

$$G_{y,n,h}^{SMR-CCS} = \kappa_G^{SMR-CCS} Q_{y,n,h}^{SMR-CCS} \quad (12)$$

$$W_{y,n,h}^{SMR-CCS} = \kappa_W^{SMR-CCS} Q_{y,n,h}^{SMR-CCS} \quad (13)$$

The parameters $Q_{y,n,h}^{SMR-CCS}, K_P^{SMR-CCS}, \text{and } K_G^{SMR-CCS}$ represent the hydrogen production rate in kW, the electricity consumption coefficients, and gas consumption coefficients per kW of hydrogen produced. In[41], The natural gas feed consumption for the SMR is reported to be 3.5 kg of natural

gas per kg of hydrogen produced. The steam methane reformer can be integrated with a carbon capture system, which significantly lowers carbon emissions. However, this setup increases the consumption of methane gas and electricity, depending on the carbon capture level. In this study, a carbon capture rate of 85% is assumed.

E. H2T

In the proposed HRS the hydrogen tank is also considered, and the (14)-(19) related to this component, the hourly stored energy of tank ($E_{y,n,h}^{H2T}$) is updated by (14). According to (15) – (17) and using binary variables ($I_{y,n,h}^{H2T+}$ & $I_{y,n,h}^{H2T-}$), this system can be used in charging ($Q_{y,n,h}^{H2T+}$) or discharging ($Q_{y,n,h}^{H2T+}$) modes. According to (18) the amount of hydrogen stored in the first hour ($E_{y,n,1}^{H2T}$) is the same as the 24th hour ($E_{y,n,1}^{H2T}$). In addition, the amount of initial charge of the tank is also defined as a variable (E_{in}^{H2T}) and its amount will be optimized by (19):

$$E_{y,n,h}^{H2T} = E_{y,n,h-1}^{H2T} + \kappa_{LHV}^{H2}(Q_{y,n,h}^{H2T+} - Q_{y,n,h}^{H2T-}) \quad (14)$$

$$Q_{y,n,h}^{H2T+} \le I_{y,n,h}^{H2T+}\overline{Q}^{H2T} \quad (15)$$

$$Q_{y,n,h}^{H2T-} \le I_{y,n,h}^{H2T-}\overline{Q}^{H2T} \quad (16)$$

$$I_{y,n,h}^{H2T+} + I_{y,n,h}^{H2T-} \le 1 \quad (17)$$

$$E_{y,n,24}^{H2T} = E_{y,n,1}^{H2T} \quad (18)$$

$$E_{y,n,0}^{H2T} = E_{in}^{H2T} \quad (19)$$

The κ_{LHV}^{H2} is related to the lower heat value of hydrogen.

F. WT

The mathematical model of the water storage tank is expressed in (20)- (25). The hourly stored water in the tank ($V_{y,n,h}^{WT}$) is updated by (20) and the WT can be used in charging($Q_{y,n,h}^{WT+}$) or discharging($Q_{y,n,h}^{WT+}$) mode by (21)-(23). According to (24) the amount of water stored in the first hour is the same as the 24th hour. In addition, the amount of initial charge of the tank is also defined as a variable and its value is optimized by (25).

$$V_{y,n,h}^{WT} = V_{y,n,h-1}^{WT} + W_{y,n,h}^{WT+} - W_{y,n,h}^{WT-} \quad (20)$$

$$W_{y,n,h}^{WT+} \le I_{y,n,h}^{WT+}\overline{W}^{WT} \quad (21)$$

$$W_{y,n,h}^{WT-} \le I_{y,n,h}^{WT-}\overline{W}^{WT} \quad (22)$$

$$I_{y,n,h}^{WT+} + I_{y,n,h}^{WT-} \le 1 \quad (23)$$

$$V_{y,n,24}^{WT} = V_{y,n,1}^{WT} \quad (24)$$

$$V_{y,n,0}^{WT} = V_{in}^{WT} \quad (25)$$

G. balance constraints

The balance constraints for electricity, water, hydrogen, and natural gas demands and supplies in the HRS are expressed in (26)- (29), respectively. The electrical energy balance is defined by (26), the water balance by (27), and the hydrogen balance by (28). Finally, (29) balances the import of gas and its consumption in the SMRs.

$$P_{n,s,h}^{D} = P_{n,s,h}^{PV} + P_{n,s,h}^{FC} - P_{n,s,h}^{P2H} - P_{n,s,h}^{SMR\_CCS} - P_{n,s,h}^{RO} \quad (26)$$

$$W_{n,s,h}^{D} = W_{n,s,h}^{RO} - W_{n,s,h}^{P2H} - W_{n,s,h}^{SMR-CCS} - Q_{n,s,h}^{WT+} + Q_{n,s,h}^{WT-} \quad (27)$$

$$Q_{n,s,h}^{D} = Q_{n,s,h}^{P2H} + Q_{n,s,h}^{SMR-CCS} - Q_{n,s,h}^{FC} - Q_{n,s,h}^{H2T+} + Q_{n,s,h}^{H2T-} \quad (28)$$

$$G_{n,s,h} = G_{n,s,h}^{SMR-CCS} \quad (29)$$

H. PV

According to Eq. (30), the amount of power generation from PV depends on the amount of radiation and the temperature of the environment [42, 43].

$$P_{y,n,h}^{PV} = S_{PV} \times \frac{R_{y,n,h}^{PV}}{R_{ref}^{PV}} \times \left[1 - N_T\left(T_{y,n,h}^{PV} + \frac{NOCT - 20}{800}R_{y,n,h}^{PV} - T_{ref}^{PV}\right)\right] \quad (30)$$

The PV power in this model represents the total power of the PV unit at the maximum power point. Also, S_{PV} shows the nominal power of the optimal size for the PV unit at the maximum power point and the standard condition of $R_{ref}^{PV} = 1000W/m^2$ and $T_{ref}^{PV} = 25\,^{\circ}C$ N_T and NOCT respectively show the power temperature coefficient at the maximum power point and nominal operating cell temperature.

IV. Solution method

In this model, the mathematical formulation is presented to minimize investment, operation, and emission costs. The problem is solved using the CBC solver within the PYOMO software package, which supports MILP formulations. PYOMO is an open-source software package based on Python that offers a wide range of optimization capabilities for formulating, solving, and analyzing optimization models [30].

The proposed on-site HRS integrates solar energy, natural gas, and seawater desalination technologies. This study considers the optimal HRS design in Gankhak-e Sheykhi, Bushehr province, Iran. This area benefits from abundant solar and natural gas resources, as illustrated in Fig. 2, and is close to seawater. Historical data on solar radiation and temperature for this region, spanning 22 years, has been sourced from NASA. Irradiance and temperature seasonal averages for typical days have been calculated, as shown in Fig. 3 and Fig. 4.

The HRS is engineered to address specific demands for electricity, water, and hydrogen. In addition to the fixed demands it must fulfill, the HRS components also have variable electricity and gas consumption, which are accounted for in the energy supply and demand balance. Basic design parameters, including energy prices, investment, operational and replacement costs, technical specifications, and parameters for each component, are detailed in Tables 2 to 5.

In this study, the HRS is designed to supply the average hydrogen load of 3200 kg/day, sufficient to refuel 100 trucks, each equipped with a 32 kg hydrogen tank. As shown in Fig.5, during the night, hydrogen demand decreases and reaches its minimum between 24:00 to 7:00. Conversely, during the day, the hydrogen demand increases, peaking between 16:00 to 18:00. Electrical demand of the on-site HRS encompasses both industrial and non-industrial consumptions. It should be mentioned that industrial electrical consumption pertains to the energy required for HRS operations, calculated hourly using mathematical models. According to Fig. 5 the assumed electrical load profile, non-industrial electrical consumption, related to non-industrial buildings such as ventilation and lighting electricity consumption is minimized during the night, specifically from 23:00 to 07:00. During the day, electricity consumption rises due to the activation of welfare services and increased cooling requirements, peaking between 11:00 to 17:00.

Fig. 2. Selected study area: Gankhak-e Sheykhi, Bushehr Province

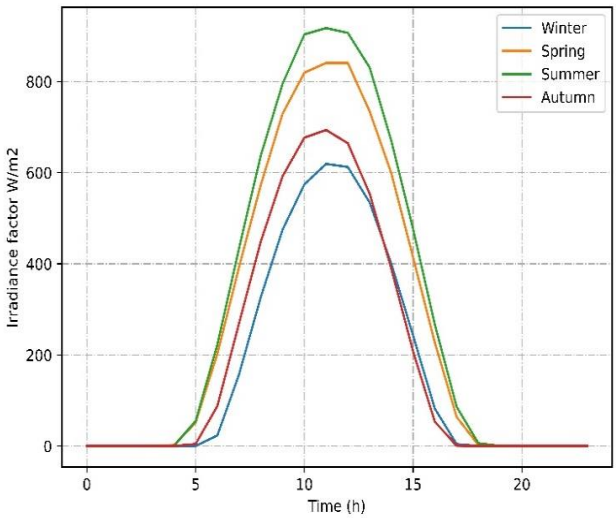

Fig. 3. Seasonal average irradiance

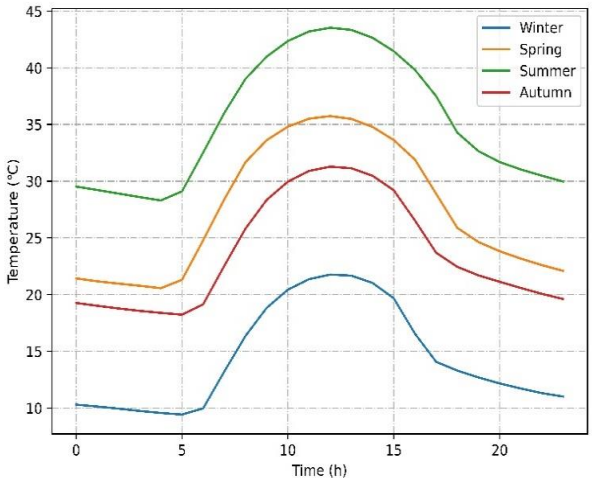

Fig. 4. Seasonal average temperature

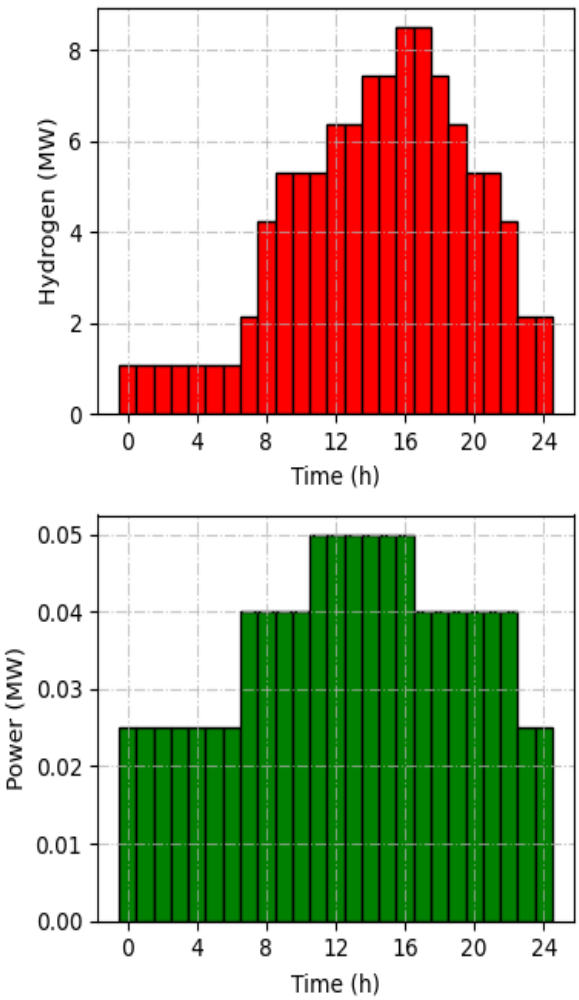

Fig. 5. Hydrogen and Electrical demand of the HRS

TABLE 2 HRS COMPONENTS COST DATA

Item	C^I		C^M		C^R	Lf
PV	1000	$/kW	10	$/kW/year	0	25
FC	1000	$/kW	0	-	500	5
P2H	872	$/kW	19.2	$/kW/year	50	15
SMR_CCS	1583	$/kW	47.5	$/kW/year	0	25
CON	200	$/kW	5	$/kW/year	0	25
H2T	700	$/kg	0	-	200	30
RO	50.8	$/m3/h	0.29	$/m3/year	0	30
WT	311	$/m3/h	31	$/m3/year	0	30

TABLE 3 HRS BASIC DATA

Item	Value	Unit
lifetime	25	year
Interest rate	8	%
Inflation rate	2	%
Annual operation days	336	day
Natural gas price	0.3	$/m3

TABLE 4 THE COEFFICIENT [44, 45]

Component	k^P [kWh/kg H_2]	k^G [kg/kg H_2]	k^W [m^3/kgH_2]
P2H	55	0	0.009
SMR_CCS	4.42	3.4	0.0097

TABLE 5 THE COMPONENT PARAMETERS [39, 46, 47]

Component	Parameters
RO	$SEC = 3.1\ kWh / m^3$
PV	$R_{ref}^{PV} = 1000W / m^2$
	$T_{ref}^{PV} = 25\,^{\circ}C$
	$N_T = -0.45\ \% / {}^{\circ}C$
	$NOCT = 45\,^{\circ}C$

V. Results and discussion

The optimal capacities of the on-site HRS components and the cost breakdown of the project are detailed in Tables 6 and 6. For hydrogen production components: 1- The optimal sizes are 7.76 MW for the SMR-CCS and 0.14 MW for the P2H. 2- The optimal capacity for the H2T is 297 kg. Comparing the capacities, it is evident that the P2H has a relatively minor role compared to the SMR-CCS, with the P2H capacity being less than 2% of the total. The energy storage capacity in the H2T, considering the LHV of hydrogen at 33.3 kWh/kg and an assumed operational limit of 90 %, total 8.9 MWh. Regarding the electricity production components: 1-The optimal sizes are 1.34 MW for the PV and 0.82 MW for the FC. 2- The PV system is notably larger compared to FC. For water supply, an RO with a capacity of 7 m³ and a WT with a capacity of 25 m³ are optimal for meeting the water requirements of the HRS. These optimal sizes ensure the efficient operation and cost-effectiveness of the HRS in meeting hydrogen, electricity, and water demands.

TABLE 6 THE HRS COEFFICIENT OPTIMAL SIZING

Components	Unit	Value
PV	MW	1.34
FC	MW	0.82
CON	MW	2.16
P2H	MW	0.14
SMR-CCS	MW	7.76
H2T	kg	297
RO	m3	7
WT	m3	25

According to the results shown in Table 7, the net present cost of this project for the optimal scheme is $53.13 billion, encompassing installation, repair, and operational expenses. The cost breakdown is as follows: investment costs ($15.22 million), maintenance costs ($5.12 million), replacement costs ($0.95 million), and natural gas purchase costs ($31.84 million). As illustrated in Fig. 6, the most significant portion of the HRS cost is attributed to natural gas expenses (60% of the total cost). The investment cost (IC), maintenance cost (MC), and replacement cost (RC) are replacement costs follow, with a share of 28.9%, 9.6 %, and 1.8%, respectively.

TABLE 7 THE COST BREAKDOWN OF OPTIMAL HRS

`Cost component	Value(M$)
IC	15.22
MC	5.12
RC	0.95
NGC	31.84
NPC	53.13

VI. Optimal operation of the HRS

Figures 7 -9 illustrate the hourly electrical, hydrogen, and water balances in the on-site HRS for the first year, across each season.

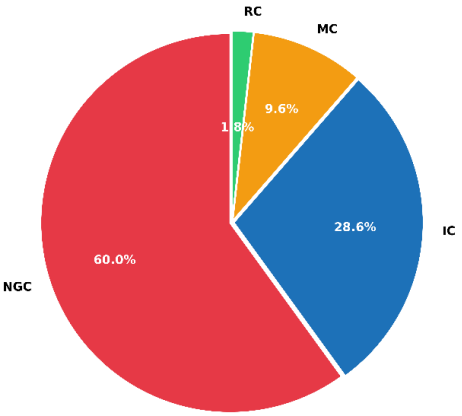

Fig. 6. Percentage of on-site HRS project costs in different sectors

According to Fig. 7, it is evident that the electricity during the day is primarily supplied by the PV system, with its output varying by season. In summer, the PV system reaches its peak output of 1.03 MW at noon, while in winter, the maximum production decreases to 0.79 MW. Conversely, the FC operates as a controllable source, balancing the electrical power when PV output fluctuates. During daylight hours, the FC's power decreases and may even be inactive during specific periods: 8:00 AM- 3:00 PM in spring, 8:00 AM- 4:00 PM in summer, 10:00 AM- 2:00 PM in autumn, and 10:00 AM- 2:00 PM in winter. At night, when solar energy is unavailable, the FC supplies the entire electrical power needed for the on-site HRS. Additionally, the power consumption for the HRS components is depicted. The SMR-CCS, which plays a significant role in hydrogen production, is the largest electricity consumer in the HRS. In the proposed HRS the maximum available power from the PV system is utilized and any surplus electricity generated is used to produce hydrogen through the P2H during the day.

The role of the on-site HRS components in hydrogen balancing is illustrated in Fig 8. In the current structure of the on-site HRS, both the SMR-CCS and P2H contribute to hydrogen production. However, the optimal results show that most of the hydrogen required is produced by the SMR-CCS across all seasons. Fig. 8 reveals that, for most of the 24-hour cycle, the SMR-CCS meets the hydrogen demand, with the P2H's contribution being minimal. Additionally, a 40% minimum production limit for the SMR-CCS results in surplus hydrogen being stored in the H2T between 22:00 and 07:00, when demand falls below this production threshold. This stored hydrogen is discharged during the day, although the discharge period varies slightly across seasons. In summer and spring, the P2H's higher participation at noon requires the H2T to release some of its stored energy in the morning to accommodate the P2H's energy needs.

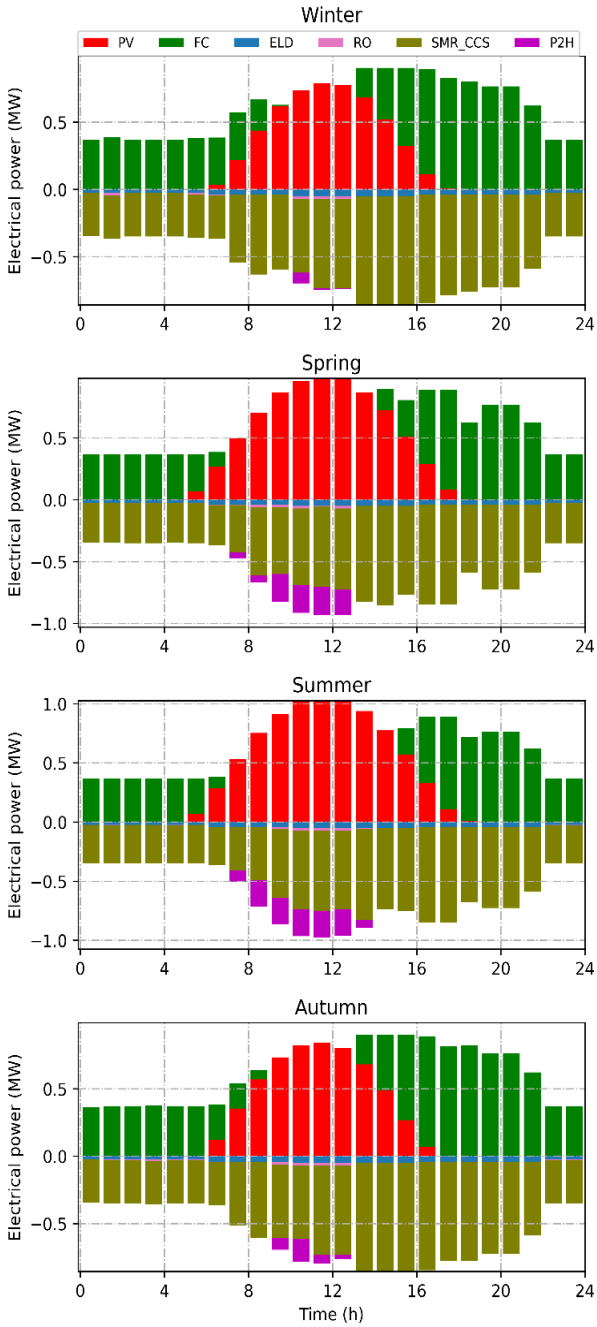

Fig. 7. Electrical power balance in various seasons

In this study, the water required for hydrogen production in the on-site HRS is supplied by an optimized reverse osmosis (RO) unit and a water tank. The RO unit desalinates seawater using electrical power. Fig. 9 shows the water balance within the on-site HRS. This unit operates predominantly during the day when solar energy is abundant. The RO's peak operation occurs between 11:00 and 14:00 in all seasons except winter. In winter, the RO operates between 11:00 and 14:00.

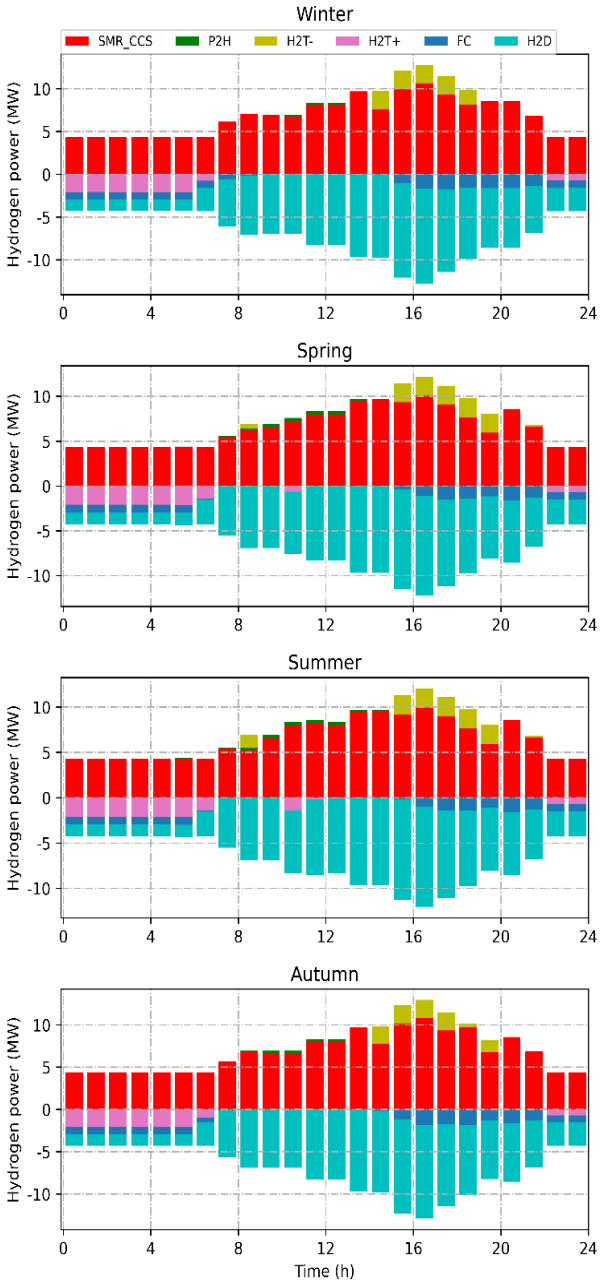

Fig. 8. Hydrogen power balance in various seasons

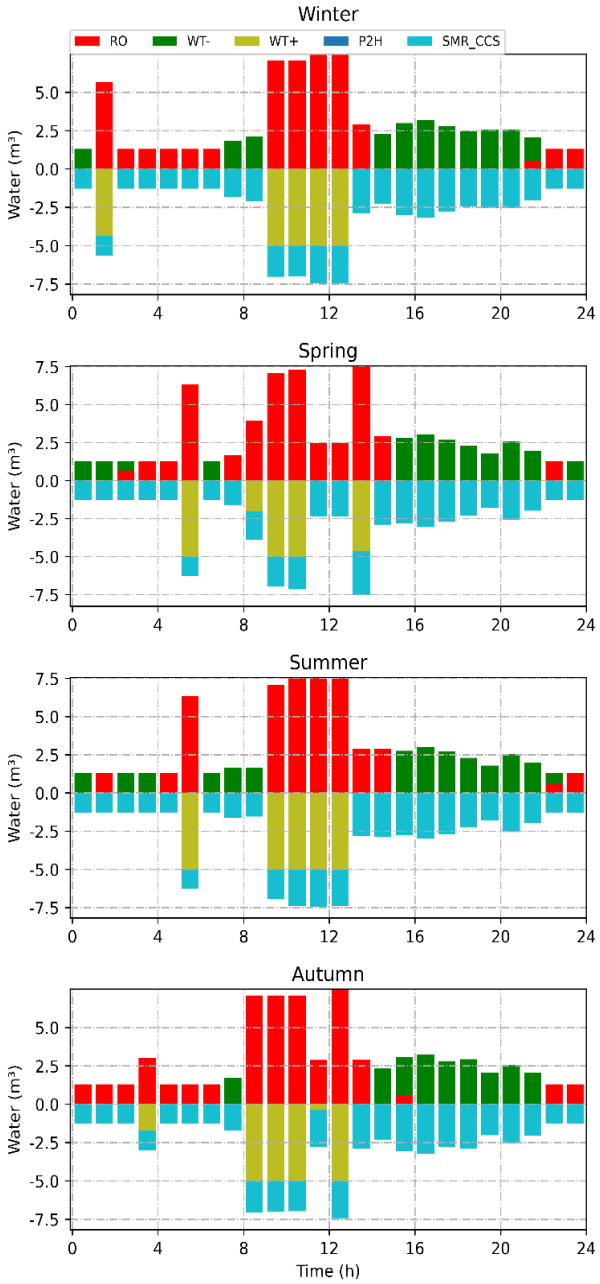

Fig. 9. Water balance in various seasons

The RO is generally inactive between 14:00 and 23:00 across all seasons except summer. During summer, due to increased electricity production from PV in the afternoon, some of the surplus electricity is used by the RO, allowing it to operate until 15:00. During this period, the water tank is adequately filled and used during the night. Additionally, since the operating hours of the RO in winter and autumn are shorter compared to other seasons, it is necessary to utilize it more during the night to balance water production and consumption. In winter, the RO is reactivated from 23:00 to 08:00, with its utilization optimized throughout these hours. Conversely, the RO's utilization is lowest during these hours in summer.

VII. The Levelized Cost of Hydrogen

The Levelized Cost of Hydrogen (LCOH) metric quantifies the ratio of NPC to cumulative hydrogen production throughout the HRS's lifespan. The LCOH will be determined using (31).

$$LCOH = \frac{NPC}{\sum_{y=1}^{Lf}\sum_{n=1}^{Nd}\sum_{h=1}^{24} Q_{y,n,h}^{D} / (1+r)^{y}} \quad (31)$$

In order to validate our research outcomes, we compared our results with established literature as presented in Table 8. This table chronicles the evolution of hydrogen production

economics through various Power-to-Hydrogen (P2H) implementations from 2020 to 2025. Our hybrid system, combining P2H with SMR-CCS, achieves a remarkable LCOH of $3.82/kg. This economic performance demonstrates a substantial advantage when contrasted with previous research efforts. Contemporary studies published in 2024 reported significantly higher production costs, with values ranging from $8.77-$19.1[33] and $11.36 [48]. Similarly, projections for 2025 technologies in earlier research anticipated costs between $13.81-$17.52 [49], while studies from 2020-2023 documented LCOH figures between $5.17 and $13.55 [21, 27, 31, 49]. The marked cost reduction achieved in our research can be attributed to the novel integration approach that leverages complementary strengths of both P2H and SMR-CCS technologies. This strategic combination optimizes resource utilization and operational efficiency, yielding a cost structure that substantially improves upon single-technology solutions. The economic advantage demonstrated here suggests promising pathways toward commercially viable low-carbon hydrogen production.

TABLE 8 LCOH in Recent Literature

Ref.	Year	Hydrogen Production Method	LCOH [$/kg]
[27]	2020	P2H	8.96-13.55
[50]	2020	P2H	5.51*-6.12*
[21]	2023	P2H	5.17*-6*
[31]	2023	P2H	6.75*
[33]	2024	P2H	8.77–19.1
[48]	2024	P2H	11.36*
[49]	2025	P2H	13.81*-17.52*
This paper	2025	P2H & SMR-CCS	3.76

*Values were converted from Euro to US Dollar using the annual average exchange rates: 1.1410 (2020), 1.0817 (2023), and 1.0820 (2024) as reported by the Federal Reserve Economic Data (FRED, Series *AEXUSEU*)[51] using the monthly average exchange rates: 1.0356 (Jan 2025) as reported by the Federal Reserve Economic Data (FRED, Series EXUSEU)[52]

VIII. Sensitivity analysis

This section presents a comprehensive sensitivity analysis of the hydrogen production system's economic performance metrics net present cost and levelized cost of hydrogen concerning six key parameters: natural gas price, investment costs, project lifetime, interest rate, and solar radiation. The analysis evaluates how variations in these parameters within a ±10% range affect the system's economic viability.

I. Parameter Impact on NPC

Figure 10 illustrates how changes in key parameters within a ±10% range affect the NPC. Natural gas price shows the most significant impact with a strong linear relationship, where a 10% increase results in approximately 12.5% higher costs from 56.3 to 62.5 million dollars, demonstrating the substantial contribution of fuel expenses to the system's economics. Interest rate displays an inverse relationship to NPC, where a 10% increase reduces costs by about 8% from 56.3 to 51.8 million dollars, reflecting how financing conditions significantly impact long-term project economics. Investment costs and project lifetime show moderate influences with similar positive slopes, indicating that higher capital costs or longer project durations both increase overall system costs proportionally. Solar Radiation exhibits an almost horizontal line with a slight negative slope, indicating minimal impact on NPC across the variation range. This stability suggests that the system design effectively mitigates potential economic risks associated with solar resource variability, making the proposed hybrid hydrogen production system resilient to fluctuations in renewable energy availability.

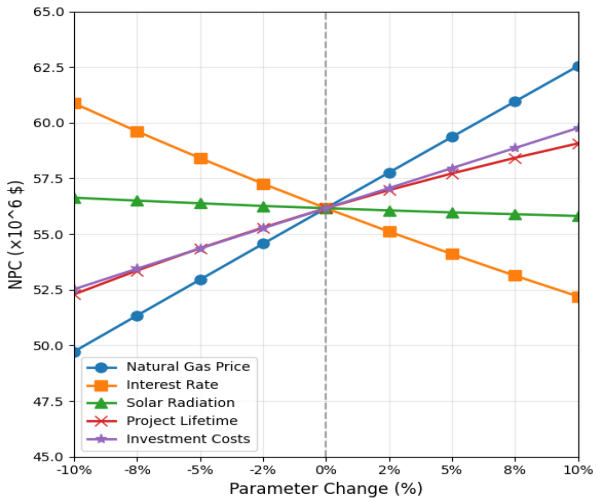

Fig. 10. Impact of varying parameters on the NPC

J. Parameter Impact on LCOH

Figure 11 illustrates how changes in key parameters within a ±10% range affect the LCOH. Natural gas price demonstrates the most significant influence, showing a strong linear relationship where a 10% increase raises LCOH from 4.02 to 4.50 $/kg while a 10% decrease reduces it to 3.58 $/kg. This substantial impact highlights the critical role of fuel costs in hydrogen production economics. Investment costs follow with moderate influence, showing a positive correlation where increased capital expenditure directly increases production costs. Project lifetime displays an inverse relationship to LCOH, with longer durations reducing unit costs as capital expenses are distributed over more production years. Interest rate shows a modest positive

correlation with LCOH, indicating that financing conditions affect production costs but less dramatically than fuel prices. Solar radiation exhibits minimal influence with an almost horizontal trend line, confirming the system's economic resilience to solar energy variability. This stability represents a valuable characteristic of the hybrid hydrogen production system, particularly in regions with seasonal weather patterns.

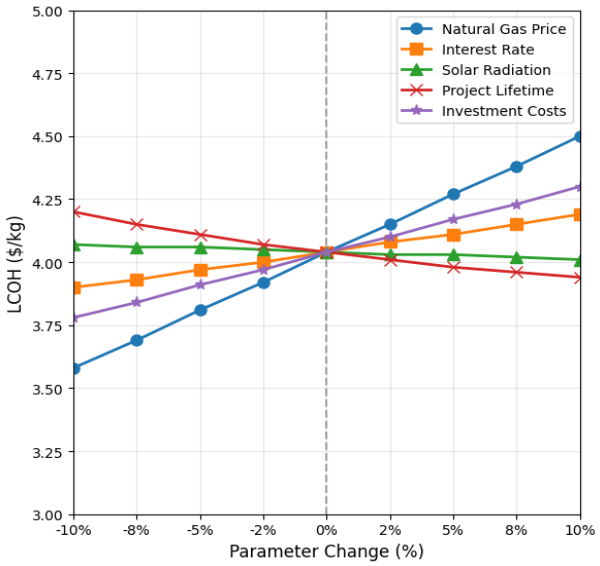

Fig. 11. Impact of varying parameters on the LCOH

IX. Practical Significance of Research Findings

To ensure the practical applicability of this research's results, the following aspects have been considered in both the mathematical modeling and the case study:

a) Considering that both hydrogen production pathways require multiple inputs, this research's mathematical modeling has comprehensively addressed resource requirements. For blue hydrogen production through SMR-CCS, the model accounts for methane gas as the main feedstock along with electricity and water consumption. Similarly, for green hydrogen production, both electricity and water requirements are incorporated in the P2H modeling. To ensure the HRS's self-sufficiency and avoid placing demands on existing infrastructure, the research includes optimal sizing and operation of seawater desalination with water storage capabilities. The electricity consumption of all processes, including desalination, has been included in the comprehensive modeling approach.

b) The HRS location in southern Iran was strategically selected to ensure reliable access to its three essential inputs: natural gas, seawater, and renewable resources. This coastal positioning guarantees uninterrupted resource availability throughout the planning horizon. To maximize renewable energy utilization, the specific site was chosen within high-potential photovoltaic areas identified by the SATBA organization in Bushehr province[53]. The design ensures complete independence in electricity supply through optimal sizing of solar components, informed by a comprehensive analysis of 22 years of historical NASA weather data. This integrated approach to site selection and renewable energy system design creates a self-sufficient hydrogen production facility with secure resource access.

Given the considerations mentioned above and based on the optimal sizing obtained for components, it is evident that implementing blue hydrogen within the planned horizon will be more optimal than green hydrogen. Research comparisons confirm that our hybrid blue-green hydrogen model achieves lower production costs than green hydrogen alternatives. Furthermore, the development of both production pathways enhances resource delivery security for hydrogen refueling stations, addressing a critical requirement for reliable hydrogen supply infrastructure.

X. Conclusion

This study presents a comprehensive approach for developing low-carbon hydrogen refueling stations with integrated water management. Key findings include:

Sustainable Water and Power Supply: The research optimizes both water and power provision through an integrated systems approach. For power management, the study incorporates photovoltaics, fuel cells, and hydrogen storage with precisely modeled component requirements. For water supply, the system includes seawater desalination and water storage facilities specifically designed to meet the substantial water demands of hydrogen production via electrolysis, ensuring a sustainable and independent water supply chain. This comprehensive approach to resource management creates a self-sufficient system capable of reliable hydrogen production without dependence on external water or power infrastructure.

Cost-Competitive Hydrogen Production: Analysis of investment, maintenance, and operational costs reveals natural gas-based hydrogen production with carbon capture remains economically dominant, comprising over 95% of the required capacity compared to electrolysis. Our hybrid system achieves an LCOH of $3.82/kg, substantially lower than comparable studies reporting costs between $5.17-$19.1/kg. This economic advantage demonstrates how strategic integration of complementary technologies improves cost efficiency.

Optimized Resource Management and System Flexibility: The integration of water desalination, storage systems, and power-to-hydrogen conversion achieves maximum renewable energy utilization by directing surplus photovoltaic energy to water treatment and green hydrogen production. This integrated approach enhances overall system flexibility, with the combination of reverse osmosis and water storage reducing optimal RO capacity by 15%.

Robust System Design: Sensitivity analysis confirms the system's remarkable resilience to parameter variations. Natural gas price shows the most impact on economics, while solar radiation exhibits minimal influence, indicating the system effectively mitigates risks associated with renewable resource variability. This stability ensures reliable performance across changing conditions.

Future work will explore the impact of PV system optimization through tracking systems to maximize solar energy capture. The research will also evaluate alternative energy management strategies and their influence on hybrid energy system design and performance. These enhancements aim to further improve system efficiency and reduce costs as electrolysis technology advances, supporting the transitional pathway from blue to green hydrogen production while maintaining consistent resource delivery security.

REFERENCES

[1] IEA, "CO2 Emissions in 2022," IEA, 2023. [Online]. Available: https://iea.blob.core.windows.net/assets/3c8fa115-35c4-4474-b237-1b00424c8844/CO2Emissionsin2022.pdf

[2] IEA, "CO2 Emissions in 2023," 2024. [Online]. Available: https://iea.blob.core.windows.net/assets/33e2badc-b839-4c18-84ce-f6387b3c008f/CO2Emissionsin2023.pdf

[3] E. Monteiro and P. S. D. Brito, "Hydrogen supply chain: Current status and prospects," *Energy Storage,* vol. 5, no. 7, p. e466, 2023, doi: 10.1002/est2.466.

[4] E. Hanson, C. Nwakile, and V. O. Hammed, "Carbon capture, utilization, and storage (CCUS) technologies: Evaluating the effectiveness of advanced CCUS solutions for reducing CO2 emissions," *Results in Surfaces and Interfaces,* vol. 18, p. 100381, 2025/01/01/ 2025, doi: 10.1016/j.rsurfi.2024.100381.

[5] A. Ajanovic, M. Sayer, and R. Haas, "The economics and the environmental benignity of different colors of hydrogen," *International Journal of Hydrogen Energy,* vol. 47, no. 57, pp. 24136-24154, 2022/07/05/ 2022, doi: 10.1016/j.ijhydene.2022.02.094.

[6] Q. Hassan, S. Algburi, A. Z. Sameen, H. M. Salman, and M. Jaszczur, "Green hydrogen: A pathway to a sustainable energy future," *International Journal of Hydrogen Energy,* vol. 50, pp. 310-333, 2024/01/02/ 2024, doi: 10.1016/j.ijhydene.2023.08.321.

[7] M. H. Ali Khan, R. Daiyan, P. Neal, N. Haque, I. MacGill, and R. Amal, "A framework for assessing economics of blue hydrogen production from steam methane reforming using carbon capture storage & utilisation," *International Journal of Hydrogen Energy,* vol. 46, no. 44, pp. 22685-22706, 2021/06/28/ 2021, doi: 10.1016/j.ijhydene.2021.04.104.

[8] S. Shiva Kumar and H. Lim, "An overview of water electrolysis technologies for green hydrogen production," *Energy Reports,* vol. 8, pp. 13793-13813, 2022/11/01/ 2022, doi: 10.1016/j.egyr.2022.10.127.

[9] O. Massarweh, M. Al-khuzaei, M. Al-Shafi, Y. Bicer, and A. S. Abushaikha, "Blue hydrogen production from natural gas reservoirs: A review of application and feasibility," *Journal of CO2 Utilization,* vol. 70, p. 102438, 2023/04/01/ 2023, doi: 10.1016/j.jcou.2023.102438.

[10] F. S. AlHumaidan, M. Absi Halabi, M. S. Rana, and M. Vinoba, "Blue hydrogen: Current status and future technologies," *Energy Conversion and Management,* vol. 283, p. 116840, 2023/05/01/ 2023, doi: 10.1016/j.enconman.2023.116840.

[11] I. B. Mansir, P. C. Okonkwo, and N. Farouk, "Technoeconomic Optimization of a Photovoltaic Wind Energy-Based Hydrogen Refueling Station: A Case Study," *Energy Technology,* vol. 11, no. 7, p. 2201490, 2023, doi: 10.1002/ente.202201490.

[12] R. Caponi, A. Monforti Ferrario, L. Del Zotto, and E. Bocci, "Hydrogen refueling stations and fuel cell buses four year operational analysis under real-world conditions," *International Journal of Hydrogen Energy,* vol. 48, no. 54, pp. 20957-20970, 2023/06/29/ 2023, doi: 10.1016/j.ijhydene.2022.10.093.

[13] H. Sun, C. He, X. Yu, M. Wu, and Y. Ling, "Optimal siting and sizing of hydrogen refueling stations considering distributed hydrogen production and cost reduction for regional consumers," *International Journal of Energy Research,* vol. 43, no. 9, pp. 4184-4200, 2019, doi: 10.1002/er.4544.

[14] M. Gökçek *et al.*, "Optimum sizing of hybrid renewable power systems for on-site hydrogen refuelling stations: Case studies from Türkiye and Spain," *International Journal of Hydrogen Energy,* vol. 59, pp. 715-729, 2024/03/15/ 2024, doi: 10.1016/j.ijhydene.2024.02.068.

[15] P. C. Okonkwo *et al.*, "Utilization of renewable hybrid energy for refueling station in Al-Kharj, Saudi Arabia," *International Journal of Hydrogen Energy,* vol. 47, no. 53, pp. 22273-22284, 2022/06/26/ 2022, doi: 10.1016/j.ijhydene.2022.05.040.

[16] J. He, Y. Wu, M. Wu, M. Xu, and F. Liu, "Two-stage configuration optimization of a novel standalone renewable integrated energy system coupled with hydrogen refueling," *Energy Conversion and Management,* vol. 251, p. 114953, 2022/01/01/ 2022, doi: 10.1016/j.enconman.2021.114953.

[17] M. Gökçek and C. Kale, "Techno-economical evaluation of a hydrogen refuelling station powered by Wind-PV hybrid power system: A case study for İzmir-Çeşme," *International Journal of Hydrogen Energy,* vol. 43, no. 23, pp. 10615-10625, 2018/06/07/ 2018, doi: 10.1016/j.ijhydene.2018.01.082.

[18] E. M. Barhoumi, P. C. Okonkwo, I. Ben Belgacem, M. Zghaibeh, and I. Tlili, "Optimal sizing of photovoltaic systems based green hydrogen refueling stations case study Oman," *International Journal of Hydrogen Energy,* vol. 47, no. 75, pp. 31964-31973, 2022/09/01/ 2022, doi: 10.1016/j.ijhydene.2022.07.140.

[19] H. Aki, I. Sugimoto, T. Sugai, M. Toda, M. Kobayashi, and M. Ishida, "Optimal operation of a photovoltaic generation-powered hydrogen production system at a hydrogen refueling station," *International Journal of Hydrogen Energy,* vol. 43, no. 32, pp. 14892-14904, 2018/08/09/ 2018, doi: 10.1016/j.ijhydene.2018.06.077.

[20] S. Bahou, "Techno-economic assessment of a hydrogen refuelling station powered by an on-grid photovoltaic solar system: A case study in Morocco," *International Journal of Hydrogen Energy,* vol. 48, no. 61, pp. 23363-23372, 2023/07/19/ 2023, doi: 10.1016/j.ijhydene.2023.03.220.

[21] E. M. Barhoumi, "Optimal design of standalone hybrid solar-wind energy systems for hydrogen-refueling station Case study," *Journal of Energy Storage,* vol. 74, p. 109546, 2023/12/25/ 2023, doi: 10.1016/j.est.2023.109546.

[22] J. Baker, M. Guler, A. Medonna, Z. Li, and A. Ghosh, "Analysis of large-scale (1GW) off-grid agrivoltaic solar farm for hydrogen-powered fuel cell electric vehicle

(HFCEV) charging station," *Energy Conversion and Management,* vol. 323, p. 119184, 2025/01/01/ 2025, doi: 10.1016/j.enconman.2024.119184.

[23] N. Li, X. Zhao, X. Shi, Z. Pei, H. Mu, and F. Taghizadeh-Hesary, "Integrated energy systems with CCHP and hydrogen supply: A new outlet for curtailed wind power," *Applied Energy,* vol. 303, p. 117619, 2021/12/01/ 2021, doi: 10.1016/j.apenergy.2021.117619.

[24] A. Riki, M. Oukati Sadegh, and O. Narouei, "Flexibility-Constrained Energy Management of Smart Energy Hubs Considering Peer to Peer Transactive Energy and Demand Response Program," *International Journal of Industrial Electronics Control and Optimization,* vol. 8, no. 1, pp. 67-82, 2025, doi: 10.22111/ieco.2024.49216.1587.

[25] M. Feili and M. T. Aameli, "The P2P Energy Management Scheme for Integrated Energy Microgrid Considering P2G and Electricity Network Fee," *International Journal of Industrial Electronics Control and Optimization,* vol. 8, no. 1, pp. 1-23, 2025, doi: 10.22111/ieco.2024.49044.1583.

[26] M. Zoghi, N. Hosseinzadeh, S. Gharaie, and A. Zare, "4E comprehensive comparison and optimization of different renewable power sources for green hydrogen production," *Renewable Energy,* vol. 240, p. 122254, 2025/02/15/ 2025, doi: 10.1016/j.renene.2024.122254.

[27] R. P. Micena, O. R. Llerena-Pizarro, T. M. de Souza, and J. L. Silveira, "Solar-powered Hydrogen Refueling Stations: A techno-economic analysis," *International Journal of Hydrogen Energy,* vol. 45, no. 3, pp. 2308-2318, 2020/01/13/ 2020, doi: 10.1016/j.ijhydene.2019.11.092.

[28] E. M. Barhoumi *et al.*, "Techno-economic analysis of photovoltaic-hydrogen refueling station case study: A transport company Tunis-Tunisia," *International Journal of Hydrogen Energy,* vol. 47, no. 58, pp. 24523-24532, 2022/07/08/ 2022, doi: 10.1016/j.ijhydene.2021.10.111.

[29] Y. Pang, L. Pan, J. Zhang, J. Chen, Y. Dong, and H. Sun, "Integrated sizing and scheduling of an off-grid integrated energy system for an isolated renewable energy hydrogen refueling station," *Applied Energy,* vol. 323, p. 119573, 2022/10/01/ 2022, doi: 10.1016/j.apenergy.2022.119573.

[30] X. Zhao, H. Mu, N. Li, X. Shi, C. Chen, and H. Wang, "Optimization and analysis of an integrated energy system based on wind power utilization and on-site hydrogen refueling station," *International Journal of Hydrogen Energy,* vol. 48, no. 57, pp. 21531-21543, 2023/07/05/ 2023, doi: 10.1016/j.ijhydene.2023.03.056.

[31] E. M. Barhoumi *et al.*, "Techno-economic optimization of wind energy based hydrogen refueling station case study Salalah city Oman," *International Journal of Hydrogen Energy,* vol. 48, no. 26, pp. 9529-9539, 2023/03/26/ 2023, doi: 10.1016/j.ijhydene.2022.12.148.

[32] R. Hemmati, S. M. Bornapour, and H. Saboori, "Standalone hybrid power-hydrogen system incorporating daily-seasonal green hydrogen storage and hydrogen refueling station," *Energy,* vol. 295, p. 131122, 2024/05/15/ 2024, doi: 10.1016/j.energy.2024.131122.

[33] Y. Choi and S. Bhakta, "Hybrid solar photovoltaic-wind turbine system for on-site hydrogen production: A techno-economic feasibility analysis of hydrogen refueling Station in South Korea's climatic conditions," *International Journal of Hydrogen Energy,* vol. 93, pp. 736-752, 2024/12/03/ 2024, doi: 10.1016/j.ijhydene.2024.11.037.

[34] Y. Wang, Z. Zhou, G. Betrie, K. Zhang, and E. Yan, "Power generation-cooling water Nexus: Impacts of cooling water shortage on power system operation - a simulation case study in Illinois, U.S," *Applied Energy,* vol. 377, p. 124440, 2025/01/01/ 2025, doi: 10.1016/j.apenergy.2024.124440.

[35] H. Shemer, S. Wald, and R. Semiat, "Challenges and Solutions for Global Water Scarcity," *Membranes,* vol. 13, no. 6, p. 612, 2023, doi: 10.3390/membranes13060612.

[36] K. Bareiß, C. de la Rua, M. Möckl, and T. Hamacher, "Life cycle assessment of hydrogen from proton exchange membrane water electrolysis in future energy systems," *Applied Energy,* vol. 237, pp. 862-872, 2019, doi: 10.1016/j.apenergy.2019.01.001.

[37] X. Shi, X. Liao, and Y. Li, "Quantification of fresh water consumption and scarcity footprints of hydrogen from water electrolysis: A methodology framework," *Renewable Energy,* vol. 154, pp. 786-796, 2020/07/01/ 2020, doi: 10.1016/j.renene.2020.03.026.

[38] H. Mehrjerdi, "Modeling and integration of water desalination units in thermal unit commitment considering energy and water storage," *Desalination,* vol. 483, p. 114411, 2020, doi: 10.1016/j.desal.2020.114411.

[39] J. Kim, K. Park, D. R. Yang, and S. Hong, "A comprehensive review of energy consumption of seawater reverse osmosis desalination plants," *Applied Energy,* vol. 254, p. 113652, 2019, doi: 10.1016/j.apenergy.2019.113652.

[40] " Enabling a low-carbon economy," in "Hydrogen Strategy," U.S. DEPARTMENT OF ENERGY, 2020. [Online]. Available: https://www.energy.gov/sites/prod/files/2020/07/f76/USDOE_FE_Hydrogen_Strategy_July2020.pdf

[41] E. Cetinkaya, I. Dincer, and G. F. Naterer, "Life cycle assessment of various hydrogen production methods," *International Journal of Hydrogen Energy,* vol. 37, no. 3, pp. 2071-2080, 2012/02/01/ 2012, doi: 10.1016/j.ijhydene.2011.10.064

[42] J. Karkhaneh, Y. Allahvirdizadeh, H. Shayanfar, and S. Galvani, "Risk-constrained probabilistic optimal scheduling of FCPP-CHP based energy hub considering demand-side resources," *International Journal of Hydrogen Energy,* vol. 45, no. 33, pp. 16751-16772, 2020, doi: 10.1016/j.ijhydene.2020.04.131.

[43] Y. Riffonneau, S. Bacha, F. Barruel, and S. Ploix, "Optimal power flow management for grid connected PV systems with batteries," *IEEE Transactions on sustainable energy,* vol. 2, no. 3, pp. 309-320, 2011, doi: 10.1109/TSTE.2011.2114901.

[44] M. Katebah, M. m. Al-Rawashdeh, and P. Linke, "Analysis of hydrogen production costs in Steam-Methane Reforming considering integration with electrolysis and CO2 capture," *Cleaner Engineering and Technology,* vol. 10, p. 100552, 2022/10/01/ 2022, doi: 10.1016/j.clet.2022.100552.

[45] A. O. Oni, K. Anaya, T. Giwa, G. Di Lullo, and A. Kumar, "Comparative assessment of blue hydrogen from steam methane reforming, autothermal reforming, and natural gas decomposition technologies for natural gas-producing regions," *Energy Conversion and Management,* vol. 254, p. 115245, 2022/02/15/ 2022, doi: 10.1016/j.enconman.2022.115245.

[46] Y. Allahvirdizadeh, H. Shayanfar, and M. P. Moghaddam, "Stochastic expansion planning of transmission system and energy hubs in the presence of correlated uncertain variables," *IET Generation, Transmission & Distribution,* vol. 17, no. 4, pp. 911-946, 2023, doi: 10.1049/gtd2.12715.

[47] F. A. Kassab, B. Celik, F. Locment, M. Sechilariu, S. Liaquat, and T. M. Hansen, "Optimal sizing and energy management of a microgrid: A joint MILP approach for

minimization of energy cost and carbon emission," *Renewable Energy,* vol. 224, p. 120186, 2024/04/01/ 2024, doi: 10.1016/j.renene.2024.120186.
[48] R. Caponi, E. Bocci, and L. Del Zotto, "On-site hydrogen refuelling station techno-economic model for a fleet of fuel cell buses," *International Journal of Hydrogen Energy,* vol. 71, pp. 691-700, 2024/06/19/ 2024, doi: 10.1016/j.ijhydene.2024.05.216.
[49] N. Wolf, R. Neuber, A. Mädlow, and M. Höck, "Techno-economic analysis of green hydrogen supply for a hydrogen refueling station in Germany," *International Journal of Hydrogen Energy,* vol. 106, pp. 318-333, 2025/03/06/ 2025, doi: 10.1016/j.ijhydene.2025.01.424.
[50] P. K. Rose and F. Neumann, "Hydrogen refueling station networks for heavy-duty vehicles in future power systems," *Transportation Research Part D: Transport and Environment,* vol. 83, p. 102358, 2020/06/01/ 2020, doi: 10.1016/j.trd.2020.102358.
[51] B. o. G. o. t. F. R. S. (US). U.S. Dollars to Euro Spot Exchange Rate [AEXUSEU] [Online] Available: https://fred.stlouisfed.org/series/AEXUSEU
[52] B. o. G. o. t. F. R. S. (US). U.S. Dollars to Euro Spot Exchange Rate [EXUSEU] [Online] Available: https://fred.stlouisfed.org/series/EXUSEU
[53] [Online]. Available: https://www.satba.gov.ir/suna_content/media/image/2021/01/8717_orig.pdf

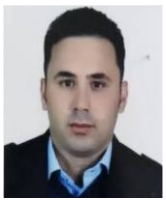

Hamed Maleki received MS degree at SBU University, Iran, 2012. He is currently pursuing his PhD's degree in electrical engineering from Shahid Beheshti University, Tehran. His research interest's energy hub optimization, planning, hydrogen and low-carbon dispatch in power systems.

Mohammad Sadegh Sepasian received the B.Sc. degree from Tabriz University (Iran) in 1990 and the M.Sc. and Ph.D. degrees from Tehran University and Tarbiat Modares University (Iran) in 1993 and 1999, respectively. Since 1994, he has been with Abbaspour Technical and Engineering Department, Shahid Beheshti University in Tehran, Iran where he is currently an associate professor. He managed several national projects for the Iranian power grid. His research interests are distribution networks, power system planning, electric vehicles, and smart grids.

Mohammad Reza Aghamohammadi was born in Iran on August 5, 1955. He received his BSC degree from Sharif University of Technology 1985, MSc degree from Manchester University (UMIST) in 1989 and his PhD from Tohoku University, Japan in 1994. He is professor of the electrical engineering department and head of Iran Dynamic Research Center. His research interest includes application of artificial intelligent techniques and non-model based approaches for dynamic security assessment and enhancement of power systems.

Mousa Marzband (SMIEEE17) is a distinguished academic and Fellow of the Higher Education Academy, recognized for his pioneering contributions to electrical engineering and clean energy systems. With over 140 publications in top-tier journals, his research has garnered more than 11,700 citations and an h-index of 61. His global influence has been acknowledged by Thomson Reuters, ranking him among the top 1% of researchers (2019–2021), and by Stanford University, listing him among the top 2% worldwide (2022–2023).Prof. Marzband has successfully secured over £2.5 million in research funding from prestigious organizations, including Innovate UK, EPSRC (UK), the Qatar National Research Fund, and the Marie Skłodowska-Curie Actions (EU). His funded projects span a wide range of industrial and academic applications, from offshore wind power systems in the UK to green hydrogen development in Azerbaijan and capacity allocation studies in Australia and the UK.with 14 years of academic leadership and over eight years of industrial experience, Prof. Marzband bridges the gap between research and real-world implementation. His expertise lies in renewable energy integration, power systems, and grid resilience, driving advancements in sustainable energy solutions and e-mobility. Through global collaborations, he continues to shape the future of energy systems, accelerating the transition toward a net-zero future.

IECO

This page intentionally left blank.

International Journal Of
Industrial Electronics Control and Optimization
Print ISSN: 3517-2645
Online ISSN: 3568-2645
Homepage: https://ieco.usb.ac.ir/

On the Advance of Flyback CCM Control Strategies: a Comprehensive Review

Saleh Mohammadi[1] | Hamidreza Izadfar[2] | Naser Eskandarian[2]

[1]Department of Electrical and Computer Engineering, Esfarayen university of technology, Esfarayen, North Khorasan, Iran
[2]Department of Electrical and Computer Engineering, Semnan university, Semnan, Iran
Corresponding author's email: s.mohammadi@esfarayen.ac.ir

Article Info

Article type:
Review Article
Article history:
Received: 20-October-2024
Received in revised form: 10-December-2024
Accepted: 17-December-2024
Published online: 23-Sep-2025
Keywords:
Flyback micro-inverter,
photovoltaic system,
right-half plane,
stability.

ABSTRACT

This research aims to provide a comprehensive review of various CCM control strategies for flyback inverters. The study is carried out based on published data in reports, papers, and other available online documents. The introduced control strategies make use of different approaches to dominate the constraints on determining the feedback control system gains caused by the zero put on right-half-plane (RHP) and dynamics of the LC filter. Thus, the tracking of the considered output current is accurately implemented and the introduced control systems carry out the attenuation of disturbances. Moreover, zero steady-state error and the stability requirements are fulfilled by properly regulating the control signal. The best control structure should be enough fast to employ the fewest number of delays in its structure resulting the burden in the computational system being considerably decreased.

NOMENCLATURE

A_e	Core cross-sectional area	K_I	Integral gain.
A_L	No gap Inductance factor.	L_m	Magnetizing inductance.
B_{sat}	Saturation flux density.	n (N_s/N_p)	Turn ratio of the flyback transformer.
d_{max}	The peak value of the converter duty cycle for DCM state.	N (f_s/f_g)	Control system delays number.
f_g	Frequency of utility voltage.	N_s	Semiconductors total number.
f_s	Switching and sampling frequency.	P_{avg}	The average value of output power
i_g	Current of grid.	R_{pv}	The dynamic resistance of PV
$I_{avgpri,s}$	The average current value associated with the primary side of the transformer in a switching cycle.	T_s	Period of switching
$I_{avgpri,g}$	The average transformer primary current in half of the utility cycle.	v_g	Voltage of grid
i_{pri}	The transformer's primary side current.	V_{rms}	Grid voltage RMS value
I_{rms}	Grid current RMS value.	V_m	The maximum value of utility voltage
I_{pv}	Photovoltaic (PV) module output current	V_{pv}	The PV panel voltage.
k_r	Repetitive controller gain.	ω	The utility voltage angular frequency.

I. Introduction

By enhancing the importance of energy derived from natural sources, photovoltaic (PV) devices have been broadly used in different scopes. The utility-tied photovoltaic systems can be grouped into three main category: the centralized, string, and ac module systems [1]-[6]. Between these systems, the low-power inverter that is stated ac module system or micro-inverter is placed on every photovoltaic system, providing the exclusively tracking the maximum power point (MPP). Consequently, the losses of power owing to inconformity of photovoltaic module and regional shading can be decreased [7]–[11]. In addition, the characteristics

Copyright © S.Mohammadi (s).
Publisher: University of Sistan and Baluchestan

like simpler preservation and high value of the micro-inverter reliability are another advantages of them [12]-[17]. Therefore, the above aspects result the ac-module a suitable method for renewable power generating systems for future times.

While at the nominal power the flyback converter works in CCM in a PV micro-inverter system, entering the DCM at momentary output powers with low values or when decreasing the solar irradiation is an unavoidable phenomenon. Thus, a hybrid operation mode can be considered for the flyback micro-inverter working in the whole utility cycle. The system with low gain is an intrinsic specification of DCM operated flyback converter. As a result, a high gain for the feedback control system should be applied for proper reference signal tracking and complete attenuation of the disturbances. However, the limitation put on the control system gain as a result of zero placed on the right-half-plane (RHP) in CCM while applying the usual PI controller is unavoidable. As a consequence, it results in power quality being unacceptable and the total harmonic distortion being high (THD) due to inaccurate DCM control system performance [18], [19]. This is the main factor for the hybrid mode confined usage of the flyback converter contrary to its outstanding specifications in micro-inverter applications.

Solving the above matter, the static reference frame proportional resonant (PR) controller [20– 22] and the digital repetitive controller [23–25] are reported in the literature. However, the simple approach, little error in steady-state, and little burden in the computational system are some benefits of the PR controller. The decline with the exponential state as a reaction of step change is an example of the constraints of the above controller. In addition, the sensitivity to the variable frequency changes of repetitive signals and the phase shift instability appearing in signals that are measured are other PR controller disadvantages [20–22]. Dealing with periodic signals, the repetitive control method is an efficient scheme. Bode plot infinite amplitudes of this control system at harmonics of the main frequency can result in controller instability. Contrary to different solutions that have been suggested to solve this matter, these schemes suffer from other constraints, such as unacceptable performance responding to disturbances with a non-intermittent nature, slow dynamic response, and vast requirements for memory space [23–25].

The harmonic control array (HCA) method that has been introduced lately, is an appropriate scheme to control systems with intermittent temper such as disturbance and/or reference signals [26-28]. Compensating periodic control signal is easily generated by applying this control scheme, tracking or rejecting considered harmonic components. Moreover, the system gain at the utility frequency and its multiples can be augmented by applying the HCA method. In the mentioned approach, the harmonic contents of the reference and control signals are calculated by using the integral of the Fourier series [26-28]. So, to implement this scheme several delays considering switching frequency should be employed. These delays sometimes cause the system's dynamic response to be unstable and very slow.

In this study, we suggest using the filtered signal instead of applying sluggish or intricate schemes controlling the flyback inverter in the CCM state. The selected structure is very easy to implement and also fast which enhances the control system gain at the utility frequency and corresponding harmonics to boost the tracking operation in both DCM and CCM operation states. Part II concisely investigates the steady-state performance of the two-switch flyback converter. Section III analyzes the control issue and the various control schemes tackling it.

II. The two-switch flyback inverter analysis in steady-state

An Illustration of the flyback two-switch ac-module main circuit is shown in Fig.1 which is composed of the flyback two-switch inverter with turn ratio n (N_s/N_p), decoupling capacitor C_{in}, a current source inverter (CSI) ($S_{ac1} - S_{ac4}$), and an output filter. The switches ($S_{1,2}$) of the flyback inverter operate concurrently with high-frequency to transmit the power of the photovoltaic system to the grid. The sinusoidal waveform is obtained from the rectified one by employing the CSI and injecting it into the grid.

The turned-on switches S_{ac1} and S_{ac4} operate as the utility positive voltage reaches. In the same way, when the negative voltage of utility reaches, S_{ac2} and S_{ac3} are turned on. Fig. 2 illustrates the inverter's main waveforms. While each switching period T_s is enhanced, the current of magnetizing inductance i_{Lm} in DCM becomes zero and the transformer is completely demagnetized. As soon as the next switching cycle starts in CCM operation, and within a switching cycle, the current in magnetizing inductance i_{Lm} is non-zero.

By assuming the lossless operation of the system and by noting the balance of power over the utility period, the output power of the PV module is expressed as [29]

$$P_{pv} = V_{pv} I_{avgpri,g} = V_{pv} I_{pv} = V_{rms} I_{rms} = P_{avg} \qquad (1)$$

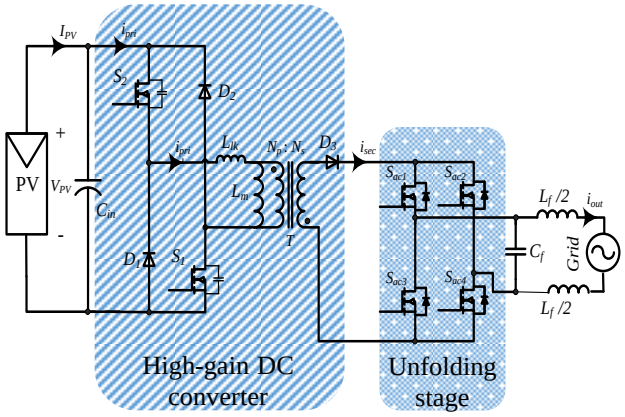

Fig. 1. The flyback two-switch micro-inverter configuration.

In a switching period, by employing the power balance equation, the converter output power can be shown as

$$P_{out}(t) = V_{pv} I_{priavg,s} = v_g(t) i_g(t) = 2V_{rms} I_{rms} \sin^2(wt) = 2P_{avg} \sin^2(wt) \qquad (2)$$

In half of the utility period T_h , the average value of the primary current of the transformer is expressed as

$$I_{avgpri,g} = \frac{1}{T_h} \int_0^{T_h} i_{pri}(t)\, dt = \frac{V_{pv} d^2_{\max}}{4 L_m f_s} \qquad (3)$$

Therefore, the calculation of the photovoltaic system output power is obtained as

$$P_{pv} = V_{pv} I_{avgpri,g} = \frac{V^2{}_{pv} d^2{}_{\max}}{4 L_m f_s} \quad (4)$$

Employing the derived equation in (4) we can determine the duty ratio in DCM as follows

$$D_{DCM}(t) = d_{\max} |\sin(\omega t)| = \frac{2}{V_{pv}} \sqrt{P_{pv} L_m f_s} |\sin(\omega t)| \quad (5)$$

The duty ratio and turn ratio *n* are not dependent in the DCM case but the duty ratio is affected by L_m and input power at given specifications in addition to selected frequency f_s. The maximum amount of the primary current in DCM by applying equation (5), is expressed as

$$I_{DCMpri,pk}(t) = \frac{V_{PV} D_{DCM}(t)}{L_m f_s} = 2\sqrt{\frac{P_{avg}}{L_m f_s}} |\sin(\omega t)| \quad (6)$$

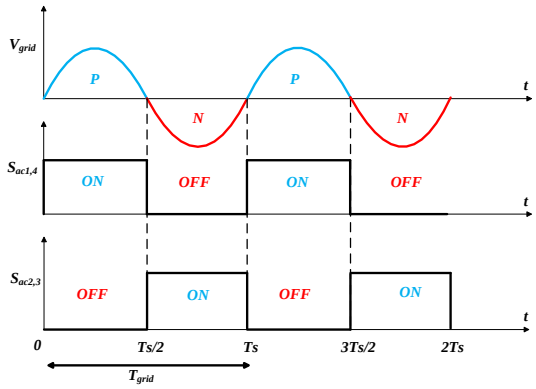

(a)

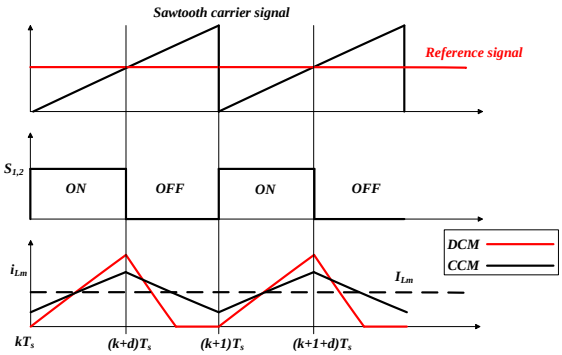

(b)

Fig. 2. The main waveforms of the flyback inverter[37]

Operating the converter in CCM, by using the inductor voltage–seconds law in a switching cycle for L_m, the duty ratio in CCM can be derived as [29]

$$D_{CCM}(t) = \frac{V_g |\sin \omega t|}{n V_{pv} + V_g |\sin \omega t|} \quad (7)$$

However, the converter duty cycle operating in CCM is impressed by the turn ratio n, it doesn't change with input power. The critical magnetizing converter inductance determining the CCM and DCM performance is expressed as

$$L_{mcri} = \frac{V_{pv}}{4 I_{pv} f_s} \frac{1}{(n V_{pv}/V_m + 1)^2} \quad (8)$$

As shown formerly, operated in DCM, the I_{pri} peak magnitude is obtained as (6). Operating in CCM, as illustrated in Fig. 2, to obtain the primary current maximum value $I_{CCMpri,pk}$, adding the two components the mean value of magnetizing current I_{Lm} and the ripple component Δi_{Lm} of that are necessary. Turning on the main switch S_1, the primary current is equal to the magnetizing current.

As a result, by dividing the average primary current and the duty cycle, the magnetizing inductance current average value can be obtained. Thus, the magnetizing inductance current average amount and its ripple component can be expressed as

$$I_{Lm}(t) = \frac{I_{avgpri,s}}{D_{CCM}(t)}$$
$$\Delta i_{Lm} = \frac{V_{pv}}{L_m f_s} D_{CCM}(t) \quad (9)$$

Thus, the maximum amount of primary current $I_{CCMpri,pk}$ is obtained as

$$I_{CCMpri,pk}(t) = \frac{I_{avgpri,s}}{D_{CCM}(t)} + \frac{V_{PV} D_{CCM}(t) T_s}{2 L_m}$$
$$= \frac{P_{out}(t)}{V_{PV}} \times \frac{n V_{PV} + |v_g(t)|}{|v_g(t)|} + \frac{V_{PV}}{2 L_m f_s} \times \frac{|v_g(t)|}{n V_{PV} + |v_g(t)|} \quad (10)$$

At different output powers, the duty cycle variation over half a utility period is illustrated in Fig.3 at specified quantities of f_s, L_m , and *n*. As shown in this scheme, for defined specifications, corresponding to the output power the duty cycle is increased by employing the fixed input voltage. The inverter operates in DCM if the momentary duty cycle at DCM operation mode is lower than the curve of CCM specified with the transformer turn ratio *n* in Fig.3; otherwise, the CCM operation mode is enabled. At a specific power, the CCM duty cycle doesn't intersect with the DCM curve, so the inverter operation is carried out only in the DCM state.

III. The flyback ac-module control structure analysis

A. The flyback ac-module control issue

Time-varying performance and nonlinearity are characteristics of flyback inverter. However, by considering small changes around its operating point it can be considered as a system with a linear time-invariant nature. As a result of changes in the performance, appropriate transfer functions should be derived with regard to each state. Good tracking performance and stability should be considered by the controller in various operating states. Unavoidably working in DCM at low power conditions of the inverter, the transfer function of control to-output current can be determined as

$$G_{id-DCM} = \frac{V_{pv}}{V_{rms}} \sqrt{\frac{P_{avg}}{2 f_s L_m}} \quad (11)$$

This relation specifies a gain with a low value in all frequencies. Having accurate and fast reference tracking and rejection of disturbances performances, the gain of the feedback controller should be enough high in the DCM state. Operating in CCM, the transfer function of the converter can be shown as [30]

$$G_{id-CCM} = \frac{M s^2 + N s + K}{s^2 (R_{pv} C_{in} L_m) + s L_m + D^2{}_{CCM} R_{pv}} \quad (12)$$

where

$$M = -\frac{I_{Lm}}{n} R_{pv} C_{in} L_m$$
$$N = -\frac{I_{Lm}}{n} L_m + R_{pv} C_{in} \frac{(1-D_{CCM})}{n} (V_{pv} + \frac{V_m}{n})$$
$$K = -D^2_{CCM} R_{pv} \frac{I_{Lm}}{n} + \frac{(1-D_{CCM})}{n} (V_{pv} + \frac{V_m}{n} - D_{CCM} I_{Lm} R_{pv}) \quad (13)$$

Observing the relation of (12), $G_{id\text{-}CCM}$ has a zero put on RHP that places limitations on the feedback controller gains satisfying the system stability. Depending on the operating point of the system the RHP zero obtains various quantities. Transferring the maximum power, the minimum value of RHP zero occurs at the maximum value of grid voltage. All the operating points should be covered by the converter's controller, lowering the feedback control system. Moreover, the poles of the operating system are calculated as

$$pole\ (G_{id-CCM}) = -\frac{1}{2}\frac{1}{R_{pv}C_{in}} \pm j\frac{1}{2}\frac{\sqrt{L^2{}_m - 4R^2{}_{Pv}D^2{}_{CCM}C_{in}L_m}}{R_{pv}C_{in}L_m} \quad (14)$$

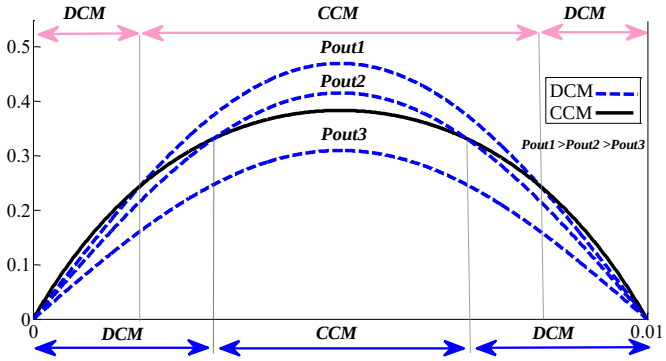

Fig. 3. Variations of duty cycle during half a grid period for CCM and DCM

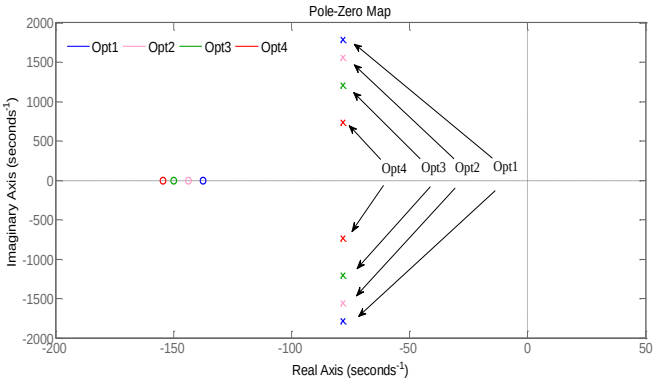

Fig. 4. Placement of Pole-zero for various operating points

TABLE 1 CHARACTERISTICS OF POLE-ZERO FOR FOUR VARIOUS PERFORMANCE STATES

Op. point	D (%)	Pout (W)	I_{Lm} (A)	V_m(V)	Zeroes	Poles
Opt_1	35.01	300	17.13	269.33	$Z_1 = 4.86\times10^5$ $Z_2 = -138$	-78.1+/-j1780
Opt_2	30.55	200	13.09	219.9	$Z_1 = 6.36\times10^5$ $Z_2 = -144$	-78.1+/-j1560
Opt_3	23.72	100	8.43	155	$Z_1 = 9.88\times10^5$ $Z_2 = -150$	-78.1+/-j1210
Opt_4	14.55	30	4.12	85.17	$Z_1 = 2.02\times10^6$ $Z_2 = -154$	-78.1+/-j739

According to the calculated relation of (12), the pole-zero scheme is demonstrated in Fig.4. The elaborate analysis of these operating points is also mentioned in Table I. As it is shown, decreasing the output power with instantaneous nature, moving the poles toward the real axis and moving away the zeroes from the origin. From the pole/zero distribution of the system, a non-minimal phase specification due to zero put on RHP is also observable. In addition, the oscillatory of the system is observable by increasing the instantaneous output power.

Compensated system Bode plots utilizing the usual PI controller with two various proportional gains are illustrated in Fig. 5. Table II lists the parameters employed in this study. Satisfying the constraint considering the minimum RHP zero of the inverter, the proportional gain of the controller should be sufficiently low.

In this regard, the gain of the system in the main frequency and its multiples in DCM is lesser than in CCM. This causes the flyback converter incapable of implementing reference tracking and rejecting the disturbances set by the photovoltaic system and utility in DCM. The proportional gain of the controller can be increased to solve this problem. However, the gain of the control system in all frequencies is increased which can make the system unstable as a result of system gain constraint regarding RHP zero. Thus, to design the flyback controller system, choosing the proper gains of the PI controller is a big problem. Various control approaches have been introduced in the literature to solve these control issues which are explained in the following part.

TABLE 2 PARAMETERS OF THE EMPLOYED FLYBACK AC-MODULE

Parameter	value	Unit
Turn ratio of transformers (Np/Ns)	1/10	
Utility voltage and frequency	220/50	V/Hz
Power of output	200	W
Sampling and switching frequency	100	kHz
Input voltage (V_{pv})	50	V
Magnetizing inductance L_m	15	µH
Leakage inductance L_{lk}	0.3	µH
Capacitor C_{in}	6.4	mF
Inductor L_f	3	mH
Capacitor C_f	0.66	µF
Core type		EE42
Rectifier diode	*D3*	IDP12E120
Clamping diodes	*D1, D2*	22GQ100
Main switches	S_1, S_2	IPB107N20N3G
Unfolding bridge switches	S_{ac1}-S_{ac4}	IRFP450B

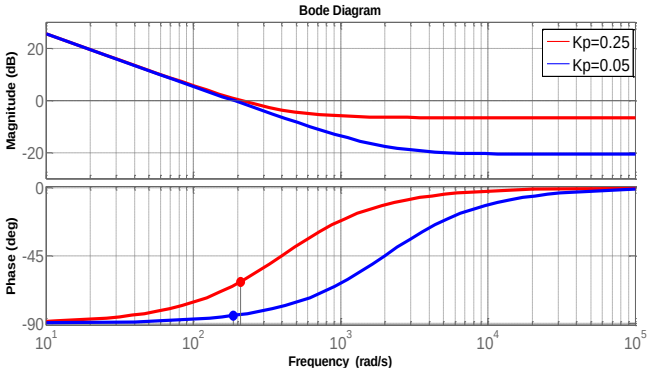

(a)

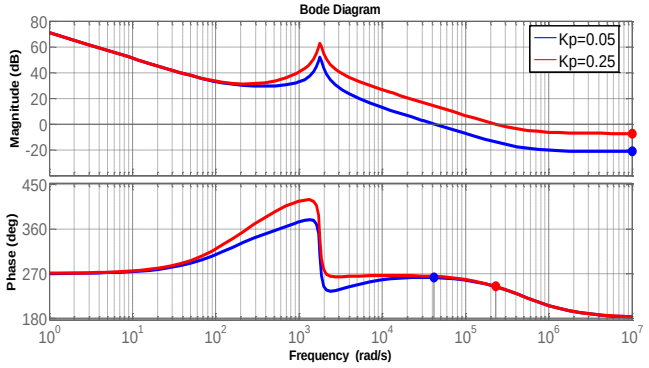

(b)

Fig. 5. The maked-up system Bode plots when the usual PI controller is employed. (a) DCM state. (b) CCM state

B. The Usual Control Systems of Flyback Micro-inverter

Improving the stability of the inverter, the usual control system of the flyback ac-module with the repetitive controller is illustrated in Fig. 6[19]. This control structure preserves the gain of the system high at only the low-frequency region, enhancing the output current tracking performance, while preventing the disturbances of grid voltage at the main and low-order harmonic frequencies. In addition, to compensate for the system phase lag in the repetitive control structure, the phase lead compensator is also employed. The above controller is obtained as

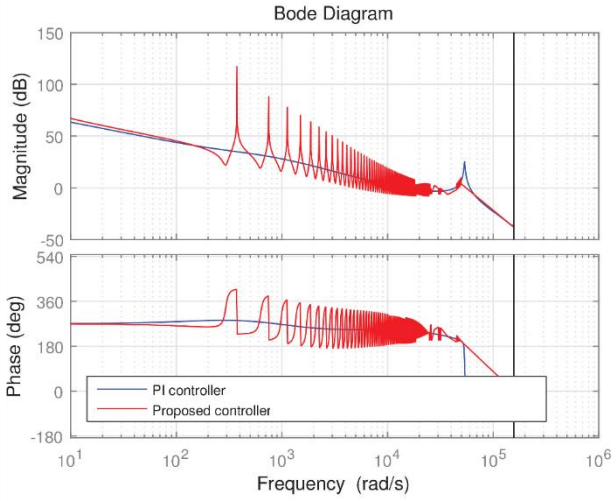

(a)

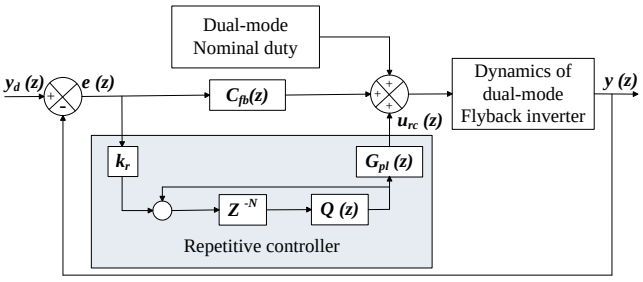

(b)

Fig. 6. Repetitive control structure (a) Bode plot (b) Control block diagram [19]

$$G_{rc}(z) = k_r \frac{z^{-N}Q(z)}{1 - z^{-N}Q(z)} G_{pl}(z) \tag{15}$$

$Q(z)$ is the low-pass filter, and $G_{pl}(z)$ is the system phase lead compensator. As Fig. 6 (b) illustrates and expressed in (15), the control system's large delays cause the dynamics of the system to be slowed down and may lead to system instability. Moreover, the Bode plot infinite amplitudes of this controller at harmonics of the main frequency can cause instability of the control system.

Indirectly controlling the output current [Fig.7] which controls the input current of the converter is applied in [29], [34] and [35]. Concerning fast and proper reference tracking performances, it is not as efficient as direct control schemes. Subharmonics phenomena and bifurcation are observable in the charge control approach under certain operating conditions [36]. Mitigating the oscillation and unsuitable operation of the usual control structure, a fourth-order model of the converter has been derived in [30]. This model of the converter including the output filter is calculated as

$$G_{id-CCM} = \frac{ps^3 + As^2 + Bs + C}{s^4 + Es^3 + Fs^2 + Hs + M} \tag{16}$$

Where A, B, C, E, F, H, M,and p are calculated in [30].The bode plot comparison of second and fourth-order models is shown in Fig. 8. As it is shown, the fourth-order model shows a resonant peak and sudden phase drop at a specified frequency. Thus, designing the appropriate controller including the output CL filter can be a big challenge. Employing the lag term with a conventional PI controller is proposed in this paper. The damping term is derived as

$$C_{lag} = \frac{1}{2.5 \times 10^{-5} s + 1} \tag{17}$$

The proposed controller is shown in Fig.9 and the bode plot of the compensated system is illustrated in Fig. 10. Although the suggested design structure of the decoupled two-stage controller is systematic way, it is a process with intricate and Time-consuming nature to determine the lag term appropriately and precisely.

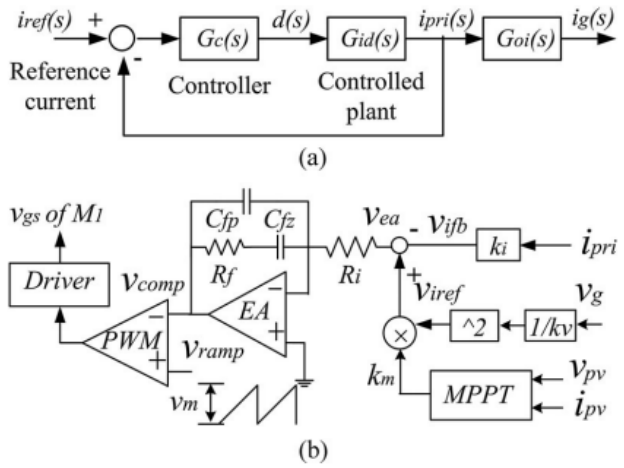

Fig.7.Controlling the flyback converter with an indirect manner[29] (a) Control block diagram(b) Detailed control system

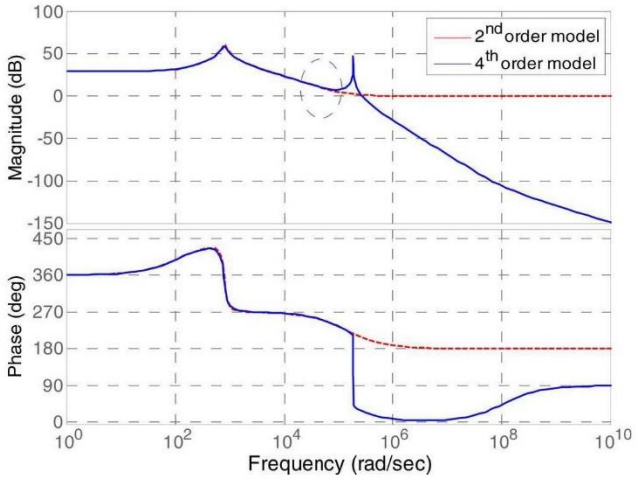

Fig.8. The bode plot comparison of second and fourth-order models [30]

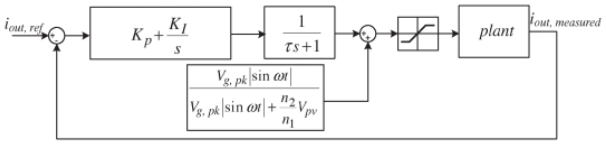

Fig.9. The proposed control system in [30]

Enhancing the stability of the usual flyback ac-module control system with the PR controller has been illustrated in Fig. 11. By applying the PR controller with HCs (harmonic compensators), high gain at the main frequency of the utility and its harmonics is reached. In addition, the bandwidth in DCM is enhanced. Thus, tracking of the reference and rejecting the disturbances as well as the suitable stability in both DCM/CCM states are fulfilled [18], [38]. The above controller with resonant gain k_{rf}, proportional gain k_p ,and cut-off frequency ω_c is expressed as

$$C_{PR}(s) = k_p + \frac{2k_{rf}\omega_c s}{s^2 + 2\omega_c s + \omega^2} \tag{18}$$

Putting the HC to the mentioned system, the errors of the considered harmonic frequencies can be alleviated, and its transfer

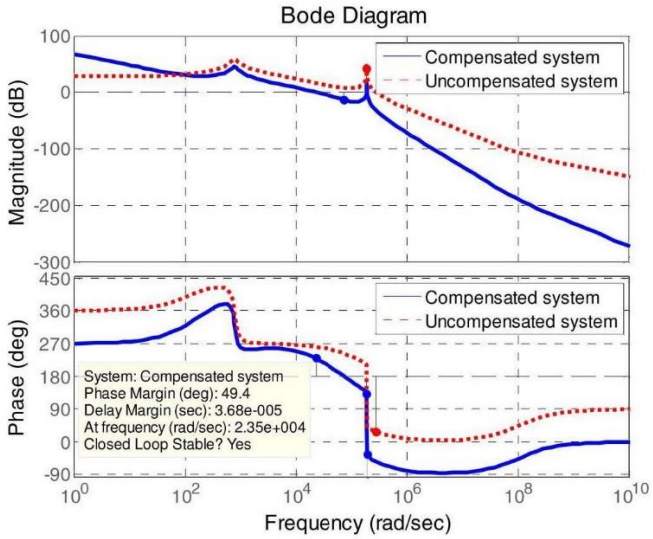

Fig.10. The bode plot of the compensated system [30]

function with the resonant gain for each harmonic k_{rfl} is expressed as

$$C_{HC}(s) = \sum_{l=3,5,7,....} \frac{2k_{rfl}\omega_c s}{s^2 + 2\omega_c s + (l\omega)^2} \tag{19}$$

As expressed in Fig. 11 (b) and stated in (18) and (19), slowing down the dynamic of the system and the possibility of unacceptable effects on the operation of the system are the consequences of adding multiple harmonic frequencies to the controller. In addition, the availability of the infinite amplitudes in the controller's Bode diagram at considered harmonic frequencies can result in instability of the control system.

Fig. 12 shows another flyback micro-inverter control system that can be employed [27]. Employing a gain with great value at the frequency of the grid and its harmonics without a high proportional gain is the property of the current control system with a harmonic control array (HCA) structure. Thus, in this scheme, the reference signal is tracked easily with zero error in steady-state accompanied by the satisfaction of the appropriate CCM stability. Three stages of this control approach are determined as:

1- The dispersing unit to diffuse harmonics

$$< x >_h [n] = \frac{1}{N}\sum_{k=n-N+1}^{n} x[k]e^{-jh\omega kT_s} = \frac{1}{N}\sum_{k=n-N+1}^{n} x[k]e^{-j2\pi hk/N} \tag{20}$$

2- The assembling unit to collect harmonics

$$f[n] = < f >_0 [n] + 2\,\mathrm{Re}\left\{\sum_{h=1}^{H} < f >_h [n] e^{j2\pi hn/N}\right\} \tag{21}$$

3- The controller section to control the whole process

$$< f >[n] = K_p < e >[n] + K_I E[n] \tag{22}$$

As it is shown in Fig. 12 and (20)-(22), several large delays are employed in the HCA control system that slow down the dynamics of the converter, and the stability of the system can be affected.

Moreover, the requirement of large memory space is another challenge of this approach.

C. Selection of the best control approach

As stated, the usual control systems present unacceptable performances concerning the aforementioned converter control problem. To have a proper and stable performance in hybrid

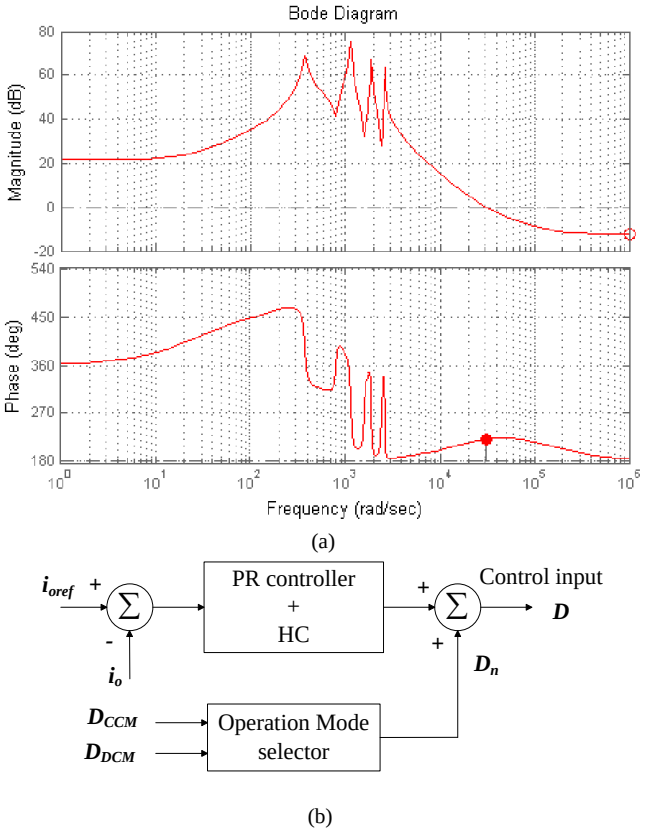

Fig. 11. Control structure of PR (a) Bode plot (b) Control block diagram [18]

CCM/DCM state, the main solution is selecting the controller gains proportional to frequency. As a result, we suggest a very simple but highly effective control structure that has been introduced in [37]. A PI control system accompanied by a low pass filter that permits only the main frequency and its low order harmonics to go across the system. The suggested control structure has a significantly fast response that is performed easily in the low-frequency section with a large proportional gain. As a result, proper implementation in both CCM and DCM states is guaranteed. The employed filter with low pass characteristics in the suggested system is determined as

$$G_f(z) = \frac{1}{\tau((1-z^{-1})f_s)+1} \tag{23}$$

where $\tau = 1/2\pi f_c$ with cut-off frequency $f_c(Hz)$. The suggested control scheme is illustrated in Fig. 13 whose simplicity and fast response are superior to the other control approaches such as repetitive controller, PR as well as HCA. The compensated system Bode plot with the presented control system is illustrated in Fig. 14. It is shown that the high gain at low order harmonics with the suggested control system is provided modifying the tracking speed and disturbance rejection performances accompanied with stability in both CCM and DCM operation states.

Various CCM control approaches employed in flyback ac-module are compared in Table III. As it is shown, the best tracking speed is presented with the aforementioned control structure and also it applies a little burden in the computational system approximately between all of the other control approaches. Moreover, the primary switches' voltage stresses are limited to the DC input voltage employing the two-switch scheme of the converter leading to using the switches with low voltage rating with low conduction losses.

IV. Conclusion

This paper presented a detailed survey of the various control structures introduced to solve the problems that come from the control to output current transfer function zero put on the right-half-plane (RHP) in the flyback micro-inverters. The working principle of each structure, features, restrictions, and recent status were investigated. As a general result, a PI controller with a low pass filter has a better performance against different types of control systems. In the mentioned control scheme, a high system gain at the main frequency and its multiples is provided with the usual PI controller accompanied by a low-pass filter. The usual control problem existing in flyback ac-modules operated at CCM is solved with this control system. It imposes an accurate and suitable DCM tracking operation and acceptable CCM stability. Also, the selected control approach presents little burden in the computational system and has a suitable dynamic response that does not exist in the usual control systems. Furthermore, the disturbances are better rejected and tracking of reference in conjunction with the other control systems is faster implemented.

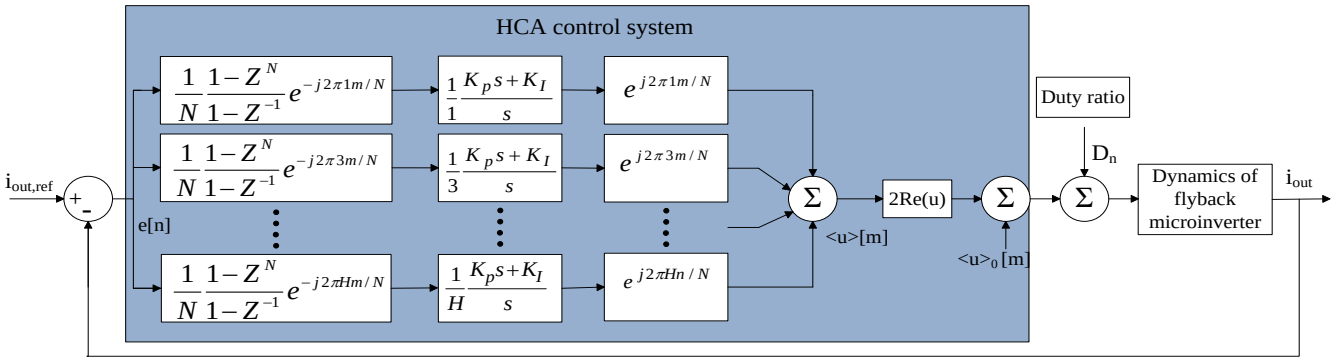

Fig. 12. The control scheme for HCA-based system [27]

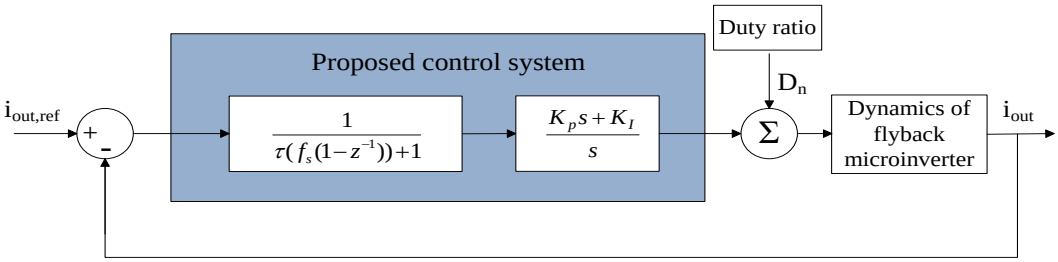

Fig. 13. The suggested control approach in [37]

TABLE 3
THE COMPARISON OF VARIOUS CCM CONTROL APPROACHES EMPLOYED IN FLYBACK AC-MODULE

Reference	Control parameter	controller	Tracking speed	Memory space requirement	Voltage stress of main switches	Power factor	MPPT efficiency (%)	MPPT Voltage range (V)	THD (%)	Efficiency (%)	**Approximate power [W]**
[18]	Output current	PR+HC	medium	large	$V_{PV}+V_m/n$	-	-	40-80 & V_{mpp}=60	2.4	96.1	**200**
[19]	Output current	repetitive	low	large	V_{PV}	-	98.5	V_{mpp}=60	2.4	96.3	**200**
[29]	Input current	type II	medium	small	$V_{PV}+V_m/n$	0.99	98	V_{mpp}=27	<5	87.4	**200**
[30]	Output current	type II	high	small	$V_{PV}+V_m/n$	-	-	25-55 & V_{mpp}=55	4	95.7	**200**
[33]	Output current	repetitive	low	large	V_{PV}	-	-	V_{mpp}=48	2.9	96	**200**
[34]	Input current	type II	medium	small	$V_{PV}+V_m/n$	-	99.5	V_{mpp}=35.6	5	90	**200**
[35]	Input current	type II	medium	small	$V_{PV}+V_m/n$	0.99	98	V_{mpp}=27	-	86.8	**200**
[36]	Input current	Charge control	medium	small	$V_{PV}+V_m/n$	0.99	98	20-27 & V_{mpp}=27	1.56	-	**200**
[37]	Output current	PI	high	small	V_{PV}	>0.98	-	V_{mpp}=50	-	96.1	**200**
[38]	Output current	PR+HC	medium	large	$V_{PV}+V_m/n$	-	-	-	2.34	-	**200**
[39]	Output current	PR+HC	medium	large	$V_{PV}+V_m/n$	-	-	V_{mpp}=38.9	2.27	94.5	**200**
[40]	Output current	PR+HC	medium	large	$V_{PV}+V_m/n$	-	-	V_{mpp}=28.7	2.1	-	**200**

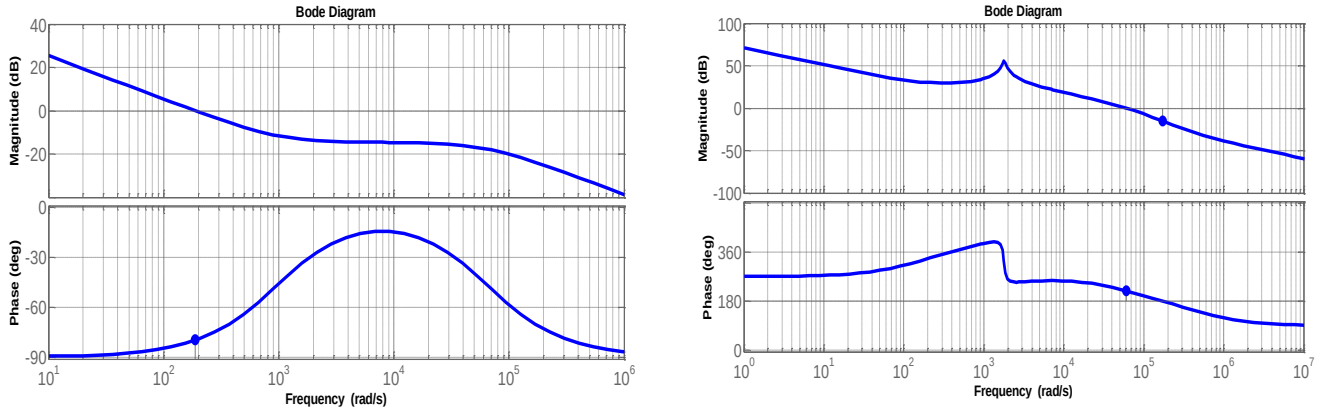

(a) (b)

Fig. 14. Open-loop Bode plots of the maked-up system by the selected appropriate controller. (a) In DCM. (b) In CCM

REFERENCES

[1] A. Mousaei, M. Gheisarnejad, M.H. Khooban, Challenges and opportunities of FACTS devices interacting with electric vehicles in distribution networks: A technological review, Journal of Energy Storage, Volume 73, Part A, 2023,108860,ISSN2352-152X,https://doi.org/10.1016/j.est.2023.108860

[2] Kim YH, Jang JW, Shin SC, Won CY. Weighted-efficiency enhancement control for a photovoltaic AC module interleaved flyback inverter using a synchronous rectifier. IEEE transactions on power electronics. 2014 Feb 13;29(12):6481-93.

[3] Rezaei MA, Lee KJ, Huang AQ. A high-efficiency flyback micro-inverter with a new adaptive snubber for photovoltaic applications. IEEE transactions on Power Electronics. 2015 Mar 5;31(1):318-27.

[4] Sukesh N, Pahlevaninezhad M, Jain PK. Analysis and implementation of a single-stage flyback PV microinverter with soft switching. IEEE transactions on industrial electronics. 2013 May 17;61(4):1819-33.

[5] Gao M, Chen M, Zhang C, Qian Z. Analysis and implementation of an improved flyback inverter for photovoltaic AC module applications. IEEE transactions on Power Electronics. 2013 Aug 27;29(7):3428-44.

[6] Christidis GC, Nanakos AC, Tatakis EC. Hybrid discontinuous/boundary conduction mode of flyback microinverter for AC–PV modules. IEEE Transactions on Power Electronics. 2015 Aug 19;31(6):4195-205.

[7] Kyritsis AC, Tatakis EC, Papanikolaou NP. Optimum design of the current-source flyback inverter for decentralized grid-connected photovoltaic systems. IEEE transactions on energy conversion. 2008 Feb 15;23(1):281-93.

[8] Mohammadi S, Izadfar HR, Eskandarian N. A new adaptive clamp for improving weighted efficiency in grid-tied photovoltaic interleaved two-switch flyback micro-inverter.

International Transactions on Electrical Energy Systems. 2019 Aug;29(8):e12033.

[9] Zhang F, Xie Y, Hu Y, Chen G, Wang X. A hybrid boost–flyback/flyback microinverter for photovoltaic applications. IEEE Transactions on Industrial Electronics. 2019 Feb 11;67(1):308-18.

[10] Sarikhani A, Allahverdinejad B, Hamzeh M, Afjei E. A continuous input and output current quadratic buck-boost converter with positive output voltage for photovoltaic applications. Solar Energy. 2019 Aug 1;188:19-27.

[11] Rahimi R, Farhangi S, Farhangi B, Moradi GR, Afshari E, Blaabjerg F. H8 inverter to reduce leakage current in transformerless three-phase grid-connected photovoltaic systems. IEEE Journal of Emerging and Selected Topics in Power Electronics. 2017 Aug 23;6(2):910-8.

[12] Mohammadi S, Zarchi HA. An interleaved high-power two-switch flyback inverter with a fast and robust maximum power point tracker. In2016 7th Power Electronics and Drive Systems Technologies Conference (PEDSTC) 2016 Feb 16 (pp. 320-325). IEEE.

[13] Mohammadi S, Zarchi HA, Amiri M. Interleaved two-switch flyback microinverter for grid-tied photovoltaic applications. InThe 6th Power Electronics, Drive Systems & Technologies Conference (PEDSTC2015) 2015 Feb 3 (pp. 59-64). IEEE.

[14] Wang F, Feng X, Zhang L, Du Y, Su J. Impedance-based analysis of grid harmonic interactions between aggregated flyback micro-inverters and the grid. IET Power Electronics. 2018 Mar;11(3):453-9.

[15] Keshani M, Adib E, Farzanehfard H. Micro-inverter based on single-ended primary-inductance converter topology with an active clamp power decoupling. IET power electronics. 2018 Jan;11(1):73-81.

[16] Mohammadi S, Izadfar HR, Eskandarian N. Performance optimisation of the grid-connected flyback inverter under improved hybrid conduction mode. IET Renewable Power Generation. 2020 Oct;14(13):2437-46.

[17] Dong D, Agamy MS, Harfman-Todorovic M, Liu X, Garces L, Zhou R, Cioffi P. A PV residential microinverter with grid-support function: Design, implementation, and field testing. IEEE Transactions on Industry Applications. 2017 Sep 14;54(1):469-81.2

[18] Lee SH, Cha WJ, Kwon JM, Kwon BH. Control strategy of flyback microinverter with hybrid mode for PV AC modules. IEEE transactions on industrial electronics. 2015 Sep 23;63(2):995-1002.

[19] Kim S, Lee SH, Lee JS, Kim M. Dual-mode flyback inverters in grid-connected photovoltaic systems. IET Renewable Power Generation. 2016 Oct;10(9):1402-12.

[20] Kim S, Lee SH, Lee JS, Kim M. Dual-mode flyback inverters in grid-connected photovoltaic systems. IET Renewable Power Generation. 2016 Oct;10(9):1402-12.

[21] Mousaei, A.; Naderi, Y. Optimal Predictive Torque Distribution Control System to Enhance Stability and Energy Efficiency in Electric Vehicles. Sustainability 2023, 15, 15155. https://doi.org/10.3390/su152015155.

[22] Karbasforooshan MS, Monfared M. Multi-resonant indirect digital current control technique for single-phase shunt active power filters. Electric Power Components and Systems. 2019 Aug 9;47(13):1196-202.

[23] Mattavelli P, Marafao FP. Repetitive-based control for selective harmonic compensation in active power filters. IEEE Transactions on Industrial Electronics. 2004 Oct 4;51(5):1018-24.

[24] Geng H, Zheng Z, Zou T, Chu B, Chandra A. Fast repetitive control with harmonic correction loops for shunt active power filter applied in weak grid. IEEE Transactions on Industry applications. 2019 Jan 25;55(3):3198-206.

[25] Pandove G, Singh M. Robust repetitive control design for a three-phase four wire shunt active power filter. IEEE Transactions on Industrial Informatics. 2018 Oct 9;15(5):2810-8.

[26] Dogruel M, Çelik HH. Harmonic control arrays method with a real time application to periodic position control. IEEE transactions on control systems technology. 2010 May 6;19(3):521-30.

[27] Karbasforooshan MS, Monfared M, Dogruel M. Application of the harmonic control arrays technique to single-phase stand-alone inverters. IET Power Electronics. 2016 Jun;9(7):1445-53.

[28] Karbasforooshan MS, Monfared M, Dogruel M. Indirect control of single-phase active power filters using harmonic control arrays. In2017 Conference on Electrical Power Distribution Networks Conference (EPDC) 2017 Apr 19 (pp. 143-148). IEEE.

[29] Li Y, Oruganti R. A low cost flyback CCM inverter for AC module application. IEEE transactions on Power Electronics. 2011 Aug 18;27(3):1295-303.

[30] Edwin FF, Xiao W, Khadkikar V. Dynamic modeling and control of interleaved flyback module-integrated converter for PV power applications. IEEE transactions on industrial electronics. 2013 Apr 16;61(3):1377-88.

[31] Sharifi S, Monfared M, Nikbahar A. Highly efficient single-phase direct AC-to-AC converter with reduced semiconductor count. IEEE Transactions on Industrial Electronics. 2020 Feb 5;68(2):1130-8.

[32] Choi HS. Transformer Design Consideration for off-line Flyback Converters using Fairchild Power Switch. Fairchild Semiconductor App. Note AN4140. 2004:1-0.

[33] Jeong YS, Lee SH, Jeong SG, Kwon JM, Kwon BH. High-efficiency bidirectional grid-tied converter using single power conversion with high-quality grid current. IEEE Transactions on Industrial Electronics. 2017 May 11; 64(11):8504-13.

[34] Thang TV, Thao NM, Jang JH, Park JH. Analysis and design of grid-connected photovoltaic systems with multiple-integrated converters and a pseudo-dc-link inverter. IEEE Transactions on industrial electronics. 2013 Sep 9; 61(7):3377-86.

[35] Li Y, Oruganti R. A low cost high efficiency inverter for photovoltaic AC module application. In2010 35th IEEE Photovoltaic Specialists Conference 2010 Jun 20 (pp. 002853-002858). IEEE.

[36] Li Y, Oruganti R. A flyback-CCM inverter scheme for photovoltaic AC module application. Australian Journal of Electrical and Electronics Engineering. 2009 Jan 1; 6(3):301-9.

[37] Mohammadi S, Izadfar HR, Eskandarian N. A simple and highly efficient flyback inverter control strategy for AC module application. IET Power Electronics. 2022 Oct 31

[38] M. Dong and X. Tian, "Dual-Mode interleaved flyback micro-inverter," 2017 Chinese Automation Congress (CAC), Jinan, China, 2017, pp. 7719-7724, doi: 10.1109/CAC.2017.8244175.

[39] Yang Jian and Ye Bingqing, "Accurate modeling and sliding mode control method to improve the current sharing performance for PV grid-connected interleaved flyback mirco-inverter," 2016 IEEE International Conference on Power and Renewable Energy (ICPRE), Shanghai, 2016, pp. 558-564, doi: 10.1109/ICPRE.2016.7871138.

[40] D. L. Caiza, S. Kouro, F. Flores-Bahamonde and R. Hernandez, "Unfolding PV Microinverter Current Control: Rectified Sinusoidal vs Sinusoidal Reference Waveform," 2018 IEEE Energy Conversion Congress and Exposition (ECCE), Portland, OR, USA, 2018, pp. 7094-7100, doi: 10.1109/ECCE.2018.8558024.

Saleh Mohammadi recieved his Ph.D. degree in power Engineering from the University of Semnan, Iran in 2020 wth an honor. In 2024, he joined the Department of Electrical and Computer Engineering at Esfarayen University of Technology, Esfarayen, Iran. His research interests include, power electronics and active filters.

Naser Eskandarian is currently an Assistant Professor in the Electrical and Computer Engineering Department of Semnan University. His research interests include computer control, robotics, power electronics, and electric vehicles. He has managed several industrial projects, some of which have won international awards.

Hamid Reza Izadfar is currently an Associate Professor in the Electrical and Computer Engineering Department of Semnan University. His main research interests are the design and analysis of electric machines and drives.

International Journal Of
Industrial Electronics Control and Optimization
Print ISSN: 3517-2645
Online ISSN: 3568-2645
Homepage: https://ieco.usb.ac.ir/

A Setting-Free Loss of Excitation Detection of Synchronous Generator in the Presence of FACTs Device

Milad Niaz Azari [1] | Iraj Ahmadi [1] | Hossein Abolqasemi [1]

Department of Electrical Engineering, University of Science and Technology of Mazandaran, Behshahr, Iran
Corresponding Author Email: miladniazazari@mazust.ac.ir

Article Info

Article type:
Research Article

Article history:
Received: 08-September-2024
Received in revised form: 28-October-2024
Accepted: 18-November-2024
Published online:23-Sep-2025

Keywords:
Loss of Excitation,
Derivative of the Resistance,
STATCOM,
Stable Power Swing.

ABSTRACT

This paper analyzes the loss of excitation (LOE) fault, as one of the most common faults in synchronous generators, and investigates the methods of its detection. Then, the performance of a power system equipped with STATCOM is simulated using Matlab/Simulink software, and the effects of the generator performance on the resistor and its derivatives in the generator terminal are analyzed. A novel LOE detection method based on a derivative of resistance is proposed. To demonstrate the efficiency of this method, various generator load sizes and conditions are considered. The simulation results show that the amount of resistance time derivative in all cases, whether with or without STATCOM, serves as a reliable new criterion for LOE detection. This method proves to be faster and more accurate than conventional methods. The simulation results at different load amounts and types confirm the validity of the proposed method.

NOMENCLATURE

E_G	Inner Voltage of The Generator	$X_{Tot}(t)$	Total Reactance
$X_G(t)$	Reactance of The Generator	$FACTS$	Flexible AC Transmission Systems
X_T	Leakage Reactance of The Transformer	SPS	Stable Power Swing
X_{syst}	Reactance of The Transmission Network	LOE_{th}	Threshold Value
E_{syst}	Voltage of The Transmission Network	R	Resistance
LOE	Loss of Excitation	Q	Reactive power
δ	Power Angle	S	Apparent Power
		P	Active Power

I. Introduction

The blackouts of August 14, 2003, in North America highlighted many aspects of system protection [1,2]. Considering that power outages in industrial centers may inflict irreparable losses when a fault occurs, the relay must detect faults, track them, measure them, and prepare the alarming devices or, if necessary, automatically take action to interrupt the electric circuit. If the fault is dangerous, only the

Copyright © M. Niaz Azari (s).
Publisher: University of Sistan and Baluchestan

faulty device should be disconnected from the circuit, and the other faultless parts of the network should continue to operate without power interruption until the fault does not threaten them. The good and reliable performance of power systems is mainly protected by protective relays. If we aim to establish a highly reliable system, all components must be protected [3]; especially, generators require robust protection as they are the main sources of energy. Therefore, any faults in these generators must be detected quickly, so they need relays that offer high and reliable protective capabilities.

Loss of Excitation (LOE) is an important fault in synchronous machines that adversely affects both the network and the generator. LOE occurs when DC sources fail due to events such as field open circuits, accidental interruptions, regulator failures, or loss of field in the exciter [5, 6]. The primary method of LOE protection involves using voltage and current transfers, which are associated with the field circuit and may glitch in some cases. Masson [11] introduced a single-phase mho component with a negative offset. Berdy [12] proposed a distance relay with two zones for LOE detection, which is now regarded as a trustworthy procedure for LOE detection. Figure 1 shows the performance waveform of this relay. This procedure may not distinguish between stable power swing (SPS) and LOE, so a time delay is used to interrupt relay maloperation. However, this solution is not a rational way because this deliberateness time delay can have additional impacts on the device and network, as the defective generator continues to draw reactive power for an extended period. Other strategies, such as those based on neural networks, require substantial training data under various circumstances and can take a considerable amount of time. Since these strategies depend on framework characteristics, they may not work well when utilizing wholly different frameworks [7, 8].

Among other strategies for LOE detection are methodologies based on fuzzy logic, which are utilized to move forward the execution of common strategies for LOE discovery by utilizing the impedance tracking and terminal voltage of the generator [9,10]. These strategies are faster and more secure than traditional impedance procedures. Researchers have also examined the influence of transmission line midpoint STATCOM on generator protection behavior [11, 12]. This research investigates a power plant with two generators under two potential LOE scenarios: complete LOE and partial LOE, based on field short circuits and sudden drops in excitation voltage at various generator loads. The findings indicate that midpoint STATCOM adversely affects the performance of LOE relays, particularly in terms of time delay. Unlike the impedance-based approach, another strategy represents the event (LOE) by utilizing the rate of change of terminal voltage and output reactive power [13]. This strategy employs the voltage derivative and reactive power derivative to introduce an index known as the Loss of Excitation Index (LOEI). If this index exceeds a threshold value (LOE_{th}), the LOE has occurred. This strategy can also distinguish between LOE and SPS and performs much faster than existing methods. Yaghubi [14] provided a quick and accurate distinction between SPS and LOE of synchronous generators. Since there is an imbalance in the SPS condition, the detection of this phenomenon remains a challenge. This study proposed a rapid diagnostic method for addressing this issue. The proposed hybrid approach was based on the derivatives of reactive output power and terminal voltage, as well as the rapid change of the Fourier transform coefficients of the three-phase active power at the relay location [14]. At the moment of an LOE fault, the proposed index exceeds the threshold value, and the active power FFT remains relatively stable. However, during the occurrence of SPS, the active power FFT exhibits significant changes. In recent years, to enhance power transmission and optimize the utilization of power system capabilities, the adoption of flexible AC transmission systems (FACTS) such as static synchronous compensators (STATCOM) has become increasingly popular. Nevertheless, STATCOM alters the voltage and current within the power system, potentially disrupting relay operation (LOE). As a result, Yaghobi [15] introduced a novel method for flux-based LOE protection in the presence of STATCOM, which relies on changes in the generator linkage flux at the relay's position. This relay operates independently of coordination with other generator protection relays.

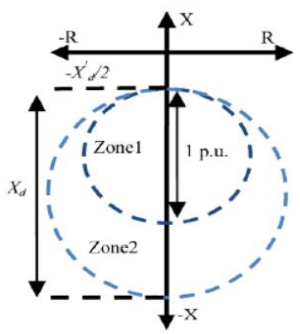

Figure (1): Two protection zones of Berdy Relay

Another paper on the protection of synchronous generator excitation loss during and after various external faults is presented by Yaghobi [16]. This method relies on changes in the magnetic flux in the air gap and the negative sequence current. In [17], the author introduced a new LOE detection method and proposed a modern approach for LOE detection that uses a combined conspire based on the derivative of the terminal voltage and power angle of the generator. Niaz Azari [18] presented a setting-free method to detect this malfunction. To address this issue, a flux derivative method was proposed for fault detection. Since the time derivative of the flux or the rate of change in the flux at the moment of LOE has a negative value, it serves as a reliable indicator for identifying this fault.

Among the methods discussed, the LOE detection method that uses distance relays is the most prevalent due to its simplicity. However, it cannot distinguish between LOE and SPS, which is the main problem with these types of relays. To address this issue, a deliberate time delay was implemented to prevent LOE from malfunctioning. However, this approach proved ineffective, as the time delay increased tension within the device and the power network. To resolve this problem, methods such as fuzzy logic, neural networks, and magnetic flux were employed. These techniques are faster and more accurate than the distance relay method, though each has its own challenges.

Section II describes a new method of LOE detection in the presence of FACTS devices, specifically STATCOM. This method is simpler than existing methods, offers appropriate accuracy, and does not require setting.

II. The Proposed LOE Detection Method

A. Without STATCOM

LOE in synchronous generators occurs when the field current is interrupted due to an open circuit in the field winding. To illustrate an LOE situation, assume that a generator is connected to the electrical network via a transformer. Figure 2 depicts the single-line connection diagram. When LOE is distinguished by relay 40, the equivalent circuit of the system after the LOE event can appear at each stage as in Figure 3, since LOE is symmetrical in nature.

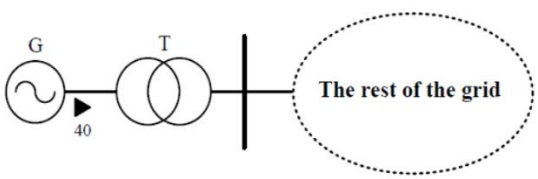

Fig. 2. The single-line diagram of the system

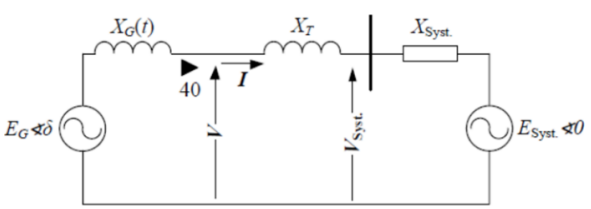

Fig. 3. The system equivalent circuit

When LOE occurs, the inner voltage of the generator (E_G) diminishes, inducing changes in the terminal voltage and current, which can result in variations in the impedance detected by the relay. During the LOE occasion, $X_G(t)$ changes, so it is sensible to think of it as a function of time from the minute of the start of the LOE. Assuming K=Esyst/EG, the time derivative of the equivalent resistance can be expressed as [3]

$$\frac{dR}{dt} = \frac{(1-K(t)^2)\cdot \sin\delta}{(1+K^2-2K\cos\delta)^2}\cdot\frac{dK}{dt}\cdot X_{Tot}(t) + \frac{K(t)\cdot\sin\delta}{1+K^2-2K\cos\delta}\cdot\frac{dX_{Tot}(t)}{dt} \quad (1)$$

It should be stated that the total reactance can be as follows:

$$X_{Tot}(t) = X_G(t) + X_T + X_{syst} \quad (2)$$

Since k is expanding, $\frac{dK}{dt}$ is positive and because ($E_{syst} < E_G$), the primary portion of (1) is positive. Based on [3], after a few seconds, the second part of Eq. (1) will be zero. At this time, E_{syst} will be more than E_G, so after a certain duration, $\frac{dR}{dt}$ will continue to be positive and LOE can be identified. In power swing conditions, $\frac{dR}{dt}$ is again negative for some time. But, the negative time is different from the LOE. When it happens, K can be assumed 1 and the value of the proposed index can be written as follows:

$$\frac{dR}{dt} = \frac{2\cos\delta(t)-2}{(1+K^2-2K\cos\delta(t))^2}\cdot\frac{d\delta}{dt}\cdot X_{Tot} \quad (3)$$

As proven in [3], the sign of $\frac{dR}{dt}$ is the opposite of $\frac{d\delta}{dt}$. The $\frac{d\delta}{dt}$ swings have a frequency of 3.0 to 7 Hz, so the longest period of $\frac{d\delta}{dt}$ that occurs during the oscillation is expected to be 3.33 seconds. As is evident in Figure 4, $\frac{d\delta}{dt}$ is positive in the primary half of periodicity, and hence $\frac{d\delta}{dt}$ will not be negative for more than 1.67 seconds during power swings. To discriminate LOE from power swings, the proposed relay must wait 1.67 seconds. If $\frac{d\delta}{dt}$ is negative, LOE will be distinguished[3].

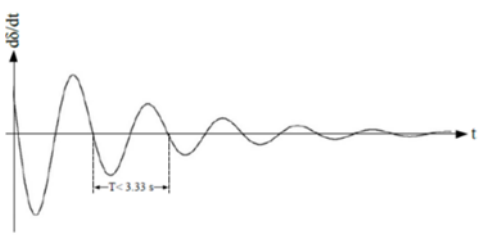

Fig. 4. $\frac{d\delta}{dt}$ diagram during power swings[3]

B. In the Presence of STATCOM

It can be assumed that in the presence of STATCOM devices, Esyst will be equal to 1pu with the compensation done. So, K will be 1/EG. Therefore, in the event of LOE, K will exceed 1. As a result, according to Eq. (3), the R time derivative will be negative when the fault occurs. It must be emphasized that if

the STATCOM compensation is extreme, Esyst will be more than 1pu and again K will be more than 1 and there will be no problem in fault detection with the proposed method.

Accordingly, Figure 5 displays the proposed method in the form of a flowchart in the presence and absence of STATCOM. First, the relay calculates $\frac{dR}{dt}$. When it is not zero, it will check its sign. If it is negative for more than 1.67 seconds, LOE can be detected and a trip signal is sent to the generator circuit breakers. If it is negative for less than this time, a power swing can be reported.

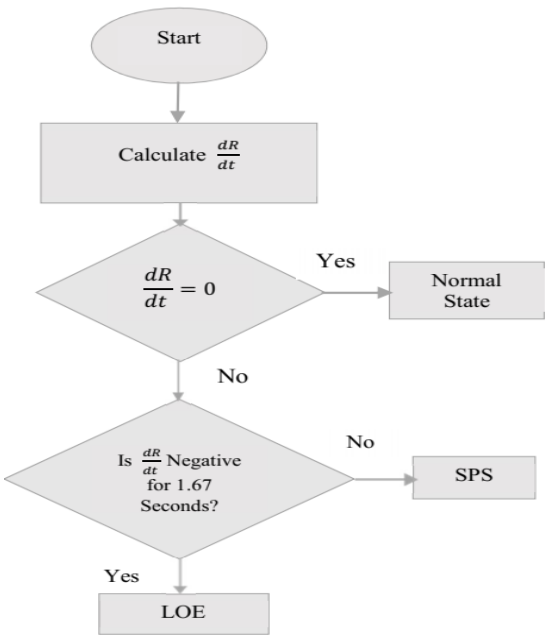

Fig .5. The algorithm of the proposed method in the presence and absence of STATCOM

III. Simulation and analysis of the results

This section analyzes the performance of the proposed method. Figure 6 shows a schematic of a power system with infinite bus. The performance of the proposed method will be compared with this method's performance in the absence of STATCOM. In this configuration, a 200 MW, 8.13 kV salient pole synchronous generator is connected to a 500 kV, 20,000 MW power grid through a transformer.

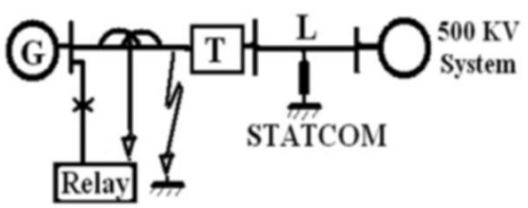

Fig. 6. The general scheme of the simulated power system

In addition, the different loads in each generator unit based on the capability curve are shown in Table 1. STATCOM is connected to the middle of the transmission line for voltage regulation, transmission, and optimal use of power. STATCOM mitigates reactive power by monitoring the terminal voltage and comparing it with the set value.

TABLE 1 Different generator loads

Load No.	S=P +jQ	Load No.	S=P +jQ
1	0.1+j0.5	11	0.9-j0.2
2	0.1+J0.2	12	0.7-J0.2
3	0.3+J0.2	13	0.7-J0.5
4	0.3+J0.5	14	0.5-J0.2
5	0.5+J0.2	15	0.5-J0.4
6	0.5+j0.4	16	0.5-j0.6
7	0.7+J0.2	17	0.3-J0.6
8	0.7+J0.4	18	0.3-J0.4
9	0.9+J0.3	19	0.3-J0.2
10	0.9+J0.1	20	0.1-J0.6

A. Simulation in the Absence of STATCOM

In this part, different loading conditions are examined to observe the behavior of the proposed LOE relay in the absence of STATCOM. First, the normal conditions are examined in the simulation and then the output waveforms for the resistance and the derivative of the resistance are displayed. Figures 7(a) and 7(b) show the output diagram of R and $\frac{dR}{dt}$ under normal conditions, respectively. Next, to show that the proposed method is reliable and efficient for all loading situations, some inductive and capacitive, heavy and light loads are tested. Since the LOE occurs in the fifth second, Figure 8 shows the diagram of R and $\frac{dR}{dt}$ in low load of L=0.1+J0.5.

The diagram illustrating the resistance indicates that in the moments preceding the fault, the resistance value follows a sinusoidal pattern with a positive value. However, when the fault occurs, the resistance value, which is dependent on the voltage, begins to decrease. The derivative of the resistance becomes negative after the LOE event that occurs in the fifth second, remaining negative until the ninth second, after which it starts to increase again. In the following, the capacitive load is examined. Figure 9 displays the value of the resistance and the derivative of the resistance in the load L=0.3-J0.2 and it can be seen that in this load and in inductive loads, the resistance value starts to decrease at the beginning of the fault but will remain positive. Furthermore, according to the diagram, the resistance derivative stays negative for longer than 1.67 seconds, so it is concluded that the proposed method can be used as a valid indicator for LOE fault identification.

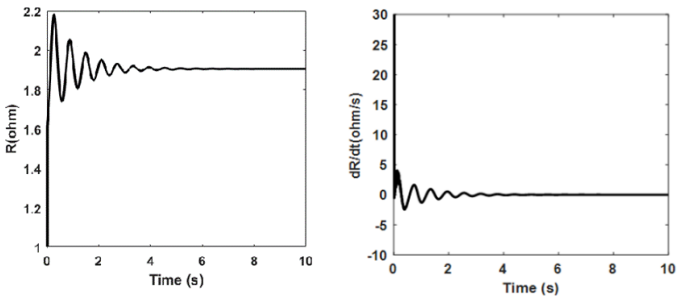

(a)-R (b)- $\frac{dR}{dt}$

Fig. 7. Diagrams derived from the simulation under normal conditions

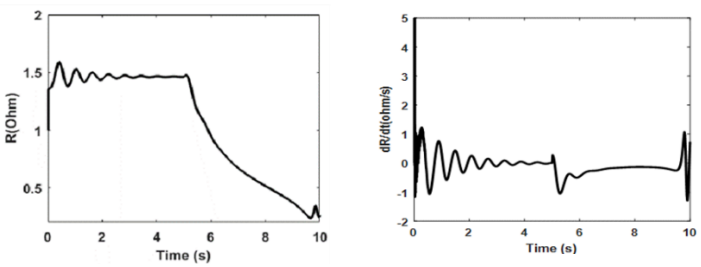

(a)-R (b)- $\frac{dR}{dt}$

Fig. 8. Diagrams derived from the LOE simulation for the load of L=0.1+J0.5

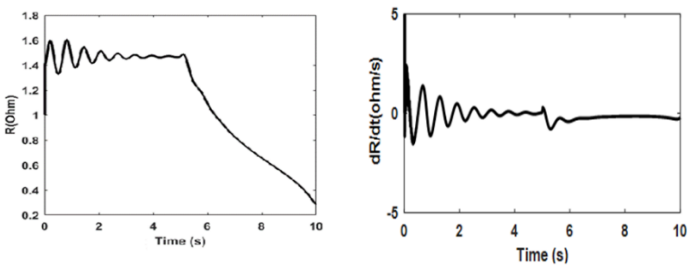

(a)-R (b)- $\frac{dR}{dt}$

Fig. 9. Diagrams derived from the LOE simulation for the load of L=0.3 J0.2

B. Simulation in the Presence of the STATCOM

This section addresses the behavior of the proposed method in the presence of STATCOM. First, Figure 10 displays the output diagram of the resistance and the derivative of the resistance in the normal state. According to this diagram, the resistance value seen in the generator terminal is sinusoidal with a positive value and is the same as in the absence of STATCOM, and the derivative diagram of resistance starts to decrease after a few oscillations and finally approaches the zero point. Now, the condition of the fault detection in different loads is examined. First, the output waveform for inductive load L=0.1+J0.5 is shown in Figure 11. According to this figure and the fact that the fault occurs in the 5th second, it can be concluded that like the case of the absence of STATCOM, the proposed method gives the correct answer to detect the LOE fault in such a way that the value of R is positive, and its derivative remains negative for a long time. Figure 12 shows the output diagram of resistance and its derivative in the case of capacitive load L=0.3-J0.2 in the presence of STATCOM. According to these diagrams and in comparison to the other situations, it can be seen that the new method can distinguish the LOE in this situation too.

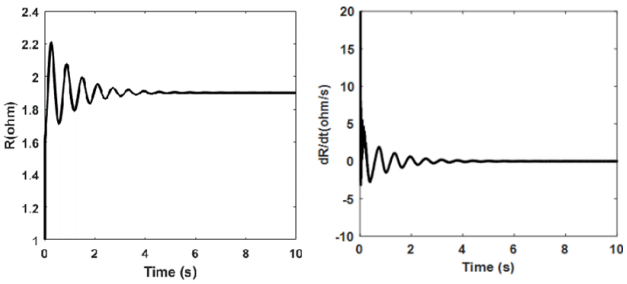

(a)-R (b)- $\frac{dR}{dt}$

Fig. 10. Diagrams derived from the simulation at Normal state in the presence of STATCOM

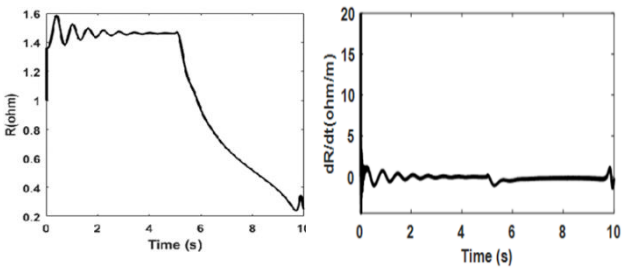

(a)-R (b)- $\frac{dR}{dt}$

Fig. 11. Diagrams derived from the simulation for the load of L=0.1+J0.5 in the presence of STATCOM

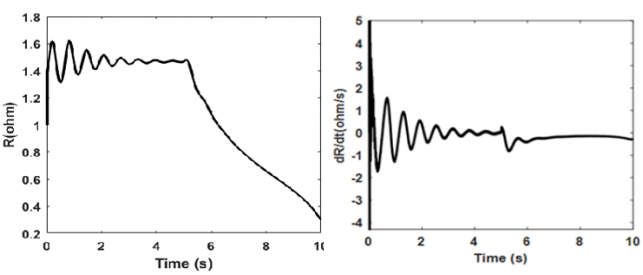

(a)-R (b)- $\frac{dR}{dt}$

Fig.12. Diagrams derived from the simulation for the load of L= 0.3-J0.2 in the presence of STATCOM

C. SPS conditions Simulation

This section discusses the conditions for detecting SPS and distinguishing it from LOE. SPS is caused by a short circuit fault. In SPS conditions, unlike LOE conditions, the dR/dt

output graph fluctuates positively and negatively and returns to normal after a few seconds. Figure 13 shows the behavior of resistance and its derivative in SPS mode at load L=0.1+J0.5 in the absence of STATCOM. SPS starts at the 3rd second and disappears at 1.3. According to the above figure, which shows that the resistance value is positive and according to its derivative becoming positive and negative and finally returning to its initial state, it can be stated that in accordance with the proposed procedure, unlike the LOE detection mode, the derivative value remains negative for a relatively long period of time. The negative time of the resistance derivative is less than 1.67 seconds, so it can distinguish SPS. Figure 14 displays the diagrams of resistance and its derivative in the event of SPS at load L=0.1+J0.5 in the presence of STATCOM. According to these diagrams, it can be expressed that the proposed procedure can detect SPS and distinguish it from LOE fault in this condition.

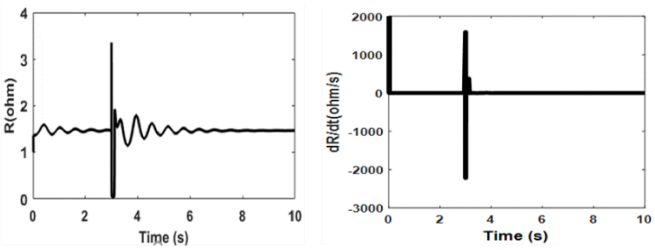

(a)-R (b)- $\frac{dR}{dt}$

Fig. 13. Diagrams for SPS condition for the load of L=0.1+J0.3 in the absence of STATCOM

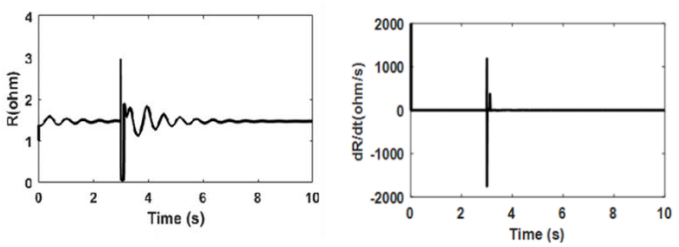

(a)-R (b)- $\frac{dR}{dt}$

Fig. 14. Diagrams for SPS condition for the load of L=0.1+J0.3 in the absence of STATCOM

IV. Comparison of Methods

Table 2 shows the operating time of different relays, both in the presence and absence of STATCOM. Based on this performance timetable, the proposed method is much faster than the common methods. Of course, the flux method and flux derivative are the fastest in operation, but as it is known, it is sophisticated to implement these methods.

In terms of computational complexity and implementation difficulty, the proposed method outperforms the other ones such as fuzzy logic [9], neural network [19], and state estimation [20] methods since they need training data and complex mathematical equations and relationships for LOE fault detection.

TABLE 2 COMPARISON OF METHODS

Relay type	Operating Time	Without STATCOM	With STATCOM	Setting Free
Positive Offset	11.2	Yes	No	**No**
Berdy	10.4s	Yes	No	**No**
Fuzzy Logic	9.1s	Yes	No	**No**
Flux	3.1s	Yes	Yes	**Yes**
Flux Derivative	1.7s	Yes	Yes	**Yes**
Proposed Method	5.35s	Yes	Yes	**Yes**

V. Conclusions

Considering that most methods of LOE fault detection and their distinguishing from SPS are based on impedance paths, these methods cannot often differentiate between the two options. Consequently, an intentional time delay is employed to prevent the improper operation of the impedance relay. However, this time delay is not an ideal solution, as it increases the stress on both the generator and the system. This paper proposed an algorithm based on the resistance derivative method that can effectively detect LOE and SPS and distinguish between them in the presence of STATCOM in different capacitive and inductive loads. Specifically, if the derivative of the resistance remains negative for longer than 1.67 seconds, it indicates an LOE fault. If it is shorter, it indicates an SPS. A key advantage of this proposed method, unlike impedance-based methods that require setting, is that it does not necessitate any adjustments.

References

[1] IEEE Power System Relaying Committee Working Group D6: ‘Power swing and out-of-step considerations on transmission lines’, June 2005.

[2] North Electric Reliability Corporation (NERC): ‘Power plant and transmission system protection coordination’, Technical Reference Document, July 2010.

[3] MAHAMEDI, Behnam; ZHU, Jian Guo; HASHEMI, Sayyed Mohammad. A setting-free approach to detecting loss of excitation in synchronous generators. IEEE Transactions on Power Delivery, 2016, 31.5: 2270-2278.IEEE Guide for AC Generator Protection, IEEE Standard C37.102-2006, Nov. 2006.

[4] REIMERT, Donald. Protective relaying for power generation systems. CRC press, 2005..

[5] MOZINA, Charles J. Lessons Learned From Generator Tripping Events. IEEE Industry Applications Magazine, 2010, 16.5: 29-36.

[6] Sharaf, A. M., and T. T. Lie. "ANN based pattern classification of synchronous generator stability and loss of excitation." IEEE transactions on energy conversion 9.4 (1994): 753-759.

[7] Fan, Bo, et al. "The research UL-P of loss-of-excitation protection for generator based on the artificial neural

networks." Power and Energy Engineering Conference, 2009. APPEEC 2009. Asia-Pacific. IEEE, 2009.
[8] Tambay, Shreesh R., and Yeshwant G. Paithankar. "A new adaptive loss of excitation relay augmented by rate of change of reactance." Power Engineering Society General Meeting, 2005. IEEE.
[9] de Morais, Adriano P., Ghendy Cardoso, and L. Mariotto. "An innovative loss-of-excitation protection based on the fuzzy inference mechanism." IEEE Transactions on Power Delivery25.4 (2010): 2197-2204.
[10] Mason, C. R. "A new loss-of-excitation relay for synchronous generators." Transactions of the American Institute of Electrical Engineers 68.2 (1949): 1240-1245.
[11] Berdy, J.: 'Loss-of-excitation protection for synchronous generators', AIEE Trans. Berdy, J.: 'Loss-of-excitation protection for synchronous generators', AIEE Trans , Power Appar. Syst., 1949, 68, pp.
[12] Elsamahy, Mohamed, Sherif Omar Faried, and Tarlochan Sidhu. "Impact of midpoint STATCOM on generator loss of excitation protection." IEEE Transactions on power delivery 29.2 (2014): 724-732.
[13] Amini, Mahdi, Mahdi Davarpanah, and Majid Sanaye-Pasand. "A novel approach to detect the synchronous generator loss of excitation." IEEE Transactions on Power Delivery 30.3 (2015): 1429-1438.
[14] Yaghobi, Hamid. "Fast discrimination of stable power swing with synchronous generator loss of excitation." IET Generation, Transmission & Distribution 10.7 (2016): 1682-1690.
[15] Yaghobi, Hamid. "Impact of static synchronous compensator on flux-based synchronous generator loss of excitation protection." IET Generation, Transmission & Distribution 9.9 (2015): 874-883.
[16] Yaghobi, Hamid, and Hashem Mortazavi. "A novel method to prevent incorrect operation of synchronous generator loss of excitation relay during and after different external faults." International Transactions on Electrical Energy Systems 25.9 (2015): 1717-1735.
[17] Milad Niaz Azari; Reza Fathi shoob. "An Investigation of a New Method to Detect Lossess of Excitation of Synchronous Generators". International Journal of Industrial Electronics Control and Optimization, 4, 1, 2021, 115-126. doi: 10.22111/ieco.2020.34337.1276
[18] Milad Niaz Azari. "A setting-free flux-based synchronous generator loss of excitation protection." Electrical Engineering100.4 (2018): 2
[19] Rahmkhoda, E., Faiz, J., & Abedini, M. "Detection of Loss-of-Excitation in Synchronous Machines using Hybrid GMDH Neural Network Intelligent Algorithm in the Presence of UPFC in Power System" *Electric Power Components and Systems*, *51*(10), 972–990.(2023)https://doi.org/10.1080/15325008.2023.2187096.
[20] Momeni, E., Yaghobi, H., Shahzadi, A.: Using dynamic state estimation to detect loss of excitation in synchronous generators. *IET Gener. Transm. Distrib.* 18,639–652(2024). https://doi.org/10.1049/gtd2.13106

Milad Niaz Azari was born in Babol, Iran. He received his B.S degree in electrical engineering from Noshirvani University of Technology, Babol, Iran in 2007. He Graduated in M.S degree in the department of Electrical Engineering, Amir Kabir University of Technology, Tehran, Iran in 2009. Also he graduated in PhD degree in Amirkabir University of Technology, Tehran, Iran in 2013. Since 2014, he has been at University of Science and Technology of Mazandaran, Behshahr, Iran, as an Associate Professor in the department of Electrical Engineering. His areas of interest are electrical machines design and power electronics (email: miladniazazari@mazust.ac.ir).

I. Ahmadi was born in Savadkooh, Iran, in 1973. He received his B.Sc. in Electronic Engineering in 1996, M.Sc. in Electrical Engineering in 1999, and Ph.D. in Electrical Engineering in 2010, from Amir Kabir University of Science and Technology, K.N.T. University of Science and Technology, and Tarbiat Modares University, Tehran, Iran, respectively. Between 1998 and 2013, he worked as an expert engineer at the Ministry of Energy. In 2013, he joined the University of Science and Technology of Mazandaran, where he is currently an Associate Professor in the Faculty of Electrical and Computer Engineering. His research interest includes power system protection, distribution system planning and reliability.

Hossein Abolqasemi was born in Sari, Iran, in 1992. He was graduated as a master's degree in electrical engineering from the University of Science and Technology of Mazandaran. His research interest is electrical power generator protection,

IECO

This page intentionally left blank.

International Journal Of
Industrial Electronics Control and Optimization
Print ISSN: 3517-2645
Online ISSN: 3568-2645
Homepage: https://ieco.usb.ac.ir/

Diagnosis of Supercapacitor State-of-Charge in Electric Vehicle Applications using Artificial Neural Networks

Seyed-Saeid Moosavi-Anchehpoli[1] | Mahmood Moghadasian [2] | Maryam Golpour [3]

[1]Clean power generation and Electrochemical laboratory, Amol University of Special Modern Technologies, Iran
[2] Shohadaye Hoveizeh Campus of Technology, Shahid Chamran University of Ahvaz, Iran
[3] Clean power generation and Electrochemical laboratory, Amol University of Special Modern Technologies, Iran
Corresponding author's email: anchepoli@um.ac.ir

Article Info

Article type:
Research Article

Article history:
Received: 21-February-2024
Received in revised form: 09-October-2024
Accepted: 12-November-2024
Published online: 23-Sep-2025

Keywords:
State-of-charge,
wavelet transform,
Artificial neural network,
Supercapacitor.

ABSTRACT

In electric vehicles, energy storage systems (ESSs) are essential for managing power fluctuations and ensuring operational safety. Supercapacitors (SCs) have recently emerged as promising ESS candidates due to their high-power density, rapid charge/discharge capabilities, and low internal losses. Integrating SCs with batteries or fuel cells in hybrid configurations can leverage the strengths of each technology while mitigating their individual weaknesses. This paper presents a novel estimation technique for supercapacitors in electric vehicles. The method involves wavelet decomposition and denoising, followed by importing low-frequency signals into a back-propagation neural network for one-step prediction to determine the state-of-charge (SOC) of the SC. The proposed method is tested with a Maxwell supercapacitor model under various charge/discharge current profiles and temperature conditions, comparing the results with conventional techniques. The artificial neural networks (ANNs) with wavelet pre-processed input demonstrate significantly improved SOC estimation accuracy across different discharge profiles.

I. Introduction

Batteries like Li-ion offer high energy density for electric vehicles, but their limited lifespan and sensitivity to charging rates and temperature present significant challenges. Combining them with supercapacitors (SCs) in a hybrid energy storage system (HESS) is a promising solution to enhance efficiency and address these limitations, as research has shown [1]. Accurately diagnosing the state-of-charge (SOC) of supercapacitors is vital for managing energy distribution between the supercapacitor and the battery, optimizing performance, and ensuring the reliability of EVs [2].

The SOC of a supercapacitor, indicating its remaining energy relative to its maximum capacity, is crucial for effective energy management, ensuring the supercapacitor operates within safe limits, and optimizing the performance and lifespan of the entire energy storage system [3].

Estimating the State of Charge of a supercapacitor, is crucial for efficient and safe operation. However, traditional methods often struggle with the inherent nonlinearities and dynamic characteristics of these devices. These methods fall into several categories:

Direct Measurement Methods: These methods rely on directly measurable parameters of the energy storage device.

Coulomb Counting: Coulomb counting is a straightforward method that integrates the current over time. While simple, this method suffers from cumulative error over time and requires an accurate initial SOC value [4].

Voltage-based: These methods estimate SOC by measuring the terminal voltage of the supercapacitor. However, the nonlinear relationship between voltage and SOC, particularly at high and low extremes, limits accuracy [5].

Current Integration: SOC is estimated by integrating the current flowing in or out of the device over time. This method suffers from drift and requires accurate initial SOC [6].

Model-Based Methods: These methods utilize mathematical models of the energy storage device.

Copyright © Anchepoli (s).
Publisher: University of Sistan and Baluchestan

Equivalent Circuit Models: Represent the device with electrical components (resistors, capacitors, inductors) to simulate behavior and estimate SOC. Accuracy depends on model complexity and parameter identification [18].

Electrochemical Models: More complex models based on the underlying electrochemical reactions within the device, offer higher accuracy but require significant computational resources [7].

Kalman Filtering: A recursive algorithm that combines model predictions with measurements to estimate SOC, reducing noise and improving accuracy. Requires a well-defined model and can be computationally demanding [1].

Data-Driven Methods: These methods leverage machine learning algorithms trained on historical or experimental data.

Artificial Neural Networks: ANNs have shown promise in SOC estimation due to their ability to capture complex, nonlinear relationships without explicit mathematical models. ANNs can learn from historical data and adapt to new conditions, making them suitable for dynamic environments like EVs [8-10].

Support Vector Machines: Effective for classification and regression tasks, can be used for SOC estimation. Require careful selection of kernel functions and hyperparameters [11].

Fuzzy Logic: Handles uncertainties and non-linearities well, suitable for complex systems. Requires expert knowledge for rule definition and membership function design [12].

Hybrid Methods: Combine multiple approaches to leverage their strengths and mitigate weaknesses. For example, combining an ECM with a Kalman filter or using an ANN to improve the accuracy of a voltage-based method [13].

This categorization is not exhaustive, and new methods are constantly being developed. The choice of the most suitable method depends on factors like the specific energy storage device, required accuracy, computational resources, and application requirements.

Modeling the behavior of supercapacitors is challenging due to their complex dependence on current, temperature, chemistry, and past conditions [8]. Traditional methods struggle with such intricate nonlinearities. Artificial Neural Networks (ANNs) offer a powerful alternative, excelling at capturing complex relationships without requiring explicit mathematical equations or physical derivations.

When tackling a nonlinear system like a supercapacitor, ANNs bypass the need for cumbersome calculations. Instead, they learn by analyzing a carefully chosen data set. By adjusting internal connections (neurons) and iteratively fine-tuning them, the ANN gradually approximates the system's behavior. Remarkably, even with limited data, ANNs can identify subtle patterns and adapt to unseen situations.

A well-trained ANN exhibits resilience to unexpected inputs, including noise and disruptions. This robustness allows it to deliver accurate predictions even in uncertain environments [9, 10].

In contrast to the aforementioned approaches, ANNs have emerged as a popular tool for estimating SOC in both batteries and supercapacitors, handling both constant and dynamic discharge currents [8, 10]. Several variables are chosen as the ANN's inputs. The weights are usually trained using a BP algorithm. Reported error margins vary, with references claiming accuracy within 10% [8]. However, recent breakthroughs have led to significantly improved accuracy, with some researchers reporting error rates as low as 1% [14-19].

For modeling supercapacitors in automotive applications, research suggests using a one-layer feed-forward ANN trained with the back-propagation algorithm [8]. Similarly, an ANN-based performance computing model for lead-acid batteries in EVs has been proposed in [10].

These neural network approaches exhibit greater accuracy compared to traditional methods like the Peukert equation (maximum error 1.724%), multilevel Peukert equation (maximum error 1.379%), and least-square method (maximum error 1.379%). Studies show that the proposed ANN models achieve significantly lower errors [8].

For energy management and optimal power control, establishing a precise model to display SC dynamics behavior is critical; however, this is difficult.

The following are the key contributions of this work:

1- To improve the conventional function of training ANN, a WT model is created. It's used to break down a voltage profile into its various components, each with its own frequency.

2- The number of neurons in multi-layer neural networks is optimized.

3- The proposed WT model and ANN’s are combined to create a complete wavelet ANN model, which greatly improves SOC estimation accuracy.

4- The proposed wavelet ANN model exhibited robust performance across a range of driving cycles (discharge current profiles), consistently providing reliable SOC estimations with low error rates. These results compare favorably to those reported in the literature.

5- The classification unit is not needed for categorizing the different discharge current profiles in this ANN system. This is yet another significant outcome of this project.

6- The given technique can be employed to precisely determine the SOC of a SCs module, which is exceptionally beneficial in EV applications.

The layout of this study is as follows: Section 2 covers the background on WT. Section 3 delves into the background of

ANN. Section 4 outlines the details of the test bench. The outcomes and relevant discussions are unveiled in Section 5. Lastly, the conclusion of this study is drawn in Section 6.

II. Wavelet Transform (WT) Specification

Given that the Fourier transform (FT) fails to pinpoint the exact moment of a specific frequency's appearance within a signal time series, it proves inadequate for examining nonstationary signals. Conversely, the wavelet transform (WT) transposes a signal from the time domain (TD) into a time-scaled frequency domain (TSFD). This method enables a nonstationary and nonlinear signal profile to be disassembled into a set of profiles, each with distinct frequencies. Wavelet [20] is a short-duration wave that develops and decays over a short period of time.

The Wavelet Transform (WT) breaks down a signal into its building blocks based on frequency. It separates the signal into two types of information:

Approximation (A) data: This captures the overall trend and low-frequency components of the signal. Think of it like the smooth outline of a painting.

Detail (D) data: This contains the high-frequency details and sharp features, like the brushstrokes and textures in the painting.

However, unlike traditional WT, which only analyzes the low-frequency part, the method used here goes further. It decomposes the signal into multiple levels (like zooming in on the painting). This allows for a more detailed understanding of both the overall shape and the fine details.

Figure 1 illustrates this three-level decomposition. In the notation Aα; β and Dα; β, α represents the level (zoom level) and β is an index that identifies specific signals within that level.

Various stages of decomposition can be undertaken, but studies indicate that the tri-level decomposition exhibits superior performance in other time series prediction applications, such as power system load forecasting in the conventional wavelet transformation [21]. WT bifurcates into two classifications: the Continuous Wavelet Transform (CWT) and the Discrete Wavelet Transform (DWT). The CWT encapsulates all the information contained in the provided signal x(t), as represented by Eq. (1).

$$W(a,b) = \int_{-\infty}^{\infty} \psi_{a,b}(t) \cdot x(t) dt \quad (1)$$

CWT, on the other hand, is computationally inefficient and needs a lot of memory compared to DWT. DWT is accurate enough to decompose a signal while still being computationally light. As a result, we use a DWT in this analysis. For a particular signal, denoted as x(t), the definition of DWT is expressed in Eq. (2).

$$W(m,n) = 2^{-(m/2)} \sum_{t=0}^{T} \psi\left(\frac{t - n \cdot 2^m}{2^m}\right) \cdot x(t) \quad (2)$$

In this context, T denotes the duration of the signal x(t), with m and n symbolizing the scaling and translational parameters in such a manner that ($a = 2^m$) and ($b = n \cdot 2^m$). Further, t represents the individual time parameter in its discrete form.

III. ANN Model Specification

The artificial neural network has long been recognized as an effective estimation method for both linear and non-linear systems. ANNs can be used to model nonlinear dynamic systems to some level of precision [22].

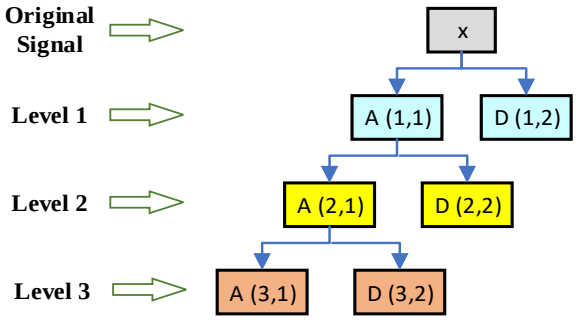

Fig. 1. A WT with Three-level. In both A (α, β) and D (α, β), α is symbolic of the levels, whereas β indicates the position of the signal within the level noted by α.

ANNs offer a multitude of benefits, comprising the capacity to discern intricate nonlinear links between dependent and independent variables, bypassing the requirement for formal statistical education. Additionally, they can identify every conceivable correlation among predictive variables and provide a plethora of training algorithms [8, 9]. Despite these advantages, they also possess certain drawbacks such as their 'black box' structure, increased computational demand, tendency towards overfitting, and the practical essence of model building [23]. The structure of a ANN outlines the configuration of neural connections, along with the categorization of units characterized by an activation function. The processing algorithm defines the method through which neurons compute the output vector, given a specific set of weights for each input vector. The training algorithm explicates how the ANN modifies its weights 'w' corresponding to all input vectors, also known as training vectors.

As a result of the training algorithm, the ANN will gain information and store it in synaptic weights. There are several different types of ANNs, but multi-layer feed-forward networks are the most common. Figure 2 shows a sample feed-forward ANN scheme (input, one hidden layer, and output layer) [24, 25].

This work employs a three-layers, Feed Forward ANN to estimate the SOC. In the construction of an ANN, neurons function as fundamental components. As illustrated in Figure 3, an ANN's single layer can have 'i' inputs given by X = [x1, x2 … xi]T and 'k' neurons. It should be noted that 'k' is typically not equal to 'i'. Furthermore, each input is linked to individual neurons through suitable weightings.

Every neuron computes the cumulative total of its inputs, factoring in the bias, and subjects this result to its activation function. Consequently, there are 'k' resultant outputs y1= [y11, y12 … y1k]T associated with the ANN represented by a singular layer (where the primary index in y1 outcomes of the first layer is detailed as y11, y12 … y1k) and,

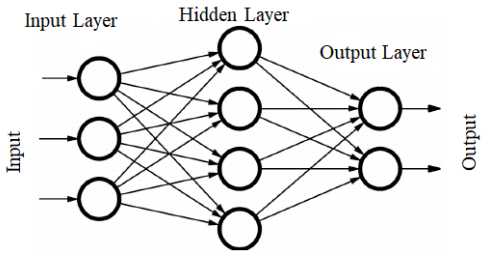

Fig. 2. Sample of a feed-forward ANN

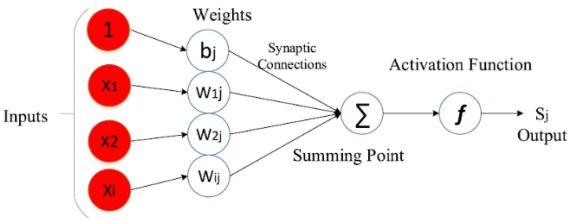

Fig. 3. The diagram of a neuron

$$y_1 = F_1 (W_1X + B_1) \quad (3)$$

The term 'F1' signifies the activation matrix pertaining to this individual layer. This matrix is characterized by being diagonal and consisting of k elements. The matrix's nature is contingent on the net inputs directed towards this specific layer.

$$F1 (S1) = \text{diag} [f1s1, f1s1 ... f1(sk)] \quad (4)$$

The elements mentioned are the activation functions for each of the 'k' nodes, which are presumed to be identical, denoted as f11=f12=...=f1k=f1. 'S1' represents the net vector, S1= [s1, s2,..., sk]T, comprising the net inputs s1, s2,..., sk for neurons 1, 2, ..., K, and S_j equals $S_j = \sum_{j=1}^{n} w_{ij} x_j (t) + b_i$. Additionally, '$w_1$' signifies the weight matrix for the output layer, which due to the predefined structure, must encompass k rows and n columns.

$$w_1 = \begin{bmatrix} w_{1,1} & w_{1,2} \cdots & w_{1,n} \\ \vdots & \ddots & \vdots \\ w_{k,1} & w_{k,2} \cdots & w_{k,n} \end{bmatrix} \quad (5)$$

The term 'w_{ij}' typically represents the weight transitioning from target node 'j' to origin node 'i', given that i and j are any numbers from 1 to k and 1 to n respectively. B1, on the other hand, signifies the bias vector for a single layer, expressed as B1 = [b11, b12, ..., b1k]T. Here, b11, b12, ..., b1k denote the individual biases of nodes ranging from 1 to k in the final layer. We can construct an ANN with three lyres by extending the aforementioned equations. In this study, a mere 10 cycles of SC voltage profiles were utilized as training data and for estimating the state-of-charge.

IV. Experimental Set-Up

Figure 4 depicts the experimental setup. The trials employed a SC cell provided by Maxwell Technologies, boasting a specified voltage of 2.7 V and a capacitance of 350 F. Comprehensive data regarding the SC cell's parameters can be found in Table I.

TABLE 1 THE SYSTEM'S EXPERIMENTAL PARAMETERS

Parameter	Value
Supercapacitor cell	Maxwell technology
Rated voltage of cell	2.7 V
Rated capacitance of cell	350 F
Sampling frequency fs	50 Hz
Operating temperature T °c	0 , 25, 35, 45 , 55
Minimum Temperature °c	-40
Maximum Temperature °c	70
Absolute maximum voltage	2.85 V
Absolute maximum Current	170 A
Maximum ESRDC initial	3.2 m.ohm
Specific energy	5.6 wh/Kg
Leakage current (at 25 °c)	0.3 mA
Maximum continuous Current 15°C	21 A
Maximum continuous Current 40°C	34 A
Life time	500000 life cycle

The SC's charge and discharge current is monitored and controlled by a battery testing and formulation system, both software and hardware, courtesy of BaSyTec technology. This system is used to generate the required current profiles and to mimic the conditions experienced during real-world Electric Vehicle (EV) driving scenarios. T=25°C, 35°C, 45°C, and 55°C are the temperatures used in the experiments. The Battery test device is limited to a sampling frequency of fs=50 Hz. For data acquisition, eight different current discharge profiles are employed, as follow:

- Worldwide harmonized Light vehicles Test Cycles (WLTC)
- Artemis cycle with maximum speeds of 130 (Art 130)
- Artemis Urban (Art Urban)
- Artemis Rural (Art Rural)
- West Virginia Suburban (WVUSUB) driving cycle
- Japan Cycle 08 (JC08)
- Japan 10-15 mode (JP1015)
- New European Driving Cycle (NEDC)

V. Results and Discussion

A diagnostic process and implementation algorithm for SOC estimation of SC are shown in Figure 5. The next step is ANN training after identifying a proper pattern with wavelet transform, as shown in figure 6 and outlined in section II. This enables one to gain a better understanding of the ANN mechanism prior to its implementation. The NN's learning algorithm is a computational method that determines the strength of connections, such as layer weights and biases in neurons. The validation data collection is used during the learning process to boost the ANN's generality. The learning process is terminated based on the validation data set when the error function starts to increase or becomes smaller than the convergence tolerance, whichever comes first.

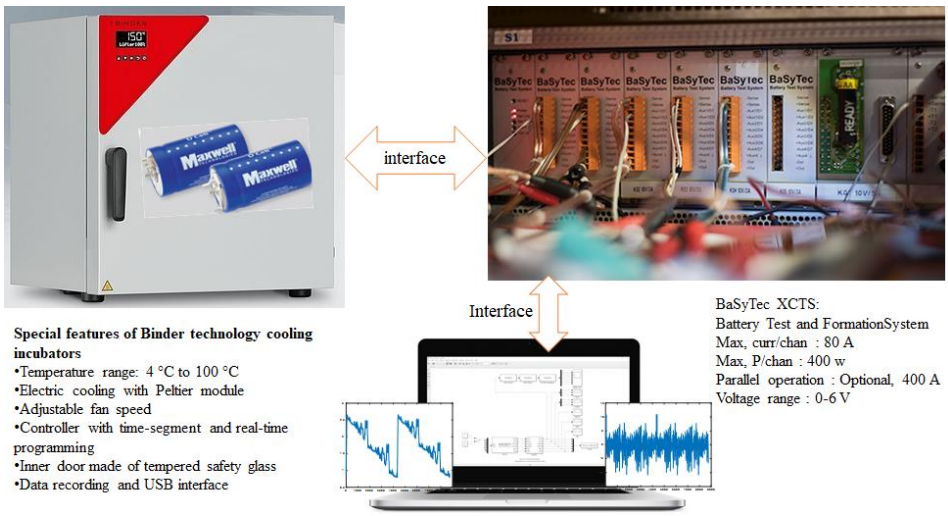

Fig. 4. Pictures of the experimental setup

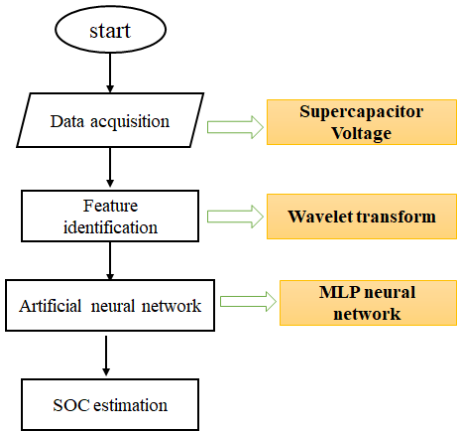

Fig. 5. SOC estimation and implementation algorithm

We use the data to train a neural network, in which, the hidden layer contains 30 neurons. Hyperbolic tangent (Tanh) function is used as an activation function. The maximum number of epochs is set to 100, and validation MSE goal is set to 1e-6. Since the Levenberg–Marquardt algorithm has a fast rate of convergence, we use it to train the parameters of the neural networks in this study. The training performance of the ANN has been shown in figure 7. The best validation MSE is 0.0001318 at epoch 87.

The data are randomly divided into three sets: training (60% of the data), testing (20%), and crossvalidation (20%) as shown in the Table II. All data are normalized in the range of [0, 1].

The accuracy of SOC estimation is analyzed using five established error metrics:

Mean Square Error (MSE), Root Mean Square Error (RMSE), and Normalized Root Mean Square Error (NRMSE): These metrics quantify the average magnitude of errors between predicted and actual SOC values.

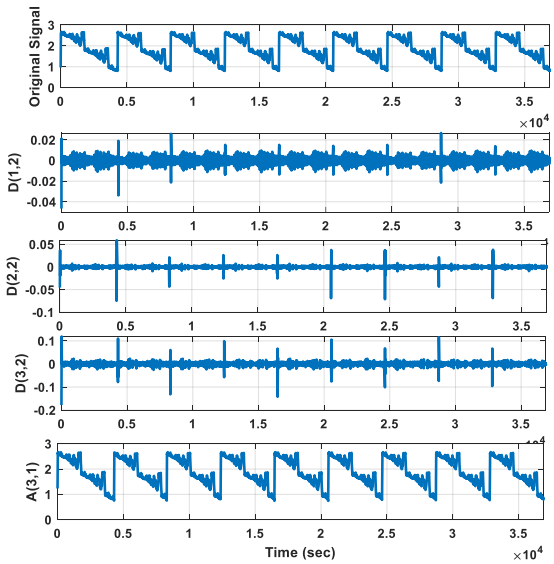

Fig. 6. Output results from a 3-level WT intended for ANN training input, derived solely from a single current discharge profile

NRMSE normalizes the error by the SOC range, allowing for comparisons across different datasets.

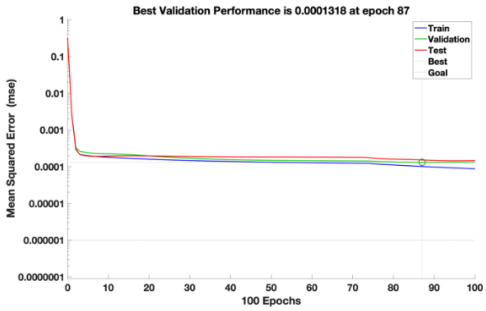

Fig. 7. Training performance of the ANN

TABLE 2 DATA DIVISION IN LEARNING PROCESS

Discharge Profile	Number of All Data Samples	Number of Training Samples	Number of Testing Samples
WLTC	40000	24000	8000
Art 130	16250	9750	3250
Art Urban	10000	6000	2000
Art Rural	2000	1200	400
WVUSUB	10000	6000	2000
JC08	8000	4800	1600
JP1015	7500	4500	1500
NEDC	10000	6000	2000

Average Relative Percentage Error (ARPE): This metric expresses the average error as a percentage of the actual SOC values, providing a relative measure of accuracy.

By analyzing these error metrics across all three data sets, this work provides a comprehensive understanding of the ANN's generalizability and effectiveness in real-world applications.

$$MSE = \frac{1}{N}\sum_{j=1}^{N}(U_a(j) - U_a(j))^2 \quad (6)$$

$$RMSE = \sqrt{\frac{\sum_{j=1}^{N}(U_e(j)-U_a(j))^2}{N}} \quad (7)$$

$$NRMSE = \frac{RMSE}{U_{max}-U_{min}} \quad (8)$$

$$MAE = \frac{\sum_{j=1}^{N}|U_e(j)-U_a(j)|}{N} \quad (9)$$

$$ARPE = \frac{1}{N}\sum_{j=1}^{N}\frac{|U_e(j)-U_a(j)|}{|U_a(j)|} \times 100\% \quad (10)$$

Wherein N signifies the quantity of training or testing data, U_{max} represents the highest recorded value, and U_{min} depicts the smallest value of the gathered data. $U_e(j)$ and $U_a(j)$ pertain to the predicted SOC yielded from the trained neural network, and the actual SOC deduced from the empirical data, respectively.

Figure 8 depicts the real and predicted SOC training outcomes for the best and worst estimated conditions using the same training data collection. For all current discharge profiles, the SOC estimate is very accurate, and the corresponding errors are close to zero, as predicted. The testing data from each test was used to determine the accuracy of the qualified ANN for SOC estimation. Figure 9 depicts a comparison of the real SOC and the predicted SOC at the temperature of 30°C for various EV discharge current profiles. To ensure the ANN's consistency, we run it 20 times at various temperatures. All estimated SOCs are found to be very similar to the corresponding real SOCs, indicating that the proposed ANN can provide reliable SOC estimation for EVs.

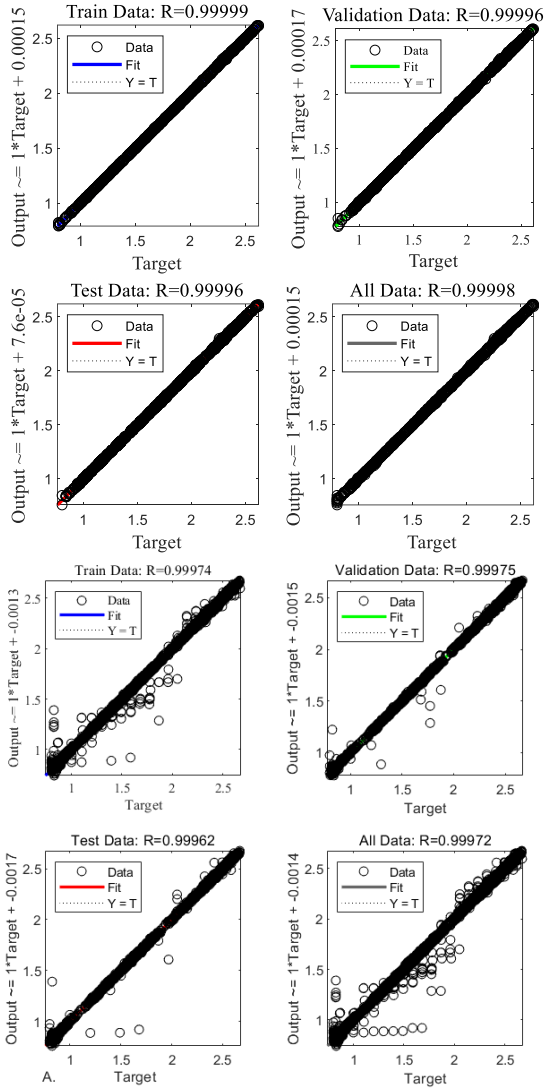

Fig. 8. Regressions of training, validation and test based outputs A. the best estimation state for JC08 driving cycle, B. the worst estimation state for ART 130 driving cycle.

specifications across various EV discharge current profiles. The JC08 profile yielded the smallest estimation error, while the ART 130 profile resulted in the largest. Benchmarking against existing methods demonstrates the proposed algorithm's effectiveness. Compared to the method in [14],

TABLE 3 SOC ESTIMATION ERROR SPECIFICATIONS IN DIFFERENT CURRENT DECHARGE PROFILES OF EVS APPLICATIONS

Driving cycle	MSE	NRMSE	ARPE	RMSE			MAE		
	This Work	This Work	This Work	This Work	Others	Improvement (%)	This Work	Others	Improvement (%)
WLTC	102e-06	0.0300	0.4393	0.0101	0.012 [14]	19.80	0.00735	0.0085[14]	15.65
ART 130	187e-06	0.0970	0.6131	0.0137			0.00854		
ART Urban	6.2e-06	0.0583	0.1060	0.0025	0.002 [19]	-4	0.00178	0.0037[15]	107.87
Art Rural	3.1e-06	0.0485	0.0737	0.0018			0.00120		
WVUSUB	4.1e-06	0.0579	0.0897	0.0020			0.00147	0.0086[16]	485.03
JC08	14e-06	0.0357	0.1710	0.0038			0.00279		
JP1015	2.4e-06	0.0462	0.0613	0.0016	0.0064[17]	300.00	0.00106	0.006 [17]	475.47
NEDC	17e-06	0.0324	0.1679	0.0042			0.00280	0.003 [18]	35.71

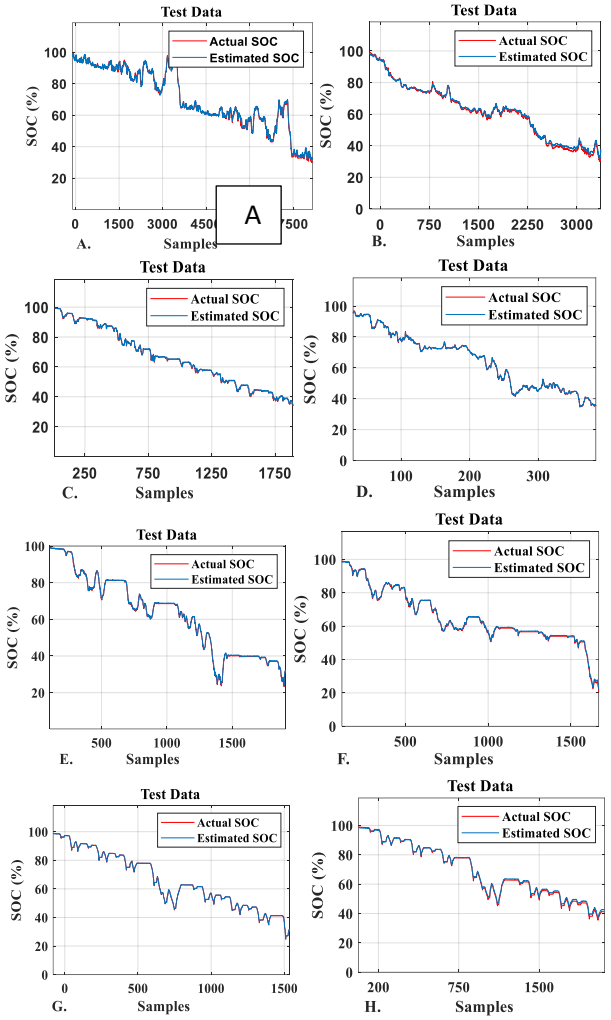

Fig. 9. Actual and estimated SOC% in different current discharge profiles, A. WLTC, B. Art 130, C. Art Urban, D. Art Rural, E. WVUSUB, F.JC08, G.JP1015, H. NEDC

Table III provides a quantitative analysis of the proposed method's robustness, presenting SOC estimation error the proposed method achieves a 19.8% reduction in RMSE and a 15.65% improvement in MAE for the WLTC profile.

While the method in [19] exhibits slightly lower RMSE for the ART Urban case, the proposed method significantly improves MAE by 107.87% compared to [15]. Furthermore, the proposed method demonstrates substantial improvements in MAE for other profiles: a 35.71% improvement for NEDC and a fivefold reduction for WVUSUB and JP1015 compared to those reported in [16] to [18], respectively.

It is worth mentioning that current ANN approach does not require the classification unit. It is another fascinating contribution of this work in comparison to other works like in [9]. The overall error of all tests for Art Rural current discharge profile is plotted in figure.10, as a typical example.

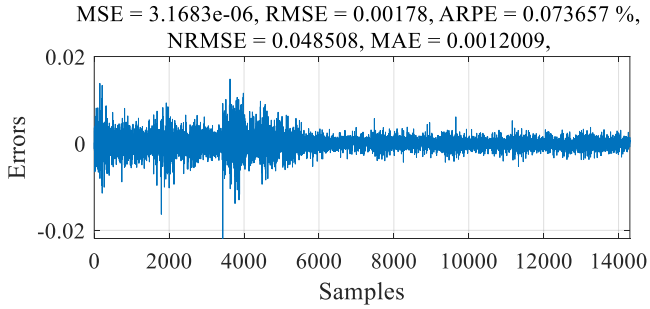

Fig. 10. Overall Errors for Art Rural current decharge profile test-set

VI. Conclusion

This paper proposes a novel ANN approach for estimating the State-of-Charge (SOC) of supercapacitors in electric vehicles (EVs). The key innovation lies in treating the SOC as the ANN's output and incorporating the distribution of discharged capacity as one of its inputs. This allows the ANN to capture the impact of varying discharge current profiles on

the SC's residual capacity, leading to more accurate estimations tailored to different EV driving cycles.

Performance is evaluated using various error metrics (MSE, RMSE, NRMSE, ARPE, MAE) on different testing datasets. The consistently low values close to zero demonstrate the proposed three-layer ANN's capability of providing reliable SOC estimation.

Furthermore, a wavelet transform model is introduced to decompose the voltage profile into its frequency components. This information is then fused with the NN model to create a comprehensive Wavelet Neural Network (WNN) model. This combined approach significantly improves the accuracy of SOC estimation compared to the NN alone.

The WNN model demonstrates high reliability under diverse driving cycle conditions, supported by detailed error statistics. While previous work presented in [9], highlighted the lack of a classification unit for various discharge profiles, this NN approach effectively addresses this challenge. It accurately estimates the SOC of a SC module, finding potential applications in various EV scenarios.

Future work could explore extending the ANN to account for multiple SC modules and ageing effects. Despite limitations in certain hybrid EVs regarding grid-based charging and unknown fully charged states, the proposed ANN method remains applicable in such situations.

Acknowledgment

This research work has been supported by a research grant from the Amol University of Special Modern Technologies, Amol, Iran.

In the conclusion, please show how the work advances the field from the present state of knowledge. Please provide a clear justification for your work in this section, and indicate uses and extensions if appropriate. Moreover, you can suggest future.

REFERENCES

[1] Lei Zhang, Zhenpo Wang, Fengchun Sun, and David G. Dorrell, “Online Parameter Identification of Ultracapacitor Models Using the Extended Kalman Filter”, Energies, Vol. 7, pp. 3204-3217, 2014.

[2] M. Jami, “Virtual Inertia Control and Small-Signal Stability Analysis of Electric Vehicle”, International Journal of Industrial Electronics, Control and Optimization (IECO), 6(4), 2023.

[3] Ramezan Havangi, Fatemeh Karimi, “Improvement of The Battery State of Charge Estimation Using Recursive Least Square Based Adaptive Extended Kalman Filter”, Industrial Electronics, Control and Optimization (IECO), 7(2), 2024.

[4] Kiarash Movassagh, Arif Raihan, Balakumar Balasingam, Krishna Pattipati, “A Critical Look at Coulomb Counting Approach for State of Charge Estimation in Batteries”, MDPI *Energies*, 14(14), 2021.

[5] Marco Mussi, Luigi Pellegrino, Marcello Restelli, Francesco Trovò, “A voltage dynamic-based state of charge estimation method for batteries storage systems”, Journal of Energy Storage, Vol. 44, Part B, 2021.

[6] Xin Zhang, Jiawei Hou, Zekun Wang, and Yueqiu Jiang, “Study of SOC Estimation by the Ampere-Hour Integral Method with Capacity Correction Based on LSTM”, MDPI *Batteries*, 8(10), 170, 2022.

[7] Jingrong Wang, Jinhao Meng, Qiao Peng, Tianqi Liu, Jichang Peng, “An electrochemical-thermal coupling model for lithium-ion battery state-of-charge estimation with improve dual particle filter framework”, Journal of Energy Storage, Vol. 87, 2024.

[8] Yoshifumi Morita, Sou Yamamoto, Sun Hee Lee, and Naoki Mizuno, “On-Line Detection Of State-Of-Charge In Lead Acid, Battery Using Radial Basis Function Neural Network”, Asian Journal of Control, Vol. 8, No. 3, pp. 268-273, 2006.

[9] W. X. Shen, K. T. Chau, C. C. Chan, and Edward W. C. Lo, “Neural Network-Based Residual Capacity Indicator for Nickel-Metal Hydride Batteries in Electric Vehicles”, IEEE transactions on vehicular technology, Vol. 54, NO. 5, pp. 1705-1712, 2005.

[10] Cheng Bo, Bai Zhifeng, Cao Binggang, “State of charge estimation based on evolutionary neural network”, Energy Conversion and Management, Vol. 49 , 2008.

[11] Juan Carlos Álvarez Antón, Paulino José García Nieto, Cecilio Blanco Viejo, José Antonio Vilán Vilán, “Support vector machines used to estimate the battery state of charge”, IEEE Trans. Power Electron. 28, 2013

[12] Simin Peng, Yifan Miao, Rui Xiong, Jiawei Bai, Mengzeng Cheng, Michael Pecht, “State of charge estimation for a parallel battery pack jointly by fuzzy-PI model regulator and adaptive unscented Kalman filter”, Applied Energy, Vol. 360, 2024.

[13] Hicham Ben Sassi, Fatima Errahimi, Najia Es-Sbai, Chakib Alaoui, “Comparative study of ANN/KF for on-board SOC estimation for vehicular applications”, Journal of Energy Storage, Vol. 25, 2019.

[14] Jie Zhang, Bo Xiao, Geng Niu, Xuanzhi Xie, Saixiang Wu, “Joint estimation of state-of-charge and state-of-power for hybrid supercapacitors using fractional-order adaptive unscented Kalman filter”, Energy, Vol. 294, 2024.

[15] Seyedmehdi Hosseininasab, Nastaran Momtaheni, Stefan Pischinger, Marco Günther, Lennart Bauer, “State-of-charge estimation of Lithium-ion batteries using an adaptive dual unscented Kalman filter based on a reduced-order model”, Journal of Energy Storage, Vol. 73, 2023.

[16] Bizhong Xia, Wenhui Zheng, Ruifeng Zhang, Zizhou Lao, and Zhen Sun, “A Novel Observer for Lithium-Ion Battery State of Charge Estimation in Electric Vehicles Based on a Second-Order Equivalent Circuit Model”, MDPI *Energies*, 2017.

[17] Yonghong Xu, Hongguang Zhang, Jian Zhang, Fubin Yang, Liang Tong, Dong Yan, Hailong Yang, Yan Wang, “State of charge estimation under different temperatures using unscented Kalman filter algorithm based on fractional-order model with multi-innovation”, Journal of Energy Storage, Vol. 56, 2022.

[18] Jinhao Meng, Daniel-Ioan Stroe, Mattia Ricco, Guangzhao Luo, and Remus Teodorescu, “A Simplified Model based State-of-Charge Estimation Approach for Lithium-ion Battery with Dynamic Linear Model”, IEEE transactions on industrial electronics, 2018.

[19] Georg Walder, Christian Campestrini, Sebastian Kohlmeier, Markus Lienkamp, Andreas Jossen, "Adaptive State and Parameter Estimation of Lithium-Ion Batteries Based on a Dual Linear Kalman Filter", Technological Advances in Electrical, Electronics and Computer Engineering, 2014.
[20] Jonghoon Kim, Hany M. Hasanien, Roland Kobla Tagayi, "Investigation of noise suppression in experimental multi-cell battery string voltage applying various mother wavelets and decomposition levels in discrete wavelet transform for precise state-of-charge estimation", Journal of Energy Storage, Vol. 73, Part C, 2023.
[21] Asmae El Mejdoubi, Amrane Oukaour, Hicham Chaoui, Youssef Slamani, Jalal Sabor, Hamid Gualous, "Online Supercapacitor Diagnosis for Electric Vehicle Applications", IEEE Transactions on Vehicular Technology, Vol. 65, Issue: 6, 2016.
[22] S.S. Moosavi, A. Kazemi, H. Akbari, "A comparison of various methods of identifying open-circuit fault in the IGBT-based DC/AC inverter used in electric vehicle", Engineering Failure Analysis, Vol. 96, Pp. 223-235, 2019.
[23] S. Saeid. Moosavi, A. Djerdir, Y. A. Amirat, D. A. Khaburi, "Artificial Neural Network based Fault Detection in the AC-DC Converter of the Power Supply of SHEV", Electrical Systems in Transportation, IET, Vol. 6, Issue 2, 2016.
[24] S. Saeid. Moosavi, A. Djerdir, Y. Aït-Amirat, D. A. Khaburi, "ANN based fault diagnosis of permanent magnet synchronous motor under stator winding shorted turn", Electric Power Systems Research, Vol. 125, 2015.
[25] M. Sifuzzaman, M. R. Islam, M. Ali, "Application of wavelet transform and its advantages compared to fourier transform", Journal of Physical Sciences, Vol. 13, 2009.

Seyed Saeid Moosavi (S'09) was born in Amol, Iran. He received the B.Sc. degree in electrical power engineering, in 2004, the M.Sc. degree from the Electrical Railway engineering department of Iran University of science and technology (IUST), Tehran, Iran, in 2009. From 2007 -2010 he was a researcher on Electrification, control and signaling of railway transportation. He received the PHD in electrical engineering at university of technology Belfort Montbeliard, in 2013. He was assistant professor in the Systems and Transport (SET) laboratory at University of Technology Belfort Montbéliard, France and researcher in the FEMTO-ST laboratory in 2014. Now he is assistant professor of Amol university of special modern technologies. His main research interests include the modeling of electrical machines (EM), hybrid/electric vehicle (H/EV) and the study and application of, condition monitoring, signal processing, fault detection and diagnosis techniques for EM and H/EV.

Mahmood Moghadasian earned his B.S. in electronics from Amirkabir University of Technology in 2005. He then received his M.Sc. in power engineering from Shahid Chamran University of Ahvaz in 2008, and his Ph.D., also in power engineering, from UPJV, Amiens, France, in 2013. He is currently an Assistant Professor at Shohadaye Hoveizeh Campus of Technology, Shahid Chamran University of Ahvaz,. His research focuses on machine learning, optimal control, and optimization.

Maryam Golpour was born in Amol, Iram. She received her B.S. and M.S. degree in Chemical Engineering from the University of Guilan, Rasht, Iran, in 2009 and 2012 respectively, and her Ph.D. degrees in Chemical Engineering from the Ferdowsi University of Mashhad, Mashhad, Iran, in 2018. From 2018 until present, she is a research assistant in clean power generation and electrochemical laboratory at Amol University of Special Modern Technologies, Amol, Iran. Her current research interests include nano technology, separation, energy production, and data science.

IECO

This page intentionally left blank.

International Journal Of
Industrial Electronics Control and Optimization
Print ISSN: 3517-2645
Online ISSN: 3568-2645
Homepage: https://ieco.usb.ac.ir/

Mobile Robot Localization in Indoor Environments Using Fuzzy Adaptive Unscented Kalman Filter and Random Tree Routing Algorithm with Fast Exploration

Mohamadrasol Hajiali[1] | Ramazan Havangi[2]
Faculty of Electrical Engineering and Computer, University of Birjand, Iran.[1,2]
Corresponding author's email: Havangi@Birjand.ac.ir

Article Info

Article type:
Research Article

Article history:
Received: 10-July-2024
Received in revised form: 25-November-2024
Accepted: 11-December-2024
Published online: 23-Sep-2025

Keywords:
Fuzzy,
Random tree routing,
Robot localization,
Unscented Kalman filter.

ABSTRACT

In the field of mobile robot navigation, challenges such as nonlinear conditions, uncertainties, and the advancement of methods have made accurate position estimation essential. This study evaluates the effectiveness of a fuzzy-based adaptive unscented Kalman filter (FAUKF) for improving the state estimation accuracy for mobile robot localization. The proposed approach leverages the FAUKF algorithm to address noise uncertainty effectively by adaptively adjusting the covariance of the measurement noise based on a defined adaptation law. The Mamdani Fuzzy Inference System (FIS) serves as an observer, enhancing the matching law and improving overall system performance. The findings of this study demonstrate that the FAUKF algorithm provides superior position estimation accuracy compared to conventional Unscented Kalman Filter (UKF) methods. Furthermore, the research introduces an innovative navigation framework for mobile robots by integrating the Random Tree Routing algorithm with Rapidly exploring Random Tree Star (RRT*) for optimal path planning in indoor environments. The RRT* integration aims to generate efficient and optimal paths while addressing safety considerations and environmental constraints. By combining the prediction and update phases of the Kalman filter, the proposed methodology effectively minimizes the propagation of uncertainty during the localization process, thereby enabling precise localization and robust path planning for designated targets. The simulation results confirmed the effectiveness of this method in maintaining constant uncertainty levels in localization over time. The proposed adaptive method enables efficient navigation in complex environments. Path planning is a critical element in robotics applications, and the RRT*-based approach presented herein offers a comprehensive solution for generating optimal and efficient paths. By providing an up-to-date perspective, this research contributes to the evolving landscape of mobile robot localization methods. The proposed method highlights the importance of utilizing adaptive algorithms and advanced path-planning techniques to enhance navigation capabilities in indoor environments.

NOMENCLATURE

v	Forward speed of the robot.	Q_k	Covariance matrix of procedure noise at moment k.
w	The robot's turning speed.	R_k	Covariance matrix of measurement noise at moment k.
θ	Orientation changes of the robot.	Z_k	Measurements of sigma points at time k.
L	The distance between the wheels.	$\overline{Z}_k$	Weighted average of forecast measurements at time k.
R	Radius of the robot wheel.	$P_{Z_kZ_k}$	Predicted measurement covariance at time k.
$\hat{X}_k$	Estimation of state at moment k.	$P_{X_kZ_k}$	Covariance between measurement and state at time k.
u_k	control input.	C_T	Theoretical covariance.
V_k	The measurement noise matrix at moment k.	C_A	True residual covariance.

I. Introduction

With technological improvements in the present era, the importance of mobile robots in various operational applications has increased. The discussion on mobile robot localization has undergone significant progress, but there are still challenges in developing efficient and reliable localization strategies for robots operating in indoor

Copyright © R. Havangi (s).
Publisher: University of Sistan and Baluchestan

environments. Existing methods are often associated with complex and dynamic environments, leading to inappropriate and suboptimal performances. The categorization of mobile robots is based on both operational specifications and the specific environmental conditions in which they function. In the current technology landscape, mobile robots play an important role in various operational scenarios. Mobile robots face complex localization challenges. Understanding and optimizing the localization patterns of these robots are essential for their effective navigation and performance. In [1], regarding the localization of mobile robots, localization problems were analyzed and showed that position tracking accounted for 55% of the challenges, followed by global localization with 26%, and the issue of retrieving a kidnapped robot with 19%. These are among the significant challenges in the field of mobile-robot localization. Accurate position tracking is the biggest challenge for autonomous robots owing to the complexity and variability of localization across different environments. In [2], mobile robots can be classified based on their movement systems, including fixed (e.g., robotic arms), ground-based, aerial, and underwater configurations. The choice of robot design is significantly influenced by the operational environment and application requirements. Mobile robots have important applications in industrial, medical, and therapeutic fields, social services, agricultural work, space research, and exploration. A moving robot requires accurate localization and high navigation accuracy to achieve control goals. Localization is a serious problem for mobile robots. For optimal navigation, the robot progresses through several key stages, including perception, localization, recognition, and motion control. During the perception phase, the robot analyzes sensor data to derive valuable insights. In the localization stage, the robot determines its present position within an operational setting by using external sensor data. Subsequently, in the recognition phase, the robot strategizes the actions necessary to achieve its objectives. The motion control step enables the robot to navigate its intended path by adjusting its motor function. Over the past decade, localization has emerged as a focal point in extensive research [3]. The odometry calculation algorithm is a common localization method used in the navigation processes of mobile robots [4-5]. Selecting a filtering method is crucial for acquiring precise assessments of the target states. Robot position estimation involves determining the current and future status of the robot by analyzing data from a moment ago and previous data [7]. In robot localization applications, states usually represent parameters such as position, velocity, and acceleration of the robot. Measurements or observations may include variables such as sensor beam angle, robot distance to obstacles, wheel odometer information, and other relevant parameters based on application-specific needs. UKF is a widely used filtering method for nonlinear systems characterized by higher-order nonlinear systems and complex models. Experimental evidence shows that the UKF provides a higher estimation accuracy than the EKF. In [30], a novel adhesion estimation method for rail systems is presented, combining an extended Kalman filter (EKF) and particle swarm optimization (PSO). This method addresses challenges in adhesion estimation and demonstrates that AI and machine learning techniques improve accuracy, potentially benefiting the rail transport industry.

In the UKF framework, it is assumed that the covariances of the process noise and measurement noise remain constant during the estimation process. In reality, the majority of nonlinear systems encounter uncertainties that are dynamic and unpredictable in their nature. To achieve a higher estimation accuracy with the UKF algorithm, adjusting or adapting the noise covariances during the estimation process is essential [8]. Various methods for matching noise covariances can be found in the literature. In [9], a Differential Drive Mobile Robot (DDMR) was proposed that uses fuzzy logic for obstacle avoidance. The robot processes the ultrasonic sensor inputs to control its motor speed, enabling effective navigation in a low-cost design. The primary trait of the FLC is its capability to regulate a nonlinear dynamic system by establishing a mapping between the input and output parameters, based on the designer or expert input, without relying on mathematical implementations [10]. Several studies have been conducted on the capabilities of the adaptive approach based on fuzzy innovation with the UKF for nonlinear systems. In [11], the use of an unscented Kalman filter for vehicle state estimation is investigated, along with an exploration of adaptive fading. In [12], a study is presented on Doppler-bearing passive target tracking (DBT) with nonlinear measurement equations, which pose notable challenges to tracking accuracy. This research focuses on improving the efficiency of sigma-point Kalman filtering by developing a transformed unscented simplex cubature Kalman filter designed to minimize dependency on prior statistical knowledge. The filter is initialized via a range-parameterized Unscented Kalman Filter, and its effectiveness is verified through Monte Carlo simulations, with tracking accuracy assessed against the Cramér-Rao lower bound (CRLB).

A comparative study of the Adaptive Fuzzy Extended Kalman Filter (AFEKF) and FAUKF for state estimation in unmanned aerial vehicles (UAVs), based on real flight data from a fixed-wing aircraft is presented in [13]. This analysis illustrates the superior performance of FAUKF in enhancing the estimation accuracy and reducing maneuvering errors in fixed-wing UAV operations, marking a notable improvement over the AFEKF method. Additionally, the combination of the adaptive fuzzy unscented Kalman filter with an adaptive fuzzy neural extension has shown promising potential for advancing the effectiveness of state estimation algorithms in

UAV applications, with particular relevance for motion planning algorithms.

Reference [14] highlighted the application of the RRT path-planning algorithm in managing robotic baggage trolleys within airport environments and demonstrated its efficacy in mitigating collision risks with both static and dynamic obstacles. A notable innovation of this approach lies in its deviation from traditional methods, which rely exclusively on rooted trees for state-space exploration. Instead, it employs a structure that traverses multiple subtrees, thereby offering greater adaptability. Each subtree independently evaluates its surroundings, while the main rooted tree consolidates this information to accelerate progress towards the target state. Comprehensive evaluations, including simulations and real-world scenarios, indicate that the RRT algorithm outperforms one-way and two-way risk-based algorithms in terms of scheduling efficiency and resilience.

Reference [15] introduced an algorithm designed to overcome the challenges of sampling efficiency and convergence rates encountered by RRT* variants in environments characterized by extended corridors. By integrating heuristic sampling into path expansion, the algorithm enables RRT* to explore the environment swiftly and iteratively optimize the sampling region to identify the most efficient path between the start and goal points. Comparative simulation results indicate that RRT* offers improved node utilization, faster convergence, and produces higher-quality paths than the traditional RRT algorithm within an equivalent number of iterations.

In summary, RRT* is a valuable algorithm for addressing path-planning challenges in complex environments. This study advances the field of autonomous navigation for mobile robots in indoor settings by introducing an innovative combination of a fuzzy-based adaptive unscented Kalman filter and random tree routing algorithm. The primary objective is to develop a robust and adaptive navigation system capable of efficiently operating in intricate and dynamic indoor spaces. This study aims to establish an optimal automatic localization strategy for mobile robots in indoor environments, demonstrating the effectiveness of the proposed approach in achieving precise navigation and localization. By integrating the adaptive unscented Kalman filter with fuzzy logic and random tree routing, this study provides valuable insights into mobile robot localization, offering practical implications for various indoor applications.

The structure of this paper is organized as follows: Section 2 provides a comprehensive overview of the robot localization problem, along with relevant equations. Section 3 delves into the localization analysis, detailing the application of the fuzzy adaptive unscented Kalman filter and RRT* path-planning algorithm, along with their associated equations. Finally, Section 4 presents the simulation results and a detailed evaluation.

II. Methodology

A. The problem of localization

The localization of mobile robots in indoor environments poses a complex challenge owing to the presence of obstacles, uncertainty of sensors, and need for real-time localization. Traditional localization strategies often have problems in dynamic environments and may not be able to realize optimal solutions in complex scenarios. A mobile robot tracks its position using an odometer while moving in a known environment. Nonetheless, owing to the inaccuracies in odometer readings, the robot's current position becomes uncertain during the localization process. Therefore, it is necessary to localize the robot based on the measurement noise. Using an adaptive approach ensures that the uncertainty in localization does not increase. External sensors such as lasers, vision, and lidar are employed to detect the operating environment and facilitate the localization of the robot. The information from the sensors can be combined with the odometer information of the robot's wheels to localize the robot accurately. Even with a global positioning sensor (GPS), the exact position of a robot cannot be measured directly [1]. Data from the robot's sensors can only be extracted to provide information about the best estimate of the robot's position. Beliefs related to robot configurations are usually represented as probability density functions (PDF) [1]. During the prediction update, the robot used external sensors to estimate its position. However, owing to the odometry error, the uncertainty of the robot configuration is greatly increased, and adaptive approaches need to be applied. The kinematics of a robotic system is intricately related to the configuration and characteristics of its wheels. Kinematics play an important role in determining the movement capabilities of robots. A common and basic configuration is the differential-drive system, which has two wheels of the same size.

The differential drive system manages both forward speed and steering angle. The kinematic model of the robot is shown in Fig.1, which allows precise calculation of the robot's position with a comprehensive understanding of its structure. Estimating the position of a mobile robot poses a challenge because sensor measurements are not directly available. Factors such as motion inaccuracy and wheel slip require an accurate robot model that limits uncertainties. The geometric characteristics of each wheel not only affect the motion of the robot but also impose limitations. For example, lateral slip in the wheels can lead to deflection and uncertainty in localization. By understanding and combining these kinematic principles, robotic systems can increase their localization accuracy and operational efficiency. Fig.2 shows the position of a robot according to the global coordinate

system. The vector represents the position of the robot at time step and is expressed as follows:

$$X_k = \begin{bmatrix} x_k \\ y_k \\ \theta_k \end{bmatrix} \quad (1)$$

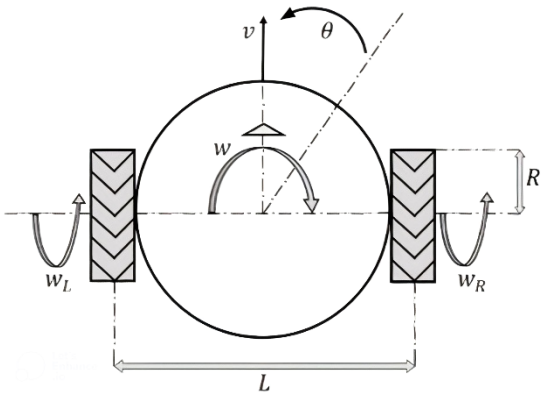

Fig.1. Kinematic model of moving robot.

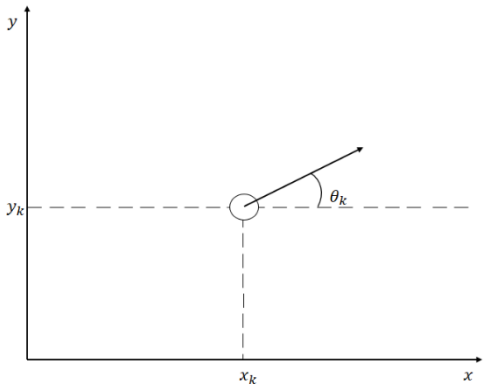

Fig.2. Position of the robot represented by coordinates (x_k, y_k, θ_k) in 2D cartesian space. The robot's orientation is represented by θ_k.

The position vector X_k consists of the x_k and y_k coordinates, which represent the robot's position in the plane, along with θ_k, the orientation of the robot, indicating its direction. Fig.1 shows the kinematic model of the moving robot. The movement of the robot is characterized by two key parameters: the forward speed v and the rotational speed w, which describe the robot's linear velocity and angular velocity, respectively. The wheel radius of the robot is represented by R, and the distance between the wheels is denoted by L. The parameter θ indicates the angular change in the robot's direction.

The robot workspace defines the range of possible positions that the robot can achieve. The wheel radius of the robot and the distance between the wheels are indicated by R and L, respectively, and θ represents the amount of angle changes. Referring to Fig.3, the distance traveled by the left wheel Δ_{s_l} and the right wheel Δ_{s_r} along with the total distance traveled by the robot which is indicated by Δs. The angle α represents the orientation of the rod connecting the wheels relative to the horizontal axis. The equations related to the calculation of Δ_{s_r} and Δ_{s_l} as well as Δs are as follows:

$$\Delta_{s_l} = R\alpha \quad (2)$$

$$\Delta_{s_r} = (R + L)\alpha \quad (3)$$

$$\Delta s = \frac{\Delta_{s_r} + \Delta_{s_l}}{2} \quad (4)$$

According to Fig.3, the distance traveled by the left wheel and the right wheel can be calculated. In the next step, the new angle of the robot is calculated as follows:

$$\Delta\theta = \frac{\Delta_{s_r} - \Delta_{s_l}}{L} \quad (5)$$

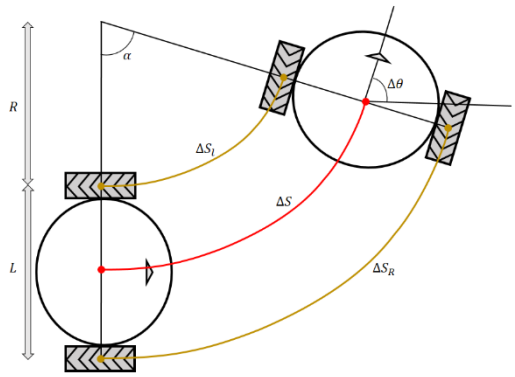

Fig.3. A simple rotation example that shows the basic parameters of the robot's kinematics.

Since the method of calculating the angle and distance traveled by the robot wheels is already available, it is possible to calculate the position of the robot. According to Fig.4, it is possible to obtain the relevant equations.

The current position of a moving robot can be estimated from its initial position information by calculating the coordinate changes over time $(\Delta x, \Delta y, \Delta\theta)$ and finally the odometry distance can be calculated as follows:

$$\Delta x = \Delta s \cos\left(\theta + \frac{\Delta\theta}{2}\right) \quad (6)$$

$$\Delta y = \Delta s \sin\left(\theta + \frac{\Delta\theta}{2}\right) \quad (7)$$

The actual state is a function that depends on the previous state. In Equation (8), X_k represents the robot's current position, while X_{k-1} denotes its position at the preceding time step $k-1$. Based on (8), the robot's current position can be determined using its previous position. It is important to highlight that the system under consideration operates in a discrete framework.

$$X_k = X_{k-1} + \begin{bmatrix} \Delta x \\ \Delta y \\ \Delta\theta \end{bmatrix} = X_{k-1} + \begin{bmatrix} \Delta s \cos\left(\theta + \frac{\Delta\theta}{2}\right) \\ \Delta s \sin\left(\theta + \frac{\Delta\theta}{2}\right) \\ \Delta\theta \end{bmatrix} \quad (8)$$

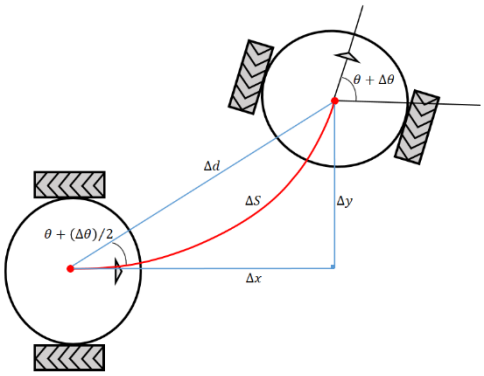

Fig.4. Kinematic parameters with which the distance traveled in the detour path is calculated.

Odometers serve as sensors designed to monitor wheel rotations over time. Typically, these devices acquire data from wheel encoders, recording the total revolutions of each wheel. Errors in odometer readings can be categorized into systematic (certain) and unsystematic (uncertain) types. Systematic errors arise from intrinsic flaws in the physical structure of the odometer system and can be mitigated through precise calibration. Conversely, unsystematic errors persist even after calibration. Significant discrepancies in calculating travel distance errors directly impact the angular orientation accuracy of the robot. Over time, the cumulative effects of directional and orientation deviations surpass navigation measurement errors, playing a more substantial role in localization inaccuracies due to their non-linear contributions.

For this purpose, measurement noise should be minimized. The basic equation for updating the odometric position for the mobile robot is according to (8). Assume that the position of the moving robot at time $k-1$ is as follows:

$$X_{k-1} = \begin{bmatrix} x_{k-1} \\ y_{k-1} \\ \theta_{k-1} \end{bmatrix} \tag{9}$$

At moment k, the robot moves to the new position X_k. Using (10), the new position $\hat{X}_k$ at time k can be predicted from the previous position X_{k-1}:

$$\hat{X}_k = f(X_{k-1}, u_k) = \begin{bmatrix} x_{k-1} \\ y_{k-1} \\ \theta_{k-1} \end{bmatrix} + \begin{bmatrix} \frac{\Delta_{s_r} + \Delta_{s_l}}{2} cos\left(\theta_{k-1} + \frac{\Delta_{s_r} - \Delta_{s_l}}{2L}\right) \\ \frac{\Delta_{s_r} + \Delta_{s_l}}{2} sin\left(\theta_{k-1} + \frac{\Delta_{s_r} - \Delta_{s_l}}{2L}\right) \\ \frac{\Delta_{s_r} - \Delta_{s_l}}{L} \end{bmatrix} \tag{10}$$

In equation (10), u_k is a variable representing a control input. Also, y_{k-1} and $x_{k-1}$are the position of the robot at time $k-1$ and θ_{k-1} is the direction of the robot at time $k-1$. The control input u_k is according to (11):

$$u_k = \begin{bmatrix} \Delta_{s_l} \\ \Delta_{s_r} \end{bmatrix} \tag{11}$$

B. Localization using fuzzy adaptive unscented Kalman filter and RRT algorithm*

In the standard implementation of the unscented Kalman filter (UKF), the noise covariance matrices are typically assumed to remain constant throughout the estimation process. However, achieving optimal performance of the UKF algorithm requires an accurate specification of the process and measurement noise covariance matrices. While existing research highlights the effectiveness of the standard UKF under Gaussian noise distributions and well-defined initial conditions, its performance significantly declines in the presence of non-Gaussian noise or uncertain conditions. In practical applications involving nonlinear dynamic systems, noise is often characterized by uncertainties and time-varying disturbances. Consequently, the real-time adjustment of noise covariances becomes crucial for enhancing UKF performance. An adaptive strategy that dynamically updates the noise covariances online offers a robust solution to these challenges, improving estimation accuracy and overall algorithm efficiency.

The techniques used for covariance adjustment can be classified into two main frameworks [16]. The first framework includes methods based on mathematical principles such as Bayesian inference, covariance matching, initial correlation techniques, and maximum likelihood estimation. On the other hand, the second framework includes techniques based on global optimization strategies. At present, AI-based approaches are increasingly popular in the optimization of these processes in various fields, and fuzzy logic stands out as an important component in the field of artificial intelligence. The dynamics of the robot and its measurement equation are presented according to Equations (12) and (13), respectively:

$$X_k = f(X_{k-1}, u_{k-1}) + W_k \tag{12}$$

$$Z_k = H(X_k) + V_k \tag{13}$$

where z_k is the measurement output vector, u_{k-1} is the input vector and X_k is the state vector. The index k represents the time step. The process noise is represented by W_k, characterized by its mean value and covariance matrix Q_k. The function H represents the nonlinear measurement model of the system. The measurement noise is denoted as V_k, which has a mean of zero and a covariance matrix R_k. For a lidar sensor, the measurement vector consists of two parameters: r, which is the distance from the robot to the lidar, and α, which is the angle between the robot and the lidar. The lidar sensor reading is accompanied by measurement noise v_k with covariance R_k. Sensor observations are denoted by Z:

$$Z_k = \begin{bmatrix} r_k \\ \alpha_k \end{bmatrix} \tag{14}$$

The nonlinear functions of the system and measurement are according to (15) and (16), respectively:

$$f(\hat{X}_{k-1}, u_{k-1}) = \begin{bmatrix} x_{k-1} + \Delta s\ cos(\Delta\theta) \\ y_{k-1} + \Delta s\ sin(\Delta\theta) \\ \theta_{k-1} + \Delta\theta \end{bmatrix} \tag{15}$$

$$H\left(\hat{X}_{k-1}, S_i\right) = \begin{bmatrix} \sqrt{\left(S_{i,x} - x\right)^2 + \left(S_{i,y} - y\right)^2} \\ atan2\left(S_{i,x} - x, S_{i,y} - y\right) - \theta \end{bmatrix} \quad (16)$$

In relation (16), S_i is a vector containing the coordinates of the turning points and their special identifiers, which are defined in advance:

$$S_i = \begin{bmatrix} x_i \\ y_i \end{bmatrix} \quad (17)$$

A key limitation of the odometry method is the accumulation of errors and the reliance on an oversimplified motion model. Odometry estimates the distance traveled by measuring wheel rotations; however, errors inevitably accumulate over time, leading to inaccuracies in the robot's position and orientation estimates. Furthermore, odometry assumes an idealized motion model in which the robot moves either in a straight line or rotates with perfect precision. In practice, nonlinear environmental factors and irregularities in motion introduce deviations from this idealized model, exacerbating errors in odometry-based calculations. For this reason, a sensor fusion approach should be used regarding this problem. The unscented Kalman filter or UKF is a derivative of the EKF. The UKF employs a deterministic sampling approach to represent the state distribution using a minimal set of carefully chosen sample points, known as sigma points. These sigma points are selected with high precision to capture the mean and covariance of the state distribution effectively. Similar to EKF, the UKF operates through two fundamental steps: model prediction and data integration [17]. Unlike the EKF, the UKF does not require the computation of the Jacobian matrix, making it particularly advantageous for systems with highly nonlinear dynamics [18]. The UKF is selecting a certain amount of points from previous milestones [19]. The robot motion mode model is presented according to the equations (12) and (13). The nonlinear functions of the system and measurement are according to (15) and (16), respectively. By receiving the error covariance matrix of the previous moment P_{k-1}, the state vector $\hat{X}_{k-1}$ and sigma points are formed as follows:

$$\begin{aligned} X_{i,k-1} &= \hat{X}_{k-1} && i = 0 \\ X_{i,k-1} &= \hat{X}_{k-1} + \left(a\sqrt{nP_{k-1}}\right)_i && i = 1, \dots, n \\ X_{i,k-1} &= \hat{X}_{k-1} - \left(a\sqrt{nP_{k-1}}\right)_i && i = L+1, \dots, 2n \end{aligned} \quad (18)$$

where a is a scalar and positive and determines the expansion of sigma points around $\hat{X}_{k-1}$. The i column of the square root of the matrix P is represented by $\left(\sqrt{P}\right)i$. The new sigma points work through the unscented conversion principle and the transfer function f of the previous sigma points:

$$X_{i,k} = f\left(X_{i,k-1}, u_{k-1}\right) \quad (19)$$

The predicted mean according is as follows:

$$\hat{X}_k = \sum_{i=0}^{2n} w_i , X_{i,k} \quad (20)$$

and the covariance of the estimation error according to (21):

$$P_k = \sum_{i=0}^{2n} w_i \left(X_{i,k} - \hat{X}_k\right)\left(X_{i,k} - \hat{X}_k\right)^T + Q_k \quad (21)$$

where in (21), $\hat{X}_k$ is the predicted value of a state parameter, P_k is the mean squared error of $\hat{X}_k$ and w_i is the weight of sigma points, also $X_{i,k}$ is the updated sampling point. The equations related to the calculation of weights are shown in (22):

$$\begin{aligned} w_i &= 1 - \frac{1}{a^2} && i = 0 \\ w_i &= \frac{1}{2na^2} && i = 1, \dots, 2n \end{aligned} \quad (22)$$

The formulation for sigma measurements is expressed in Equation (23):

$$Z_k = H\left(X_{i,k}, u_k\right) \quad (23)$$

The weighted average of the predicted measurements is as follows (24):

$$\overline{Z}_k = \sum_{i=0}^{2n} w_i Z_k \quad (24)$$

UKF gain is calculated according to the following relations:

$$P_{Z_k Z_k} = \sum_{i=0}^{2n} w_i \left(Z_k - \overline{Z}_k\right)\left(Z_k - \overline{Z}_k\right)^T + R_k \quad (25)$$

$$P_{X_k Z_k} = \sum_{i=0}^{2n} w_i \left(X_{i,k} - \hat{X}_k\right)\left(Z_k - \overline{Z}_k\right)^T \quad (26)$$

$$K_k = P_{X_k Z_k} {P_{Z_k Z_k}}^{-1} \quad (27)$$

UKF has updated the measurement as follows in the update phase:

$$\hat{X}_k = \hat{X}_k + K_k\left(Z_k - \overline{Z}_k\right) \quad (28)$$

$$P_k = P_k - K_k P_{Z_k Z_k} {K_k}^T \quad (29)$$

where $P_{Z_k Z_k}$ is the covariance parameter of the predicted measurement, $P_{X_k Z_k}$ is the covariance parameter between the measurement and the state, K_k is the Kalman gain, P_k is the covariance parameter and $\hat{X}_k$ is the state evaluation [20].

B.1. RRT path planning algorithm*

The Rapidly-exploring Random Tree Star (RRT*) algorithm is a sampling-based path planning approach designed to identify efficient and feasible paths for robotic systems navigating complex environments [21]. RRT* incrementally constructs a tree structure, starting from an initial configuration and progressing towards a target configuration, effectively exploring the state space to determine optimal paths [22]. A notable feature of RRT* is its capability to dynamically refine the tree structure by reorganizing nodes, thereby enhancing path quality and ensuring convergence [23]. This adaptive framework makes RRT* particularly suitable for addressing challenges in high-dimensional spaces and systems with non-holonomic

constraints [24–25].

The configuration of the unknown region is denoted as X, where X is a set with members $X = \{x, y, \theta\}$. Here x and y represent the two-dimensional coordinates, while θ represents the direction. In addition, X_{obs} includes all regions with obstacles, while X_{free} refers to the parts of the environment that are free of obstacles. The equation (30) expresses the mathematical connection between these two sets:

$$X_{free} = \frac{X}{X_{obs}} \tag{30}$$

In the following, more important concepts are presented for consideration. These concepts are: x_{init} and x_{goal}, which mean the starting point and the goal point, respectively [25]. The solution of the motion planning problem is $\sigma: [0,1] \rightarrow X_{free}$ where $\sigma(0) = x_{init}$ and $\sigma(1) = X_{goal}$. In RRT*, a tree pattern $T = (V, E)$ is also constructed, which consists of the set of vertices $V \subset X$ and branches $E \subset V \times V$. The sample randomly samples a state $x_{rand} \in X_{free}$ from the unobstructed space. Distance with two states $x, x' \in X$, the function $dist(x, x')$ returns the cost of connecting path x and x'. The cost used in this article is in terms of Euclidean distance. $Nearest$ and $Near$ are defined by a set $V \subset X$ and state $x \in X$. These two procedures return the nearest node in the tree and all the nearest nodes that are centered inside a sphere of volume $\gamma\,((log\ n)/n)^{1/d}$. About x in terms of distance γ is a constant as described in [25], d is the dimension of X space and n is the number of vertices. Steer function $Steer(x, x')$ returns a path $\sigma: [0,1] \rightarrow X$ connecting x and x'. Checking for a collision with a path $\sigma: [0,1] \rightarrow X$, the function $InCollision(\sigma)$ checks whether the path is in X_{free}, and if not, returns the first failed state $xfail$. The cost function with a vertex x, let $C(x)$ be the cost of the entire unique path that starts from the root vertex x_{init}, goes along the nodes of the tree and reaches the state x, while $c(\sigma)$ is the cost function of the path is $\sigma: [0,1] \rightarrow X$. Sorting a list L, an ordered set of elements of the form (c_i, x_i, σ_i), the $L.sort()$ function sorts all elements of L based on c_i in ascending order. In configuration, RRT* builds the search tree based on nodes by randomly collecting samples incrementally, so they are constructed in a way that rapidly reduces the expected distance of randomly selected nodes in the tree. As the nodes grow, using x_{rand} (random nodes), it is generated to connect x_{near} node and x_{rand} node [25]. It is shown in Fig.5 that by repeating this process, the nodes form a tree together to reach the target state.

The pseudo code of the RRT* algorithm is in the form of Fig.6. The RRT* algorithm is sampling-based and decentralized, reducing the process waste of dealing with too

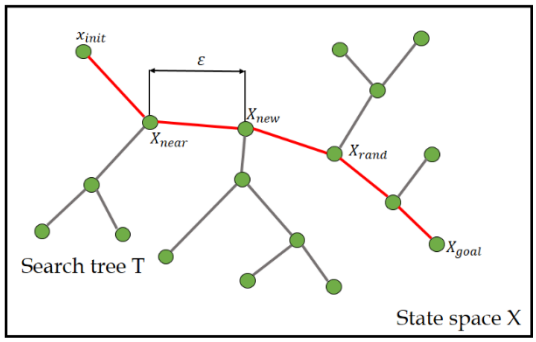

Fig.5. RRT* path planning development.

many data sets for the processor. Additionally, during exploration, RRT* finds an optimal path to avoid obstacles. This means that the robot can navigate in an unknown area using obstacle avoidance and routing by generating probabilistic models of the environment. RRT* is close to reality considering the robot model, without assuming that the robot has the ability to move in all directions. Based on kinematic models, it is known that any number of positions can be achieved by the robot after a certain period of time, and accordingly, the number of new positions is created based on the previous position.

Algorithm 1: The RRT* Algorithm

1: $V \leftarrow \{X_{init}\}; E \leftarrow \emptyset; T \leftarrow (V, E)$;
2: **for** $i = 1 \rightarrow N$ **do**
3: $X_{rand} \leftarrow Sample(i)$;
4: $X_{near} \leftarrow Near(V, X_{rand})$;
5: **if** $X_{near} = \emptyset$ **then**
6: $X_{near} \leftarrow Nearst\ (V, X_{rand})$;
7: **end if**
8: $X_{parent} \leftarrow Find\ Best\ Parents\ (X_{near}, X_{rand})$;
9: **if** $X_{parent} \neq$ Null **then**
10: $V \leftarrow V \cup \{X_{rand}\}; E \leftarrow E \cup \{(X_{near}, X_{rand})\}$;
11: $E \leftarrow Rewire(E, X_{near}, X_{rand})$;
12: **end if**
13: **end for**
14: **return** T = (V, E);

Fig.6. RRT* Pseudo Code.

This creates a large number of possible values over time. Given any expected X_{rand} position, the nearest X_{near} position can always be found in a large number of values. Then, a set of corresponding trajectories is obtained by inverting the status points. The method used here is similar to the random sampling strategy, and then the best control input is selected from the sample results. It is also very simple to deal with obstacle related problems: when X_{rand} is hitting an obstacle, it is directly ignored, and if the path intersects the obstacle, another X_{near} is directly selected. This leads to a series of different paths to avoid collisions

with obstacles. Then, based on this, a route plan is generated and the results can be drawn and checked.

B.2. matching AUKF with fuzzy system

The proposed methodology involves combining a fuzzy-based adaptive unscented Kalman filter with a random tree routing algorithm to enhance the precision and efficiency of data processing within indoor environments. This integration leverages the complementary strengths of both techniques, effectively addressing the challenges associated with measurement noise and the uncertainties inherent in external sensing sensors. The core of the proposed approach is a fuzzy-based adaptive unscented Kalman filter, designed to estimate the position of a mobile robot in the presence of uncertainties. By incorporating fuzzy logic, the filter can effectively handle uncertainties that traditional Kalman filters may have difficulty dealing with. This approach enables real-time adjustment of the measurement noise covariance based on the evolving characteristics of the data, ensuring robust performance in dynamic scenarios. The moving robot uses RRT* routing algorithm. This algorithm uses an optimal structure for dynamic routing in the map and minimizes delay. Fig.7, which shows the different steps of the approach, provides an overview of the method.

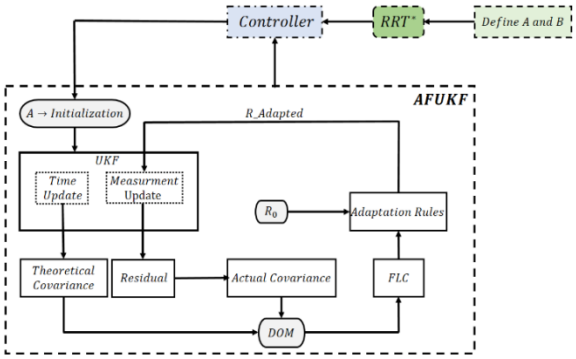

Fig.7. Schematic representation of the FAUKF approach.

In Fig.7, the starting and target points are defined as A and B, respectively. Then, the RRT* algorithm receives these points and designs an optimal path for robot operation according to the map environment. The designed path contains the coordinates transferred to the controller, which follow these points. The task of the UKF block is to estimate the position of the robot. The UKF receives point A as the initialization, and thus the estimation starts online. In the time-update phase, the covariance is computed theoretically to predict the state of the system and uncertainty. Subsequently, in the second phase, known as the Measurement Update, measurement data are incorporated into the filter, contributing to the calculation of the residual value. These values are transferred to the fuzzy block after mathematical operations as DOM, i.e. deviation angle. The fuzzy rules, when applied and considering the initial measurement covariance, facilitate the computation of adaptive measurement noise. This process provides an overview of the FAUKF system, with each component detailed in the subsequent sections. In contrast to this adaptive approach, the standard Unscented Kalman Filter typically assumes constant noise covariances across successive iterations.

The precise definition of measurement and process noise covariance matrices is critical for the optimal functioning of the UKF algorithm. However, the algorithm's performance may degrade when faced with non-Gaussian noise distributions and uncertainties. In practical applications, particularly those involving nonlinear dynamical systems, time-varying uncertainties and disturbances are common. Consequently, online adaptation of the measurement noise covariance is essential to enhance the UKF's performance. Employing an adaptive strategy that dynamically adjusts the noise covariance parameters can effectively address these challenges, thereby improving estimation accuracy in complex and uncertain environments. Strategies for adapting noise covariance can be categorized into two primary frameworks. The first framework involves mathematical approaches, including Bayesian techniques, covariance matching, principal correlation analysis, and maximum likelihood estimation. The second framework relies on optimization methodologies. Recently, artificial intelligence (AI)-based techniques, particularly those utilizing fuzzy logic, have gained prominence in process optimization across various domains. Fuzzy logic, a key component of AI, has garnered increasing attention in the scientific community due to its unique ability to handle the uncertainties and ambiguities inherent in complex systems. Its strength lies in providing an approximate representation of such systems, making it a powerful tool for managing dynamic complexities. Notably, the integration of fuzzy logic with Kalman filter-based estimation methods has become a significant area of research, offering promising solutions in diverse application fields.

The standard unscented Kalman filter algorithm faces challenges when faced with uncertain or unknown noise distributions, leading to ambiguity and inaccuracy that can compromise estimation accuracy. To address this issue, researchers have turned to fuzzy set theory as a promising solution. Fuzzy set theory, which is famous for its efficiency in managing uncertainties, serves as a powerful mathematical tool to reduce uncertainty in system modeling and estimation processes. It is worth noting that the structure of fuzzy logic reflects the complex functioning of the human brain, which operates through linguistic variables to guide complex decision-making scenarios with elegance and adaptability. The main elements of a fuzzy logic controller (FLC) include a structured sequence of processes aimed at effectively managing complex system dynamics. The initial phase, known as fuzzification, involves converting input and

output data into precise linguistic terms, laying the groundwork for subsequent operations. After fuzzification, two critical components—the database and rule base—come into play, whose membership functions are carefully determined by domain experts or operators. This step is seamlessly integrated with the inference engine and collectively forms the FIS. Fuzzy inference, akin to approximate reasoning, facilitates the evaluation of linguistic descriptions and finally produces results as processed parameter values. Subsequently, in the defuzzification phase, the outputs of the comprehensive system are transformed into measurable numerical values through the hub method, ensuring a seamless transition from linguistic representations to practical, quantitative data for informed decision-making processes.Regarding advanced estimation techniques, the integration of fuzzy logic principles into the FAUKF framework provides a robust approach to enhancing tracking performance. In this method, a Mamdani fuzzy inference system dynamically adjusts the measurement noise covariance, as presented in Equation (34). At the core of this process is the degree of match (DOM) parameter, defined as the ratio between the actual residual covariance C_A and the theoretical covariance C_T. This index serves as a key indicator of deviation or relative differences between covariances and guides the adjustment mechanism with accuracy and efficiency.

The FIS acts as a complex decision engine and generates a scaling parameter that fine-tunes the noise covariance in the measurement space and optimizes estimation accuracy.

The adaptation law governing the iterative adjustment of R_T, described in Equation (35), is carefully established through a methodical trial-and-error approach and employs fuzzy logic principles to refine estimation tracking performance. This innovative integration of fuzzy logic and adaptive strategies represents a paradigm shift in estimation methodology, demonstrating the transformative potential of fuzzy-based approaches to optimize noise covariance control mechanisms and enhance system performance. The difference between predicted and actual measurements is determined using Equation (31).

$$e_k = Z_k - \overline{Z}_k \tag{31}$$

$$C_T = P_{Z_k Z_k} = \sum_{i=0}^{2n} w_i \left(Z_k - \overline{Z}_k\right)\left(Z_k - \overline{Z}_k\right)^T + R_k \tag{32}$$

$$C_A = \frac{1}{W} \sum_{k-W+1}^{k} e_k e_k^T \tag{33}$$

$$DOM = \frac{tr(C_A)}{tr(C_T)} \tag{34}$$

$$\Delta R_k = \alpha^3 \times R_{k-1} \tag{35}$$

$$\Delta R_{k+1} = R_k + \Delta R_k \tag{36}$$

Here, only R_k is adapted for two reasons: first, it is assumed that the noise associated with the measurement information significantly affects the filter in any form. The second reason is to reduce the computational load of the filter. The outline of the proposed algorithm is shown in Figure 8. This algorithm is executed iteratively until the end of the simulation time. The proposed FAUKF pseudocode, illustrating the different steps for better understanding, is also presented in Fig. 8. Here, kkk represents the number of Monte Carlo runs, and TTT denotes the total simulation time.

Algorithm 2 : Pseudede of the Proposed FAUKF

Require: Initialization of x_0, P_0, Q, R, UKF and system parameters.
Ensure: Demention of f_k, h_k, Z_k and others.
for i = 1 : Time Vector **do**
for k = 1 : T **do**
Find residual by using(31).
Caculate C_T and C_A from (32) and (33).
Find DOM to FIS from (34).
Caculate tuning parameter (α) from FIS.
Update (ΔR_k) as given in (35) ($\Delta R_k \rightarrow \Delta R_{k+1}$).
Stored states and other required parameters.
end for
Stored parameters for each Monte Carlo run.
end for

Fig.8. Algorithm.2. FAUKF a Pseudo Code.

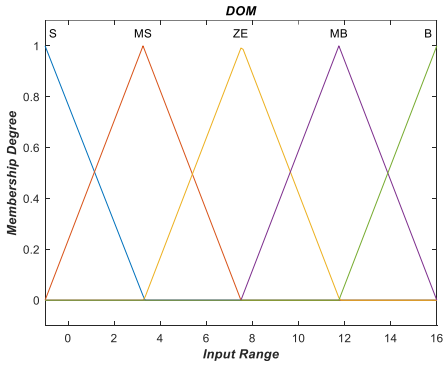

(a)

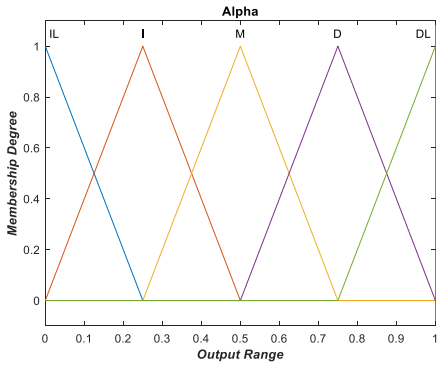

(b)

Fig.9. Membership functions: (a) input membership function (b) output membership function.

Five sets of triangular membership functions are considered for input (DOM) and output (α) parameters.

Membership functions for input and output parameters are shown in Fig.9 MS (small medium), ZE (zero), MB (large medium), B (large) and IL (large increase), I (increase), M (maintain), R (decrease), RL (large decrease) respectively . To avoid the computational complexity of the problem, a fuzzification strategy based on the conventional method is used. Fuzzy rules (IF-THEN) for input and output parameters are as follows:

1) If DOM was in part S, then α is equal to RL.
2) If DOM was in the MS part, then α is equal to R.
3) If DOM was in part ZE, then α is equal to M.
4) If DOM was in the MB part, then α is equal to I.
5) If DOM was in part B, then α is equal to IL.

A fuzzification method is needed to convert the fuzzy output into a crisp value. Here the center of area or center of gravity method is implemented for this purpose. It is very common and widely used. Mathematically, it is expressed as follows:

$$\alpha = \frac{\sum_{j=1}^{m} \alpha_j \mu_{a,j}}{\sum_{j=1}^{m} \mu_{a,j}} \quad (37)$$

where α_jth clear value, m is the number of rules and $\mu_{a,j}$. j represents the membership function of j according to the defined fuzzy rule. Furthermore, for a more detailed theoretical background and mathematical formulation of fuzzy logic, the interested reader can refer to the following references: [26-29].

III. Test Results

A. Evaluation of Performance

The robot moves within the map environment, recording measurement data from its internal wheel movement sensors and collecting measurements related to environmental signs and obstacles using its external sensors. The corresponding simulation environment is implemented in MATLAB. To address the navigation accuracy problem, the FAUKF-based localization method and RRT*-based route planning method are introduced. The robot simulation environment is designed to resemble a hypothetical closed environment. Fig.10 shows the actual path of the robot and the map of the environment, with the robot's path marked in red. The robot's path is designed using the random tree algorithm with fast exploration. Localization is performed by identifying landmarks from the measured data and matching them with the landmarks on the map. The difference between the positions of the estimated and measured landmarks is used to calculate the robot's position and state. The robot is equipped with a lidar sensor, which is installed at the front and measures the distance and angle to the observed target. The speed of the robot is 1 m/s and the maximum steering angle is 1.59 degrees. The distance between the wheels is 0.05 and the maximum range of the laser range finder is 0.5 meters and its field of view is 90 degrees. The control frequency is 50 Hz and the standard deviation of the noise of direct speed and angular speed are as follows σ_v and σ_γ respectively:

$$\sigma_v = 0.01 m/s \ \ , \sigma_\gamma = 0.017^\circ \quad (38)$$

$$\gamma = [0.1\ 0.001\ 0.001\ 0.001\ ] \quad (39)$$

The sampling frequency of the sensors is 5Hz and the standard deviation of the measurement noise in distance and direction is as (39):

$$\sigma_r = 0.5 m/s \ \ , \sigma_\theta = 0.05^\circ \quad (40)$$

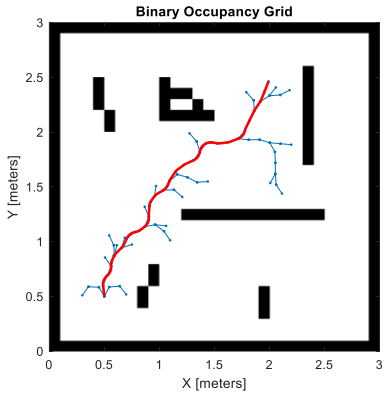

Fig.10. path designed by RRT* algorithm and environment map.

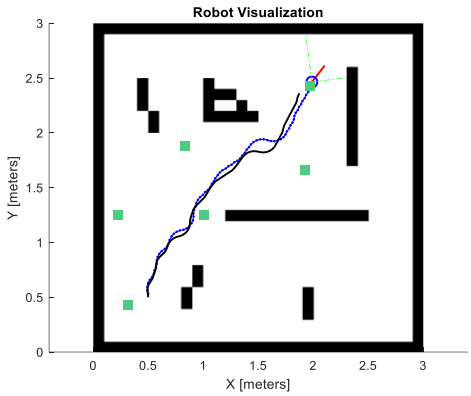

Fig.11. Real path and robot position estimation by odometry.

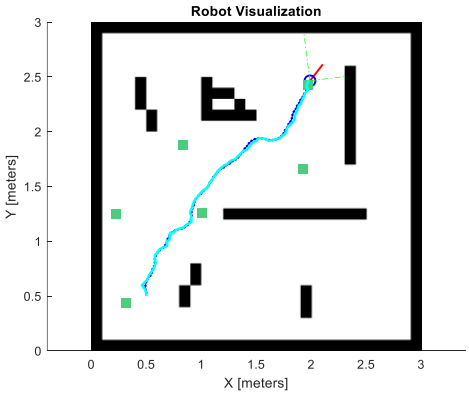

Fig.12. Real path and robot position estimation by FAUKF.

Fig.11 and Fig.12 show the results of positioning based on odometry and FAUKF. The signs on the map are marked with the symbol ■. In Fig.11, the black line corresponds to the localization of the robot by odometry. In Fig.12, the

turquoise color corresponds to FAUKF estimation. It is clear that the performance results of FAUKF method are better than odometry. In other words, in positioning with the proposed algorithm, the estimated path of the robot is as close as possible to the real path. The robot has successfully localized from the starting point to the target point and according to the route planning designed by the RRT* algorithm, it has reached the target point. In the combination of FAUKF and RRT* algorithm, it is clear that the path generated by the simulation of the proposed algorithm is optimal. Fig.12 shows the localization accuracy of FAUKF.

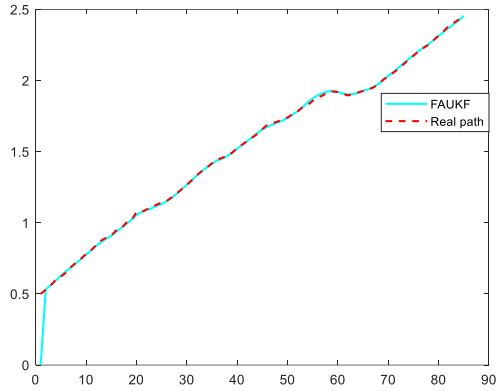

Fig.13. The accuracy of FAUKF related to the estimation of the real position of the moving robot.

In Fig.13, the localization error and the generated angle error are very small and the error is not additive. As a result, the proposed approach has increased the localization accuracy significantly compared to odometry. Fig.14 to Fig.16 show the localization error in the X and Y axes, as well as the orientation of the front angle of the robot relative to the path angle.

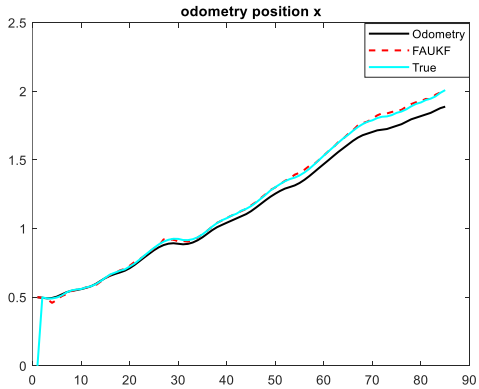

Fig.14. Accuracy of FAUKF compared to odomety in X axis.

In Fig.14, the localization error of FAUKF is compared with odometry in the X axis. The odometry only worked according to the real position of the robot in the initial moments, and the accumulation of noises caused the unsuccessful performance of the odometry. This is because the noise of the sensors and related noises are not considered. It is angular velocity and forward velocity. And as for localization with FAUKF, because the characteristics of noises are taken into account and the information of internal and external sensors are combined, this has made the robot no longer face the problem of accumulating errors. In Fig.15, FAUKF localization error and odometry are compared in Y axis. Localization errors, such as system error and sensor error, which are created using the odometry algorithm, are continuously accumulating. Therefore, the accuracy of odometry localization results is poor.

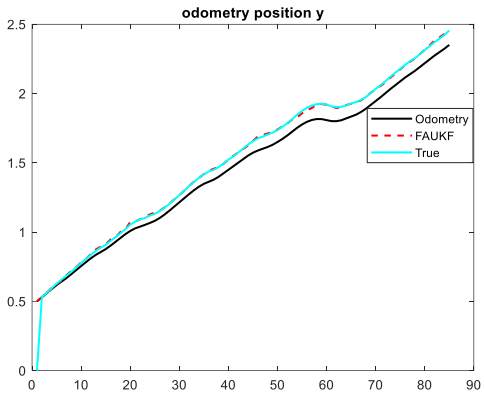

Fig.15. Accuracy of FAUKF compared to Y-axis odometry.

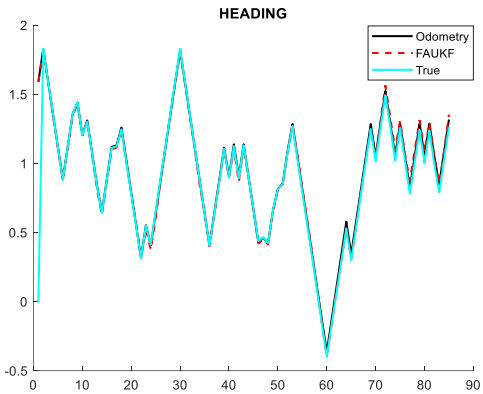

Fig.16. Accuracy of FAUKF compared to odometry related to the differential angle of the robot in orientation.

In Fig.16, the orientation of the front angle of the robot has followed the path angle almost correctly. The root mean square error (RMSE) is a measure commonly used to measure the difference between predicted values and actual values in regression analysis. RMSE shows the average deviation or error between the predicted and actual values of a model's predictions. By taking the root mean square of the errors between the predicted values and the actual values, it is calculated. A lower RMSE value indicates a better fit of the model. According to the explanation, the simulation results are given in Table (1).

A disadvantage of the proposed method is its longer processing time due to its complexity, whereas the other methods demonstrate shorter processing times because of

their simplicity. However, this trade-off is outweighed by the superior performance and accuracy of the proposed method,

TABLE 1:PERFORMANCE COMPARISON OF LOCALIZATION TECHNIQUES.

Average error in different directions and RMSE					
Technique	X	Y	z	RMSE	**Processing Time(sec)**
FAUKF+RRT*	0.001	0.01	0.012	0.046	**6.5 sec**
UKF + RRT*	0.002	0.019	0.020	0.047	**1.49 sec**
EKF + RRT*	0.027	0.025	0.095	0.055	**1.23 sec**
Odometry	0.037	0.06	0.032	0.077	**1.36 sec**

which is essential for achieving reliable results in our application. Table 2 shows the advantages and disadvantages of the proposed method compared to other methods. Fig.17 to Fig.20 show the navigation simulation results. In order to make the simulation results more objective, the navigation simulation of the mobile robot is carried out in four different groups of selected paths. The mobile robot moves from the starting point to the target point. The red paths show the results of the RRT* algorithm. The black lines are results based on odometric calculations. The cyan paths are the position estimation by FAUKF algorithm and the green dots are the map markers.

TABLE 2: COMPARISON OF THE PROPOSED METHOD COMPARE WITH OTHERS METHOD

Method	Advantage	Disadvantage
Proposed Method	High accuracy	Longer processing time
	Robust performance	
Other Method	Faster processing time	Low accuracy
	Simplicity	Limited robustness

The FAUKF approach shows the lowest value of RMSE (root mean square error) compared to other methods. UKF also performs well, with a root mean square error of 0.047, which is slightly higher than the FAUKF approach. Also, EKF has a root mean square error of 0.055, which is higher than FAUKF and UKF approaches. And finally, the odometric approach that relies solely on the robot's internal sensors has the highest error squared, i.e. 0.077, which indicates a greater deviation from the actual path compared to other methods. Table 1 shows that the FAUKF approach, when integrated with the RRT* route planning method, provides the most accurate route estimation among the techniques evaluated. The low RMSE values for the FAUKF and UKF approaches indicate that these methods can better handle the time-varying noise characteristics of the system compared to the oedometric and EKF methods. The RMSE difference between the FAUKF and UKF approaches, although small (0.001), shows that the FAUKF approach has been able to perform better. Therefore, according to these results, it can be said that the FAUKF approach has performed promisingly and has made a significant improvement over the conventional UKF. This shows that combining fuzzy logic with UKF has been able to increase the accuracy of the system. The Table 1 shows that the FAUKF approach has the longest run time of 6.5 seconds. This delay in the FAUKF approach's run time could be a significant weakness, as it may not be suitable for time-sensitive robotic localization and navigation tasks.

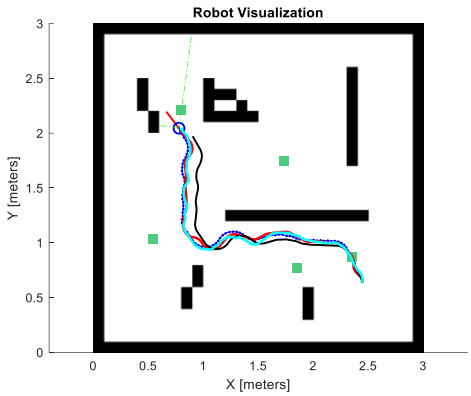

Fig.17. The first path estimated by the FAUKF.

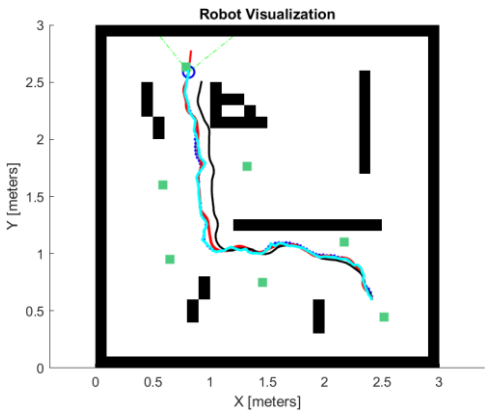

Fig.18. The second path estimated by the FAUKF.

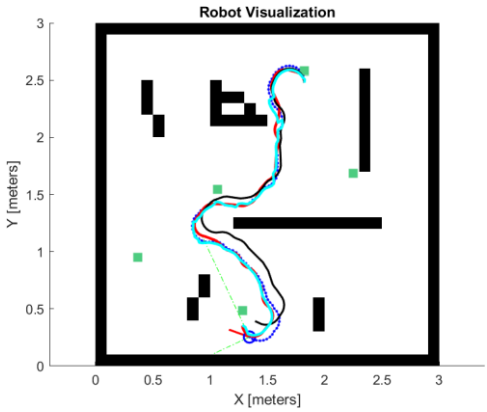

Fig.19. The third path estimated by the FAUKF.

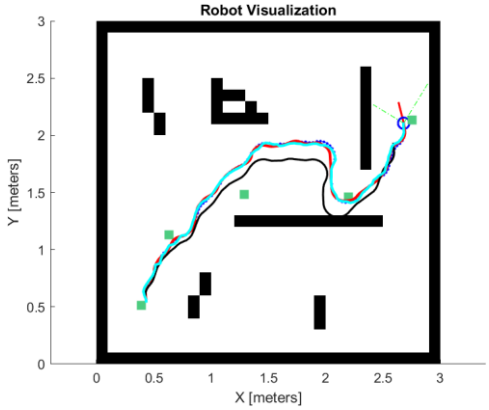

Fig.20. The Fourth path estimated by FAUKF.

The findings clearly demonstrate the effectiveness of the RRT* routing algorithm in constructing optimal paths. The results indicate that the algorithm not only ensures route optimization but also prioritizes safety requirements and adheres to the constraints defined by the operational environment. Simulations presented in the conclusion section further affirm that the RRT* algorithm successfully designs safe and efficient paths, transmitting the path information as control inputs to the robot. Additionally, it is evident that the FAUKF provides accurate estimations of the robot's actual position across various trajectories, even when odometry data deviates significantly from the true position. This highlights the high precision and adaptability of the mobile robot, showcasing the method's overall efficiency and stability. These results suggest the potential for broader application of this approach in dynamic and uncertain environments.

B. Evaluation of Stability

The stability of FAUKF is achieved through the adaptive tuning of the measurement noise covariance, which is controlled by a fuzzy logic system. This tuning mechanism helps the filter remain stable by responding dynamically to variations in measurement noise, particularly in nonlinear or fluctuating environments. Additionally, the Unscented Kalman Filter framework itself contributes to stability by accurately propagating sigma points through nonlinear functions without requiring linearization, which reduces approximation errors and enhances convergence stability.

In terms of robustness, the FAUKF demonstrates resilience against modeling inaccuracies and unexpected disturbances. The adaptive fuzzy component plays a critical role in adjusting the filter to real-time conditions by refining noise covariance values, which helps maintain accurate state estimation even when system dynamics deviate from expected models. This approach ensures that FAUKF can handle diverse operational conditions and provides consistent performance across a variety of nonlinear and unpredictable scenarios.

Checking the stability of a filter through consistency analysis is crucial for evaluating its performance, particularly in terms of reliable and accurate state estimation. To assess the filter's consistency, the estimated values are compared with the probability density function (PDF) of an ideal filter. Consistency is verified by the normalized estimation error squared (NEES):

$$NEES = (x - \hat{x})^T P^{-1} (x - \hat{x})$$

where x is the ground truth, $\hat{x}$ is the estimated mean, and P is the estimated covariance. Consistency is further evaluated by performing multiple Monte Carlo runs and calculating the average NEES (ANEES). Given N runs, the ANEES is computed as:

$$ANEES = \frac{1}{N} \sum_{i=1}^{N} NEES$$

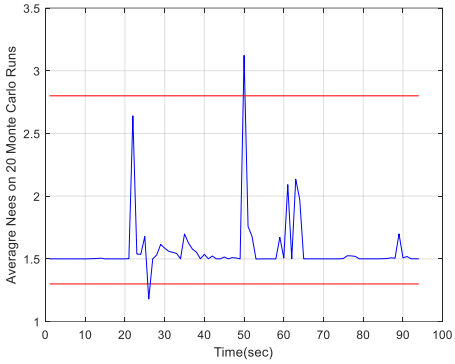

Fig.21. Consistency of Proposed Method.

The NEES value indicates whether the estimated covariance P accurately reflects the error in state estimates. For a stable and consistent filter, NEES values should be statistically bounded within certain confidence limits based on the degrees of freedom in the state vector. If NEES consistently falls outside these bounds, it may indicate that the filter's assumptions or adjustments are inadequate or not well-tuned. For the 2-dimensional vehicle position with 20 Monte Carlo simulations the two-sided 95% probability concentration region for $ANEES$ is bounded by interval [1.3, 2.79] and algorithm is consistent if $ANEES$ with probability 95% belong to [1.3, 2.79]. Fig.21 shows that the proposed method is consistent.

IV. Conclusions

In this study, the performance of an adaptive unscented Kalman filter has been investigated. This method involves matching the covariance of the measurement noise using an adaptation rule to handle uncertainty in the noise, and utilizing the output of the Mamdani fuzzy inference system as the adjustment factor for the adaptation rules, with triangular membership functions. The comparative analysis of this approach showed that the FAUKF method outperforms odometry, EKF, and UKF methods. Notably, the proposed FAUKF method demonstrated a square root

error of 0.046, which is lower than the values of 0.077 for odometry, 0.055 for EKF, and 0.047 for UKF. This indicates a significant improvement in accuracy, highlighting the superiority of the FAUKF method in state estimation accuracy for robot localization tasks. To further validate the effectiveness of the proposed method, experiments using the Random Tree Routing Algorithm with Rapid Exploration (RRT)* were conducted across four different paths.

The FAUKF technique exhibited the longest runtime of 6.5 seconds, substantially exceeding the execution times of the other evaluated methods. To mitigate this weakness, the researchers should consider optimizing the FAUKF algorithm or investigating alternative approaches that can achieve comparable accuracy without the considerable runtime overhead. The results emphasize the robustness and versatility of the FAUKF method, confirming its potential to revolutionize the accuracy of state estimation in indoor environments. The integration of the FAUKF method with the RRT* algorithm presents a promising approach to enhance state estimation performance and optimize robot localization tasks in dynamic indoor settings. Enhancing the computational efficiency of the FAUKF technique would be a crucial step to improve its practicality and applicability for real-time robotic tasks in dynamic environments.

REFERENCES

[1] Panigrahi, P.K. and S.K. Bisoy, Localization strategies for autonomous mobile robots: A review. Journal of King Saud University-Computer and Information Sciences, 2022. 34(8): p. 6019-6039.

[2] Y. Liu, S. Wang, Y. Xie, T. Xiong, and M. Wu, "A Review of Sensing Technologies for Indoor Autonomous Mobile Robots," Sensors, vol. 24, no. 4, p. 1222, Feb. 2024.

[3] Siegwart, R., I.R. Nourbakhsh, and D. Scaramuzza, Introduction to autonomous mobile robots. 2011: MIT press.

[4] Zheng, L., et al., Heading estimation for multimode pedestrian dead reckoning. IEEE Sensors Journal, 2020. 20(15): p. 8731-8739.

[5] Madray, I., et al., Relative angle correction for distance estimation using K-nearest neighbors. IEEE Sensors Journal, 2020. 20(14): p. 8155-8163.

[6] Guo, S., et al., An improved PDR/UWB integrated system for indoor navigation applications. IEEE Sensors Journal, 2020. 20(14): p. 8046-8061.

[7] Wang, X.-l., L.-q. Li, and W.-x. Xie, A novel TS fuzzy particle filtering algorithm based on fuzzy C-regression clustering. International Journal of Approximate Reasoning, 2020. 117: p. 81-95.

[8] A. H. Hassaballa, A. M. Kamel, I. Arafa, and Y. Z. Elhalwagy, "Adaptive Precise Attitude Estimation Using Unscented Kalman Filter in High Dynamics Environments," Unmanned Systems, vol. 12, no. 04, pp. 653–665, 2024.

[9] R. D. Puriyanto and A. K. Mustofa, "Design and Implementation of Fuzzy Logic for Obstacle Avoidance in Differential Drive Mobile Robot," Journal of Robotics and Control (JRC), vol. 5, no. 1, 2024.

[10] Shaheen, O., et al., Stable adaptive probabilistic Takagi–Sugeno–Kang fuzzy controller for dynamic systems with uncertainties. ISA transactions, 2020. 98: p. 271-283.

[11] Liu, Y. and D. Cui, Vehicle state estimation based on adaptive fading unscented kalman filter. Mathematical Problems in Engineering, 2022. 2022(1): p. 7355110.

[12] S. H. Hashemi and N. Pariza, "Adaptive Transformed Unscented Simplex Cubature Kalman Filter for Target Tracking," Automatika, vol. 62, no. 3, pp. 3279–3287, 2021.

[13] Al-sudany, H.N. and B. Lantos, Comparison of Adaptive Fuzzy EKF and Adaptive Fuzzy UKF for State Estimation of UAVs Using Sensor Fusion. Periodica Polytechnica Electrical Engineering and Computer Science, 2022. 66(3): p. 215-266.

[14] Sun, Z., et al., Multi-Risk-RRT: An Efficient Motion Planning Algorithm for Robotic Autonomous Luggage Trolley Collection at Airports. IEEE Transactions on Intelligent Vehicles, 2024.

[15] Ding, J., et al., An improved RRT* algorithm for robot path planning based on path expansion heuristic sampling. Journal of Computational Science, 2023. 67: p. 101937.

[16] Szabat, K., et al., A fuzzy unscented Kalman filter in the adaptive control system of a drive system with a flexible joint. Energies, 2020. 13(8): p. 2056.

[17] Fang, Y., et al., Adaptive Unscented Kalman Filter for Robot Navigation Problem (Adaptive Unscented Kalman Filter Using Incorporating Intuitionistic Fuzzy Logic for Concurrent Localization and Mapping). IEEE Access, 2022. 10: p. 101869-101879.

[18] V. E. Papageorgiou and G. Tsaklidis, "An improved epidemiological-unscented Kalman filter (hybrid SEIHCRDV-UKF) model for the prediction of COVID-19: Application on real-time data," *Chaos*, vol. 2022, Article 112914, 2022.

[19] Kumar, M. and S. Mondal, A Fuzzy-based Adaptive Unscented Kalman Filter for State Estimation of Three-dimensional Target Tracking. International Journal of Control, Automation and Systems, 2023. 21(11): p. 3804-3812.

[20] K. Feng, J. Wang, X. Wang, G. Wang, Q. Wang, and J. Han, "Adaptive state estimation and filtering for dynamic positioning ships under time-varying environmental disturbances," *Ocean Engineering*, vol. 2024, Article 117798, 2024.

[21] X. Cui, C. Wang, Y. Xiong, L. Mei, and S. Wu, "More Quickly-RRT*: Improved Quick Rapidly-exploring Random Tree Star algorithm based on optimized sampling point with better initial solution and convergence rate," Engineering Applications of Artificial Intelligence, vol. 108, p. 108246, 2024.

[22] Orthey, A., C. Chamzas, and L.E. Kavraki, Sampling-based motion planning: A comparative review. Annual Review of Control, Robotics, and Autonomous Systems, 2023. 7.

[23] Y. Lee, "Trajectory Manifold Optimization for Fast and Adaptive Kinodynamic Motion Planning," arXiv preprint arXiv:2410.12193, 2024.

[24] D. Debnath, F. Vanegas, J. Sandino, A. F. Hawary, and F. Gonzalez, “A Review of UAV Path-Planning Algorithms and Obstacle Avoidance Methods for Remote Sensing Applications,” *Remote Sens.*, vol. 16, no. 21, p. 4019, 2024.

[25] Szabat, K., et al., A fuzzy unscented Kalman filter in the adaptive control system of a drive system with a flexible joint. Energies, 2020. 13(8): p. 2056.

[26] Woo, R., E.-J. Yang, and D.-W. Seo, A fuzzy-innovation-based adaptive Kalman filter for enhanced vehicle positioning in dense urban environments. Sensors, 2019. 19(5): p. 1142.
[27] Asl, R.M., et al., Fuzzy-based parameter optimization of adaptive unscented Kalman filter: Methodology and experimental validation. IEEE Access, 2020. 8: p. 54887-54904.
[28] J. C. R. Alcantud, A. Z. Khameneh, G. Santos-García, et al., "A systematic literature review of soft set theory," *Neural Comput. Appl.*, vol. 36, pp. 8951–8975, Jun. 2024.
[29] Matía, F., et al., The fuzzy Kalman filter: Improving its implementation by reformulating uncertainty representation. Fuzzy Sets and Systems, 2021. 402: p. 78-104.
[30] R. Havangi and M. Moradi, "PSO Based EKF Wheel-rail Adhesion Estimation," *Research Articles*, University of Birjand, doi: 10.22111/ieco.2023.43360.1446, in press.

MohammadRasool Hajiali received the B.S. degree in Electronic Engineering from Imam Ali Kordkuy University, Kordkuy, Iran, in 2020. He then completed the M.S. degree in Control Engineering from the University of Birjand, Birjand, Iran, in 2024. His research interests include control engineering, parameter estimation, soft computing, industrial automation, robotics, robot navigation, and robot localization. He is currently working with the academic community to advance knowledge and innovation in these areas through his research and academic work. Additionally, he is exploring new developments and applications within his fields of interest with the goal of making meaningful contributions to the industry and research landscape.

Ramazan Havangi received his M.S. and Ph.D. degrees from the K.N. Toosi University of Technology, Tehran, Iran, in 2003 and 2012, respectively. He is currently an Associate Professor of control systems with the Department of Electrical and Computer Engineering, University of Birjand, Birjand, Iran. His main research interests are inertial navigation, integrated navigation, estimation and filtering, evolutionary filtering, simultaneous localization and mapping, fuzzy, neural network, and soft computing.Email: Havangi@Birjand.ac.ir

IECO

This page intentionally left blank.

International Journal Of
Industrial Electronics Control and Optimization
Print ISSN: 3517-2645
Online ISSN: 3568-2645
Homepage: https://ieco.usb.ac.ir/

Enhanced Speed Loop Control Strategy for Yokeless Axial Flux-Switching Permanent Magnet Motors

Javad Rahmani-Fard | Saeed Hasanzadeh
Department of Electrical and Computer Engineering, Qom University of Technology, Qom, Iran
Corresponding Author Email: rahmanifard@qut.ac.ir

Article Info

Article type:
Research Article

Article history:
Received: 28-May-2024
Received in revised form: 10-December-2024
Accepted:28-December-2024
Published online: 23-Sep-2025

Keywords:
Sliding Mode Control,
Flux-Switching motor,
Fault-tolerant,
EVs.

ABSTRACT

This paper presents an Enhanced Model-Free Sliding Mode Control (EMFSMC) method tailored for the speed loop of a 12-slot/19-pole yokeless and segmented armature axial flux-switching permanent magnet (12S/19P YASA-AFFSSPM) motor, focusing on robustness against parameter perturbations. Traditional control techniques, such as Proportional-Integral (PI) control and Model-Free Sliding Mode Control (MFSMC), have shown limitations in handling the motor's nonlinear behavior and susceptibility to disturbances. The proposed EMFSMC algorithm optimizes speed loop performance by establishing a hyperlocal model of the YASA-AFFSSPM motor, which accounts for parameter variations. An improved double-power combinatorial reaching law is developed to enhance convergence rates during the sliding surface approach phase, while an Extended Sliding Mode Disturbance Observer (ESMDO) provides real-time monitoring of unknown disturbances affecting speed control. Simulation results demonstrate that the EMFSMC significantly accelerates the speed response time to approximately 0.015 seconds with minimal overshoot, compared to 0.04 seconds and a 12.5% overshoot with the MFSMC. Additionally, under sudden load conditions, the EMFSMC controller exhibits a speed drop of only 4 rpm, recovering to stability in about 0.01 seconds, while the MFSMC controller experiences a 9 rpm drop with a recovery time of 0.03 seconds. These findings confirm that the EMFSMC enhances the speed response rate and robustness of the speed loop, outperforming traditional control methodologies across various operating conditions.

NOMENCLATURE

u_d, u_q	d-q axis voltages	s	Sliding variable
R_{so}	Nominal value of the stator phase winding resistance	L_{do}, L_{qo}	Nominal values of the stator winding d-q axis inductances
i_d, i_q	d-q axis current components	α, β	Exponents in the reaching law
k_1, k_2,k_3	Positive constants used in reaching laws	ε_1, ε_2	Exponential parameters in the reaching law
ω_e	Rotor electrical angular velocity	x_1, x_2	State variables of speed error and its integral
ψ_{ro}	Permanent magnet flux linkage	s_1	Sliding surface for speed error
J	Moment of inertia	s_2	Sliding surface for speed estimation error
ΔR_s	Perturbation of resistance	ζ, δ	Parameters in the extended hyper-local model
ΔL_d, ΔL_q	Perturbations of the stator inductance parameters	F	Unknown part of the system
$\Delta\psi_r$	Variation of the magnetic flux linkage of the permanent magnet	$\hat{F}$	Real-time estimation of the unknown part of the system
T_e	Output electromagnetic torque	$\hat{\omega}$	Real-time speed estimation
n_p	Number of rotor poles	u_c	Control input of the speed loop feedback controller
ΔT_e	Torque disturbance due to parameter perturbation	$\omega_{e}*$	Given speed of the motor
Δu_d, Δu_q	Uncertain quantities caused by parameter changes in the d-axis and q-axis	l	Observer gain in the extended sliding mode disturbance observer
$R(t)$	Rate of change of the unknown quantity	s	Sliding variable
η_1, η_2	Positive constants in the observer control law	k_1, k_2,k_3	Positive constants used in reaching laws

Copyright © J. Rahmani-Fard (s).
Publisher: University of Sistan and Baluchestan

I. Introduction

Permanent Magnet Synchronous Motors (PMSMs) play a crucial role in various industries, serving as a cornerstone in applications that demand high precision and efficiency, such as robotics, aerospace, automotive, and renewable energy systems. In recent times, a specific type of PMSM known as the Flux Switching Permanent Magnet (FSPM) motor has emerged as a promising alternative, offering advancements in power density and control flexibility [1-2]. The 12Slots/19 poles yokeless and segmented armature flux-switching sandwiched permanent magnet (12S/19P YASA-AFFSSPM) machines represent an innovative category of flux machines with a unique topology. This design provides several benefits, including increased torque density, minimized cogging torque, and electrical as well as magnetic isolation between phases [3, 4]. Consequently, the 12S/19P YASA-AFFSSPM configuration shows significant potential as an in-wheel direct drive motor for Electric Vehicles (EVs). Since the system equations of FSPM motors closely resemble those of PMSMs, control strategies developed for PMSMs can be effectively adapted for FSPM motors.

While traditional Proportional-Integral (PI) control is simple and easy to implement, it lacks robustness against external disturbances and changes in system parameters due to the nonlinear and strongly coupled nature of Permanent Magnet Synchronous Motors (PMSMs). To address this limitation, advanced control methods such as model predictive control [5], model-free control [6], neural network control [7], and sliding mode control [8] have been proposed. Model-free control is notable for its insensitivity to both internal and external disturbances and its robustness in scenarios where dynamic effects on the system are poorly modeled. Sliding mode control also offers advantages in insensitivity to parameter variations and strong robustness. Thus, combining sliding mode control with model-free control effectively reduces the reliance on accurate motor system models and mitigates the impacts of system parameter changes and external disturbances. However, integrating sliding mode control and model-free control can introduce chattering, which is a common issue with sliding mode methods. Therefore, enhancing system response speed while reducing chattering has become a primary focus in model-free sliding mode control research. Approaches like the one suggested in [9] are often used to lessen chattering. In robotic systems, Reference [10] developed a model-free control scheme that combines adaptive dynamic sliding mode control with a voltage control strategy, addressing uncertainties in practical applications by estimating lumped uncertainty, thus improving tracking performance and ensuring system stability, as validated through simulation results. Building on this, References [11] and [12] introduced double power-law and multi-power-law approach laws to expedite convergence rates and minimize chattering through the incorporation of power-law terms. Subsequently, Reference [13] proposed double power-law combination approach laws derived from the double power-law approach laws, enhancing system performance across different states. Recent advancements in control strategies, particularly sliding mode control (SMC), have shown promise in managing chaotic systems with uncertainties. Reference [14] illustrates that SMC can stabilize time-varying chaotic systems by defining a sliding surface that mitigates the effects of disturbances, ensuring fixed-time stability. Reference [15] effectively reduced chattering by using an extended state observer for improved estimation accuracy compared to traditional observers [16]. However, challenges such as managing multiple parameters and intricate tuning arose. To address these issues, Reference [17] developed an extended sliding mode disturbance observer, enhancing system robustness. Additionally, Reference [18] introduced an adaptive fuzzy fractional-order fast terminal sliding mode control approach, employing a novel fractional-order sliding surface and fuzzy system to eliminate chattering and ensuring finite-time stability via Lyapunov's theorem.

To tackle parameter perturbations affecting the robustness of control systems for the 12-slot/19-pole yokeless and segmented armature axial flux-switching sandwiched permanent magnet (12S/19P YASA-AFFSSPM) motor, this study presents the Enhanced Model-Free Sliding Mode Control (EMFSMC) algorithm. This algorithm features a novel double-power combination sliding mode reaching law to enhance convergence rates during the sliding mode approach while reducing chattering. The integration of the Extended Sliding Mode Disturbance Observer (ESMDO) allows for real-time monitoring and estimation of unknown disturbances affecting speed control, improving overall accuracy and stability.

Simulation and experimental results indicate that EMFSMC outperforms MFSMC in speed response time, stability, and robustness under various operating conditions, leading to significant reductions in speed drop and recovery time during sudden load changes. These advancements enhance the performance of the YASA-AFFSSPM motor, making it a promising candidate for applications in electric vehicles and other precision-demanding industries. Comprehensive validations demonstrate the effectiveness of the proposed control algorithms in significantly improving the performance of the 12S/19P YASA-AFFSSPM motor.

II. Configuration

In [3], a novel motor structure without yoke and armature segmentation is proposed to maximize slot space and coil winding capacity, thereby enhancing the slot fill factor and torque density. The YASA-AFFSSPM motor, depicted in Fig. 1, features a stator with 12 modular units, each containing 3 "I"-shaped stator teeth, 2 "I"-shaped permanent

magnets, and 1 winding coil. This yokeless stator design optimizes coil winding space, resulting in increased average torque output. The motor also uses two rotors positioned 180 degrees apart electrically, which effectively eliminates high-order harmonics of back-EMF and reduces cogging torque.

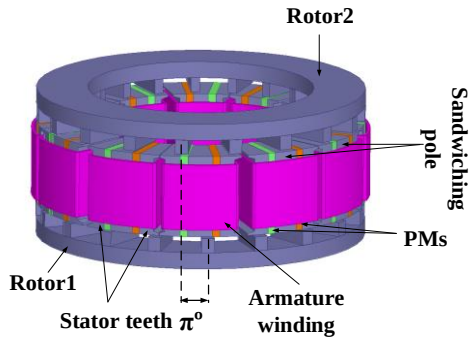

Fig. 1. Machine topology.

$$\begin{cases} u_d = R_{\mathrm{so}} i_d + L_{do}\frac{\mathrm{d}i_d}{\mathrm{d}t} - \omega_{\mathrm{e}} L_{q0} i_q + \Delta u_d \\ u_q = R_{\mathrm{so}} i_q + L_{q0}\frac{\mathrm{d}i_q}{\mathrm{d}t} + \omega_{\mathrm{e}} L_{d0} i_d + \omega_{\mathrm{e}}\psi_{\mathrm{ro}} + \Delta u_q \end{cases} \quad (1)$$

Here, u_d and u_q are the d-q axis voltages; R_{so} is the nominal value of the stator phase winding resistance; i_d and i_q are the d-q axis current components; L_{do} and L_{qo} are the nominal values of the stator winding *d-q* axis inductances; ω_e is the rotor electrical angular velocity; ψ_{ro} is the nominal value of the PM flux linkage; Δu_d and Δu_q are the uncertain quantities caused by parameter changes in the *d*-axis and *q*-axis of the motor, expressed as :

$$\begin{cases} \Delta u_d = \Delta R_s i_d + \Delta L_d\frac{\mathrm{d}i_d}{\mathrm{d}t} - \omega_{\mathrm{e}}\Delta L_q i_q \\ \Delta u_q = \Delta R_s i_q + \Delta L_q\frac{\mathrm{d}i_q}{\mathrm{d}t} - \omega_{\mathrm{e}}\Delta L_d i_d + \omega_{\mathrm{e}}\Delta\psi_{\mathrm{r}} \end{cases} \quad (2)$$

Here, where, ΔR_s is the perturbation of resistance, ΔL_d and ΔL_q are the perturbations of the stator inductance parameters; $\Delta\psi_r$ is the variation of the magnetic flux linkage of the permanent magnet. The electromagnetic torque equation is given by:

$$\begin{aligned} T_e &= \frac{3}{2} n_p\left[\psi_{ro} + \left(L_d - L_q\right) i_d\right] i_q + \Delta T_e \\ &= \tfrac{3}{2} n_p \psi_{ext} i_q + \Delta T_e \end{aligned} \quad (3)$$

where $\psi_{\mathrm{ext}} = \psi_{\mathrm{ro}} + \left(L_d - L_q\right) i_d$ is effective magnetic flux linkage, T_e represents the output electromagnetic torque, n_p is the rotor poles number and ΔT_e represents the torque disturbance due to parameter perturbation, expressed as:

$$\Delta T_{\mathrm{e}} = \frac{3}{2} n_{\mathrm{p}}\left[\Delta\psi_{\mathrm{r}} + \left(\Delta L_d - \Delta L_q\right) i_d\right] i_q \quad (4)$$

The mechanical motion equation in the d-q coordinate system is given by:

$$T_e = T_{\mathrm{L}} + \frac{J}{n_{\mathrm{p}}}\frac{\mathrm{d}\omega_e}{\mathrm{d}t} + B\omega_{\mathrm{m}} \quad (5)$$

here, T_L represents the load torque, J is the moment of inertia, B is the torque damping coefficient, and $B\omega_m$ is the damping torque. By combining Equations (3) and (5), the speed state equation of YASA-AFFSSPM under parameter perturbation can be obtained as

$$\frac{\mathrm{d}\omega_{\mathrm{e}}}{\mathrm{d}t} = \frac{3}{2}\frac{n_{\mathrm{p}}^2}{J}\psi_{\mathrm{ext}} i_q - \frac{B}{J}\omega_{\mathrm{e}} + \frac{n_{\mathrm{p}}}{J}\left(\Delta T_{\mathrm{e}} - T_{\mathrm{L}}\right) \quad (6)$$

III. Controller Design

A. Improved reaching Law Design

Reference [13] indicates that the double-power reaching law outperforms other reaching laws such as the constant-speed, exponential. The double-power reaching law is expressed as:

$$\dot{s} = -k_1|s|^{\alpha}\mathrm{sgn}\,(s) - k_2|s|^{\beta}\mathrm{sgn}\,(s) \quad (7)$$

The double-power combined reaching law exhibits superior performance compared to both the double-power reaching law and the fast-power reaching law. Therefore, this paper proposes a new reaching law based on the double-power combined reaching law, represented as:

$$\dot{s} = \begin{cases} \begin{pmatrix} -k_1|s|^{\alpha}\,\mathrm{sgn}(s) \\ -k_2|s|^{\beta}\,\mathrm{sgn}(s) - \varepsilon_1|x_1|^{\lambda_1}s \end{pmatrix}, & |s| > 1 \\ \begin{pmatrix} -k_1|s|^{\alpha}\mathrm{sgn}(s) \\ -k_3 s - \varepsilon_2|x_1|^{\lambda_2}s \end{pmatrix}, & |s| \leqslant 1 \end{cases} \quad (8)$$

In Eq.s (7) and (8): k_1, k_2, k_3, ε_1, ε_2 are all greater than 0; $0<\alpha$; $\lambda_2<1$; $1<\beta$, λ_1 and *sgn*(*s*) denotes the sign function. The new reaching law introduces exponential terms $\varepsilon_1|x_1|^{\lambda_1}s$ and $\varepsilon_2|x_1|^{\lambda_2}s$ to improve the convergence rate. Moreover, by introducing the state variables x_1 the exponential parameter can be adaptively changed. Through proper setting of all parameters, it can effectively suppress vibration generation.

B. Analysis of Convergence Rate of Enhanced reaching Law

Assuming the initial state $\boldsymbol{s}$ is $s(0)$, and $s(0)>1$, the convergence process of the system can be divided into two stages.

$s(0)\rightarrow s(T1)=1$, where $T1$ is the required time. For Eq. (8), since $0<\alpha$, $\lambda 2<1$, and $1<\beta$, $\lambda 1$, the $k_1|s|^{\alpha}\mathrm{sgn}\,(s) \ll k_2|s|^{\beta}\mathrm{sgn}\,(s) + \varepsilon_1|x_1|^{\lambda_1}s$ convergence rate in this stage is mainly affected by $-k_2|s|^{\beta}\,\mathrm{sgn}(s) - \varepsilon_1|x_1|^{\lambda_1}s$. The reaching law (8) can be written

$$\dot{s} = -k_2|s|^{\beta}\mathrm{sgn}\,(s) - \varepsilon_1|x_1|^{\lambda_1}s \quad (9)$$

Solving equations with multiple power terms is somewhat challenging. They can be considered as multiple equations to solve and compare separately. Thus, Equation (9) can be divided into $\dot{s} = -k_2|s|^{\beta}\mathrm{sgn}\,(s)$ and $\dot{s} = -\varepsilon|x_1|^{\lambda_1}s$, respectively. By separately considering the convergence rate under the influence of $-k_2|s|^{\beta}\mathrm{sgn}\,(s)$ and $-\varepsilon|x_1|^{\lambda_1}s$, the required convergence time for this stage of the new convergent rate must be less than either of the two solutions.

Solving $\dot{s} = -k_2|s|^{\beta}\mathrm{sgn}\,(s)$, and rearranging the original equation, we get

$$\frac{\dot{s}}{s^{\beta}} = -k_2 \quad (10)$$

Let t_0 be the time taken by $s(0)\rightarrow s(t_0)=1$ under the influence of $\dot{s} = -k_2|s|^{\beta}\mathrm{sgn}\,(s)$ only. Integrating Eq. (10) from $t=0$ to $t=t_0$ to get the convergence time t_0 as

$$t_0 = \frac{1-s(0)^{1-\beta}}{k_2(\beta-1)} \tag{11}$$

Solving can be obtained for $\dot{s} = -\varepsilon|x_1|^{\lambda_1}s$. Arrange the original equation to get:

$$\frac{\dot{s}}{|x_1|^{\lambda_1}s} = -\varepsilon_1 \tag{12}$$

Let t_1 be the time taken by $s(0)\rightarrow s(t_1)=1$ under the influence of only $\dot{s} = -\varepsilon|x_1|^{\lambda_1}s$. Integrating Eq.(12) from $t=0$ to $t=t_1$, the convergence time t_1 can be obtained:

$$t_1 = -\frac{1}{\varepsilon_1}\int_0^t \frac{1}{|x_1|^{\lambda_1}}\,\mathrm{d}(\ln\, s) \tag{13}$$

Therefore, for the new reaching law, the time T_1 required from $s(0)$ to $s(T_1)$ is

$$T_1 \leqslant \min(t_0, t_1) \tag{14}$$

2) $s(T_1)\rightarrow s(t)=0$, let the required time be T_2. For equation (8), since $0<\alpha$, $\lambda 2<1$, $1<\beta$, $\lambda 1$ and $k_3 s \ll k_1|s|^{\alpha}\mathrm{sgn}\,(s) + \varepsilon_2|x_1|^{\lambda_2}s$, the convergent rate at this stage is mainly affected by $k_1|s|^{\alpha}\mathrm{sgn}\,(s) + \varepsilon_2|x_1|^{\lambda_2}s$ and the convergent law (8) can be written as

$$\dot{s} = -k_1|s|^{\alpha}\mathrm{sgn}\,(s) - \varepsilon_2|x_1|^{\lambda_2}s \tag{15}$$

Similarly, Equation (15) can be divided into $\dot{s} = -k_1|s|^{\alpha}\mathrm{sgn}\,(s)$ and $\dot{s} = -\varepsilon_2|x_1|^{\lambda_2}s$. By separately considering the convergence rate under the influence of $k_1|s|^{\alpha}\mathrm{sgn}\,(s)$ and $\varepsilon_2|x_1|^{\lambda_2}s$, the required convergence time in this stage must be less than either of the two solutions.

Solving $\dot{s} = -k_1|s|^{\alpha}\mathrm{sgn}\,(s)$ and rearranging the original equation, we get

$$\frac{\dot{s}}{s^{\alpha}} = -k_1 \tag{16}$$

Let $t2$ be the time required for $s(T1)\rightarrow s(t2')=0$ under the sole action of $\dot{s} = -k_1|s|^{\alpha}\mathrm{sgn}\,(s)$. Thus, integrating both sides of equation (16) from $t=T_1$ to $t=t_2'$, we can obtain the approximate time t_2.

$$t_2 = \frac{1}{k_1(1-\alpha)} \tag{17}$$

The given equation is $\dot{s} = -\varepsilon_2|x_1|^{\lambda_2}s$. Upon rearranging:

$$\frac{\dot{s}}{|x_1|^{k_2}s} = -\varepsilon_2 \tag{18}$$

Similarly, let t_3 be the time required for $s(T_1)\rightarrow s(t'_3)=0$ under the sole action of $s = -\varepsilon_2|x_1|^{\lambda_2}s$. Thus, integrating both sides of equation (18) from $t=T_1$ to $t=t'_3$, we can obtain the approximate time t_3.

$$t_3 = -\frac{1}{\varepsilon_2}\int_{T_1}^{t'_3} \frac{1}{|x_1|^{\lambda_2}}\,\mathrm{d}(\ln s) \tag{19}$$

Therefore, for the new modeled approximation law, the time T_2 required for $s(T_1)$ to reach $s(t)=0$ is obtained as:

$$T_2 \leqslant \min(t_2, t_3) \tag{20}$$

To sum up, it can be seen that the convergence time of the new reaching law is approximately $T=T_1+T_2 \leq t_0+t_2$, and the convergence time of the double power combination reaching law is approximately $T_3=t_0+t_2$. Additionally, it is known that the convergence time of the double power-law convergence law is T_4+T_3. Thus, we have $T \leq T_3 < T_4$. Therefore, the new reaching law exhibits superior convergence speed compared to both the double power reaching law and the double-power combined reaching law.

C. Analysis on the Existence and Reachability of reaching Law

The theorem states that when the initial state of the system $s(0)$ is not on the sliding surface, then the system state can asymptotically converge to the sliding surface under the action of the sliding mode convergence law (8).

Proof: Let the Lyapunov function be $V=s^2/2$. According to equation (8), we can obtain the relationship can be obtained as:

$$\dot{V} = s\dot{s} = \begin{cases} s\begin{bmatrix} -k_1|s|^{\alpha}\mathrm{sgn}\,(s) \\ -\varepsilon|x_1|^{\lambda_1}s \\ -k_2|s|^{\beta}\,sgn(s)) \end{bmatrix} < 0, |s| > 1 \\ s\begin{bmatrix} -k_1|s|^{\alpha}\,\mathrm{sgn}(s)) \\ -k_3 s \\ -\varepsilon|x_1|^{\lambda_2}s \end{bmatrix} \leqslant 0, \quad |s| \leqslant 1 \end{cases} \tag{21}$$

From equation (21), we can see that $\dot{V} = s\dot{s} = 0$ if and only if $s=0$. According to the conditions of existence and reachability of reaching law, if the designed reaching law satisfies the Lyapunov stability condition, namely, if the first-order derivative of the Lyapunov function V is negative ($\dot{V} < 0$), then the reaching law is both existent and reachable. Therefore, the reaching law (8) can lead the system state to asymptotically converge to the sliding surface.

D. Design of improved model-free sliding mode controller for speed loop

Based on the hyperlocal model theory [20], a hyperlocal model of the speed loop is established based on the input and output of the YASA-AFFSSPM motor speed loop.

$$\dot{\omega}_e = F + \alpha i_q \tag{22}$$

where, α represents the to-be-designed q-axis stator current parameter, and F represents the known part of the system as well as the uncertain parameters.

Based on the hyper-local model [20], the model-free controller for the speed loop can be designed as follows.

$$i_q = \frac{-F+\dot{\omega}_e^*+u_c}{\alpha} \tag{23}$$

Here, ω_e^* is the given speed of the motor; u_c is the control input of the speed loop feedback controller. By combining Equation (22) and Equation (23), we can obtain:

$$(\dot{\omega}_e^* - \dot{\omega}_e) + u_c = 0 \tag{24}$$

Designing the speed loop feedback controller as a sliding mode controller allows for the integration of model-free control with sliding mode control methods. Using the YASA-AFFSSPM speed error as a state variable:

$$\begin{cases} x_1 = \omega_e^* - \omega_e \\ x_2 = \int x_1\,\mathrm{d}t \end{cases} \tag{25}$$

By combining Equation (24) and Equation (25), and then differentiating Equation (25), we obtain:

$$\begin{cases} \dot{x}_1 = -u_c \\ \dot{x}_2 = \omega_e^* - \omega_e \end{cases} \tag{26}$$

Select the sliding surface as

$$s_1 = x_1 + cx_2 \tag{27}$$

where c is a parameter to be designed, and $c>0$. Differentiating Equation (27) and substituting Equation (26), we get:

$$\dot{s}_1 = cx_1 - u_c \tag{28}$$

To improve the convergence rate during the sliding mode approach phase and reduce chattering during the sliding phase, we select an improved double power combination reaching law for designing the controller. Therefore, by combining Equation (8), (26), and (28), we obtain:

$$u_c = \begin{cases} \begin{pmatrix} c(\omega_e^* - \omega_e) + k_1|s_1|^{\alpha} sgn(s_1) \\ +k_2|s_1|^{\beta} \operatorname{sgn}(s_1) + \varepsilon|x_1|^{\lambda_1} s_1 \end{pmatrix}, |s_1| > 1 \\ \begin{pmatrix} c(\omega_e^* - \omega_e) + k_1|s_1|^{\alpha} sgn(s_1) \\ +k_3 s_1 + \varepsilon|x_1|^{\lambda_2} s_1 \end{pmatrix}, |s_1| \leqslant 1 \end{cases} \quad (29)$$

In order to ensure stability of the designed controller, the sliding mode reachability condition needs to be satisfied:

$$\dot{V}_1 = s_1 \dot{s}_1 \leqslant 0 \quad (30)$$

We select the Lyapunov function $V_1=s_1^2/2$. Since we choose the improved reaching law as the sliding mode convergence rate, substituting equations (28) and (29) into the function (30), we obtain:

$$\dot{V}_1 = s_1 \dot{s}_1 = \begin{cases} s_1 \cdot \begin{bmatrix} -k_1|s_1|^{\alpha} \operatorname{sgn}(s_1) \\ -\varepsilon|x_1|^{\lambda_1} s_1 \\ -k_2|s_1|^{\beta} \operatorname{sgn}(s_1) \end{bmatrix}, |s_1| > 1 \\ s_1 \cdot \begin{bmatrix} -k_1|s_1|^{\alpha} \operatorname{sgn}(s_1) \\ -k_3 s_1 - \varepsilon|x_1|^{\lambda_2} s_1 \end{bmatrix}, |s_1| \leq 1 \end{cases} \quad (31)$$

From equation (31), we can see that the controller satisfies the sliding mode reachability condition. By combining equations (23) and (29), we obtain the designed YASA-AFFSSPM motor vector control system's speed loop improved model-free sliding mode control law:

$$i_q = \begin{cases} \frac{1}{\alpha} \begin{pmatrix} -F + \dot{\omega}_e^* + c(\omega_e^* - \omega_e) \\ +k_1|s_1|^{\alpha} \operatorname{sgn}(s_1) \\ +\varepsilon|x_1|^{\lambda_1} s_1 \\ +k_2|s_1|^{\beta} \operatorname{sgn}(s_1) \end{pmatrix} |s_1| > 1 \\ \frac{1}{\alpha} \begin{pmatrix} -F + \dot{\omega}_e^* + c(\omega_e^* - \omega_e) \\ +k_1|s_1|^{\alpha} \operatorname{sgn}(s_1) \\ +k_3 s_1 + \varepsilon|x_1|^{\lambda_2} s_1 \end{pmatrix} |s_1| \leq 1 \end{cases} \quad (32)$$

E. ESMDO Design

From the control law equation (32), we can see that there exist unknown parts F in the system. Therefore, we design an extended sliding mode disturbance observer to observe and compensate for the unknown part *F*. The extended hyper-local model for YASA-AFFSSPM motor is given by:

$$\begin{cases} \frac{d\omega_c}{dt} = \zeta i_q - \delta \omega_e + F \\ \frac{dF}{dt} = R(t) \end{cases} \quad (33)$$

In equation (33), R(t) represents the rate of change of the unknown quantity *F*, and ζ and δ are parameters to be designed. For equation (33), the system is designed with the following extended sliding mode disturbance observer as:

$$\begin{cases} \frac{d\hat{\omega}_e}{dt} = \zeta i_q - \delta \omega_e + \hat{F} + u_{\text{smo}} \\ \frac{d\hat{F}}{dt} = l u_{\text{smo}} \end{cases} \quad (34)$$

In the equation $\hat{\omega}$ represents the real-time speed estimation, $\hat{F}$ represents the real-time estimation of the unknown part of the system, u_{smo} is the sliding mode function to be designed, *l* is the observer u_{smo} gain.

By combining equations (33) and (34), the observation error is given by:

$$\begin{cases} \dot{x} = \delta x + \tilde{F} + u_{smo} \\ \frac{d\tilde{F}}{dt} = l u_{smo} - R(t) \end{cases} \quad (35)$$

The error terms are as follows: speed estimation error: $\dot{x} = \hat{\omega}_e - \omega_e$, system disturbance observation error: $\tilde{F} = \hat{F} - F$. We choose the speed error as the sliding surface s_2 as:

$$s_2 = \dot{x} = \hat{\omega}_e - \omega_e \quad (36)$$

To ensure performance during the sliding mode approach phase, we choose exponential convergence law for the reaching law:

$$\dot{s}_2 = -\eta_1 \operatorname{sgn}(x) - \eta_2 x \quad (37)$$

where η_1 and η_2 are positive constants. Then, the sliding mode observer control law u_{smo} is:

$$u_{smo} = -\delta x - \tilde{F} - \eta_1 \operatorname{sgn}(x) - \eta_2 x \quad (38)$$

Theorem 2: If we choose equation (36) as the sliding surface, and $\eta_1 \geq \|\tilde{F}\|$, then the observer in equation (34) is asymptotically stable.

Proof: Let the Lyapunov function be $V_2 = s_2^2/2$.

$$\begin{aligned} &\dot{V}_2 = \dot{s}_2 s_2 = x\left(\delta x + \tilde{F} + u_{\text{smo}}\right) = \\ &x\left(\tilde{F} - \eta_1 \operatorname{sgn}(x) - \eta_2 x\right) = \\ &x\tilde{F} - \eta_1 x \operatorname{sgn}(x) - \eta_2 x^2 \leqslant \|x\|\left(\|\tilde{F}\| - \eta_1\right) \end{aligned} \quad (39)$$

Therefore, as long as $\eta_1 \leq \|\tilde{F}\|$, $\dot{V} \leq 0$ is guaranteed.

$$\hat{F} = l \int \left(-\delta x - \eta_1 \operatorname{sgn}(x) - \eta_2 x\right) dt \quad (40)$$

Substituting the observed value $\hat{F}$ obtained from equation (40) into equation (32), we obtain the model-free sliding mode control law for the speed loop as:

$$i_q = \begin{cases} \frac{1}{\alpha} \begin{pmatrix} -\hat{F} + \dot{\omega}_e^* + c(\omega_e^* - \omega_e) \\ +k_1|s_1|^{\alpha} \operatorname{sgn}(s_1) \\ +\varepsilon|x_1|^{\lambda_1} s_1 \\ +k_2|s_1|^{\beta} \operatorname{sgn}(s_1) \end{pmatrix} |s_1| > 1 \\ \frac{1}{\alpha} \begin{pmatrix} -F + \dot{\omega}_e^* + c(\omega_e^* - \omega_e) \\ +k_1|s_1|^{\alpha} \operatorname{sgn}(s_1) \\ +k_3 s_1 + \varepsilon|x_1|^{\lambda_2} s_1 \end{pmatrix} |s_1| \leq 1 \end{cases} \quad (41)$$

In summary, we obtain the model-free Enhanced sliding mode controller (ESMC) for the YASA-AFFSSPM motor system as shown in Figure 2. The feedback controller u_c in the controller incorporates the improved sliding mode control law with the enhanced double power combination reaching law. The disturbance F is observed in real-time by the extended sliding mode disturbance observer.

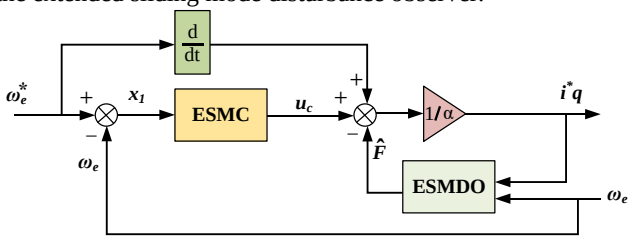

Fig. 2 Enhanced model-free sliding mode controller.

IV. Simulation Results and Analysis

In order to further verify the feasibility of the IMFSMC algorithm and its better robustness against load disturbances and parameter perturbations, a MATLAB/SIMULINK model was constructed to compare and verify the simulation results of the EMFSMC, MFSMC, control algorithms. parameters of 12S/19P YASA-AFFSSPM motor are shown in table 1. After conducting a theoretical analysis of the vector control technology for permanent magnet synchronous motors, in this paper simulation models are constructed to the SVPWM module, coordinate transformation module, and proposed control module within the vector control system. Ultimately, these modules are integrated to complete the simulation of a dual closed-loop vector control system with id = 0. The analysis also examines the responsiveness and stability of the system based on the mathematical model of the motor in the dq axes. The system control block diagram of traditional MFSMC and EMFSMC motor are shown in the Fig. 3. Moreover, motor parameter settings are shown in the Table1. The parameters of the control methods are as follows. EMFSMC parameters: k_1=10, k_2=200, k_3=10, ε_1= 0.1, ε_2=0.55, α=1, c=70, λ_1=1.5, λ_2=0.5, β=1.5, ζ=10, l=1, δ=100. MFSMC parameters: k_1=10, k_2=200, k_3=10, ε_1= 0.1, ε_2=0.55, α=1, c=70, λ_1=1.5, λ_2=0.5, β=1.5.

A. *Analysis of simulation results under parameter perturbation*

Setting the initial torque of the motor to 0 N.m, at 0.2 s, the torque increases to 10 N.m. Setting the initial value of the rotor flux to 0.062 Wb, at 0.1 s, the rotor flux decreases to 0.042 Wb. The q-axis inductance of the motor decreases from 0.47 mH to 0.29 mH at 0.3 s. Figure 4 shows the motor speed response curve. It shows the simulation results of the 12S/19P YASA-AFFSSPM control system under the Traditional MFSMC and EMFSMC controllers.

TABLE. 1: 12S/19P YASA-AFFSSPM MOTOR PARAMETERS

Parameter	Symbol	Value	Unit
d-axis inductance	L_d	0.2e-3	H
q-axis inductance	L_q	0.47e-3	H
DC bus voltage	U_{dc}	311	V
Rotor flux	Ψ	0.062	Wb
Phase resistance	R	0.025	Ω
Load torque	T	12	N·m
Moment of inertia	J	0.00302	Kg.m^2

With the MFSMC controller, it takes a long time for the motor to reach the preset speed from a no-load start, approximately 0.04 seconds, with a significant overshoot of about 12.5%. Compared with traditional MFSMC control, with the EMFSMC controller 12S/19P YASA-AFFSSPM response time is significantly reduced, about 0.015s, and it reaches the given speed quickly without overshoot.

At 0.1 s when the rotor flux decreases, the speed curve of EMFSMC is also superior to MFSMC, with the speed curve of EMFSMC stabilizing after 0.08 s following a 0.1 rpm fluctuation, while MFSMC control requires 0.05 s to stabilize after fluctuations of 0.15 rpm, showing inferior performance compared to EMFSMC. At 0.3 s, when the q-axis suddenly decrease, the speed curve of EMFSMC shows even smaller speed fluctuations compared to MFSMC control method. Therefore, it is evident that in speed control, EMFSMC is more precise and stable than MFSMC. When a load of 10N·m is suddenly added to the 12S/19P YASA-AFFSSPM at 0.2s, the MFSMC control produces a rotational speed drop of about 9 rpm, and returns to the steady state after about 0.03s; the rotational speed drop using the improved EMFSMC control is only about is 4 rpm, and the speed recovery time is shortened to about 0.01s. Figure 5 shows the torque response curves of the two control methods.

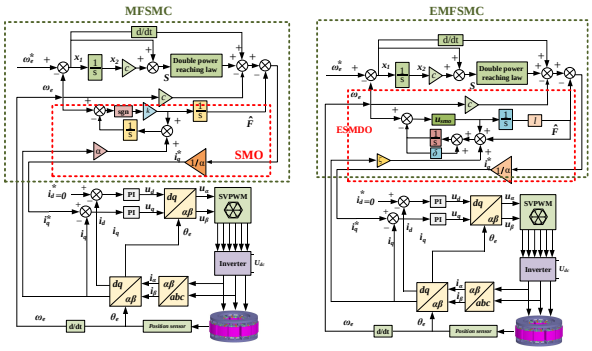

(a) (b)

Fig. 3 Control block diagram. (a) Traditional MFSMC (b) EMFSMC.

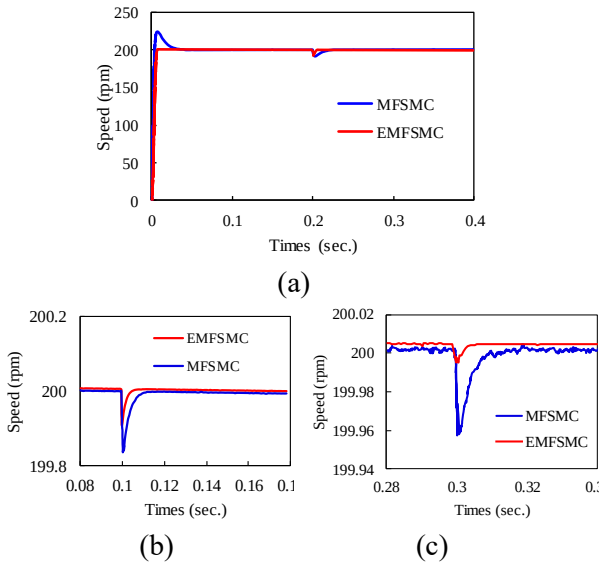

(a) (b) (c)

Fig4. Comparison of the speed (a) Global speed comparison waveforms (b) Local magnified waveforms under demagnetization fault at t=0.1sec. (c) Local magnified waveforms under decrease of q-axis inductance. at t=0.3sec.

From the analysis of Figure 6 (a), it can be seen that the three-phase current waveform when using the MFSMC controller has obvious current distortion, while the current waveform of Figure 6 (b) when using the EMFSMC controller is smoother and close to sinusoidal wave.

Through comparison, it can be seen that the torque ripple under the MFSMC controller is larger, about 1.6N·m, while using the EMFSMC controller, the torque ripple is significantly reduced, about 1N·m and the dynamic response speed of the motor's electromagnetic torque is significantly improved. Figure 6 shows the current response waveform before and after the load torque changes suddenly.

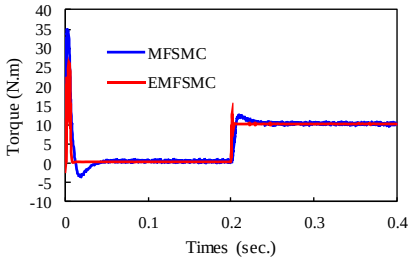

Fig. 5 Torque response curve

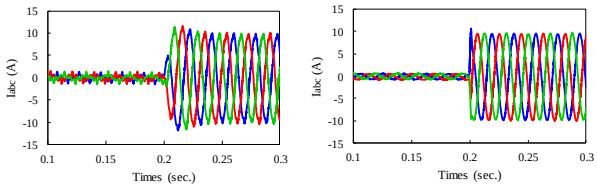

(a) (b)

Fig. 6 Three-phase current response curve (a) MFSMC controller (b) EMFSMC controller

Figure 7 is a comparative simulation diagram when the speed control system starts without load and the speed suddenly changes to 400r/min in 0.2s. Through analysis, it can be seen that the EMFSMC controller proposed in this article can be used under variable speed conditions, and the speed regulation performance is relatively ideal. Compared with the MFSMC controller, it can significantly reduce the overshoot phenomenon after a large speed mutation, and quickly reach the given rotating speed value.

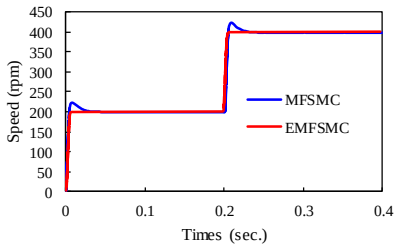

Fig. 7 Speed response curve.

V. Experimental Results

In order to evaluate the performance of the proposed control on 12S/19P YASA-AFFSSPM motor, a prototype motor is manufactured. The system employs vector control, facilitated by a three-phase converter, with the vector control algorithm implemented through a MicroLab digital controller. Figure 8 depicts the experimental arrangement for the proposed method.

In the experiment, the initial torque of the motor is set to 5 *Nm*, and at 0.2 seconds, the torque increases to 15 Nm. The initial value of the motor rotor magnetic flux linkage is set to 0.062 Wb, which decreases to 0.042 Wb at 0.3 seconds.

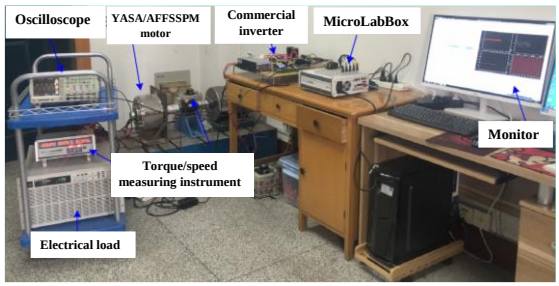

Fig. 8. Motor testing platform.

The q-axis inductance of the motor decreases from 0.47 mH to 0.29 *mH* at 0.4 seconds, while the d-axis inductance decreases from 0.2 *mH* to 0.14 *mH* at 0.5 seconds. The motor resistance increases to 0.035 Ω at 0.6 seconds. Figures 9, 10, and 11 illustrate the experimental waveforms of the d-q axis currents, speed, and torque for the MFSMC and EMFSMC control methods under motor parameter perturbations. To ensure consistency, the parameter design and parameter perturbation time were aligned with the parameters used in the simulation experiments.

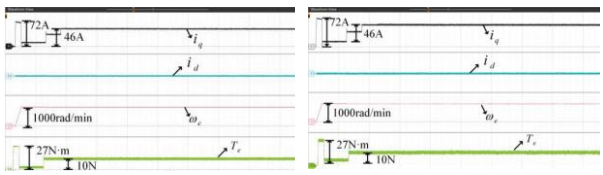

200 m/s 200 m/s

(a) (b)

Fig. 9. waveforms under load and parameter disturbances. (a) EMFSMC. (b) MFSMC.

Upon analyzing the experimental results, it can be seen that the overall trend and effectiveness of the semi-physical experiment are consistent with the simulation. In comparison of Figures 10(a) and 10(b), after 0.05 seconds of motor startup, when the speed stabilizes at 1000 rad/min, the speed fluctuation of EMFSMC is only ±0.004 rad/min, whereas the speed fluctuation for the MFSMC control method is ±0.03 rad/min. Therefore, the speed curve of the EMFSMC is smoother and exhibits less jitter compared to that of the MFSMC control method. Similarly, when the torque stabilizes at 15 N·m, the torque variation of EMFSMC is ±1.5 N·m, while the torque fluctuation for MFSMC control is greater, at ±2.5 N·m. Thus, it is evident that the torque experimental waveform variation of the EMFSMC is smaller than that of the MFSMC control, showcasing stronger

robustness. Comparing Figures 11(a) and 11(b), which depict the d-q axis current experimental waveforms for EMFSMC and MFSMC control, we observe that after approximately 0.45 seconds of parameter perturbation and once the current reaches stability, the variation in the q-axis current for EMFSMC is ±2.5 A, while the variation for the MFSMC control method is ±3.1 A.

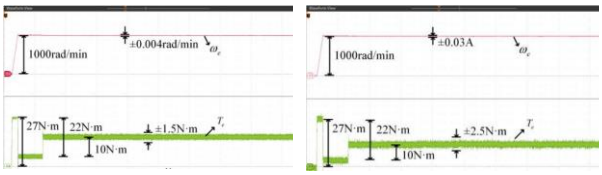

200 m/s (a) 200 m/s (b)

Fig. 10. Speed and torque waveforms. (a) EMFSMC. (b) MFSMC.

Therefore, the magnitude of the current experimental waveform variation for EMFSMC is smaller than that of the MFSMC control. Thus, whether comparing the speed and torque experimental waveforms or the current experimental waveforms, IMFSMC exhibits smaller fluctuations and operates more stably under both steady-state conditions and parameter perturbations.

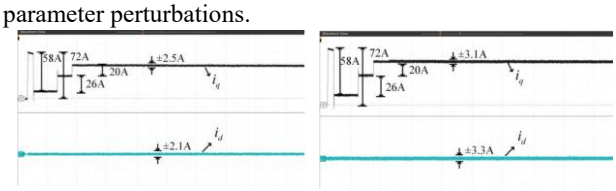

200 m/s (a) 200 m/s (b)

Fig. 11. d-q axis current waveforms. (a) EMFSMC. (b) MFSMC.

Quantitative and qualitative comparison between EMFSMC and MFSMC is given in Table 2. In summary, the EMFSMC method, while more complex and requiring more parameters, offers superior convergence speed and robustness against disturbances compared to both MFSMC and traditional PI control. The MFSMC provides a balance between complexity and performance but falls short in speed and robustness. PI control remains the simplest but is less effective in dynamic applications where precision and responsiveness are critical.

TABLE 2: COMPARISON BETWEEN EMFSMC AND MFSMC.

Criterion	EMFSMC	MFSMC
Time response	~0.015S	~0.04 sec.
Overshoot	At least	~12.5%
Speed drop under sudden load	~4 rpm	~9 rpm
Recovery time to steady state	~0.01 sec.	~0.03 sec.
Speed fluctuations	~0.1 rpm	~0.15 rpm
Torque fluctuations	~1 N·m	~1.6 N·m
Current fluctuations	±2.5 A	±3.1 A
Response to load changes	Fast and stable	Slow and unstable
Control accuracy	higher	lower
Strength against disturbances	higher	lower

VI. Conclusion

Considering the impact of external conditions on motor parameter perturbations that reduce the robustness of speed loop control systems, an Enhanced Model-Free Sliding Mode Control (EMFSMC) algorithm is proposed. The following conclusions are drawn from mathematical analysis and experimental verification: 1) An improved double-power combination sliding mode reaching law is employed to redesign the sliding mode controller, enhancing system stability and reducing chattering typical of traditional reaching laws. 2) Integrating the Extended Sliding Mode Disturbance Observer (ESMDO) with the improved model-free sliding mode controller enables real-time estimation of unknown disturbances in the speed loop, significantly boosting the motor system's response capability. Specifically, EMFSMC reduces speed response time from approximately 0.04 seconds with Model-Free Sliding Mode Control (MFSMC) to about 0.015 seconds, marking an improvement of approximately 62.5%. Under sudden load conditions, speed drop is minimized from 9 rpm with MFSMC to 4 rpm with EMFSMC, achieving a reduction of about 55.6%. The recovery time to stability is also enhanced, decreasing from 0.03 seconds with MFSMC to 0.01 seconds with EMFSMC, a 66.7% improvement. These enhancements in speed response, stability, and robustness highlight the effectiveness of EMFSMC in dynamic applications, especially in electric vehicles and precision-demanding industries.

REFERENCES

[1] J. F. Gieras and J.-X. Shen, *Modern Permanent Magnet Electric Machines*. CRC Press, 2022.

[2] FNU Nishanth, Joachim Van Verdeghem, and E. L. Severson, "A Review of Axial Flux Permanent Magnet Machine Technology," *IEEE Transactions on Industry Applications*, vol. 59, no. 4, pp. 3920–3933, Jan. 2023.

[3] J. R. Fard and M. Ardebili, "Design and Control of a Novel Yokeless Axial Flux-Switching Permanent-Magnet Motor," *IEEE Transactions on Energy Conversion*, vol. 34, no. 2, pp. 631–642, Jun. 2019.

[4] J. Rahmani Fard and M. Ardebili, "Optimal Design and Analysis of the Novel Low Cogging Torque Axial Flux-Switching Permanent-Magnet Motor," *Electric Power Components and Systems*, vol. 46, no. 11–12, pp. 1330–1339, Jul. 2018.

[5] A. Brosch, O. Wallscheid, and Joachim Böcker, "Time-Optimal Model Predictive Control of Permanent Magnet Synchronous Motors Considering Current and Torque Constraints," *IEEE Transactions on Power Electronics*, vol. 38, no. 7, pp. 7945–7957, Apr. 2023.

[6] S. Lin, Y. Cao, C. Li, Z. Wang, T. Shi, and C. Xia, "Two-Degree-of-Freedom Active Disturbance Rejection Current Control for Permanent Magnet Synchronous Motors," *IEEE Transactions on Power Electronics*, vol. 38, no. 3, pp. 3640–3652, Nov. 2022.

[7] X. Sun, F. Cai, Z. Yang, and X. Tian, "Finite Position Control of Interior Permanent Magnet Synchronous Motors at Low

Speed," *IEEE Transactions on Power Electronics*, vol. 37, no. 7, pp. 7729–7738, Jul. 2022.

[8] J. Yim, S. You, Y. Lee, and W. Kim, "Chattering Attenuation Disturbance Observer for Sliding Mode Control: Application to Permanent Magnet Synchronous Motors," *IEEE transactions on industrial electronics*, vol. 70, no. 5, pp. 5161–5170, May 2023.

[9] J. Huang, X. Zhu, Y. Li, G. Qi, Y. Wu, and Y. He, "A New Composite Sensorless Control Strategy for PMSM Used in Electric Vehicle," *2022 IEEE Transportation Electrification Conference and Expo, Asia-Pacific (ITEC Asia-Pacific)*, Oct. 2022.

[10] M. R. Shokoohinia and M. M. Fateh, "Model-Free Tracking Control via Adaptive Dynamic Sliding Mode Control With Application To Robotic Systems," *International Journal of Industrial Electronics Control and Optimization*, vol. 3, no. 4, pp. 431–438, Sep. 2020.

[11] C. Gao, J. Dai, J. Li, and J. Li, "Finite-Time Convergence ESO-Based Nonsingular Fast Terminal Sliding Mode Control for PMSM with Unknown Parameters and Time-Varying Load," *Mathematical Problems in Engineering*, vol. 2022, pp. 1–13, Nov. 2022.

[12] D. Jin, L. Liu, S. Liu, and D. Liang, "Modified Deadbeat Predictive Current Control for PMSM Drive System via a Composite Integral Sliding Mode Observer," *2022 IEEE Energy Conversion Congress and Exposition (ECCE)*, pp. 1–8, Oct. 2022.

[13] Y. Wei, D. Ke, X. Yu, F. Wang, and José Rodríguez, "Adaptive Inertia Observer-based Model-Free Predictive Current Control for PMSM Driving System of Electric Vehicles," *IEEE Transactions on Industry Applications*, vol. 60, no. 4, pp. 6252–6262, May 2024.

[14] A. Rezaie, "Sliding Mode Control for Chaotic Systems with Unknown Uncertainties," *International Journal of Industrial Electronics Control and Optimization* , vol. 7, no. 1, pp. 53–60, Mar. 2024.

[15] Z. Zhang, Q. Xu, and Y. Wang, "A New Sliding-Mode Observer-Based Deadbeat Predictive Current Control Method for Permanent Magnet Motor Drive," *Machines*, vol. 12, no. 5, pp. 297–297, Apr. 2024.

[16] J. Yim, S. You, Y. Lee, and W. Kim, "Chattering Attenuation Disturbance Observer for Sliding Mode Control: Application to Permanent Magnet Synchronous Motors," *IEEE transactions on industrial electronics*, vol. 70, no. 5, pp. 5161–5170, May 2023.

[17] X. Wang, Q. Xu, Y. Whang, X. Zhang, S. Liu, and Y. Miao, "Model-Free Predictive Current Control of PMSM Based on Sliding Mode Disturbance Observer," *2021 24th International Conference on Electrical Machines and Systems (ICEMS)*, pp. 3739–3744, Nov. 2023.

[18] A. Razzaghian , R. Kardehi , and N. Pariz, "Adaptive fuzzy fractional-order fast terminal sliding mode control for a class of uncertain nonlinear systems," *International Journal of Industrial Electronics Control and Optimization* , vol. 5, no. 1, pp. 77–87, Mar. 2022.

[19] X. Sun, J. Cao, G. Lei, Y. Guo, and J. Zhu, "A Composite Sliding Mode Control for SPMSM Drives Based on a New Hybrid Reaching Law With Disturbance Compensation," *IEEE Transactions on Transportation Electrification*, vol. 7, no. 3, pp. 1427–1436, Sep. 2021.

[20] W. Li, H. Yuan, S. Li, and J. Zhu, "A Revisit to Model-Free Control," *IEEE transactions on power electronics*, vol. 37, no. 12, pp. 14408–14421, Dec. 2022.

Javad Rahmani-Fard received the B.S. degree from Shahed University, Tehran, Iran, in 2009, and the M.S. and Ph.D. degrees in electrical engineering from the K.N. Toosi University of Technology, Tehran, in 2012 and 2018, respectively. Currently, he is an assistant professor of the electrical engineering at Qom University of Technology, Qom, Iran. His research interests include the analysis and design of electrical machines, and sensor-less variable-speed drives, multiphase variable-speed drives.

Saeed Hasanzadeh received the B.S. degree from Shahroud University of Technology, Shahroud, Iran, in 2003, and the M.Sc. and Ph.D. degrees from University of Tehran, Tehran, Iran, in 2006 and 2012, respectively, all in electrical engineering. He joined the faculty of Electrical and Computer Engineering, Qom university of Technology as an Assistant Professor in 2013. His research interests include Power Electronics, Inductive Power Transfer Systems, Electrical Machines and Drives, Electric Vehicles, Magnetic Levitation Systems.

IECO

This page intentionally left blank.

International Journal Of
Industrial Electronics Control and Optimization
Print ISSN: 3517-2645
Online ISSN: 3568-2645
Homepage: https://ieco.usb.ac.ir/

Bidirectional High-Efficiency Converter Based on the Capacitive Wireless Power Transfer Technique for Electric Vehicle Charging and Energy Storage Application

Jasem Shahsevani | Reza Beiranvand

Faculty of Electrical and Computer Engineering, Tarbiat Modares University, Tehran, Iran.[1,2]
Corresponding author's email: beiranvand@modares.ac.ir

Article Info

Article type:
Research Article

Article history:
Received: 23-August-2024
Received in revised form: 17-December-2024
Accepted: 28-December-2024
Published online: 23-Sep-2025

Keywords:
Capacitive wireless power transfer,
Electric vehicle charger,
Resonant conversion,
Step up/down.

ABSTRACT

This article presents a transformer-less bidirectional converter, which is designed with dual resonant frequencies. It supports Electric Vehicle (EV) charging systems, via capacitive coupling wireless power transfer (CCWPT) technique. In addition, its bidirectional power transfer feature can be used to return energy to the stations of the power-wall systems. This converter smoothly operates in both voltage step-up and step-down operation modes, which provides soft switching conditions for all semiconductor switches. The capacitive coupling technique provides robust galvanic isolation between the primary and secondary sides circuits, while the transformer-less design improves its efficiency and reduces its volume and cost, significantly. The proposed converter supports both full-bridge and half-bridge configurations to adapt to diverse power transfer requirements. The cost-effective CCWPT setup enables multi-EV charging from a single station. A prototype of the given converter has been meticulously developed and experimentally validated, demonstrating excellent performance. The converter efficiently converts output power in a wide range from 200 W to 1000 W, accommodates input voltage from 300 to 500 V, and delivers a 400 V output voltage, which is suitable for EV battery charging. It also achieves a maximum efficiency value of 96%, in practice.

NOMENCLATURE

$C_{relative}$	Relative cost.	n	Transformer turn-ratio.
C_r	Resonant capacitor.	Q	The quality factor of the resonant circuit.
C_{r_eq}	Equivalent resonant capacitor.	r	Intrinsic resistor.
C_o	Output capacitor.	S_N	Normalized cumulative maximum power through all switches and diodes.
D	Diode component.	$t_{body(on)}$	Body diode conducting time.
E_{CN}	Normalized cumulative energy is stored in all capacitors.	$t_{delay(on)}$	Power MOSFET delay for turning on.
E_{LN}	Normalized cumulative energy is stored in all inductors.	t_{dis}	2Cdc discharge time from input voltage to 0 V.
F	Normalized switching frequency.	t_{dead}	Dead time between gate-source signals.
f_r	Resonant frequency.	$t_{ds(on)}$	Power MOSFET conducting time.
f_s	Switching frequency.	T_s	Switching time ($1/f_s$).
G_{v_g}	Converter voltage gain transfer function.	V_{bF}	Forward voltage of the MOSFET body diode.
G_{ω_s}	Output voltage sensitivity to the control signal.	V_{ds}	Power MOSFET drain-source voltage.
I_{ds}	Power MOSFET drain-source current.	V_{gs}	Power MOSFET gate-source voltage.
I_{gs}	Power MOSFET gate-source current.	Z_{in}	Input impedance.
L_m	Magnetizing inductor.	Z_o	Output impedance.
L_r	Resonant inductor.		

Copyright © R. Beiranvand (s).
Publisher: University of Sistan and Baluchestan

I. Introduction

In recent years, the proliferation of Electric Vehicles (EVs) has underscored the significance of efficient EV charging and power management within the industry [1]. Concurrently, advancements in Power-Wall technology have aimed to enhance energy storage efficiency by storing energy during periods of low demand and releasing it when needed, offering various advantages [2]. Short-distance wireless power transfer (WPT) methods, typically effective over distances of less than one meter, include Inductive Coupling [3] and Capacitive Coupling [4], where the Capacitive Coupling Wireless Power Transfer (CCWPT) method has emerged as a safer, more cost-effective, and reliable alternative to the Inductive Coupling Wireless Power Transfer (ICWPT) [5].

A compact ICWPT charger for EVs has been introduced in [6], while the charger achieves higher efficiency by eliminating the transformer in its converters, its portable two-section design makes it impractical for large-scale charging stations serving multiple EVs. Another study, given in [7], modified the resonant capacitor of an LLC resonant converter to enable CCWPT. While both configurations ,7] [8 maintain structural simplicity, they suffer from inefficiencies.

Converters employed for CCWPT in prior research [9-11], encountered limitations such as increased power loss due to excessive parallel components. For CCWPT-based EV charging applications [12-15] converters integrated within a car's bumper [12] faced some drawbacks, including hard-switching, low switching frequency, and reduced efficiency. Additionally, CCWPT configurations between the floor and the vehicle's underbody [13-15] exhibited inefficiency caused by high return current and increased power loss, particularly under no-load conditions. A bidirectional converter proposed in [16] suffers from incomplete filtering of switching harmonics, leading to transformer overheating and degraded efficiency. Similarly, a CCWPT solution proposed in [17] positions charging plates between the car's floor and the ground. However, under typical scenarios with standard ground clearance, power transfer remains limited, resulting in suboptimal charging rates. Overall, resonant converters with transformers provide galvanic isolation and voltage regulation. Nevertheless, operating these converters at frequencies deviating from their resonant frequencies introduces additional harmonics into the transformer, which increases its power dissipation. Moreover, considering the cost-effectiveness and structural simplicity of the CCWPT relative to the ICWPT [4], hybrid WPT or ICWPT solutions are financially unsuitable for large-scale deployment.

Many resonant converters equipped with parallel resonant tank components can operate in both step-up and step-down operation modes. However, bidirectional converters are essential for applications such as Power-Wall systems. A previous study introduced a bidirectional resonant converter, but during reverse conduction, switching harmonics are inadequately filtered, resulting in higher power losses. While subsequent studies [19 ,18] attempted to resolve these issues, the incorporation of a transformer led to additional costs, energy losses, and high volume. Although another research work [18], which proposes a three-level bidirectional CLLC converter with a wide input voltage range, has been designed to enhance voltage regulation, it exhibits significant efficiency drops under light-load conditions, alongside higher losses due to the employed transformer, similar to [20]. Furthermore, the present paper provides a comprehensive structure with experimental validation and deeper mathematical analysis.

In [21] and [22], transformer-less converters have been introduced. Although these converters feature a low component count, they experience hard-switching events, causing higher electromagnetic noise and switching power losses. While such issues are not critical at low power levels, they become significant in high-power EV applications, directly affecting efficiency and limiting the converter's suitability for high-power industries. In [23], an EV charger has been proposed; however, the lack of empirical evidence and detailed mathematical analysis limits further investigation. The converter also needs a broad switching frequency range and lacks constant current control. Similarly, in [24], a DC-DC converter has been introduced with persisting issues of noise and incomplete soft-switching operation. Other research works in [25, 26] introduce some converters that lack adequate filtering before the transformer, allowing harmonics to pass through the transformer and cause heating, which ultimately restricts power density. Some other converters for EV charging with soft-switching operation are proposed in [27-29], but their employed transformers increase their sizes, cost, and power losses. These converters operate at wide switching frequency ranges, which reduce their efficiencies and result in significant circulating currents under off-resonant conditions. In terms of multi-output charging, most of these converters incorporated transformers, which, while supporting high-power applications, escalated costs and posed control challenges under varying load conditions. In [30] multi-output transformers faced similar drawbacks, including a high number of components. The problem of input/output isolation, as well as broad switching frequency ranges, persisted in [31-33], complicating control over a wide power range.

This paper introduces a bidirectional transformer-less isolated resonant converter, which can be designed specifically for CCWPT applications. Using the CCWPT

technique not only reduces costs but also enables the charger to accommodate multiple vehicles simultaneously. The transformer-less architecture contributes to enhancing efficiency and reducing the weight, while capacitive coupling ensures reliable input-output isolation. The optimally designed resonant tank mitigates harmonics in both forward and backward power flow operation modes. The bidirectional capability further supports Power-Wall applications, enabling flexible battery allocation. Additionally, the CCWPT inherently provides robust isolation between the input and the output ports. To limit frequency variations, a combination of the half-bridge and the full-bridge topologies has been adopted, which minimizes the frequency deviations and enhances the efficiency, in practice.

The proposed converter and its key waveforms are given in Section II, and then its mathematical analysis is given in Section III. Next, a design procedure is introduced in Section IV, in detail. The proposed converter experimental results are described in Section V. Finally, the paper is concluded in Section.

II. Proposed Converter and Its Key Waveforms

The proposed converter, shown in Fig. 1, is a novel transformer-less bidirectional resonant converter tailored specifically for Capacitive Coupling Wireless Power Transfer (CCWPT) applications. By reconfiguring the resonant capacitors into two series connections, the design achieves effective isolation between the input and output ports, eliminating the need for a transformer. This architecture is optimized for wireless power transfer (WPT) applications, with the primary side of the resonant capacitors installed on a wall structure and the secondary side embedded within the EV's bumper. Fig. 2 illustrates the key waveforms of the converter, highlighting essential operational characteristics and performance metrics. These waveforms include critical parameters such as input voltage, input current, output voltage, output current, and switching signals, offering a comprehensive view of the converter's behavior across varying operating conditions. Fig. 3 demonstrates a typical EV charging scenario, displaying the converter's practical application in real-world conditions. In this setup, capacitive plates are strategically positioned on both the wall and the car's bumper, separated by a dielectric foam layer. As the EV approaches the wall, the plates align, with the dielectric layer preventing any short circuits. With a separation distance of around 1 mm, it is possible to achieve capacitance values in the Nano Farad (*nF*) range. The foam layer on the wall side provides flexibility, ensuring reliable and consistent contact between the plates. A notable advantage of the proposed design is that all key components are housed on the wall side, resulting in a lighter and more compact setup on the vehicle. This centralized configuration enhances cost-effectiveness by allowing the wall-side infrastructure to be universally applied to multiple vehicles, making it more economical than designs with components embedded within each vehicle. While a hybrid WPT setup with an inductor on the vehicle side is considered, the use of the car's bumper for CCWPT requires an alternative approach to inductive coupling. Given the diversity of vehicles that may adopt this technology, extensive inductive windings on each vehicle would be cost-prohibitive.

In summary, the proposed converter offers a transformer-less, cost-effective solution for efficient CCWPT in EV charging applications. Its design ensures robust input-output isolation and demonstrates the feasibility and practicality of implementing the CCWPT through capacitive coupling techniques.

III. Mathematical Analysis

Text Both First Harmonic Approximation (FHA) and small signal models of the converter, as well as its different components power losses, are given here, respectively.

A. FHA model

To enable a streamlined yet effective analysis of the proposed converter, the FHA method is applied, which is solely focused on the first harmonics of the different switching waveforms of the converter, while omitting higher-order harmonics, as detailed in [33].

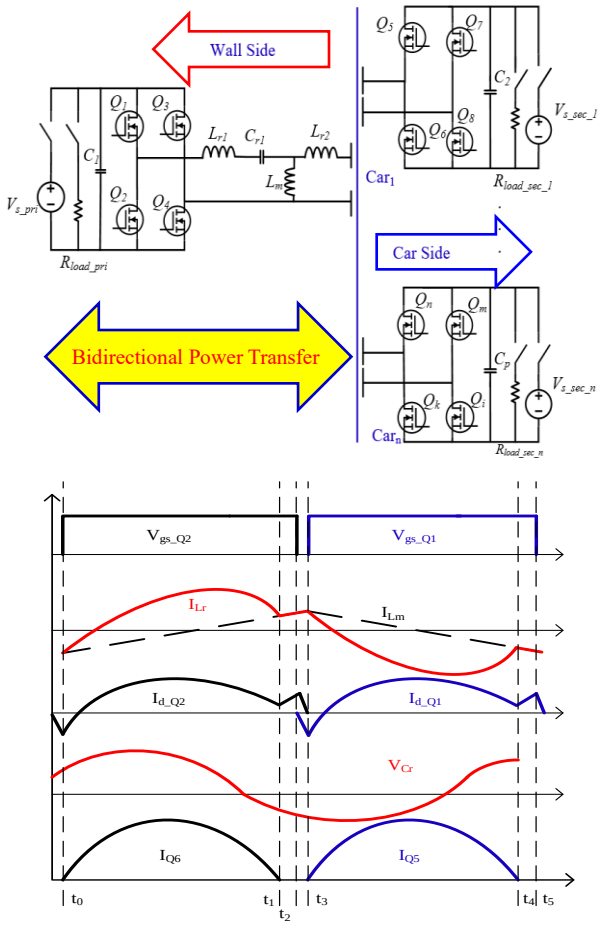

Fig. 1. Key waveforms of the proposed converter.

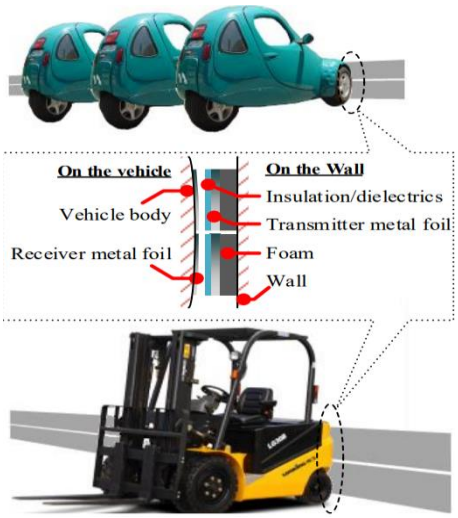

Fig. 3. A typical application of the proposed converter.

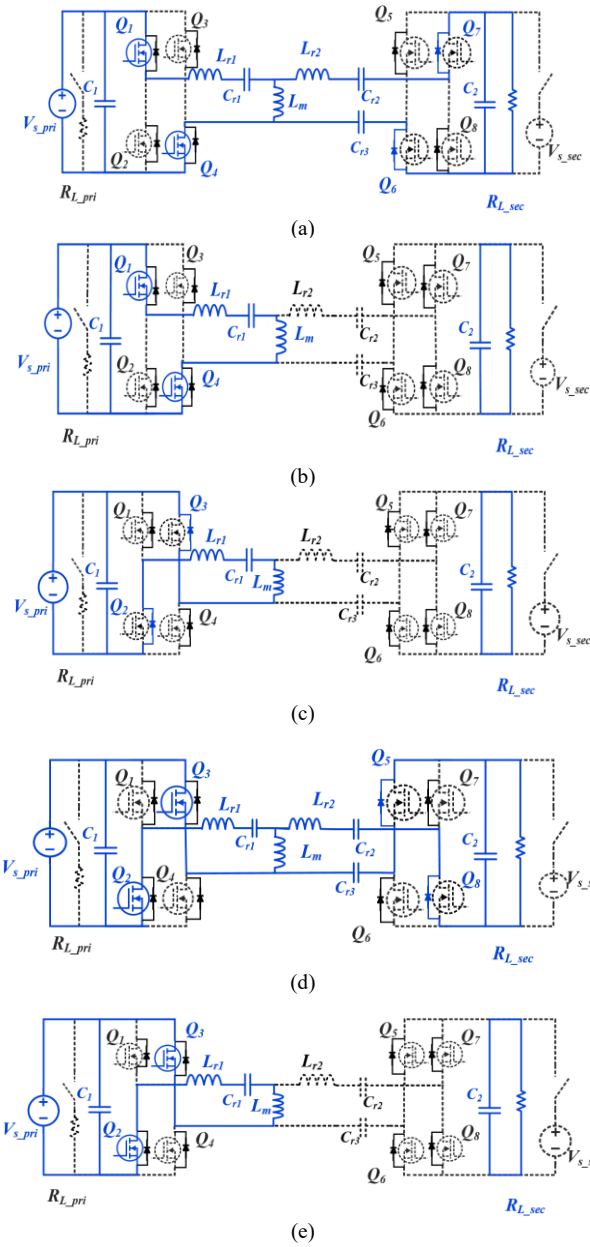

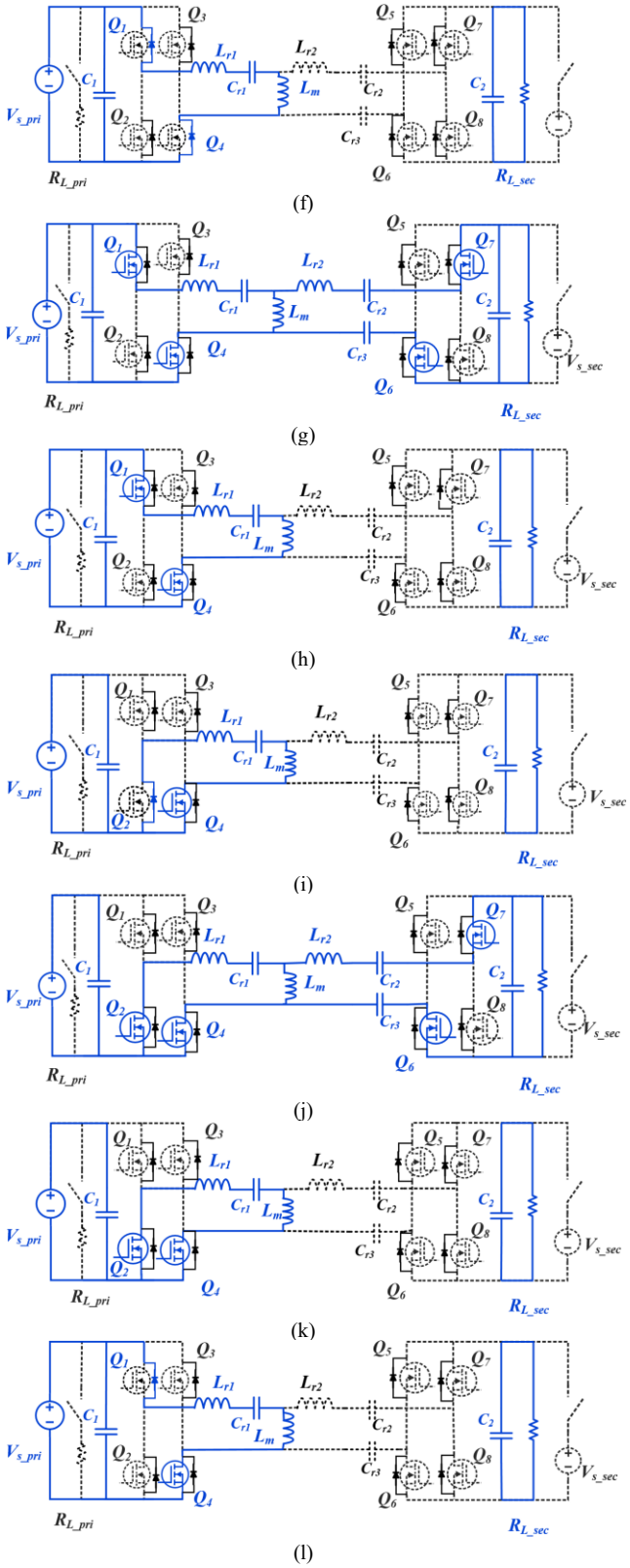

Fig. 4. Different operational states of the proposed converter in forward operation mode, (a)-(f) full-bridge configuration, and (g)-(l) half-bridge configuration.

Using the FHA approach, equivalent circuits of the converter are derived, creating a simplified framework for evaluating the converter's performance and core

characteristics. Fig. 5(a) shows the equivalent circuit of the proposed converter based on the FHA method, which reduces the complexity of the overall structure by focusing exclusively on the first harmonic components. This simplification enhances understanding and analysis of the converter's behavior. Additionally, Fig. 5(b) provides a more condensed representation of the FHA-based equivalent circuit, aiding in mathematical analysis and extraction of key converter parameters. The following equations describe the relationships between various parameters within the FHA framework:

$$\begin{cases} i_{L1}(t) = C_{r3}\dfrac{d}{dt}v_{c3}(t), \\ i_{L2}(t) = C_{r_{eq}}\dfrac{d}{dt}v_{ce}(t), \\ i_{Lm}(t) = i_{L1}(t) - i_{L2}(t). \end{cases} \quad (1)$$

$$C_{r_{eq}} = \frac{C_{r1}C_{r2}}{C_{r1}+C_{r2}}, R_{eq} = \frac{8}{\pi^2}R_L, F = \frac{f_s}{f_r}, \quad m = 1 + \frac{L_m}{L_r}. \quad (2)$$

$$\begin{cases} V_1 = \dfrac{2V_{in}}{\pi} sin(2\pi f_s t) \ \ For\ Full\ bridge, \\ V_1 = \dfrac{V_{in}}{\pi}\sin(2\pi f_s t) \ \ For\ Half\ bridge. \end{cases} \quad (3)$$

$$Q = \frac{\sqrt{L_r/C_r}}{R_e}, C_r = \frac{1}{2\pi f_s R_e Q}, L_r = \frac{1}{(2\pi f_s)^2 C_r}. \quad (4)$$

$$f_{r1} = \frac{1}{2\pi\sqrt{L_{r1}C_{r1}}}, \quad f_{r2} = \frac{1}{2\pi\sqrt{(L_{r1}+L_m)C_{r1}}}. \quad (5)$$

The first harmonic approximation strikes a balance between accuracy and complexity reduction in the analysis. Considering the given simplified equivalent circuit of the proposed converter, as shown in Fig. 5(b), we can write:

$$v_1(t) - v_{Lr1}(t) - v_{Lm}(t) - v_{c1}(t) = 0 \quad (6)$$

$$v_2(t) - v_{Lr2}(t) - v_{Lm}(t) - v_{ce}(t) = 0 \quad (7)$$

Here, Q represents the converter quality factor, F is the normalized switching frequency, and f_s is the switching frequency. Additionally, f_{r1} and f_{r2} denote the converter's first and second resonant frequencies, respectively. n also denotes the transformer turn ratio. The converter's voltage gain is derived through straightforward algebraic calculations as follows:

$$\frac{V_o}{V_{in}} = \frac{(m-1)F^2}{n\sqrt{(F^2m-1)^2 + F^2(F-1)^2(m-1)Q^2}}. \quad (8)$$

Fig. 6 shows the proposed converter voltage gain versus the normalized switching frequency in full- and half-bridge configurations, by considering (8) under different conditions.

B. Small Signal Model

In the resonant converters, absence of the DC current and voltage components across certain circuit elements of the resonant tank can complicate small-signal modeling by using the traditional methods. However, as outlined in [34], if the modulation frequency is significantly lower than the switching frequency, the resonant capacitor can be approximated as an inductor, thereby simplifying the small-signal model of the converter.

Since the proposed converter employs an LLC resonant circuit; its seventh-order model can be reduced to a third-order LLC model. Furthermore, according to [34], this third-order model can be further simplified to a second-order model, as depicted in Fig. 7, with the relevant equations derived in (9) to (15) in this section.

The frequency response of this small-signal model is shown in Fig. 8(a). To regulate the output voltage under step input voltage and load changes, a conventional Proportional-Integral (PI) controller is employed, where its frequency response is plotted in Fig. 8(b). The closed-loop system frequency response is also given in Fig. 8(c), while Fig. 8(d) shows the time-domain response of the closed-loop configuration, demonstrating robust performance under input and output disturbances. The converter with its control scheme is illustrated in Fig. 8(e), too. For simplicity, the forward conduction mode is depicted, here; however, the converter operates similarly during backward conduction mode. A microcontroller (μC) is utilized as a voltage-controlled oscillator (VCO) to implement the conventional pulse-frequency modulation (PFM) technique. The microcontroller dynamically determines whether the converter operates in its half-bridge or full-bridge operation mode depending on the output power and input voltage conditions.

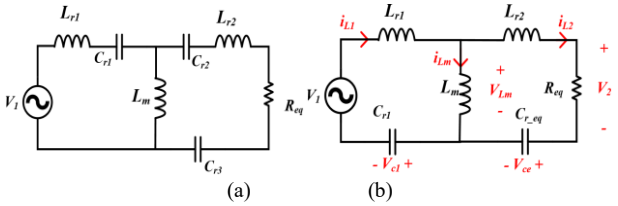

Fig. 5. (a) FHA equivalent circuit of the proposed converter and (b) its simplified equivalent circuit.

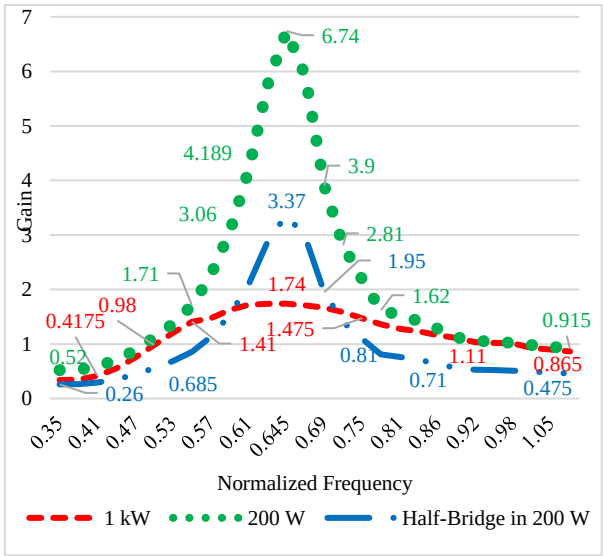

Fig. 6. Voltage gain of the proposed converter versus normalized switching frequency in the full- and half-bridge configuration.

Some key transfer functions and main parameters of the proposed converter are summarized, here, as follows:

$$G_{\omega_s}(s)=\frac{\hat{V}_o(s)}{\hat{\omega}_s(s)}=\frac{G_{DC}\left(X_{eq}^2+R_{eq}^2\right)}{\left(s^2L_e^2+sL_eR_{eq}+X_{eq}^2\right)}\times\frac{1}{\left(1+R_LC_fs\right)+R_{eq}\left(sL_e+R_{eq}\right)} \quad (9)$$

$$G_{DC}=\frac{V_g}{2n}\frac{L_n}{\omega_o\omega_n}\times\frac{\left(\frac{1}{\omega_n^2}-\omega_n^2\right)\left(\frac{\pi^2}{8}QL_n\right)^2-\left(L_n+1-\frac{1}{\omega_n^2}\right)\left(\frac{2}{\omega_n^2}\right)}{\left(\sqrt{\left(L_n+1-\frac{1}{\omega_n^2}\right)^2+\left(\left(\frac{1}{\omega_n}-\omega_n\right)\frac{\pi^2}{8}QL_n\right)^2}\right)^3} \quad (10)$$

$$L_e=\left(1+\frac{\Omega_o^2}{\Omega_s^2}\right)L_r,\ X_{eq}=\Omega_sL_r-\frac{1}{\Omega_sC_r},\ L_n=\frac{L_m}{L_r} \quad (11)$$

$$G_{v_g}(s)=\frac{\hat{V}_o(s)}{\hat{V}_g(s)}=\frac{M_{st}}{2n}\times\frac{R_{eq}^2+X_{eq}^2+L_eR_{eq}s}{\left(s^2L_e^2+sL_eR_{eq}+X_{eq}^2\right)}\times\frac{1}{\left(1+R_LC_fs\right)+R_{eq}\left(sL_e+R_{eq}\right)} \quad (12)$$

$$M_{st}=\left\|\frac{j\omega_nL_n}{j\omega_n\left(L_n+1-\frac{1}{\omega_n^2}\right)+\frac{\pi^2}{8}Q(1-\omega_n^2)L_n}\right\| \quad (13)$$

$$Z_o(s)=\frac{R_L\left(s^2L_e^2+X_{eq}^2+sL_eR_{eq}\right)}{\left(s^2L_e^2+sL_eR_{eq}+X_{eq}^2\right)}\times\frac{1}{\left(1+R_LC_fs\right)+R_{eq}\left(sL_e+R_{eq}\right)} \quad (14)$$

$$Z_{in}(s)=\frac{\pi^2}{2}\times\frac{\left(s^2L_e^2+sL_eR_{eq}+X_{eq}^2\right)}{s^2L_eC_fR_L+sL_e+sX_fR_L\frac{R_{eq}^3}{R_{eq}^2+X_{eq}^2}+R_{eq}}\times\left(1+R_LC_fs\right)+R_{eq}\left(sL_e+R_{eq}\right) \quad (15)$$

C. Power Losses Analysis

Here, power losses of the different components of the proposed converter are given, in summary.

1. Diode Power Loss

$$i_{D1}(t)=\begin{cases}nI_{Rm}\sin(\omega_rt), & 0\le t<\frac{1}{2}T_o\\ 0. & \frac{1}{2}T_o\le t<T_s\end{cases} \quad (16)$$

$$i_{D2}(t)=\begin{cases}0, & 0\le t<\frac{1}{2}T_s\\ nI_{Rm}\sin(\omega_rt), & \frac{T_s}{2}\le t<\frac{T_s+T_0}{2}\\ 0. & \frac{T_s+T_0}{2}\le t<T_s\end{cases} \quad (17)$$

Where, $\omega_r=2\pi f_r$. The average and RMS current values of each diode are respectively equal to:

$$I_{D1avg}=\frac{I_o}{2}=\frac{\pi I_o}{4}\sqrt{\frac{f_r}{f_s}},\quad I_{RMS}=\frac{\pi I_o}{2n\frac{f_s}{f_r}} \quad (18)$$

Power losses due to the forward voltage drop, V_f, and conduction resistance, r_f, of each diode are respectively equal to:

$$P_{Vf}=V_fI_{D1avg}=V_f\frac{I_o}{2}=\frac{V_f}{V_o}\frac{P_o}{2} \quad (19)$$

$$P_{rf}=I_{D1rms}^2r_f=\frac{\pi^2}{16}\frac{f_r}{f_s}\frac{r_f}{R_L}P_o \quad (20)$$

Therefore, each diode's total conduction loss is identified, easily.

$$P_D=P_{D1}+P_{D2}=\left(\frac{V_f}{V_o}+\frac{\pi^2}{8}\frac{f_r}{f_s}\frac{r_F}{R_L}\right)P_o \quad (21)$$

2. Output Capacitor Power Loss

Output capacitor current can be identified as follows:

$$I_{Co}(t)=\begin{cases}nI_{Rm}\sin(2\omega_rt)-I_o, & 0\le t<\frac{T_0}{2}\\ -I_o. & \frac{T_0}{2}\le t<T_s\end{cases} \quad (22)$$

$$I_{Co\_rms}=I_o\sqrt{\frac{\pi^2}{8}\frac{f_r}{f_s}-1} \quad (23)$$

Therefore, its power loss is given as follows:

$$P_{r_{Co}}=I_{Co_{rms}}^2r_{Co}=\left(\frac{\pi^2}{8}\frac{f_r}{f_s}-1\right)I_o^2r_{Co}=\left(\frac{\pi^2}{8}\frac{f_r}{f_s}-1\right)\frac{r_{Co}}{R_L}P_o \quad (24)$$

In addition, the following parameters are defined here to calculate each MOSFET total power loss.

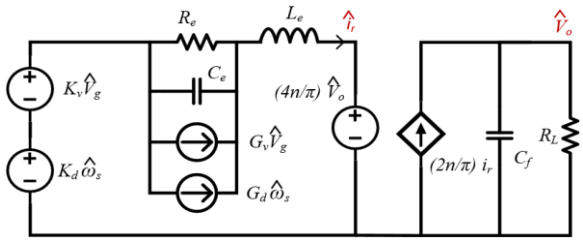

Fig. 7. Small-signal model of the proposed converter.

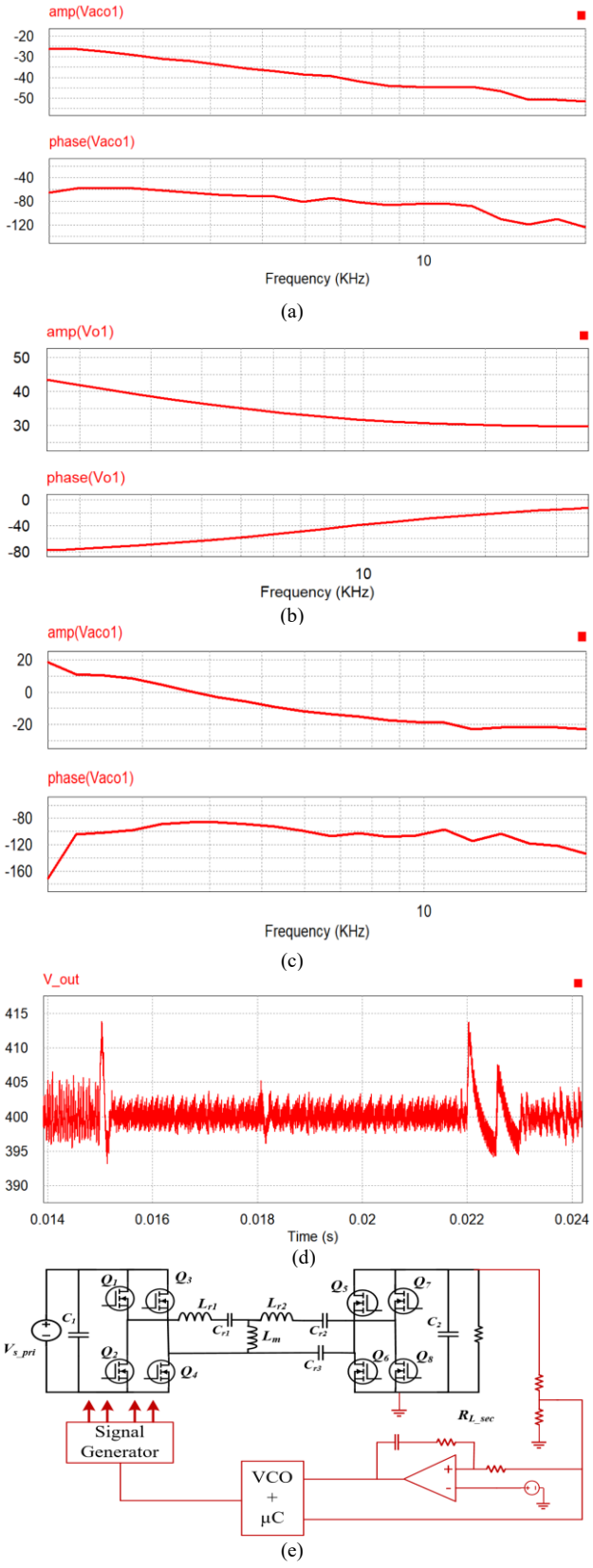

Fig. 8. Bode diagrams of proposed converter (a) without compensation, (b) PI-controller designed for the converter, (c) closed loop structure of the proposed converter, (d) simulated output voltage of the proposed converter under load and input voltage step variations, and (e) proposed converter and its control circuit in one operation mode.

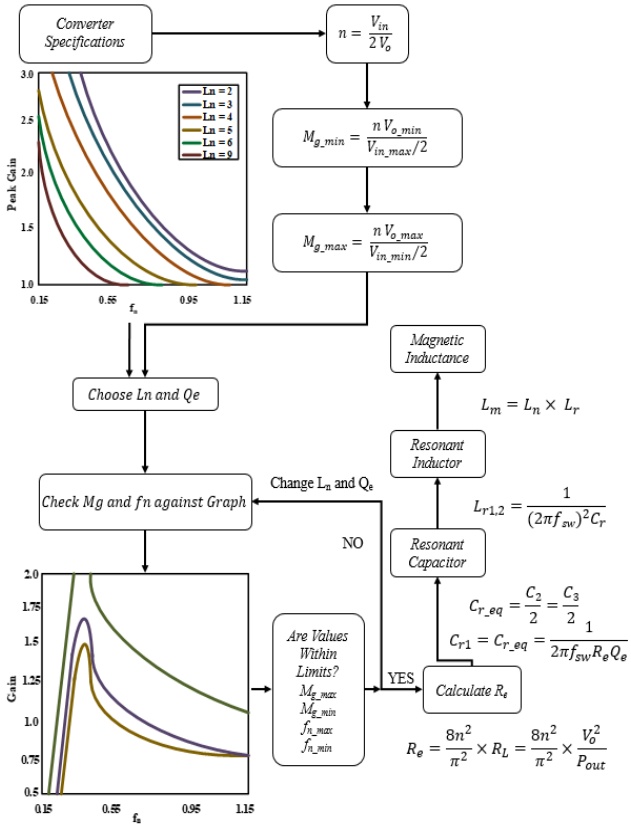

Fig. 9. Design procedure of the proposed converter.

t_{dis}: $2C_{dc}$ discharge time from input voltage to 0 V.
t_{dead}: dead-time between gate-source signals.
$t_{delay(on)}$: power MOSFET turning on the delay time.
$t_{body(on)}$: body diode conducting time.
V_{gs}: power MOSFET gate-source voltage.
V_{bF}: power MOSFET body diode forward voltage.
$t_{ds(on)}$: power MOSFET conducting time.

3. Driving MOSFET Power Loss

This loss is due to gate-source power MOSFET capacitor charge and discharge, which is given as follows:

$$P_{drive} = 2\left(\frac{1}{2}C_{gs}V_{gs}^2\right)f_s \tag{25}$$

4. Power Loss of Body Diode of Each Power MOSFET

$$t_{dis} = \frac{8}{M_g}L_m(C_{ds1} + C_{ds2})f_s \tag{26}$$

$$t_{body(on)} = t_{dead} - t_{dis} + t_{delay(on)} \tag{27}$$

$$P_{body} = 2V_{bF}\left[\left(\frac{n.V_o}{L_m}\left(\frac{1}{4}\frac{1}{f_s} - t_{dis}\right)\right)\right]t_{body(on)}.f_s \tag{28}$$

5. Power MOSFETs Turning off Power Loss

Two assumptions are made, here: the first one is in the meanwhile of power MOSFET turning off, the power MOSFET current is near the magnetizing inductor current. The second one is rising voltage and the magnetizing inductor current is linear.

$$V_{ds}(t) = V_{ds(on)} + \frac{V_{in} - V_{ds(on)}}{t_{dis}}t \tag{29}$$

$$i_{ds}(t) = \frac{nV_o}{L_m}\frac{1}{4f_s}\left(1 - \frac{t}{t_{dis}}\right) \quad (30)$$

$$p_{tf} = 2f_s \int_0^{t_{dis}} v_{ds}(t) i_{ds}(t) dt = \frac{nV_o t_{dis}\left(V_{in} + 2V_{ds(on)}\right)}{12L_m} \quad (31)$$

6. Body Diode MOSFET Power Loss

$$t_{dis} = \frac{8}{M_g} L_m (C_{ds1} + C_{ds2}) f_s \quad (32)$$

$$t_{body(on)} = t_{dead} - t_{dis} + t_{delay(on)} \quad (33)$$

$$P_{body} = 2V_{bF}\left[\left(\frac{n.V_o}{L_m}\left(\frac{1}{4}\frac{1}{f_s} - t_{dis}\right)\right)\right] t_{body(on)}.f_s \quad (34)$$

TABLE I Main Specifications of the Proposed Converter Prototype.

Parameter	Value
Input Voltage	300-500 *V*
Output Voltage	400 *V* (suitable for EV charging)
Switches	N60E23
Microcontroller	STM32F103
Gate-Drive	TC4427
Switching Frequency	470-715 *kHz*
Output Power	200-1000 *W*
C_1 , C_2	2×10 *nF*
C_3	5 *nF*
L_{r1} , L_{r2}	2×10 *μH*
L_m	14 *μH*
C_{out}	5 *μF*

IV. Design procedure

A design procedure is given here for the proposed converter to determine the optimal values of its key components to achieve the desired performance and operational characteristics. The symmetrical configuration of the proposed converter simplifies its design procedure and improves overall efficiency. Specifically, the capacitance values are chosen to establish a symmetrical structure, such that $C_{r2}=C_{r3}=2C_{r1}=2C_{r\_eq}$, and the inductance values are selected to ensure symmetry, with $L_{r1}=L_{r2}$. By adopting this symmetrical structure, the converter can be analyzed as an LLC resonant structure, where the resonant frequencies f_{r1} and f_{r3} are equal:

$$f_{r1} = \frac{1}{2\pi\sqrt{L_{r1}C_{r1}}} = f_{r3} = \frac{1}{2\pi\sqrt{L_{r2}C_{r_{eq}}}} \approx f_s \quad (35)$$

These resonant frequencies are two critical design parameters, which significantly affect the converter performance. The selection of capacitance and inductance values is based on achieving the desired resonant frequencies, which are determined by considering input and output voltage requirements, power ratings, and efficiency targets. These factors influence the choice of switches, capacitors, and inductors. Furthermore, the design methodology incorporates considerations beyond electrical specifications, such as physical layout optimization, effective thermal management, and mitigation of electromagnetic interference (EMI). This comprehensive approach aims to enhance various aspects of the converter's performance, including efficiency, compactness, cost-effectiveness, and reliability. Throughout the design phase, simulation tools, and rigorous mathematical analyses are utilized to validate the system's performance and fine-tune component values for optimal results.

The different design steps for the proposed converter are outlined in summary as follows:

Step (I) Determine the Input and Output Voltages Variation Ranges: Establish the maximum and minimum values of the input and output voltages based on the design specifications.

Step (II) Calculate Transformer Turns Ratio (n): Use the given input and output voltage values to calculate the required transformer turns ratio.

Step (III) Set Voltage Gain Boundaries: Determine the minimum and maximum voltage gain boundaries based on the design requirements and constraints.

Step (IV) Determine Quality Factor (Q) and Inductance Ratio (L_n): Calculate the necessary Q-factor and inductance ratio (L_n) using the gain-frequency characteristics of the LLC resonant converter.

Step (V) Calculate Resonant Tank Component Values: Using (4) and (5), calculate the values of the resonant tank components (i.e., L_r, L_m, and C_{r_eq}) to ensure optimal performance.

The overall design procedure is summarized in Fig. 9, which provides a visual representation of the systematic design process for the proposed converter.

V. Experimental Results

The proposed transformer-less bidirectional converter underwent a thorough experimental evaluation, combining simulation analyses with practical testing. Tailored for applications such as EV charging and Power-Wall energy storage, the converter leverages CCWPT technology to enable both step-up and step-down operation modes.

It functions efficiently between two defined resonant frequencies, ensuring seamless transitions between these operating modes. When the switching frequency surpasses the upper limit, the converter intuitively transitions from a full-bridge to a half-bridge configuration. A prototype converter, as shown in Fig. 10 and specified in Table I, is implemented and subjected to comprehensive testing under extreme conditions to validate its performance. Experimental results, detailed in Figs. 11 and 12, highlight

the converter's reliable functionality even under demanding scenarios.

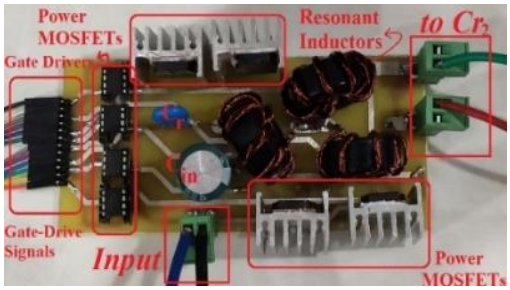

(a)

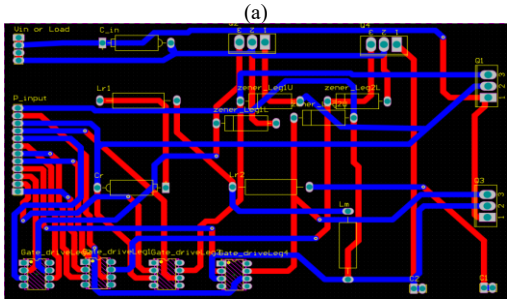

(b)

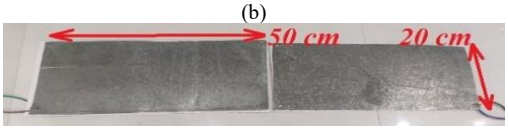

(c)

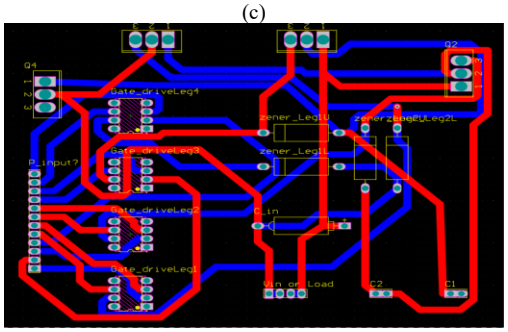

(d)

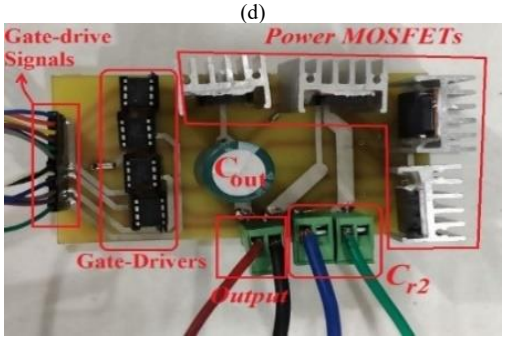

(e)

Fig. 10. Prototype of the proposed converter (a) primary section, (b) PCB of the primary section, (c) capacitors for the CCWPT part, (d) PCB of the secondary section, and (e) secondary part of the prototype converter.

The recorded waveforms from testing substantiate the system's ability to maintain stable and efficient operation across its range of applications. A detailed comparison of the proposed transformer-less bidirectional resonant converter with other EV chargers in the literature is tabulated in Table II and illustrated in Fig. 13. This analysis evaluates key performance metrics, including efficiency, operational complexity, size, cost, and reliability. Using [5], (36), and (37), this comparison highlights several distinct advantages of the proposed converter over the existing solutions, as follows for the papers in Table II:

$$\begin{cases} E_{LN} = \dfrac{\left(\frac{1}{2}L_r I_{Lr}^2\right)}{P_{max}T_s}, \\ E_{CN} = \dfrac{\frac{1}{2}C_r V_{Lr}^2}{P_{max}T_s}, \\ S_N = \dfrac{1}{P_{max}}(V_{max\,S}I_{max\,S} + V_{max\,D}I_{max\,D}). \end{cases} \tag{36}$$

$$\begin{cases} C_{relativve} = \\ \dfrac{n}{P_{max}}(3(V_{max\,S}I_{max\,S}) + V_{max\,D}I_{max\,D}) \\ n = 1 \rightarrow LOW\ \ nom.of\ Components, \\ n = 1.25 \rightarrow MED.\ nom.of\ Components, \\ n = 1.5 \rightarrow HIGH\ \ nom.of\ Components. \end{cases} \tag{37}$$

1) The bulky transformer is not used in the transformer-less architecture, which significantly reduces its size, weight, and cost as compared to the traditional transformer-based topologies [27-29, 34-37]. This reduction in physical component count not only reduces the manufacturing and maintenance costs, but also improves the power density.
2) The proposed methods use the CCWPT to ensure robust isolation between the input and output ports without requiring a magnetic transformer, simplifying the overall design and reducing electromagnetic interference (EMI).
3) The proposed converter's high efficiency is another critical advantage in comparison to [7, 12, 27, 34, 35]. Experimental validation, as shown in Fig. 14, demonstrates a maximum efficiency of up to 96%, outperforming most other solutions listed in Table II. This high efficiency is achieved through the implementation of soft-switching techniques, such as ZVS and ZCS.
4) The converter ZVS and ZCS soft-switching operations minimize the EMI noise and power switching losses that make it possible to design the converter at high switching frequencies. High-frequency operation reduces volumes of the passive components including the required filters and resonant tank components, achieving a more compact, efficient, high power density, and reliable structure, in practice. These features not only improve energy conversion performance but also reduce thermal stress on the components, extending their operational lifespan, too.
5) Furthermore, the flexibility of the proposed converter stands out in its ability to seamlessly transition between half-bridge and full-bridge configurations, which enables the converter to operate efficiently in both step-up and step-down operation modes, maintaining consistent performance across a wide range of input and output voltage conditions contrary to converters in [7, 12]. In contrast, many conventional chargers are limited to either step-up or

step-down operation, which restricts their application scope such as converters in [27-29, 34-37].

6) The ability to adapt the switching frequency within a controlled range further minimizes switching stress, enhancing reliability and operational stability.
7) Reliability and safety are other advantages of the proposed method. The converter incorporates an overload protection mechanism, which defines a safe power margin and employs current protection to prevent damage under fault conditions. This feature, combined with the compact and simplified design, ensures dependable performance even under the worst-case scenarios.

Table II demonstrates that the proposed converter outperforms others in terms of operational simplicity and robustness, making it a more viable option for practical applications. In summary, the proposed transformer-less bidirectional resonant converter offers several benefits over the other existing methods, including superior efficiency, compactness, operational flexibility, and reliability. These attributes, as highlighted in Table II and supported by experimental results, establish the proposed solution as a cutting-edge alternative for EV charging and Power-Wall applications, addressing the limitations of current technologies while meeting the demands of modern power conversion systems.

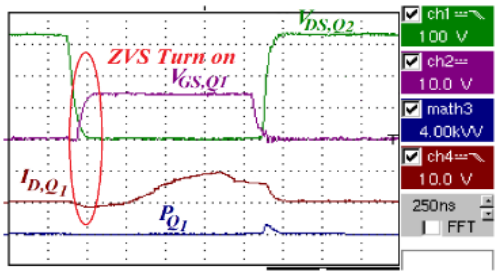

(a)

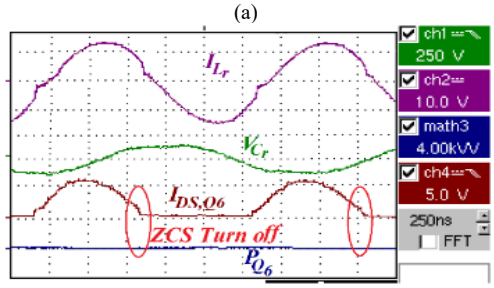

(b)

Fig. 11. Experimental open-loop waveforms of the proposed converter at 300 V input voltage and 1 kW output power: (a) gate-source voltage of Q_1, drain-source voltage of Q_2, and drain current and loss of Q_1, respectively, and (b) Current through L_r, voltage across C_r, and current and loss of Q_6, respectively.

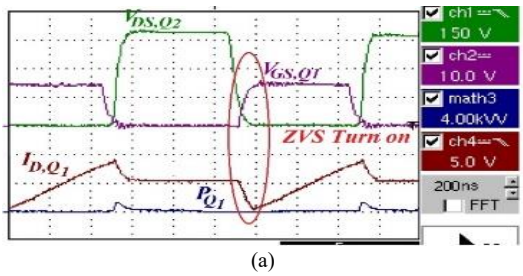

(a)

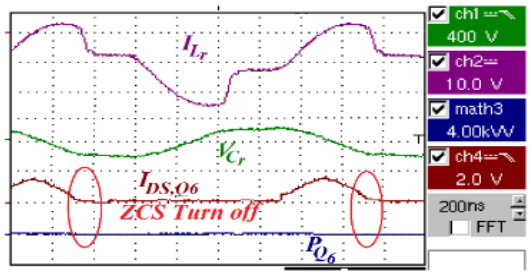

(b)

Fig. 12. Experimental open-loop waveforms of the proposed converter under 500 V input voltage and also 200 W output power values, (a) gate-source voltages of Q_1 and drain-source of Q_2, Q_1 drain current and loss, respectively, and (b) L_r current, C_r voltage, Q_6 current and its loss, respectively.

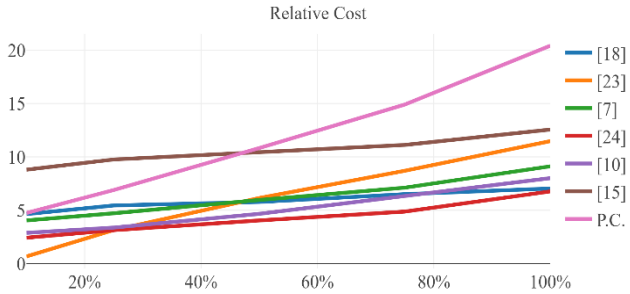

*P.C.: Proposed Converter

(a)

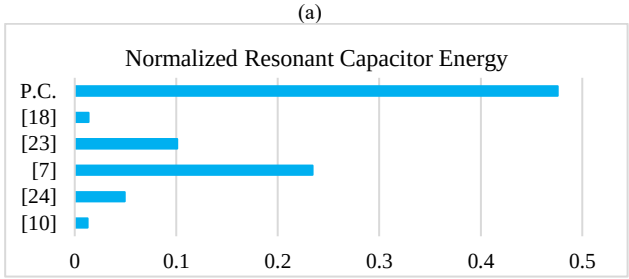

(b)

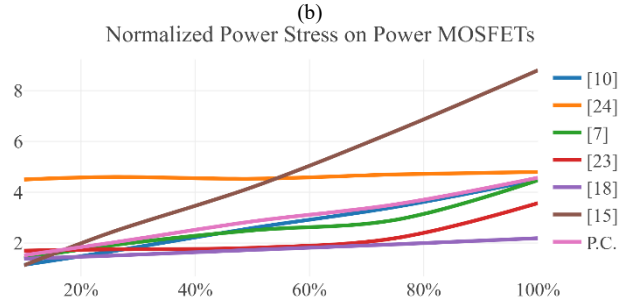

(c)

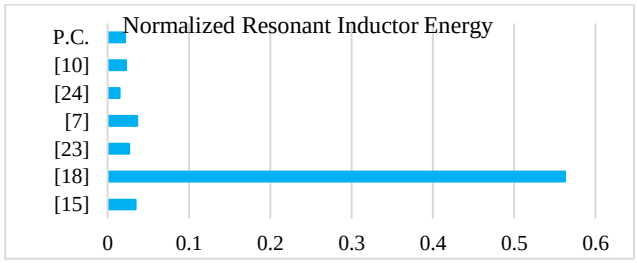

(d)

Fig. 13. Comparison of the proposed converter (P.C.) with some conventional converters including a comparison of (a) relative cost, (b) normalized resonant capacitor energy (c) normalized power stress on power MOSFETs, and (d) normalized resonant inductor energy.

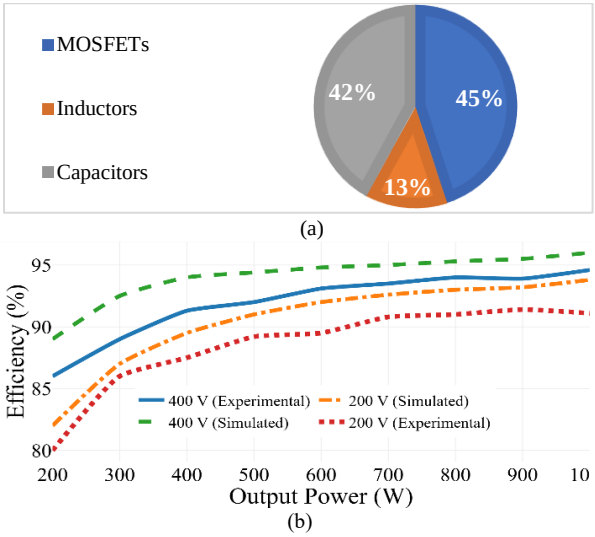

Fig. 14. (a) Power losses of the MOSFETs, inductors, and capacitors used in the prototyped converter and (b) simulated and experimental efficiency curves of the proposed converter versus output power.

VI. Conclusion

This paper proposes a novel transformer-less bidirectional resonant converter utilizing the CCWPT technique for EV charging and Power-Wall applications. By eliminating the transformer and employing capacitive coupling, the design achieves robust input-output port isolation, a maximum efficiency of 96%, reduced volume, weight, and cost, as well as high power density—addressing critical challenges in modern power conversion systems. The bidirectional functionality enables seamless integration with Power-Wall systems, supporting partial allocation of EV battery storage. The converter's ZVS and ZCS soft-switching operations, experimentally validated, minimize EMI noise and switching losses, allowing for high-frequency operation. This reduces the volume of passive components, including filters and resonant tank elements, resulting in a compact, efficient, high-power-density, and reliable design. Additionally, the converter generates sinusoidal current and voltage waveforms with low harmonic distortion, ensuring efficient power transfer across capacitive plates and magnetic components. The ability to transition between half-bridge and full-bridge configurations reduces the switching frequency range, facilitating both step-up and step-down operations with minimal switching stress. Experimental results underscore the converter's potential as an efficient and practical solution for wireless EV charging and energy storage systems, advancing the state of power electronics research.

TABLE II Comparison of the Proposed Converter with Conventional Resonant Converters

Application	Reference	Input voltage (V)	Output voltage (V)	Output power (W)	Maximum Efficiency (%)	Switching frequency (kHz)	L_r (µH)	C_r (nF)	L_m (µH)	Control complexity	Number of components
EV Charger	[34]	100	100	200	92	NM*	41	120	NM	Low	15
	[35]	400	50-450	300	94	32-100	34	70	108	Low	19
	[29]	350-400	200-700	1000	96	65-150	21	94	140	Low	14
	[28]	540	120	1500	96	100	9	2.5	17	Low	20
	[27]	400	670-800	2000	91	75-130	35.2	71	105.6	Low	18
	[36]	120	0-80	600	96	140	30	60	45	Medium	12
	[37]	400	150-450	3300	96.9	150-250	18.4	22	2× 50	Low	20
ICWPT	[7]	100	24	33	95	100	800	3	12000	Low	14
CCWPT	[12]	240	185	1000	92	1000	NM	10	NM	Medium	12
	The proposed Converter	300-500	400	1000	96	470-720	10	5	13	Low	17

* Not Mentioned

REFERENCES

[1] M. Eberhard and M. Tarpenning, "The 21 st century electric car tesla motors," *Tesla Motors*, vol. 17, 2006.

[2] P. Bulman, "Tesla's Powerwall battery production requires 'super-charged'supply chain," *Renewable Energy Focus*, vol. 16, no. 5-6, pp. 126-127, 2015.

[3] Y. Zhang, S. Chen, X. Li, and Y. Tang, "Design of high-power static wireless power transfer via magnetic induction: An overview," *CPSS Transactions on Power Electronics and Applications*, vol. 6, no. 4, pp. 281-297, 2021, doi: 10.24295/CPSSTPEA.2021.00027.

[4] F. Lu, H. Zhang, and C. Mi, "A review on the recent development of capacitive wireless power transfer technology," *Energies*, vol. 10, no. 11, p. 1752, 2017, doi: 10.3390/en10111752.

[5] J. Shahsevani and R. Beiranvand, "An Application-Oriented Review of the LLC-Based Resonant Converters," *IEEE Access*, 2024, doi: 10.1109/ACCESS. 2024.3386430..

[6] J. Shahsevani and R. Beiranvand, "A Compact, High Efficiency, and Portable Wireless EV Resonant Charger," *International Journal of Industrial Electronics Control and Optimization*, 2024, doi: 10.22111/ieco.2024.49636. 1611.

[7] T. Mohamed, A. Becetti, and S. Bayhan, "Design and analysis of full bridge LLC resonant converter for wireless power transfer applications," pp. 1-5, 2018, doi: 10.1109/CPE.2018.8372606.

[8] D. Rozario, N. A. Azeez, and S. S. Williamson, "A modified resonant converter for wireless capacitive power transfer systems used in battery charging applications," in *2016 IEEE Transportation Electrification Conference and Expo (ITEC)*, 2016: IEEE, pp. 1-6, doi: 10.1109/ ITEC.2016.7520272.

[9] H. Zhang, F. Lu, H. Hofmann, W. Liu, and C. C. Mi, "A four-plate compact capacitive coupler design and LCL-compensated topology for capacitive power transfer in electric vehicle charging application," *IEEE Transactions on Power Electronics*, vol. 31, no. 12, pp. 8541-8551, 2016, doi: 10.1109/TPEL.2016.2520963.

[10] E. Abramov, I. Zeltser, and M. M. Peretz, "A network-based approach for modeling resonant capacitive wireless power transfer systems," *CPSS Transactions on Power Electronics and Applications*, vol. 4, no. 1, pp. 19-29, 2019, doi: 10.24295/CPSSTPEA.2019.00003.

[11] M. P. Theodoridis, "Effective capacitive power transfer," *IEEE Transactions on Power Electronics*, vol. 27, no. 12, pp. 4906-4913, 2012, 10.1109/TPEL.2012.2192502.

[12] J. Dai and D. C. Ludois, "Capacitive power transfer through a conformal bumper for electric vehicle charging," *IEEE Journal of Emerging and Selected Topics in Power Electronics*, vol. 4, no. 3, pp. 1015-1025, 2015, doi: 10.1109/JESTPE.2015.2505622.

[13] S. Sinha, B. Regensburger, K. Doubleday, A. Kumar, S. Pervaiz, and K. K. Afridi, "High-power-transfer-density capacitive wireless power transfer system for electric vehicle charging," in *2017 IEEE energy conversion congress and exposition (ECCE)*, 2017: IEEE, pp. 967-974, doi: 10.1109/ECCE.2017.8095890.

[14] B. Regensburger, J. Estrada, A. Kumar, S. Sinha, Z. Popović, and K. K. Afridi, "High-performance capacitive wireless power transfer system for electric vehicle charging with enhanced coupling plate design," in *2018 IEEE energy conversion congress and exposition (ECCE)*, 2018: IEEE, pp. 2472-2477, doi: 10.1109/ ECCE.2018.8557881.

[15] F. Lu, H. Zhang, and C. Mi, "A two-plate capacitive wireless power transfer system for electric vehicle charging applications," *IEEE Transactions on Power Electronics*, vol. 33, no. 2, pp. 964-969, 2017, doi: 10.1109/TPEL.2017.2735365.

[16] S. Zou, J. Lu, A. Mallik, and A. Khaligh, "Bi-directional CLLC converter with synchronous rectification for plug-in electric vehicles," *IEEE Transactions on Industry Applications*, vol. 54, no. 2, pp. 998-1005, 2017, doi: 10.1109/TIA.2017.2773430.

[17] V.-B. Vu, M. Dahidah, V. Pickert, and V.-T. Phan, "An improved LCL-L compensation topology for capacitive power transfer in electric vehicle charging," *IEEE Access*, vol. 8, pp. 27757-27768, 2020, doi: 10.1109/ACCESS. 2020.2971961.

[18] Z. U. Zahid, Z. Dalala, and J.-S. J. Lai, "Design and control of bidirectional resonant converter for Vehicle-to-Grid (V2G) applications," in *IECON 2014-40th Annual Conference of the IEEE Industrial Electronics Society*, 2014: IEEE, pp. 1370-1376, doi: 10.1109/IECON.2014. 7048680.

[19] J.-H. Jung, H.-S. Kim, M.-H. Ryu, and J.-W. Baek, "Design methodology of bidirectional CLLC resonant converter for high-frequency isolation of DC distribution systems," *IEEE Transactions on Power Electronics*, vol. 28, no. 4, pp. 1741-1755, 2012, doi: 10.1109/TPEL.2012. 2213346.

[20] J. Min and M. Ordonez, "Bidirectional resonant CLLC charger for wide battery voltage range: Asymmetric parameters methodology," *IEEE Transactions on Power Electronics*, vol. 36, no. 6, pp. 6662-6673, 2020, doi: 10.1109/TPEL.2020.3033982.

[21] S. Toofan, B. Fathipour, and E. Babaei, "A Single Switch Transformer-Less DC-DC Converter with Continuous Input Current for Photovoltaic Applications," *International Journal of Industrial Electronics Control and Optimization*, 2024, doi: 10.22111/ieco.2024.48295. 1548.

[22] S. Hasanpour and K. Yari, "A Minimum Phase DC-DC Converter with Continuous Input Current and High Voltage Gain," *International Journal of Industrial Electronics Control and Optimization*, 2024, doi: 10.22111/ieco.2024.48842.1572.

[23] J. Shahsevani and R. Beiranvand, "A Bidirectional Resonant Converter for Capacitive Power Transmission in Electric Vehicle and PowerWall Applications," in *2023 31st International Conference on Electrical Engineering (ICEE)*, 2023: IEEE, pp. 264-270, doi: 10.1109/ICEE 59167.2023.10334783.

[24] S. Harini, N. Chellammal, and C. B. Ramesh, "Power flow and reliability analysis of a non-isolated PV/grid connected quasi resonant converter for off-board EV charging station," *International Journal of Modelling and Simulation*, 2024.

[25] F. Nasr Esfahani, A. Darwish, and X. Ma, "Design and Control of a Modular Integrated On-Board Battery Charger for EV Applications with Cell Balancing," *Batteries*, vol. 10, no. 1, p. 17, 2024.

[26] H. Sarnago and Ó. Lucía, "Design and Experimental Verification of a Bidirectional EV On-Board Charger Featuring Multi-Phase Operation in Full Power/Voltage Ranges," *IEEE Open Journal of the Industrial Electronics Society*, 2024, doi: 10.1109/OJIES.2024.3406732.

[27] S.-T. Wu and Y.-W. Chiu, "Implementation of a Bidirectional 400–800V Wireless EV Charging System,"

IEEE Access, vol. 12, pp. 26667-26682, 2024, doi: 10.1109/ACCESS.2024.3366997.

[28] R. Patel and C. K. Panigrahi, "GaN based isolated bidirectional multiport DC-DC converter for electric vehicle charging," *e-Prime-Advances in Electrical Engineering, Electronics and Energy*, vol. 8, p. 100574, 2024, doi: 10.1016/j.prime.2024.100574.

[29] Y. Yue, Y. Liu, J. Zhang, H. Zhao, and J. Yang, "Hybrid Control Method of Full-Bridge LLC Resonant Converter Based on Electric Vehicle," *IEEE Access*, 2024.

[30] R. Gopalasami and B. Chokkalingam, "A photovoltaic-powered modified multiport converter for an EV charger with bidirectional and grid connected capability assist PV2V, G2V, and V2G," *World Electric Vehicle Journal*, vol. 15, no. 1, p. 31, 2024, doi: 10.3390/wevj15010031.

[31] Z. Gholami, R. Ildarabadi, H. Heydari-Doostabad, M. Monfared, and T. O'Donnell, "Bidirectional wide range and high voltage gain buck-boost DC-DC converter for EV chargers empowering V2G-G2V applications," *IET Power Electronics*, vol. 17, no. 2, pp. 230-250, 2024.

[32] D. Pesantez, H. Renaudineau, S. Rivera, A. Peralta, A. Marquez Alcaide, and S. Kouro, "Transformerless partial power converter topology for electric vehicle fast charge," *IET Power Electronics*, vol. 17, no. 8, pp. 970-982, 2024.

[33] W. M. Utomo and A. A. Bakar, "Power converter for battery charger of electric vehicle with controllable charging current," *International Journal of Power Electronics and Drive Systems (IJPEDS)*, vol. 15, no. 2, pp. 968-977, 2024, doi: 10.11591/ijpeds.v15.i2.pp968-977.

[34] S. Hu, X. Li, and A. K. Bhat, "Operation of a bidirectional series-resonant converter with minimized tank current and wide ZVS range," *IEEE Transactions on Power Electronics*, vol. 34, no. 1, pp. 904-915, 2018, doi: 10.1109/TPEL.2018.2818145.

[35] Y. Zuo, X. Pan, and C. Wang, "A Reconfigurable Bidirectional isolated LLC Resonant Converter for Ultra-Wide Voltage-gain Range applications," *IEEE Transactions on Industrial Electronics*, 2021, doi: 10.1109/TIE.2021.3088355.

[36] K. Colak, E. Asa, M. Bojarski, and D. Czarkowski, "A novel LLC resonant converter with semi bridgeless active rectifier," in *2014 IEEE Transportation Electrification Conference and Expo (ITEC)*, 2014: IEEE, pp. 1-6, doi: 10.1109/ITEC.2014.6861808.

[37] X. Tang, Y. Xing, H. Wu, and J. Zhao, "An improved LLC resonant converter with reconfigurable hybrid voltage multiplier and PWM-plus-PFM hybrid control for wide output range applications," *IEEE Transactions on Power Electronics*, vol. 35, no. 1, pp. 185-197, 2019, doi: 10.1109/TPEL.2019.2914945.

Jasem Shahsevani received his M.Sc. degree in power electronics engineering from Tarbiat Modares University, Tehran, Iran, in 2023. His current research interests include DC/DC converter, LLC-based resonant converter, Grid-Connected inverters, wireless power transfer, electric vehicle charging, soft-switching techniques, and PV-based renewable energy systems.

Reza Beiranvand received the MSc and PhD degrees in electrical engineering from Sharif University of Technology, Tehran, Iran, in 1999 and 2010, respectively. From 2010 to 2012, he was a Postdoctoral research fellow with the Electrical Engineering College, Sharif University of Technology. From 1999 to 2007, he was an engineer at the R&D centers of PARS-Electric and RADIO SHAHAB MFGs, Tehran, Iran, where he was engaged in designing the LCD, and LED TVs based on the ST, LT, NXP, and Fairchild devices.

He is currently Head of the Power Electrical Department and Associate Professor with the Faculty of Electrical and Computer Engineering, Tarbiat Modares University, Tehran, Iran. His research interests include power electronics converters, soft switching techniques, SCCs, SMPS, Capacitive-Coupling Power Transfer and Inductive Power Transfer techniques, and PV-based renewable energy systems.

Dr. Beiranvand was the IEEE Consultant (2017-2019), Head of the Power Electrical Department (2018-2020), and Founder of the Power Electronics Converters Lab. of the Tarbiat Modares University. He is between the top 2 % scientists of the world, based on the Stanford University; Stanford, CA, USA released lists, 2020-2024.

IECO

This page intentionally left blank.

International Journal Of
Industrial Electronics Control and Optimization
Print ISSN: 3517-2645
Online ISSN: 3568-2645
Homepage: https://ieco.usb.ac.ir/

Particle Filter Design for Fuel Temperature and Precursor Concentration Estimation under Different Power Conditions in a Nuclear power plant

Hossein Zahmatkesh[1] | Hussein Eliasi[2]

Faculty of Electrical and Computer Engineering, University of Birjand, Birjand, Iran.[1,2]
Corresponding author's email: h_eliasi@birjand.ac.ir

Article Info

Article type:
Research Article

Article history:
Received: 10-November-2024
Received in revised form: 16-January-2025
Accepted:08-February-2025
Published online: 23-Sep-2025

Keywords:
Pressurized Water Reactor,
Precursors concentrations,
Kalman filter (KF),
Extended Kalman filter (EKF),
Particle filter (PF).

ABSTRACT

State estimation of nuclear reactors often plays a crucial role in accomplishing load-following control. This study presents a novel approach that leverages a weighted particle filter to address the challenges associated with estimating these crucial parameters, including relative precursor concentration (C_r) and fuel temperature (T_f), under varying reactor power conditions. A high-fidelity nonlinear dynamic reactor model was developed, incorporating noises in both process and measurement models. The proposed method was evaluated by extensive simulations under a wide range of operational scenarios. The particle filter demonstrated exceptional performance in tracking the time-varying states of the nuclear reactor. Comparative analysis with a conventional Kalman filter and the extended Kalman filter revealed the superior robustness of the particle filter in handling nonlinearities inherent in nuclear systems. The proposed approach offers several advantages, including the ability to capture multimodal distributions, handle non-Gaussian noise, and provide probabilistic estimates. Despite the increased computational cost associated with particle filtering, the benefits in terms of estimation accuracy and reliability justify its application in nuclear power plant monitoring and control systems.

I. Introduction

Nuclear power plants are essential to the global energy landscape, providing a reliable and low-carbon source of electricity. However, these complex systems exhibit nonlinear behaviors, making their operation intricate and demanding precise control. Parameters such as precursor concentration and fuel temperature are crucial for maintaining reactor stability and preventing accidents. Accurate estimation of these parameters is vital for optimizing plant performance, ensuring safety, and extending the lifespan of nuclear fuel. By leveraging advanced modeling techniques and real-time monitoring, engineers can gain valuable insights into the reactor's internal state, enabling proactive decision-making and timely interventions [1].

Precursor concentration and fuel temperature play a pivotal role in reactor dynamics, influencing factors such as reactivity, power distribution, and thermal-hydraulic conditions. However, the radioactive environment within the reactor core renders direct measurement of these quantities exceedingly difficult, if not impossible. Consequently, advanced estimation techniques, such as those based on mathematical models and statistical inference, are essential for inferring these critical states from available sensor measurements. By employing these techniques, we can gain valuable insights into the reactor's internal state, enabling proactive monitoring, control, and decision-making, ultimately enhancing both safety and operational efficiency [2].

Jiuwu Hui [3] researched the application of the Extended State Observer (ESO) for regulating power levels in nuclear power plants. The study aimed to create a control strategy that integrates ESO with Adaptive Dynamic Sliding Mode Control (ADSMC) techniques. This ESO-ADSMC approach effectively tackles the challenges posed by the dynamic behavior and uncertainties inherent in nuclear power plant operations. Qadeer and Bhatti [4] introduced an innovative

Copyright © H. Eliasi (S)
Publisher: University of Sistan and Baluchestan

technique to estimate the states of automotive engines through a super-twisting second-order sliding mode observer. This observer demonstrated exceptional accuracy in estimating the dynamic states of the system, effectively handling variations and disturbances that may arise during operation.

Jiuwu Hui and Jingqi Yuan [5] suggested the application of a particle filter for accurate linear state estimation in the presence of perturbations within a modular high-temperature gas-cooled reactor. This approach leverages a set of particles to effectively capture and address uncertainties and disturbances, representing the potential states of the system. In 2019, Dong et al. [6] proposed an adaptive state observer designed to estimate the concentrations of poisons in nuclear power plants. This innovative approach utilizes adaptive algorithms to continuously refine estimations by incorporating real-time measurements and the dynamics of the system. In 2018, Ansarifar et al. [7] employed a Higher-Order Sliding Mode Observer (HOSMO) in a Pressurized Water Reactor (PWR) to estimate the nonlinear dynamics of poisons present in a nuclear power plant. The development of the HOSMO, focused on xenon concentration, requires the formulation of a control strategy aimed at maintaining stable and accurate reactor performance in response to varying power demands. Wang et al. [8] explored the application of Artificial Neural Networks (ANNs) to estimate poison concentrations in nuclear power plants. They developed an ANN model by training it with historical operational data, which was then employed for real-time estimation of poison concentrations. Zhe Dong et al. [9] utilized a high-order ESO as a state estimation method to assess state variables and disturbances within energy systems. They particularly focused on nuclear reactors. Koul et al. [10] explored the use of the Rao-Blackwellized unscented Kalman filter for adaptive state estimation in nuclear reactors. This approach merges the advantages of the unscented Kalman filter with the Rao-Blackwellization principle, thereby improving the accuracy and adaptability of state monitoring. In 2015, an Extended Kalman Filter (EFK) was designed by Ansarifar et al. [11]. They used the EKF approach to estimate the poison concentrations and precursor density in a nuclear power plant with three groups of delayed neutrons.

In [12], a study was conducted to estimate dynamic variables in power systems using various Bayesian filters, including the EKF, unscented Kalman filter, ensemble Kalman filter, and particle filter. The study identified that while some filters excelled in accuracy, others offered greater robustness under noisy conditions, highlighting trade-offs in effectiveness and computational complexity. In [13], a novel method was introduced for estimating adhesion in rail systems, combining an EKF with particle swarm optimization. This approach addresses the challenges associated with adhesion estimation and shows that the application of artificial intelligence and machine learning techniques can improve accuracy, offering potential advantages for the rail transport industry. In [14], a novel linear parameter varying estimator was developed to estimate the hydrazine molar concentration in the secondary circuit of nuclear power plants. The proposed method utilizes dynamic shaping filters of arbitrary order to define estimation performance objectives, leveraging L_2-gain synthesis based on uncertainty characterization through static integral quadratic constraint multipliers. In [15], a study was conducted to develop a novel approach for reactor power level control in PWRs by integrating Nonlinear Generalized Predictive Control (NGPC) with an EKF. The research demonstrated that this NGPC + EKF methodology could effectively address the challenges of nonlinearity, model mismatch, and noise and significantly enhance the reliability and performance of nuclear reactor control systems. This innovative approach represents a valuable advancement in nuclear engineering.

By incorporating the particle filter approach into our estimation framework, we aim to address the difficulties related to the precise estimation of fuel temperature and precursor concentrations within a nuclear power plant setting. Our research seeks to enhance both the accuracy and reliability of these concentration estimates significantly. The results from our simulations provide strong support for the effectiveness of the proposed observer. Additionally, a comprehensive assessment of the particle filter, along with the Kalman filter and EKF, demonstrates significant improvements in tracking actual system variables and greater resilience to noises. The particle filter, in particular, shows exceptional capabilities in effectively mitigating noises, illustrating its superior performance [16].

The article is organized into a structured framework as follows: Section II introduces a comprehensive mathematical model for the PWR. Section III provides detailed design procedures for the KF, EKF, and PF algorithms with a focus on the estimation of the states within the PWR system. Section IV presents numerical simulations that assess and compare the estimation performance of the different approaches. Finally, Section V concludes with a summary of the key findings.

II. PWR Formulation

A nuclear reactor model is a sophisticated mathematical representation that encapsulates the physical characteristics and dynamic behavior of a nuclear reactor system. These models are vital for simulating the performance of nuclear reactors under various operational scenarios, providing insights into their efficiency, safety, and overall functionality. The development of these models typically involves a blend of fundamental physical principles, empirical data, and engineering approximations to accurately capture the intricacies of reactor operation [17].

Assumption 1: The groups of precursors are considered as a single group. This assumption is made to simplify the model and facilitate the analyses, which will allow for the examination of the overall behavior of these groups rather than the separate effects of the individual precursors.

A. Representation of PWR Equations

In nuclear power plants, the term "neutronics" pertains to the investigation of neutron behavior and interactions within the reactor core. The dynamics of neutrons are governed by a series of equations known as the neutron transport equations. These equations detail the movement of neutrons through the reactor core while considering factors such as neutron production, absorption, scattering, and leakage. A one-point kinetic nuclear reactor model is mathematically represented by the following equations [18], [19]:

$$\frac{dn_r}{dt} = \frac{(\rho - \beta)}{\Lambda} n_r + \frac{\beta}{\Lambda} C_r \tag{1}$$

$$\frac{dC_r}{dt} = \lambda n_r - \lambda C_r \tag{2}$$

where n_r denotes the relative changes in neutron density compared to its initial value, C_r is the delayed neutron precursor concentration, normalized with respect to its initial value, β and λ denote one group delayed neutron yield and decay constant, respectively, and Λ denotes prompt neutron lifetime. Reactor nominal power is outlined below:

$$p(t) = p_0 n_r \tag{3}$$

where p_0 denotes the first changes in reactor power level. Xenon poison is the most significant poison in nuclear reactors. For a one-dimensional model of a nuclear reactor core, the fluctuations of this poison can lead to a power plant shutdown. The production rate of this poison has a significant effect on the power of the reactor. The equations of poisons in the nuclear power plant, which include I-135 and X-135, can be expressed as follows [20]:

$$\frac{dI}{dt} = \gamma_I \Sigma f \phi - \lambda_I I \tag{4}$$

$$\frac{dX}{dt} = (\gamma_x \Sigma f - \sigma_x X)\phi - \lambda_x X + \lambda_I I \tag{5}$$

where I and X denote iodine and xenon concentrations respectively, σ_x denotes microscopic thermal neutron absorption cross-section of xenon, γ_x and γ_I denote xenon and iodine yield per fission and λ_x and λ_I denote xenon and iodine decay constants, respectively, Σf represents the macroscopic fission cross-section, and ϕ is the neutron flux represented as follows:

$$\phi = \upsilon n_0 n_r \tag{6}$$

where υ and n_0 denote the mean velocity of thermal neutron and initial equilibrium neutron density, respectively. By incorporating the influence of both fuel and coolant temperatures, it is possible to construct a simplified lumped parameter model to analyze thermal transients. The presented model is outlined as follows: [21], [22]:

$$\frac{dT_f}{dt} = \frac{1}{\mu_f}\left[f_f p - \Omega(T_f - T_C)\right] \tag{7}$$

$$\frac{dT_C}{dt} = \frac{1}{\mu_c}\left[(1 - f_f)p + \Omega(T_f - T_C) - 2M(T_C - T_{in})\right] \tag{8}$$

where T_f, T_C and T_{in} are fuel temperature, coolant average temperature, and coolant inlet temperature, respectively. The parameter f_f is a fraction of reactor power deposited in the fuel. Also, μ_f , μ_c, Ω, and M are the total heat capacity of the fuel, the total heat capacity of the coolant, the heat transfer coefficient between fuel and coolant, and the mass flow rate multiplied by the heat capacity of the coolant, respectively. The reactivity model ρ of a PWR is influenced by the control rod movement, xenon, and temperature feedback. This model includes the sum of three components where $\delta\rho_{ext}$ represents reactivity caused by control rod movement, $\delta\rho_T$ denotes thermal reactivity feedback referring to the change in reactivity due to changes in temperature, and $\delta\rho_X$ denotes variations in xenon concentration which lead to alterations in feedback reactivity. The one-point reactivity model is depicted as follows:

$$\rho = \delta\rho_{ext} + \delta\rho_T + \delta\rho_X \tag{9}$$

where

$$\frac{d(\delta\rho_{ext})}{dt} = G_r Z_{rod} \tag{10}$$

$$\delta\rho_T = \alpha_f(T_f - T_{f0}) + \alpha_C(T_C - T_{C0}) \tag{11}$$

$$\delta\rho_X = -\frac{\sigma_X(X - X_0)}{\sum f} \tag{12}$$

where G_r and Z_{rod} denote the total reactivity of the control rod and control rod speed. α_f and α_C denote the thermal reactivity coefficient of the fuel and coolant, respectively. T_{f0}, T_{C0} and X_0 denote the initial conditions of fuel temperature, liquid coolant temperature, and xenon, respectively. The above equations should be written as (13-18) to adhere to the framework of state equations [12].

$$\dot{x} = f_C(x, u) + w_c$$
$$y = h_C(x, u) + v_c \tag{13}$$

$$E[w_c w_c^T] = Q \tag{14}$$

$$E[v_c v_c^T] = R \tag{15}$$

$$x = [n_r, C_r, I, X, T_f, T_c, \delta\rho_{ext}]^T \tag{16}$$

$$u = Z_{rod} \tag{17}$$

$$y = n_r \tag{18}$$

where x is the state vector, y is the output vector, u is the input vector, the functions fc and hc represent the state and output equations, respectively, and the subscript c indicates

TABLE I NOMENCLATURE

Parameters	Symbols
Initial neutron density	n_{r0}
Initial nominal power	p_0
Initial equilibrium neutron density	n_0
Mean velocity of thermal neutron	v
Effective prompt neutron lifetime	Λ
Fraction of delayed neutron production	β
Radioactive decay constant	λ
I-135 decay constants	λ_I
X-135 decay constants	λ_x
Total reactivity of the control rod	G_r
Fuel total heat capacity	μ_f
Coolant total heat capacity	μ_c
Fraction of reactor power deposited in the fuel	f_f
Inlet coolant temperature	T_{in}
Macroscopic fission cross-section	Σ_f
I-135 yield per fission	γ_I
X-135 yield per fission	γ_x
Combined effect of mass flow rate and heat capacity of the coolant	M
Heat transfer coefficient fuel-to-coolant	Ω
X-135 microscopic absorption cross-section	σ_x
Thermal reactivity coefficient of fuel	α_f
Thermal reactivity coefficient of coolant	α_C
Initial condition of liquid coolant temperature	T_{c0}
Initial condition of fuel temperature	T_{f0}
Initial condition of xenon	X_0
Control rod speed	Z_{rod}
Average liquid coolant temperature	T_c
Fuel temperature	T_f
Xenon concentration	X
Iodine concentration	I
Neutron flux	Φ

TABLE II VALUES OF THE PWR PARAMETERS

Symbols	Values	Units
n_{r0}	1	-
p_0	2500	MW
n_0	$\frac{p_0}{2500} \times (2.5 \times 10^8)$	-
v	2.2×10^5	cm/s
Λ	2×10^{-5}	s
β	6.019×10^3	-
λ	0.150	s^{-1}
λ_I	2.88×10^{-5}	s^{-1}
λ_x	2.08×10^{-5}	s^{-1}
G_r	14.5×10^{-3}	-
μ_f	26.3	$MW.s/℃$
μ_c	$\left(\frac{160}{9} n_{r0} + 540\right)$	$MW.s/℃$
f_f	0.92	-
T_{in}	291.3	℃
Σ_f	0.3358	cm^{-1}
γ_I	0.0639	-
γ_x	0.00228	-
M	$(28 \times n_{r0}) + 74$	$MW.C^{-1}$
Ω	$\left(\frac{5}{3} n_{r0} + 4.93\right)$	$MW.C^{-1}$
σ_x	2.36×10^{-18}	cm^2
α_f	$(n_{r0} - 4.24) \times 10^{-5}$	$\frac{\delta k}{k}$ /℃
α_C	$(-4n_{r0} - 17.3) \times 10^{-5}$	$\frac{\delta k}{k}$ /℃
T_{c0}	303.55	℃
T_{f0}	653.80	℃
X_0	8.11×10^{15}	-

the continuous state. w_c and v_c are the process and output noises, respectively, which are modeled as Gaussian (with zero means), and their covariance matrix is defined according to Eq. (14) and (15), respectively, where $E[.]$ is the statistical math expectation. All the parameters of PWR have been described in Table I. Also, Table II presents the parameter values of the reactor model.

B. Discretization of PWR Equations

To implement the proposed filters, the continuous equations of the nuclear reactor must first be discretized [23]. In order to make the equations discrete, the definition of the derivative for the variable x is used as described in Eq. (19).

$$\dot{x} = \frac{x(k) - x(k-1)}{\Delta t_s} \rightarrow x(k) = x(k-1) + \dot{x}\Delta t_s \quad (19)$$

where Δt_s is sampling interval and k and $k-1$ are the same as $k\Delta t_s$ and $(k-1)\Delta t_s$. By substituting the aforementioned relationship into the state matrix equations, we arrive at Eq. (20) as follows:

$$x(k) = x(k-1) + \Delta t_s \times (f_C(x,u) + w_c) \quad (20)$$

By simplifying Eq. (20), we obtain the following relation:

$$\begin{aligned} x_k &= f(x_{k-1}, u_{k-1}) \times \Delta t_s + x_{k-1} + w_{k-1} \\ y_k &= h(x_k, u_k) + v_k \end{aligned} \quad (21)$$

the above equations represent the discretized form of a nuclear power plant, which is used to implement the proposed filters.

III. Preliminary

This section will explore the Kalman filter, the EKF, and the particle filter, which are used to estimate precursor concentration and fuel temperature.

A. Kalman filter

This method is a computational technique based on mathematical principles, designed to accurately estimate the true states of a system by integrating predictions from a mathematical model with sensor measurements. The method consists of two fundamental steps: prediction and update. In the prediction step, the previous state estimate and the system model are utilized to project the current state forward in time, incorporating information about the system's dynamics to create an expected state prediction. During the update process, the Kalman filter computes the Kalman gain, which determines the appropriate weight to be assigned to

the new measurement data versus the predicted state estimate. The steps of the KF method for the nonlinear PWR dynamics are outlined as [24], [11]:

Prediction step:

In Eq. (22) and (23), the state and covariance matrix of the states are predicted.

$$\hat{x}_k^- = A_k \hat{x}_{k-1} + B_k u_k \quad (22)$$

$$P_k^- = A_k P_{k-1} A_k^T + Q_d \quad (23)$$

$$\hat{x}(0) = \bar{x}_0 \quad P(0) = P_0 \quad (24)$$

where $\hat{x}_k^-$ is the prediction at the current time, $\hat{x}_{k-1}$ denotes the state estimation at time $k-1$, Parameter Q_d depicts the process covariance noise, P_k^- represents the covariance matrix which is predicted from the prediction step, parameters $\bar{x}_0$ denotes the initial mean, and P_0 represents the initial covariance estimation error.

Update step:

$$\tilde{y}_k = y_k - H\hat{x}_k^- \quad (25)$$

$$K_k = P_k^- H^T (H P_k^- H^T + R_k) \quad (26)$$

$$\hat{x}_k = \hat{x}_k^- + K_k \tilde{y}_k \quad (27)$$

$$P_k = (I - K_k H) P_k^- \quad (28)$$

where H is the measurement matrix. $\tilde{y}_k$ signifies the deviation of the observed measurement y_k, and the predicted measurement $H\hat{x}_k^-$. The measurement noise covariance is R_k. Kalman gain, denoted by K_k, determines the weight or importance given to the measurements relative to the predicted state estimate, $\hat{x}_k$ represents the state estimation, which is adjusted using the Kalman gain and residual measurement, and P_k is the updated covariance matrix of errors. The given nonlinear model is approximated linearly around the operating conditions (equilibrium point): x_{eq_k} and u_{eq_k}. A_k denotes the transfer function of states, B_k is the input matrix applied to the input vector u_k. A_k and B_k are outlined below:

$$A_k = \left.\frac{\partial f}{\partial x}\right|_{x_{eq_k}, u_{eq_k}} \quad B_k = \left.\frac{\partial f}{\partial u}\right|_{x_{eq_k}, u_{eq_k}} \quad (29)$$

where $f(.)$ is a function of the states and input of the system mentioned in Eq. (21).

B. Extended Kalman filter (EKF)

The previously described Kalman filter relied on linearization at the equilibrium point, which renders the A_k and B_k matrices invalid. To address this issue, an EKF is employed. The EKF is a widely used technique for state estimation, operating iteratively to estimate system dynamics from a series of noisy measurements. It consists of two main stages: prediction and update. In the prediction phase, the state estimate and its covariance are advanced in time by applying the nonlinear system dynamics. Then, during the update phase, the projected state estimate is adjusted using the new measurement data. This adjustment utilizes the Kalman gain, which is calculated through the linearization of the system and measurement equations [25]. As outlined by the modified Euler's discretization presented in Eq. (21), the EKF estimation process consists of two key steps: prediction and update. The equations governing the EKF are defined as follows [25]:

Prediction step:

$$\hat{x}_k^- = f(\hat{x}_{k-1}, u_{k-1}) + w_{k-1} \quad (30)$$

$$P_k^- = F_{k-1} P_{k-1} F_{k-1}^T + Q_d \quad (31)$$

Update step:

$$\tilde{y}_k = y_k - h(\hat{x}_k^-, u_k) \quad (32)$$

$$K_k = P_k^- H^T (H P_k^- H^T + R_k) \quad (33)$$

$$\hat{x}_k = \hat{x}_k^- + K_k \tilde{y}_k \quad (34)$$

$$P_k = (I - K_k H) P_k^- \quad (35)$$

where $\tilde{y}_k$ represents the measurement residual, y_k and $h(\hat{x}_k, u_k)$ indicate measurement and estimated measurement, respectively, K_k represents the estimator gain, $\hat{x}_k$ and P_k represent updated states and covariance estimates, respectively, F_k represents the variables transition jacobian, and H_k denotes the observation jacobian expressed as follows:

$$F_k = \left.\frac{\partial f(x_k, u_k)}{\partial x}\right|_{\hat{x}_k^-, u_{k-1}} \quad (36)$$

$$H_k = \left.\frac{\partial h(x_k)}{\partial x}\right|_{\hat{x}_k^-, u_k} \quad (37)$$

C. Particle filter

According to the approaches reviewed in the previous sections, in the Kalman filter, matrices A_k and B_k are constants. So, if the equilibrium point changes, matrices A_k and B_k cannot be used anymore. On the other hand, in the EKF, if the accurate mathematical model of the system is not available, it may be difficult to estimate the states. Therefore, in order to improve the state estimation according to the mentioned limitations, a PF is evaluated for precursor concentration and fuel temperature estimations.

the particle filter is a state estimation technique used for nonlinear systems with high-dimensional state spaces. It estimates the state's posterior probability distribution by using a set of particles. Each particle represents a potential system state, and its weight indicates the likelihood of that state being true. The particle filter overcomes the limitations of the KF and EKF by employing resampling with replacement, addressing particle degeneracy, improving computational efficiency, and providing a better representation of the posterior distribution, particularly in high dimensional spaces. The particle filter utilizes a set of discrete samples with associated weights to approximate a probability distribution function. This representation is described as follows [26], [27]:

$$P(x_k|y_k) \approx \sum_{i=1}^{N} [W_k^i \tilde{\delta}(x_k - x_k^i)] \quad (38)$$

Eq. (38) represents the posterior distribution $P(x_k|y_k)$ of the state x_k given the observations y_k in the context of a particle filter. The equation approximates this posterior distribution as a sum of contributions from N particles, represented by the index i. Each particle x_k^i is assigned a weight W_k^i, reflecting how likely that particle is given the observations. These weights are updated at each time step to ensure that the particles representing more probable states are emphasized in the approximation and correspond to:

$$\sum_{i=1}^{N} W_k^i = 1 \quad (39)$$

The delta function $\tilde{\delta}(x_k - x_k^i)$ signifies that each particle contributes to the posterior only when the current state x_k matches the value of the particle x_k^i. This allows for the representation of the posterior as a weighted sum of discrete points in the state space. This formulation effectively captures the complexities of the posterior distribution in nonlinear and non-Gaussian systems using a finite number of particles. Each particle serves as a sample of the possible states, allowing for flexible and robust estimation of the state variable x_k based on the observations y_k. The PF algorithm is succinctly outlined as follows:

Initialization: Start with a collection of samples $\{x^i(0)\}_i^N$ that are stochastically selected from initial state distribution $P(0)$ and let $W_k^i = 1/N,\ i = 1, \dots, N$.

Prediction: For each particle, propagate it forward in time using the system dynamics. This involves applying the state transition function to each particle, considering the process noise. The prediction stage is outlined as:

$$x_k^i = f(x_{k-1}^i, u_{k-1}) + w_{k-1}^i \quad (40)$$

In (40), w_{k-1}^i indicates white noise with covariance Q.

Update: Calculate the weight of each particle based on how well it matches the new measurement, which is done using the measurement model and the current measurement. The update step consists of two parts: particle weight and normalization, which are expressed as follows:

Particle weight:

$$W_k^i = P(y_k|x_k^i) W_{k-1}^i \quad (41)$$

Normalization:

$$W_k^i = \frac{W_k^i}{\sum_{i=1}^{N} W_k^i} \quad (42)$$

Resampling:

$$\frac{1}{\sum_{i=1}^{N} W_k^i} < N_{eff_{th}} \quad (43)$$

Resample the particles with replacement, based on their weights. This step aids in discarding particles with diminished weights, thus prioritizing states with higher likelihoods, $N_{eff_{th}}$ is a predetermined threshold and let $W_k^i = 1/N,\ i = 1, \dots, N$.

State estimation:

$$\hat{x}_k = \sum_{i=1}^{N} [x_k^i W_k^i] \quad (44)$$

Set $k = k + 1$ and repeat the process from step (b).

Assumption 2: It is assumed that the measurement and process noise are Gaussian distributed, which is a common assumption in filtering techniques.

IV. Simulation Results

This section compares the designed Kalman Filter (KF) and EKF [11] in the presence of process and measurement noises for a PWR to demonstrate the superiority of the designed Particle Filter (PF). A feedback linearization controller was implemented to regulate the system dynamics, and numerical simulations were carried out using MATLAB/Simulink. Three scenarios for power level changes were considered to evaluate the estimation approaches. To evaluate the performance of the KF, EKF, and PF, three error detection criteria were employed: Integral Absolute Error (IAE), Mean Error (ME), and Root Mean Square Error (RMSE). This section summarizes the assessment of these filters for state estimation. Metrics such as ME, IAE, and RMSE were used to gauge transient estimation and steady-state accuracy. So, 200 particles were used for simulation in the PF. All system initial conditions are deviated by 5% from their nominal values.

$$IAE = \int_0^{\Phi} |e(.)| dt \quad (45)$$

$$ME = \frac{1}{s} \sum_{i=1}^{s} e_i \quad (46)$$

$$RMSE = \sqrt{\frac{1}{s} \sum_{i=1}^{s} (y^i - \hat{y}^i)^2} \quad (47)$$

The symbol ϕ represents total simulation time, while $e(.)$ represents the error of estimation associated with it. Parameter s represents sample size, and y^i and $\hat{y}^i$ indicate the true and predicted values, respectively.

A. The First Scenario

In the first scenario, the reactor is initially operating at its nominal power level, representing an equilibrium state. At the 18-second mark, the power level is decreased to 80% of the nominal value. Subsequently, at the 108-second mark, the power level is increased back to the nominal value. Fig. 1 shows the first power level changes in the nuclear power plant. Figs. 2 and 3 compare the estimated and actual values of the precursor concentration and fuel temperature for the three filters described in Section III.

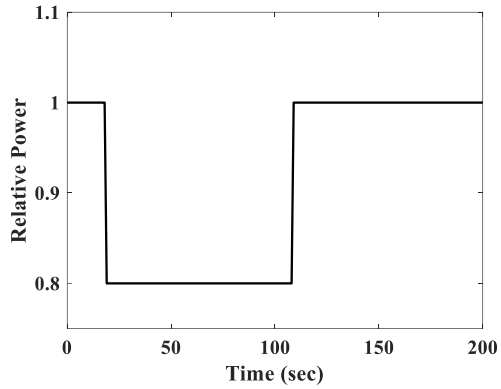

Fig. 1. Relative power changes in the first scenario

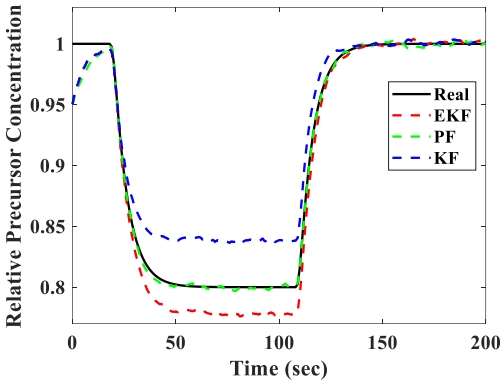

Fig. 2. Precursor concentration estimation with three studied filters

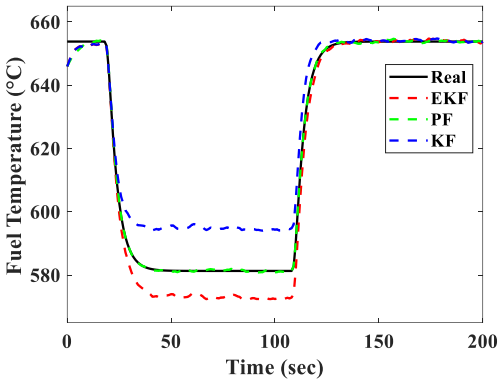

Fig. 3. Fuel temperature estimation with three studied filters

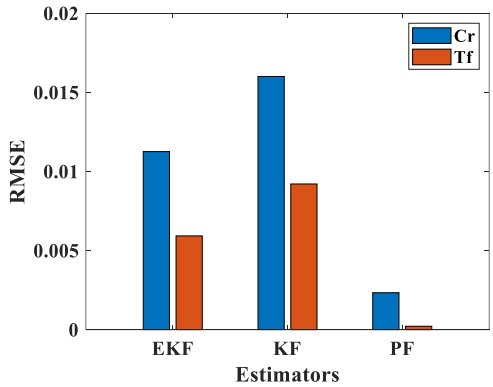

Fig. 4. Comparing RMSE of studied filters in the first scenario

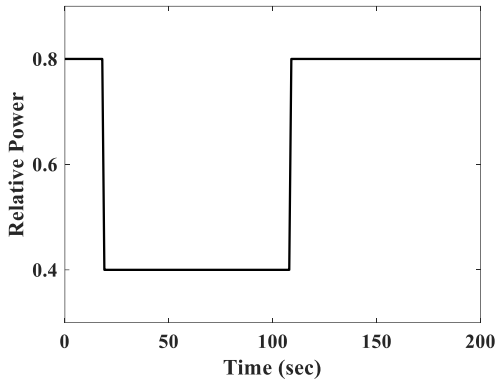

Fig. 5. Relative power changes in the second scenario

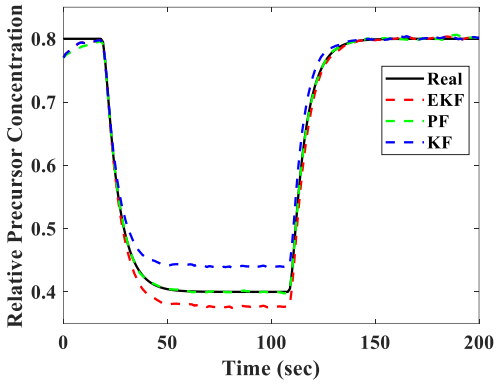

Fig. 6. Precursor concentration estimation with three studied filters

Fig. 4 compares the RMSE of the proposed filters in the first scenario. The results demonstrate that the proposed PF exhibits superior convergence between the estimated and actual states compared to other methods in the first scenario. Furthermore, comprehensive evaluations consistently indicate the superior performance of the PF over both KF and EKF methods.

B. The Second Scenario

In the second scenario, it is assumed that the power of the reactor is at 80% of the rated power. Then, after 18 seconds, the power of the reactor is reduced to 40% of its rated power.

After 108 seconds, the power is increased by 40%. Fig. 5 shows the second power level changes in the nuclear power plant. Figs. 6 and 7 compare the estimated and actual values of the precursor concentration and fuel temperature for the three filters described in Section III. Fig. 8 presents a comparative analysis of the RMSE for the proposed filters under the second scenario. This visualization allows us to directly assess the accuracy of each filter in estimating the true system state, providing valuable insights into their relative performance. The evaluation results indicate that the proposed PF exhibits faster convergence and lower estimation error than the KF and EKF algorithms in the second scenario.

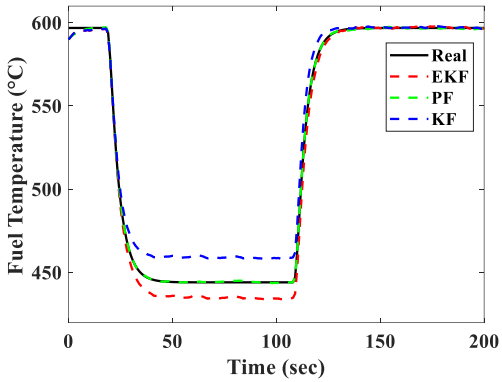

Fig. 7. Fuel temperature estimation with three studied filters

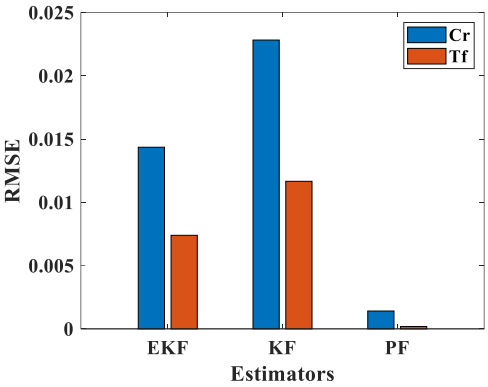

Fig. 8. Comparing RMSE of studied filters in the second scenario

C. The Third Scenario

In the third scenario, the reactor is subjected to a specific power cycle. It begins operating at 40% of its maximum power capacity. After 18 seconds, the reactor's power output is decreased to 20%. The reactor maintains this reduced power level for 108 seconds before returning to its initial 40% power level. Fig. 9 presents the modeled relative neutron density during this sequence. Fig .10 compares the estimated and the actual value of the precursor concentration for the three filters described in Section III. In addition, Fig. 11 compares the estimated and actual value of the fuel temperature for the three filters. Fig. 12 is a comparative analysis of the RMSE for the proposed filters under the third scenario.

The evaluation results suggest that the proposed PF demonstrates better performance in terms of convergence speed and estimation accuracy when compared to both the KF and EKF algorithms. Specifically, the PF achieves faster convergence, meaning that it reaches accurate estimates more quickly than its counterparts. This characteristic is crucial in applications requiring real-time processing and rapid decision-making. Additionally, the PF exhibits lower estimation errors, which implies that the estimates produced are closer to the true values of the variables being estimated, enhancing overall system reliability.

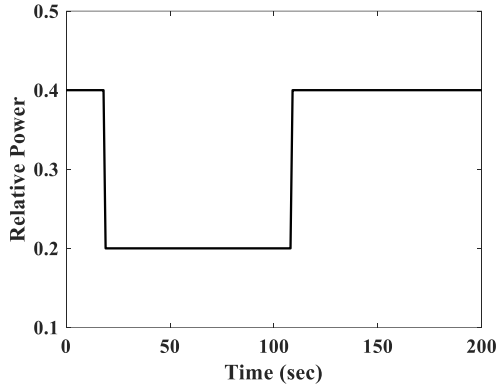

Fig. 9. Relative power changes in the third scenario

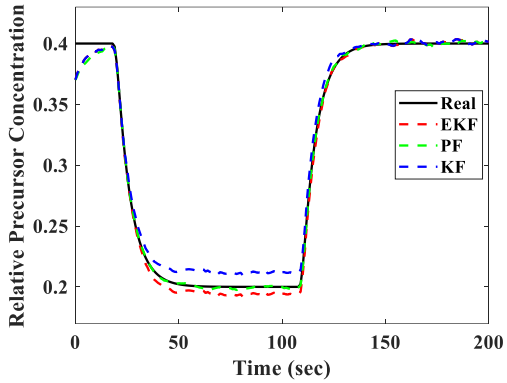

Fig. 10. Precursor concentration estimation with three studied filters

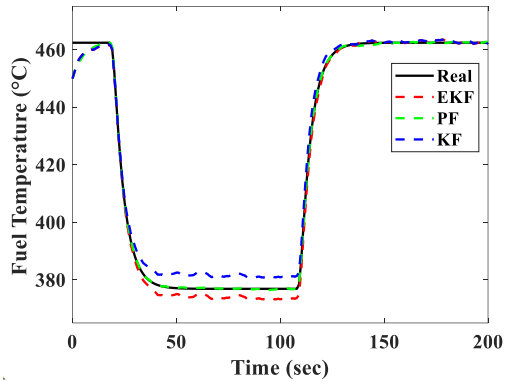

Fig. 11. Fuel temperature estimation with three studied filter

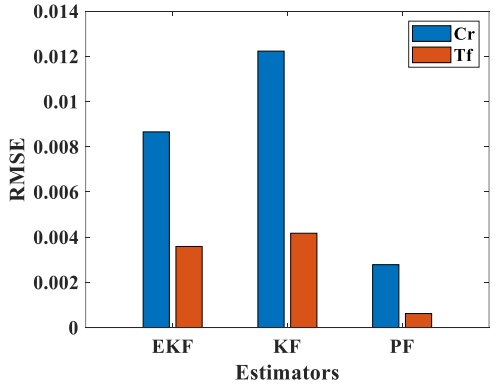

Fig. 12. Comparing RMSE of studied filters in the third scenario

TABLE III OVERVIEW ERROR METRICS FOR PRECURSOR CONCENTRATION AND FUEL TEMPERATURE ESTIMATION AT THREE SCENARIOS

Powers	Estimation errors	Indices	KF	EKF	PF
First scenario	$e(C_r)$	ME	0.0194	0.0119	0.0032
		IAE	3.8934	2.3928	0.6380
	$e(T_f)$	ME	0.0099	0.0062	0.00065
		IAE	1.9833	1.2493	0.1317
Second scenario	$e(C_r)$	ME	0.0253	0.0152	0.0032
		IAE	5.0925	3.0459	0.6134
	$e(T_f)$	ME	0.0123	0.0077	0.0007
		IAE	3.4774	1.5496	0.1424
Third scenario	$e(C_r)$	ME	0.0173	0.0104	0.0049
		IAE	3.4840	2.0834	0.9803
	$e(T_f)$	ME	0.0058	0.0040	0.0011
		IAE	1.1568	0.8131	0.2235

This study employs two error metrics, ME and IAE, to evaluate the estimation accuracy of precursor concentration and fuel temperature across three power levels. Table III presents the results of the two error metrics, ME and IAE, evaluated across three different scenarios. ME serves as a fundamental metric for assessing the average deviation in estimations, offering insights into the overall accuracy of predictions relative to actual measurements. It is calculated as the average of the differences between predicted values and observed values, helping to identify systematic biases in the estimation model and providing a more comprehensive understanding of the model's performance.

In contrast, IAE offers a more comprehensive analysis of estimation accuracy over time. Unlike ME, which may be misleading in the presence of compensating errors, IAE accumulates the absolute discrepancies, capturing the magnitude of all errors made during the estimation process. By analyzing both ME and IAE, a nuanced understanding of the estimation errors associated with precursor concentration and fuel temperature can be derived, thereby enhancing the reliability of predictive models at varying power levels. One notable drawback of the proposed method is its extended processing time, attributed to its inherent complexity, while alternative methods benefit from shorter processing durations due to their simpler designs. Nevertheless, this trade-off is justified by the superior performance and accuracy of the proposed method, which are critical for ensuring reliable outcomes in our application. Table IV outlines the comparative advantages and disadvantages of the proposed method relative to others.

TABLE IV COMPARISON OF THE PROPOSED METHOD COMPAIR WITH OTHER METHODS

Method	Advantage	Disadvantage	Processing Time
Particle filter	High Accuracy	Longer processing time	4.4 sec
	Robust performance		
KF and EKF	Faster processing time	Low accuracy	0.8 sec and 1.37 sec
	Simplicity	Limited robustness	

D. Limitations

One of the limitations identified in this study is the unavailability of comprehensive data on nuclear power plants globally, which hampers the ability to conduct a thorough analysis. This scarcity of data is attributed to several factors, including the diversity of regulatory frameworks in different countries, the proprietary nature of information related to nuclear energy, and the varying levels of transparency associated with national energy policies.

Many nations have imposed strict controls and regulations on the dissemination of information pertaining to nuclear facilities, resulting in fragmented data that can hinder accurate comparisons and assessments. Furthermore, the sensitive nature of nuclear operations often results in limited public access to detailed operational metrics and safety records, which are crucial for comprehensive analysis. Many existing databases either provide outdated information or lack the granularity necessary for robust evaluations of nuclear power plants and their performance. Such challenges underscore the complexities involved in researching nuclear energy infrastructure on a global scale. Therefore, at this stage of the research, reliable data in this area remain unobtainable, which poses significant constraints on the depth and breadth of the analysis that can be undertaken.

Another limitation of this study is the computational cost of the PF. The PF utilizes a set of particles to estimate the state; as the number of particles increases, the accuracy of the estimation improves. However, the computational expense of the PF also rises significantly. The mathematical relationship between the number of particles and the computational load can be expressed as follows:

$$C(N) = k \times N \tag{48}$$

where $C(N)$ represents the computational complexity for N particles and k is a constant value that represents

the amount of computation for each particle. The Eq. (48) illustrates a fundamental characteristic of PFs, where the total computational cost is directly proportional to the number of particles utilized in the estimation process. This linear relationship signifies that as the number of particles increases, the computational demands escalate correspondingly, thereby requiring additional computational resources and time. This understanding emphasizes the trade-off between accuracy and efficiency in particle filtering; while increasing the number of particles can enhance the accuracy of state estimates, it also incurs a substantial increase in computational load. Consequently, careful consideration must be given to the selection of the number of particles in practical applications to achieve a balance between desired accuracy and available computational resources.

V. Conclusions

This study provided a detailed evaluation of the PF's performance in estimating precursor concentration and fuel temperature, positioning it against both the standard KF and the EKF. The comparison revealed significant advantages of the PF, particularly in terms of accuracy and reliability under different operational scenarios. Three scenarios were analyzed: high power, medium power, and low power. In all three cases, the PF demonstrated a superior ability to minimize estimation errors as defined by RMSE (Root Mean Error), ME (Mean Error), and IAE. These metrics reflect the filter's capacity to closely track the true values of precursor concentration and fuel temperature, particularly during periods of dynamic changes in power levels. The findings highlight the robustness of the PF, especially in high power scenarios where rapid fluctuations are expected. In these conditions, the PF outperformed its Kalman counterparts by efficiently handling the non-linearities and noises associated with the estimation process. In the second and third scenarios, the PF continued to maintain its edge, exhibiting lower error rates and demonstrating better consistency in performance. Furthermore, the ability of the PF to adapt to varying conditions suggests its potential application in more complex systems where precision in estimation is critical.

The results advocate for the adoption of the particle filtering approach in relevant fields, particularly in systems that are subject to rapid changes and unpredictable dynamics. Overall, this study reinforces the importance of advanced filtering techniques in achieving accurate estimations in practical applications. Further investigations could explore the integration of the PF with other methodologies or its application in additional contexts, ensuring continuous improvement in data estimation efforts. This research not only contributes valuable insights into filtering techniques but also emphasizes the ongoing need for innovative solutions in the realm of estimation and control systems.

Future works

The promising results obtained from the PF in estimating precursor concentration and fuel temperature open several avenues for future research and application. One potential direction is the exploration of hybrid filtering techniques that integrate the strengths of the PF with those of other estimation methods, such as deep learning algorithms or multi-model approaches. By leveraging the adaptive capabilities of these methodologies, it may be possible to further enhance estimation accuracy in highly dynamic environments.

Acknowledgements

The authors are grateful to the anonymous reviewers for their valuable suggestions and comments to improve the quality of the paper.

REFERENCES

[1] P. Fernández-Arias, D. Vergara, and J. A. Orosa, "A global review of PWR nuclear power plants," *Applied Sciences*, vol. 10, no. 13, p. 4434, 2020.

[2] Y. Liu, H. He, T. Zhang, and X. Liu, "Pressurized water reactor fuel corrosion-related unidentified deposit and its related safety issues–I. Corrosion product deposition and heat transfer," *Annals of Nuclear Energy*, vol. 208, p. 110758, 2024.

[3] J. Hui, S. Ge, J. Ling, and J. Yuan, "Extended state observer-based adaptive dynamic sliding mode control for power level of nuclear power plant," *Annals of Nuclear Energy*, vol. 143, p. 107417, 2020.

[4] Q. Ahmed and A. I. Bhatti, "Estimating SI engine efficiencies and parameters in second-order sliding modes," *IEEE Transactions on Industrial Electronics*, vol. 58, no. 10, pp. 4837-4846, 2010.

[5] J. Hui and J. Yuan, "Kalman filter, particle filter, and extended state observer for linear state estimation under perturbation (or noise) of MHTGR," *Progress in Nuclear Energy*, vol. 148, p. 104231, 2022.

[6] Z. Dong, M. Liu, Z. Guo, X. Huang, Y. Zhang, and Z. Zhang, "Adaptive state-observer for monitoring flexible nuclear reactors," *Energy*, vol. 171, pp. 893-909, 2019.

[7] G. Ansarifar, "Estimation of the poisons reactivity in the PWR Nuclear Reactors using modified higher order sliding mode observer based on the multi-point nuclear reactor model," *Annals of Nuclear Energy*, vol. 112, pp. 158-169, 2018.

[8] J. Zou, S. Liu, C. Jin, Y. Cai, L. Wang, and Y. Chen, "Optimization method of burnable poison based on genetic algorithm and artificial neural network," *Annals of Nuclear Energy*, vol. 192, p. 109985, 2023.

[9] Z. Dong, B. Li, J. Li, X. Huang, and Z. Zhang, "Online reliability assessment of energy systems based on a high-order extended-state-observer with application to nuclear

reactors," *Renewable and sustainable energy reviews*, vol. 158, p. 112159, 2022.
[10] A. Koul, "Development of data-driven method for capacity estimation and prognosis for lithium-ion batteries," 2020.
[11] M. Z. Ygane and G. Ansarifar, "Extended Kalman filter design to estimate the poisons concentrations in the PWR nuclear reactors based on the reactor power measurement," Annals of Nuclear Energy, vol. 101, pp. 576-585, 2017.
[12] S. Javadi and A. Hesami Naghshbandy, "Comparison of Dynamic State Estimation Methods in the Time Domain," *International Journal of Industrial Electronics Control and Optimization*, 2024.
[13] R. Havangi and M. Moradi, "PSO based EKF wheel-rail adhesion estimation," *International Journal of Industrial Electronics Control and Optimization*, vol. 6, no. 1, pp. 49-62, 2023.
[14] D. Henry and S. Ygorra, "Hydrazine Concentration Estimation in the Secondary Circuit of a Nuclear Power Plant: a IQC LPV approach," *IFAC-PapersOnLine*, vol. 58, no. 13, pp. 697-702, 2024.
[15] Y. Fang, M. Fei, and H. Qian, "Pressurized Water reactor power level control: A nonlinear generalized predictive control with extended Kalman filter method," *Nuclear Engineering and Technology*, p. 103147, 2024.
[16] J. Elfring, E. Torta, and R. Van De Molengraft, "Particle filters: A hands-on tutorial," *Sensors*, vol. 21, no. 2, p. 438, 2021.
[17] D. Hetrick, "Dynamics of Nuclear Reactors, American Nuclear Society," La Grange Park, IL, 1993.
[18] H. Eliasi, M. Menhaj, and H. Davilu, "Robust nonlinear model predictive control for a PWR nuclear power plant," Progress in Nuclear Energy, vol. 54, no. 1, pp. 177-185, 2012.
[19] H. Eliasi, "Design an anti-windup controller for a PWR power-level control in the presence of control rod speed saturation," Annals of Nuclear Energy, vol. 132, pp. 415-426, 2019.
[20] H. Parhizkari, M. Aghaie, A. Zolfaghari, and A. Minuchehr, "An approach to stability analysis of spatial xenon oscillations in WWER-1000 reactors," Annals of Nuclear Energy, vol. 79, pp. 125-132, 2015.
[21] C. An, F. C. Moreira, and J. Su, "Thermal analysis of the melting process in a nuclear fuel rod," Applied Thermal Engineering, vol. 68, no. 1-2, pp. 133-143, 2014.
[22] E. E. Lewis, Fundamentals of nuclear reactor physics. Elsevier, 2008.
[23] H. Liu, F. Hussain, C. L. Tan, and M. Dash, "Discretization: An enabling technique," Data mining and knowledge discovery, vol. 6, pp. 393-423, 2002.
[24] M. S. Grewal and A. P. Andrews, Kalman filtering: Theory and Practice with MATLAB. John Wiley & Sons, 2014.
[25] P. Kaniewski, "Extended Kalman filter with reduced computational demands for systems with non-linear measurement models," Sensors, vol. 20, no. 6, p. 1584, 2020.
[26] J. Elfring, E. Torta, and R. Van De Molengraft, "Particle filters: A hands-on tutorial," Sensors, vol. 21, no. 2, p. 438, 2021.
[27] E. Gasmi, M. A. Sid, and O. Hachana, "Nonlinear event-based state estimation using particle filter under packet loss," *ISA transactions*, vol. 144, pp. 176-187, 2024.

Hossein Zahmatkesh was born in Mashhad, Iran, in 1998. He received the B.Sc. degree in electrical engineering from Sadjad University, Mashhad, Iran, in 2021 and the M.Sc. degree in control engineering from the University of Birjand, Birjand, Iran, in 2024. His research interests include Control, Nonlinear Dynamic Systems, Power Systems, State Estimation, Filtering and Transient Stability in Load Following by Nuclear Power Plants.

Hussein Eliasi received the B.S. degree in electrical engineering from the Ferdowsi University of Mashhad (FUM), Iran, in 2001. He received the M.S. and the Ph.D. degrees in nuclear engineering from Amirkabir University of Technology (Tehran), Iran, in 2005 and 2011, respectively. He is currently an associate professor in the Faculty of Electrical Engineering at the University of Birjand, Iran. His research interests include Constrained Nonlinear Dynamics Systems, Robust Control, State Estimation and Filtering, Parameter Optimization of Model Predictive Control, Transient Stability in Power Systems and Load Following by Nuclear Power Plants.

IECO

This page intentionally left blank.

International Journal Of
Industrial Electronics Control and Optimization
Print ISSN: 3517-2645
Online ISSN: 3568-2645
Homepage: https://ieco.usb.ac.ir/

A New Protection Strategy for Microgrid based on Integration of Active Power Index and Fault Current Differential Energy

Reza Karimi[1], Abbas Ketabi[2], Seyyed Moammad Nobakhti[3]

Department of Electrical and Computer Engineering, University of Kashan, 6 km Ghotbravandi Blvd, Postal Code: 8731753153, Kashan, Iran [1,2]
Department of Electrical Engineering, National University of Skills (NUS), Tehran, Iran[3]
Corresponding author's email: aketabi@kashanu.ac.ir

Article Info

Article type:
Research Article

Article history:
Received: 27-July-2024
Received in revised form: 15-September-2024
Accepted: 03-October-2024
Published online: 23-Sep-2025

Keywords:
Active power flowing,
Distributed generation,
Energy difference signal,
Fault current direction,
Microgrid protection.

ABSTRACT

The integration of distributed generation (DG) sources into distribution systems has experienced significant growth due to their numerous advantages. However, DG integration has also introduced substantial challenges to distribution system protection, such as variations in fault current levels and bidirectional fault current flow. Under these conditions, directional overcurrent relays may not operate as intended. This paper proposes a directional comparison protection scheme for safeguarding lines and zones in active distribution systems, based on the calculation of incremental active power transient energy. Additionally, a differential protection scheme, based on the Teager–Kaiser Energy Operator (TKEO), is incorporated to enhance the performance of the directional identification algorithm. The proposed scheme is capable of detecting symmetric and unsymmetric faults on microgrid lines at both low and medium voltage levels and is adaptable to changes in microgrid configurations and load-switching transients. The proposed methods offer the advantages of simplicity in calculation and high accuracy. An AC active distribution system incorporating inverter-based DG sources is modeled in PSCAD-EMTDC software to simulate various fault types, and the simulation results are subsequently transferred to MATLAB for the implementation of the proposed algorithms.

I. Introduction

Electricity has been a fundamental requirement for human society since the early stages of civilization. The rapid growth in electricity consumption has significantly impacted energy resources, particularly fossil fuels, leading to a decline in these reserves. In addition, the increase in fossil fuel consumption and the associated undesirable environmental effects have created a basis for the development and use of renewable energy. The deployment of distributed generation resources in distribution systems has increased markedly in recent years. Distributed generation resources are those located at or near the point of electricity consumption and inject their generated electricity directly into the distribution grid. Distributed generation (DG) resources offer several advantages over centralized generation resources. The reduction of distribution network losses is one of the most important advantages of distributed generation (DG) resources, as they are typically located near the point of consumption, which reduces the distance that electricity must travel through the network. Distributed generation (DG) resources can significantly improve the reliability of the power grid by providing a local source of backup power in the event of a power outage from centralized generation sources. DG resources can also enhance the stability of a power grid by supplying local, flexible, and responsive power during periods of increased grid load. The use of renewable energy sources for electricity generation can lead to a significant reduction in air pollution and environmental impacts. The rapid growth of distributed generation resources in distribution systems has created conditions for the development and operation of microgrids. The emergence of microgrids, which are small-scale power systems, has revolutionized the landscape of electricity supply. These innovative systems harness local generation resources such as solar, wind, and small-scale generators, offering a sustainable and flexible solution for regions lacking access to the main grid or facing grid constraints.

Copyright © A. Ketabi (s).
Publisher: University of Sistan and Baluchestan

Microgrids, while capable of connecting to the main grid, also possess the ability to operate in island mode. This capability eliminates over-reliance on the central grid, significantly enhancing system stability and security. Microgrids can be broadly categorized into two types based on their connection to the main grid:

1. Grid-Connected Microgrids: Grid-connected microgrids establish a connection with the main grid, enabling them to exchange power with the broader electricity network. This bidirectional power flow allows these microgrids to: Supplement Electricity Supply: During periods of peak demand, grid-connected microgrids can draw power from the main grid to meet local electricity needs. Inject Excess Generation: Conversely, when microgrid generation exceeds local demand, surplus electricity can be injected into the main grid, contributing to overall grid stability and resource optimization. Grid-connected microgrids are particularly well-suited for electrifying remote areas and regions with weak or unreliable grid infrastructure.

They offer several advantages, including:

Enhanced System Stability and Security: The ability to draw power from the main grid during disturbances ensures uninterrupted power supply to critical loads. Reduced Reliance on Central Grid: By generating and consuming electricity locally, grid-connected microgrids lessen dependence on the main grid, increasing energy autonomy. Improved Power Quality: Active regulation of voltage and frequency within the microgrid enhances power quality for consumers. Increased Flexibility and Efficiency: Real-time energy management and optimization enable grid-connected microgrids to respond effectively to demand fluctuations and optimize resource utilization.

2. Island Microgrids: Island microgrids operate autonomously, disconnected from the main grid. They rely solely on local generation resources to meet their electricity needs. This self-sufficiency provides several benefits, particularly in remote or grid-constrained areas: Uninterrupted Power Supply: Island microgrids are immune to disruptions in the main grid, ensuring a continuous and reliable power supply for critical infrastructure and communities. Energy Independence: By generating electricity locally, island microgrids eliminate reliance on imported fossil fuels, promoting energy independence and sustainability. Resilience in Remote Locations: Island microgrids provide a stable power source for remote areas that are difficult or expensive to connect to the main grid.

Despite their advantages, island microgrids also present certain challenges: Higher Initial Investment: The upfront costs of establishing an island microgrid, including local generation and storage infrastructure, can be higher compared to grid-connected systems. Need for Advanced Control Systems: Island microgrids require sophisticated control and management systems to ensure real-time balancing of supply and demand and to maintain grid stability. Limited Scalability: The capacity of island microgrids is typically constrained by local generation resources, limiting their ability to serve large-scale loads. In addition to the categorization of microgrids based on their grid connection type and location, another classification scheme exists based on the type of power transfer employed within the microgrid. This classification encompasses three primary microgrid types:

1. AC Microgrids: In AC microgrids, all system components, including generation sources, loads, and transmission lines, utilize alternating current (AC) for power transmission. AC, as the prevalent standard in the electricity industry, offers advantages such as simplicity of structure, ease of connection to existing power grids, and high efficiency in power transmission over long distances.

2. DC Microgrids: DC microgrids employ direct current (DC) for power transmission throughout the system's components. DC presents benefits such as lower losses over short distances, compatibility with renewable energy generation sources like solar panels and batteries, and enhanced controllability and manageability.

3. Hybrid Microgrids: Hybrid microgrids represent a combination of AC and DC microgrids. In this type of microgrid, both AC and DC are utilized for power transmission in different parts of the system. This approach simultaneously harnesses the advantages of both AC and DC systems, leading to increased flexibility and efficiency within the microgrid.

Microgrid Selection: Selecting the appropriate microgrid type depends on various factors, including the nature of generation sources, load types, transmission line lengths, and the control and protection requirements of the system. In certain scenarios, employing a combination of AC and DC microgrids, forming a hybrid microgrid, may constitute a more optimal solution. The impact of these resources on the performance of protective systems has also increased with the growing penetration of distributed generation resources (DGs) in power distribution networks. Among the most significant impacts of DGs on the protection of distribution systems are the following: Voltage variations: DGs are typically small-scale and installed at various points in the distribution network. Therefore, they may cause variations in the network voltage levels, which can lead to disruptions in the network and equipment damage. Influence of distributed generation on network losses: Distributed generation can cause either a reduction or an increase in network losses, depending on the capacity, location, and type of distributed generation. Changes in network losses can lead to improper operation of protective equipment. The structure of distributed generation (DG), the reduced level of fault current in islanded mode, the change in fault current level with the transition of microgrid mode from connected to disconnected, and the low inertia of microgrids are all factors

that affect the protection of active distribution systems and the performance of directional overcurrent relays.[17]. The structure of DG can influence the magnitude of the fault current. DG connected to the distribution system through a point of common coupling (PCC) can increase the fault current. However, DG isolated from the distribution system or connected to the distribution system through a microgrid can reduce fault current [18-20]. In islanded mode, the DG can lower the fault current by providing a local source of power. This can impact the operation of the overcurrent relays, which are designed to function based on the magnitude of the fault current. Microgrids can operate in either connected or islanded mode. In connected mode, the microgrid is linked to the distribution system. In islanded mode, the microgrid is isolated from the distribution system [13, 19]. The change in the microgrid mode from connected to islanded can alter the magnitude of fault current. This is because the distributed generation (DG) connected to the microgrid can provide a local source of power in the islanded mode. Microgrids with low inertia are more vulnerable to faults, as they can experience larger transient overvoltage and overcurrent during a fault [16]. Despite the operational challenges associated with the use of distributed energy resources (DERs) in distribution systems, their unique benefits are clear. These benefits include reduced energy loss, improved network stability, and increased power supply reliability. Consequently, researchers have been investigating the effects of DERs on distribution systems and have provided various solutions for the optimal utilization of these resources. The authors in [17] propose a multi-agent system-based protection scheme for protecting distribution systems that contain distributed generation resources. The proposed scheme can achieve satisfactory performance for protection under low-impedance fault conditions. In [21], a wave-polarity-based protective technique for fault detection is proposed. This technique can accurately and quickly detect faults by comparing the polarities of the traveling waves at two points in the network. A protection scheme for locating faults in radial distribution systems is proposed in [22]; however, it does not function properly when distributed generation resources are utilized. Moreover, the proposed scheme does not perform well in radial distribution systems with increased fault impedance. In [23], an automatic coordination mechanism based on the exchange of information was used to achieve coordination between the overcurrent relays. This mechanism automatically establishes coordination between relays using current and voltage information at the relay connection point. The main challenge of this mechanism is the need for a telecommunications infrastructure to exchange information between relays. In [24], an adaptive protection scheme based on non-standard characteristic curves was proposed. This scheme can provide satisfactory protection performance under various network conditions by leveraging the flexibility of non-standard characteristic curves. However, this scheme has a major drawback in that it does not consider islanding performance. In [19], the authors proposed a novel protection scheme based on the optimization of relay parameters by considering multiple characteristic curves for directional overcurrent relays. This scheme can provide satisfactory protection under various network conditions. In [25], a novel method was proposed for identifying single-phase faults in active power distribution systems using zero- and negative-sequence current. This method can identify single-phase faults under various network conditions by utilizing the features of zero- and negative-sequence currents. Considering the impact of solid-state transformers on the coordination of overcurrent relays, the authors in [5] introduced a novel protection scheme. However, it fails to operate under conditions with inverter-based distributed generation resources and high-impedance faults. In [26], the authors propose a novel adaptive optimization method for directional overcurrent relay coordination to achieve optimal protection coordination in microgrids with diverse topologies. This innovative approach utilizes advanced optimization algorithms to optimally adjust relay parameters under various network conditions, ensuring robust protection coordination against a wide range of faults. The method first employs powerful feature extraction algorithms to extract the characteristics of zero-sequence and negative-sequence currents. Subsequently, these extracted features are fed into an advanced prediction model to accurately estimate the fault probability at different points in the network. Finally, relay parameters are optimally tuned based on the predicted fault probability to guarantee seamless coordination among relay operations under various network scenarios. However, the proposed method may not perform effectively in protecting microgrids against high-impedance faults In[27], the authors proposed an optimized approach for current protection of power grids that utilizes local current information. This method dynamically updates the relay operating characteristics based on the grid's operational conditions and distributed generation (DG) outages. This dynamic adaptation enhances the protection's flexibility and optimizes system performance against faults. Building upon this work, the authors in [28 and 29] introduced novel current-time-voltage (I-T-V) tripping characteristics to further improve current protection efficiency. These new characteristics enable faster and more reliable protection by optimizing the total relay operation time. The formulation of these characteristics was framed as a constrained nonlinear programming (NLP) problem based on standard overcurrent protection (OCR) characteristics. Despite the notable advantages of the methods presented in [27, 28, and 29], their effectiveness may be compromised in certain scenarios due to the neglect of diverse grid operational conditions, including fault type, fault magnitude, and pickup current values. For instance, the extensive integration of DGs into

the grid can significantly impact system behavior under fault conditions, which is not fully considered in these approaches. Therefore, it is crucial to continue research in current protection of power grids with a focus on DG integration and considering the diversity of grid operational conditions. The development of adaptive and dynamic protection schemes that can effectively accommodate varying system conditions is of paramount importance. In the research presented in [30 and 31], a novel approach to coordinating directional overcurrent protection relays for the protection of distribution system microgrids in grid-connected and islanded operating modes was introduced. This innovative method effectively addresses the inherent challenges of microgrid protection by employing a fault current limiter at the point of common coupling (PCC). Furthermore, in [32], microgrid protection using directional overcurrent relays and an agent-based communication system was investigated. This approach provides fast and accurate protection against a wide range of faults by relying on dynamic information exchange between the relays. Aiming to address the inherent challenges of protection coordination in microgrids, a novel protection coordination scheme utilizing dual-setting directional overcurrent relays was proposed in [33]. This innovative scheme significantly reduces the complexity and cost of the protection system by eliminating the requirement for fault current limiters. In [34], a novel scheme is proposed to enhance the protection level of meshed microgrids. The scheme is based on the employment of a set of directional overcurrent relays with two settings. In [35], a novel hybrid optimization method based on the integration of the firefly algorithm and linear programming is proposed to enhance the performance of directional overcurrent relays. By leveraging the strengths of both algorithms, this innovative approach can achieve more desirable and time-efficient results compared to traditional methods. In [36], a novel differential protection scheme for microgrid lines was proposed based on the definition of the islanding correlation index in the presence of inverter-based resources. This scheme, utilizing the correlation index, can detect fault conditions in microgrid lines with higher accuracy and speed than traditional protection schemes. In [37], a novel differential protection scheme based on the calculation of line impedances was proposed for active distribution system lines containing inverter-based distributed generation resources. A fault direction-finding algorithm that utilizes the calculation of incremental changes in voltage and current flowing through the lines, along with an adaptive differential protection algorithm for fault detection and protection of microgrid lines and zones, was proposed in [10]. In [38], the authors proposed a novel differential protection scheme for distribution lines based on the calculation of current signal energy. The use of dual settings for the coordination of directional overcurrent relays, employing genetic algorithms to optimize relay settings, was proposed in [39]. However, achieving coordination for a large number of overcurrent relays with dual settings is often challenging. Fault direction identification using a power-based index for microgrid line protection has been investigated in [40]. The proposed scheme identifies faults based on the degree of network unbalance caused by the fault and determines the fault direction based on the direction of negative sequence reactive power flow. Accordingly, the proposed method is capable of satisfactory performance only for asymmetric faults. The use of derivatives of active power flowing through lines for fault direction detection has been investigated in [41]. Although the proposed scheme demonstrates desirable performance in the occurrence of high-impedance faults, its nature may lead to activation during load switching in the network. In [42], the Stockwell transform and deep neural networks were employed for fault detection and localization. The proposed method effectively visualizes the time-frequency information of current and voltage signals, thereby enhancing the speed of fault detection. Nevertheless, the utilization of variable-length windows to generate time-frequency representations for the input signal could potentially reduce redundancy in the time-frequency domain. Furthermore, the computational complexity associated with this approach constitutes another limitation. In [43], an autoregressive technique was proposed for fault detection. High computational speed is one of the advantages of the suggested method. However, this model heavily relies on historical data for accurate predictions, making it susceptible to performance degradation in the presence of data anomalies. Moreover, the computational complexity of the proposed method increases with the number of parameters and data points, which may potentially compromise its accuracy. In [44], fault detection is proposed using zero-sequence current component decomposition to extract fault features. Additionally, a whale optimization algorithm is employed to enhance the decomposition process. Subsequently, shape-based time series analysis utilizing dynamic time warping derivatives is applied for comparison. However, computational complexity poses a limitation to this approach. Fault detection and classification using positive sequence impedance energy calculation is proposed in [45]. A novel fault detection and classification method is proposed in [46], which simultaneously utilizes both temporal and frequency domain variations of current signals and defines a differential index. The weakness of the proposed method lies in its inability to operate under symmetrical fault conditions within the network Studies have shown that most proposed methods for the protection of active distribution systems are based on optimization problems and coordination among multiple relays. This can inherently lead to increased operational time of protection systems. Moreover, achieving coordination among multiple overcurrent relays is challenging. Given that identifying the

direction of an error can simplify both error detection and localization, novel approaches have been introduced in this regard. One such approach is the method proposed in [10]. A limitation of this approach is its inability to identify the direction of fault current flow under single-phase fault conditions. Furthermore, the proposed scheme has been investigated and evaluated for three-phase faults with an impedance of 0.1 ohms. This paper presents a fault direction recognition scheme based on the derivatives of active power flow and the calculation of its energy polarity for the protection of lines and microgrid areas. The objective is to identify the fault current direction resulting from various fault types and to increase the fault impedance value compared to similar methods. Additionally, to prevent the fault direction scheme from being affected by factors such as load switching and the occurrence of faults outside the protection zone, a sub-differential scheme based on the calculation of the transient energy difference of line current signals is proposed. Table 1 presents the results of the study.

The following are the main contributions of this work that demonstrate its novelty for the microgrid protection:

TABLE 1 PERFORMANCE COMPARISON OF THE PROPOSED METHOD WITH EXISTING METHODS

Ref.	direction detection	Operation in island mode	Inverter based sources	High penetration of resources
[24]	×	×	✓	✓
[25]	×	✓	×	✓
[26]	×	✓	✓	✓
[10]	✓	✓	✓	×
[38]	×	✓	✓	×
Proposed Strategy	✓	✓	✓	✓

The proposed directional algorithm offers a straightforward approach to fault detection in lines and areas of a microgrid. This is because it solely relies on the active power flow through lines and areas for fault detection. By utilizing power derivatives, the transient energy of the active power flow can be easily calculated.

The proposed directional algorithm is capable of protecting microgrid lines and areas by effectively distinguishing between internal and external faults

The proposed method is a two-stage protection scheme that employs a differential protection approach based on the energy difference of current signals flowing through lines and areas. This ensures reliable operation in the event of an internal fault within the protected zone while preventing false tripping in the case of external faults or heavy loading conditions.

The proposed directional method is capable of identifying the direction of fault current under various fault conditions and microgrid configurations.

Moreover, the structure of the paper is organized as follows:

Section II introduces the proposed fault direction recognition method and the sub-differential scheme based on the energy difference of signals. Section III evaluates the performance of the proposed methods. Finally, Section IV presents the conclusions.

II. Methodology

A. Fault current direction identification algorithm

The increasing penetration of inverter-based distributed generation resources in distribution systems leads to a significant reduction in system inertia. In this case, the fault current is much lower than in traditional distribution systems that use machine-based distributed generation resources. The significant reduction in fault current in distribution systems with inverter-based distributed generation resources can pose serious challenges to conventional protection methods. Therefore, the proposed algorithms offer a novel and innovative approach to the protection of active distribution systems, which are described below. The presence of distributed generation resources in local distribution systems results in a bidirectional fault current. Therefore, identifying the direction of the fault current at the time of its occurrence is of utmost importance. However, the commonly used sequence components-based directional algorithms presented in [25] may fail for microgrids with inverter-based DERs. This is because inverter-based DERs produce few or no zero- or negative-sequence components during faults. The proposed direction-finding algorithm uses the magnitudes of the power flowing through the microgrid lines and the transient increasing energy of the real power to identify the direction of the fault current at the time of occurrence. To analyze three-phase networks, we consider the following balanced sinusoidal phase and line voltages:

$$\begin{cases} v_a(t) = \sqrt{2}\,V\cos(\omega t + \varphi_V) \\ v_b(t) = \sqrt{2}\,V\cos(\omega t + \varphi_V - \frac{2\pi}{3}) \\ v_c(t) = \sqrt{2}\,V\cos(\omega t + \varphi_V + \frac{2\pi}{3}) \end{cases} \quad (1)$$

$$\begin{cases} i_a(t) = \sqrt{2}\, I\, cos(\omega t + \varphi_I) \\ i_b(t) = \sqrt{2}\, I\, cos(\omega t + \varphi_I - \frac{2\pi}{3}) \\ i_c(t) = \sqrt{2}\, I\, cos(\omega t + \varphi_I + \frac{2\pi}{3}) \end{cases} \quad (2)$$

The phase angles of the voltage and current, φ_V and φ_I, respectively, are represented with respect to a specified reference. The above voltages and currents are characterized by the presence of a sinusoidal component in their positive-sequence components. This indicates that they are sinusoidal and balanced. The voltage and current phasors can be transformed to the stationary reference frame using (3):

$$\begin{bmatrix} v_\alpha \\ v_\beta \end{bmatrix} = \sqrt{\frac{2}{3}} \begin{bmatrix} 1 & -\frac{1}{2} & -\frac{1}{2} \\ 0 & \frac{\sqrt{3}}{2} & -\frac{\sqrt{3}}{2} \end{bmatrix} \begin{bmatrix} v_a \\ v_b \\ v_c \end{bmatrix} \quad (3)$$

Currents can be transformed to a stationary reference frame by using similar equations. In Equation (4), the voltages and currents that have been converted to a fixed reference frame are given.

$$\begin{cases} v_\alpha = \sqrt{3} V cos(\omega t + \varphi_V) \\ v_\beta = \sqrt{3} V sin(\omega t + \varphi_V) \\ i_\alpha = \sqrt{3} I cos(\omega t + \varphi_I) \\ i_\beta = \sqrt{3} I sin(\omega t + \varphi_I) \end{cases} \quad (4)$$

where v_α, v_β, i_α and i_β are the transformed voltages and currents with respect to the reference axes αβ. The Clarke transform and its inverse preserve instantaneous power in three-phase systems. This property makes the Clarke transform a very useful and efficient tool for analyzing instantaneous power in three-phase systems. The instantaneous three-phase active power is calculated using the instantaneous phase voltages and line currents based on Equation (5).

$$P_{3\varphi}(t) = v_a(t) i_a(t) + v_b(t) i_b(t) + v_c(t) i_c(t) \quad (5)$$

The initial definition of p and q as given in [47] is according to Equation (6).

$$\begin{bmatrix} p \\ q \end{bmatrix} = \begin{bmatrix} v_\alpha & v_\beta \\ -v_\beta & v_\alpha \end{bmatrix} \begin{bmatrix} i_\alpha \\ i_\beta \end{bmatrix} \quad (6)$$

The above equation can be employed as a valuable analytical tool for investigating the real power fluctuations in three-phase systems. The fault location algorithm is based on the integral of active power changes that pass through the lines according to Equations (7) and (8).

$$\Delta p = p^{fault} - p^{pre} \quad (7)$$

$$Energy(t) = \int_0^T \Delta p(t) dt \quad (8)$$

In this equation, the change in active power flowing through the protected area is denoted by Δp. The active power flowing through the protected area at the time of the fault and after the fault are denoted by p^{fault} and p^{pre}, respectively. In this algorithm, the active power value in each cycle is compared with that in the three previous cycles to detect changes in the active power flowing through a protected area. The difference between the two values is used to determine whether a fault has occurred. Fig. 1 illustrates the proposed energy algorithm for the protected area.

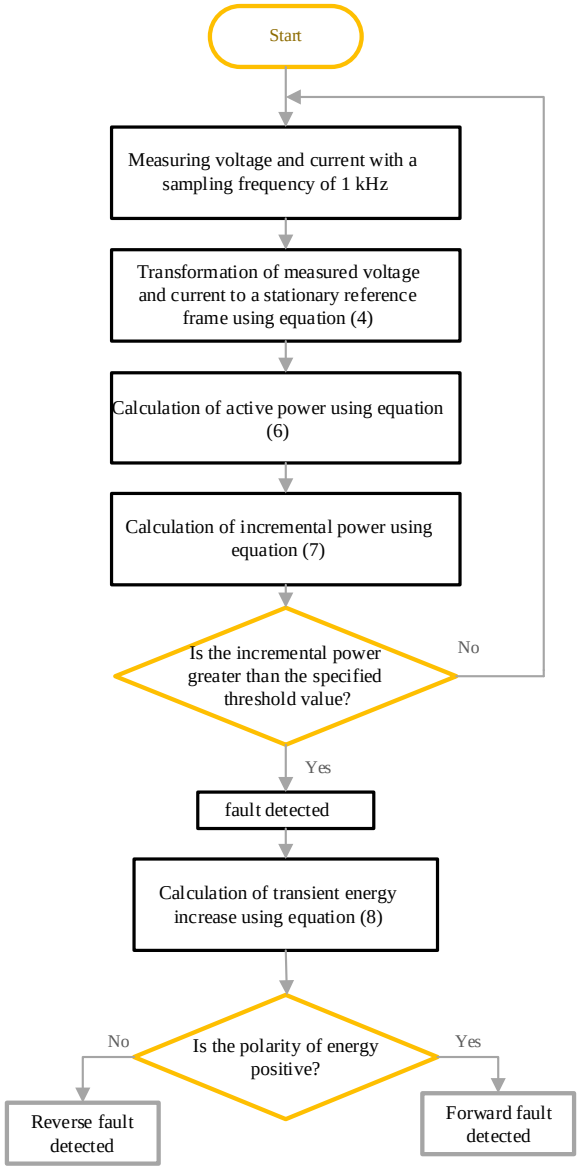

Fig. 1. Fault direction identification algorithm.

The measured voltage and current signals, sampled at a frequency of 1 *kHz*, constitute the input data for the algorithm. If the active power samples exceed the preset threshold for three consecutive samples, a fault is detected. In this paper, the fault detection threshold is set to five

percent of the nominal current. If the polarity of energy is positive, a forward fault is detected. If the polarity of energy is negative, a backward fault is detected. The received energy from both sides of the line is positive in the context of the proposed scheme for a bidirectional transmission line. However, the detection of negative energy polarity on one side of a transmission line indicates an external protection zone fault. In the event of a fault on the middle line of a distribution system, the direction of the fault current from the network to the faulted area is indicated by the positive polarity of upstream energy.

B. Differential protection scheme based on Tiger-Kaiser energy calculation method

Building on Teager's original concept, J. F. Kaiser introduced a straightforward algorithm to compute the energy present in a signal, based on its amplitude and frequency of oscillation. For a continuous sinusoidal signal, as depicted in equation (9), the energy required to generate the signal is proportional to the product of the square of its fundamental frequency and the square of its amplitude.

$$\zeta = \alpha \cos(\omega t + \phi) \tag{9}$$

Where ω and f are the angular frequency and base frequency, respectively.

$$\omega = 2\pi f \tag{10}$$

This energy measure is commonly referred to as the Teager–Kaiser Energy Operator (TKEO) [48]. Furthermore, the derived identity effectively links the Teager–Kaiser energy of the signal with its key parameters, offering a reliable metric for signal energy computation as shown in equation (11).

$$\dot{\zeta}(t)^2 - \zeta(t).\ddot{\zeta}(t) = \alpha^2.\omega^2 \tag{11}$$

The first and second-order derivatives of the signal $\zeta(t)$ are denoted by $\dot{\zeta}(t)$ and $\ddot{\zeta}(t)$, respectively, and play a pivotal role in deriving the mathematical identity associated with signal energy. Therefore, the continuous form of TKEO, is expressed as

$$\psi_{\zeta(t)} = \dot{\zeta}(t)^2 - \zeta(t).\ddot{\zeta}(t) \tag{12}$$

Further, this technique can also be implemented for discrete signal, shown in (13).

$$\zeta[n] = \alpha \cos(\Omega n + \phi) \tag{13}$$

Where Ω represents the digital frequency in radians per sample for the sample n, and ϕ denotes the phase as shown in equation (14).

$$\Omega = \frac{2\pi f}{f_s} \tag{14}$$

In this equation, f_s is the sampling frequency in Hz. The two adjacent points referenced in equation (13) can be represented as a set of equations, as shown in equation (15).

$$\zeta[n-1] = \alpha \cos(\Omega[n-1] + \phi)$$
$$\zeta[n+1] = \alpha \cos(\Omega[n+1] + \phi) \tag{15}$$

To compute the Teager-Kaiser Energy Operator (TKEO) for a discrete-time signal, three consecutive signal samples are required. The resulting energy value is calculated using the expression provided in equation (16).

$$\zeta[n+1].\zeta[n-1] = \zeta[n]^2 - \alpha^2 \sin^2(\Omega) \tag{16}$$

Subject to a small value of ω, the sampling frequency can be increased to more than eight times the signal frequency by imposing a limitation of π/4 on the value of This leads to a reduction in the relative error to 11%. Under these conditions, the energy operator yields a result that is expressed in Equation (17) and represents the energy contained in the signal [40].

$$\zeta[n]^2 - \zeta[n+1].\zeta[n-1] = \alpha^2\Omega^2 \tag{17}$$

Thus, the formulation of the Teager-Kaiser Energy Operator (TKEO) for discrete signals is expressed as presented in equation (18) [38],[48].

$$\psi_{\zeta[n]} = \zeta[n]^2 - \zeta[n+1].\zeta[n-1] \tag{18}$$

It is important to highlight that the TKEO is an efficient algorithm, requiring only two multiplications and one subtraction per data point to estimate the signal energy. This simplicity in computational operations contributes to its speed, making it well-suited for real-time applications and systems where rapid energy estimation is critical.

Fig. 2 presents the schematic diagram of differential current protection operation for a line.

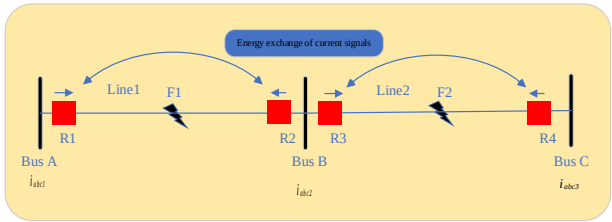

Fig. 2. Performance of the proposed differential scheme for the line under protection.

Under normal operating conditions, the differential current energy between protective relays R1 and R2 at the beginning and end of line j is zero. In the event of a short-circuit fault on line j, the difference between the energy integrals of the current relays at the two ends of the line becomes non-zero, indicating a fault on the protected line. Considering the characteristics of this type of protection, it can be considered an effective method for line protection. However, in situations where the penetration level of distributed generation sources on the system bus is high, the effectiveness of this method will decrease significantly [38].

The implementation of differential protection schemes in an extensive protection zone encompassing sources, loads, lines, and buses necessitates the definition of an operational

threshold for the proposed scheme. This method employs Equations (19) and (20) to calculate the energy of current signals at the inception and termination points of the protected area. Subsequently, Equation (21) is utilized to determine the energy difference between these two signals [38].

$$E_{1(j)p\in a,b,c} = I_{1(j)p}[n]^2 - I_{1(j)p}[n+1] \cdot I_{1(j)p}[n-1] \quad (19)$$

$$E_{2(j+1)p\in a,b,c} = I_{2(j+1)p}[n]^2 - I_{2(j+1)p}[n+1] \cdot I_{2(j+1)p}[n-1] \quad (20)$$

$$Energy_{dif} = E_{1(j)p\in a,b,c} - E_{2(j+1)p\in a,b,c} \quad (21)$$

Exceeding the predetermined threshold of the calculated energy difference confirms the occurrence of a fault within the protected zone. Fig. 3 illustrates the differential current protection algorithm in an extended protection zone. The proposed differential protection scheme, in conjunction with the directional identification algorithm, facilitates the isolation of faulty zones from healthy zones and prevents misoperation of the protective relay. The operating threshold of the differential current protection scheme is determined based on the calculation of fault energy for internal and external faults, considering an allowable load of 10% for the connected state and 5% for the islanded state. This threshold is set to prevent the algorithm from malfunctioning under permissible conditions, such as loading.

I. Test Results

A. Case study system:

To evaluate the performance of the proposed scheme, an active distribution network with a 50 Hz frequency was simulated using the PSCAD software. The data obtained from this simulation was processed and used to implement the proposed algorithms in MATLAB [37]. Fig. 4 illustrates the studied system. The system consists of two 0.4 kV and 10 kV feeders that are connected to the 35 kV main grid via a transformer. The short-circuit capacity at the coupling point of these feeders to the main grid is 500 MVA, and the R/X ratio is 0.1. The nominal powers of the distributed generation (DG) sources in the 0.4 kV feeder are 200 kVA, 100 kVA, and 50 kVA, respectively. The nominal power of the DG source located at the end of the 10 kV feeder is 600 kVA. DG1 is a battery energy storage system (BESS), DG2 is a combined cooling, heating, and power (CCHP) system, and DG3 is a photovoltaic (PV) system connected to the low-voltage feeder. The DG source in the 10 kV feeder is a machine-based source (diesel generator). The positive and negative sequence resistances and inductances of the 0.4 kV feeder are 0.32 Ω/km and 0.261 mH/km, respectively. The zero sequence resistance and inductance of this part of the network are 1.1 Ω/km and 0.955 mH/km, respectively. The nominal powers of loads 1 to 6 in the 0.4 kV (low-voltage) feeder are 40 kVA, 20 kVA, 40 kVA, 40 kVA, 5 kVA, and 25 kVA, respectively. It is worth noting that a shunt capacitor with a nominal reactive power of 20 kVAR is used in one part of the network. The positive and negative sequence resistances and inductances of the 10 kV subnetwork are 0.38 Ω/km and 1.432 mH/km, respectively. The zero sequence resistance and inductance are 0.76 Ω/km and 4.2 mH/km, respectively. The nominal powers of loads 7 to 9 in this part of the network are 100 kVA, 500 kVA, and 500 kVA, respectively. The 0.4 kV feeder consists of inverter-based distributed generation (DG) sources that can supply the loads of this feeder in case of grid islanding during grid restructuring.

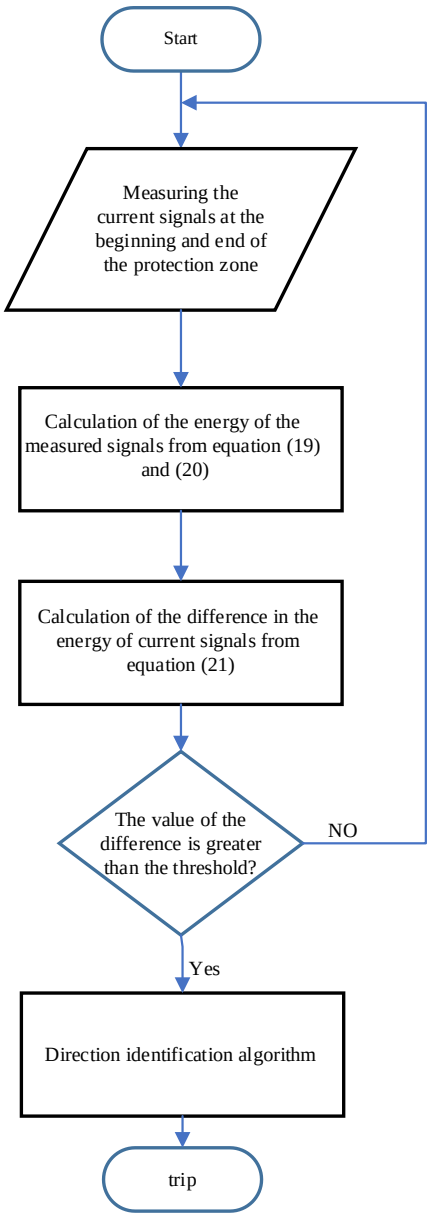

Fig. 3. Energy difference algorithm of current signals.

Table 2 demonstrates a comprehensive comparison between the proposed method and a similar method conducted in [10] for identifying the fault current direction.

The operating mode of energy storage batteries or distributed generation (DG) sources with combined cooling, heating, and power (CCHP) changes from P-Q to V-f control to support voltage and frequency during grid islanding transitions from grid-connected to island mode. However, the operation of photovoltaic (PV) systems is such that P-Q control is maintained in both grid-connected and island modes.

TABLE 2 COMPARISON OF THE PROPOSED DIRECTION IDENTIFICATION METHOD AND THE METHOD PROPOSED IN REFERENCE [10]

		Ref [10]		Proposed Strategy	
Fault resistance	**Fault type**	**Traditional differential**	**Fault direction**	**Energy-based differential**	**Corrected fault direction detection**
0.1 ohm	A-g	✓	×	✓	✓
	BC	✓	✓	✓	✓
	BC-g	✓	✓	✓	✓
	ABC	✓	✓	✓	✓
	ABC-g	✓	✓	✓	✓
20 ohm	A-g	×	×	✓	✓
	BC	×	×	✓	✓
	BC-g	×	×	✓	✓
	ABC	×	×	✓	✓

It is noteworthy that the output current of the inverter-based distributed generation (DG) sources used in this network is limited to 1.5 times the nominal current in case of a fault. It is also worth noting that the data presented in [49] to [51] were used to implement the proposed network.

A. Analysis of Fault Current Behavior

The performance of the proposed scheme for determining fault current direction based on the polarity of the incremental active power, aiming to identify faults inside and outside the protection zone, and the performance of the proposed scheme for the protection of active distribution lines in the following subsections have been investigated.

Case 1: Internal Faults: The performance of the proposed fault current direction detection scheme is depicted in Fig. 5, focusing on a fault event on line 4. Relay 4 acts as the input measurement for the designated protection zone, while Relay 6 serves as the output measurement. Analyzing the directional measurements from these relays reveals that, in scenarios where a fault occurs outside the protection zone or during load switching external to this zone, the energy calculated by both the input and output relays maintains the same polarity. In contrast, when a fault is detected within the protection zone, the input and output relays indicate an incremental energy transient characterized by opposite polarities.

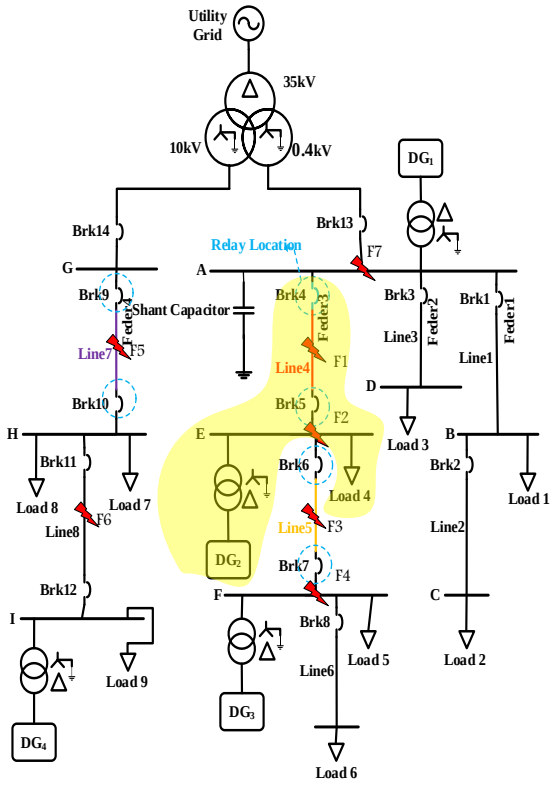

Fig. 4. Case study system.

In Fig. 6, the effectiveness of the proposed approach for identifying the direction of fault current in the event of a fault at bus E is presented. The results shown in Fig. 5 and 6 demonstrate that for faults that occur within the protection zone, the calculated energy polarity at both the beginning and the end of this zone is found to be opposite. This characteristic serves as a significant indicator for recognizing internal faults and can be considered a reliable standard for measuring the effectiveness of the zone protection system. Moreover, the proposed index is capable of identifying faults occurring within the distribution lines of active distribution systems. Considering relays 4 and 5 as the beginning and end relays of line 4, respectively, whenever a fault occurs on line 4, the energy polarity of the relays at the beginning and end of the protected line is positive, indicating a fault ahead of the protective relays. As evident from Fig. 5, for a fault occurring on line 4, the calculated transient energy polarity at both the beginning and end of the line is positive.

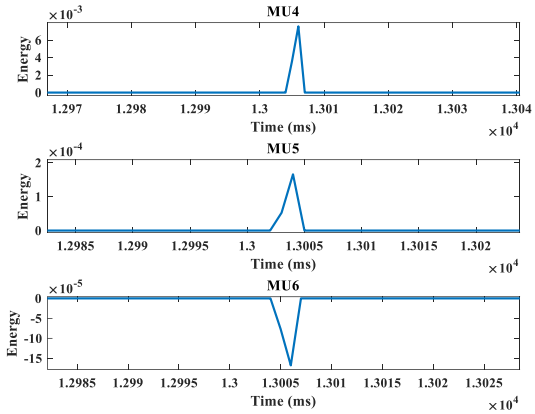

Fig. 5. Performance of the directional protection scheme under three-phase fault conditions on line 4 in grid connected mode.

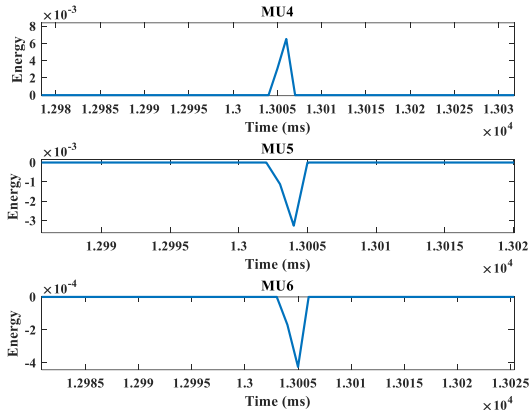

Fig. 6. Performance of Directional Protection Scheme under a Single Line-to-Ground Fault (A-G) on Bus E in Grid-Connected Mode.

However, as clearly shown in Fig. 6, for a fault occurring outside the line, the energy polarity of the incoming relay is positive, indicating a fault current flow direction from the network towards the downstream. Under such conditions, the calculated energy polarity for the outgoing relay is negative, indicating a fault behind the relay. Fig. 7 illustrates the identification of the fault direction on line 4 as an internal fault.

As shown in Fig. 7, when a fault occurs on bus E, the calculated energy polarity by the relay at the beginning of line 4 is positive, and the energy polarity for the relay at the end of the line is negative. This condition indicates a fault outside the line. Additionally, since the fault occurs within the protected zone, the energy polarity of relay 4 is positive and the energy polarity of relay 6 is negative, which indicates a fault within the protected zone. The results demonstrate that the proposed scheme is capable of accurately and rapidly detecting faults within the protected zone.

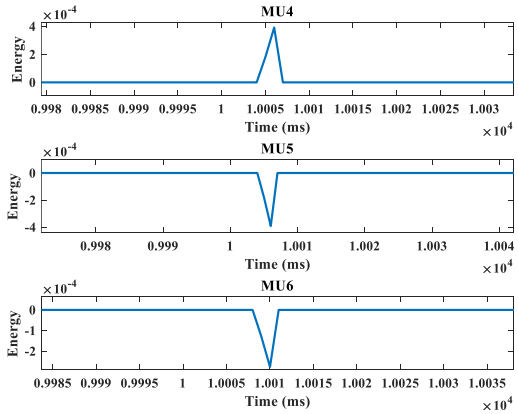

Fig. 7. Performance of Directional Protection Scheme under a Double Line-to-Ground Fault (AB-G) on Bus E in Islanded Mode.

Case 2: External faults: One of the distinguishing features of the proposed method is its ability to differentiate between faults inside and outside the protection zone. Fig. 8 illustrates the performance of the directional protection scheme when a fault occurs outside the protection zone. As evident from Fig. 8, when a fault occurs on line 5, the energy polarity calculated by relay 4 is positive, indicating a fault ahead of the relay. In this situation, the energy polarity calculated by relay 5 is negative, confirming a fault outside line 4. Moreover, the positive energy polarity of the outgoing relay corroborates the occurrence of a fault outside the protection zone. Fig. 9 presents the results of fault current direction finding under fault conditions outside the protection zone during islanding mode operation.

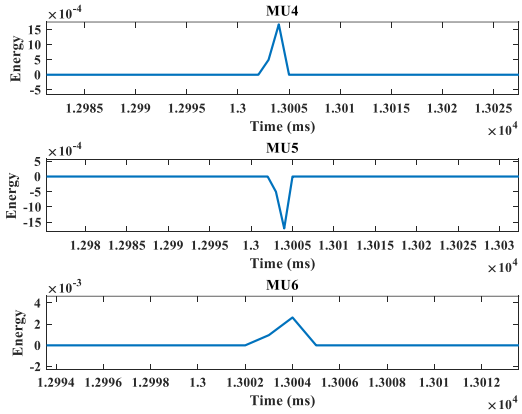

Fig. 8. Performance of the directional protection scheme under a single-phase-to-ground fault (B-G) on line 5 in grid-connected mode.

As evident from Fig. 9, when a fault occurs on bus A, the energy polarity measured by relay 4 is negative. This indicates that the fault current direction is from the load side

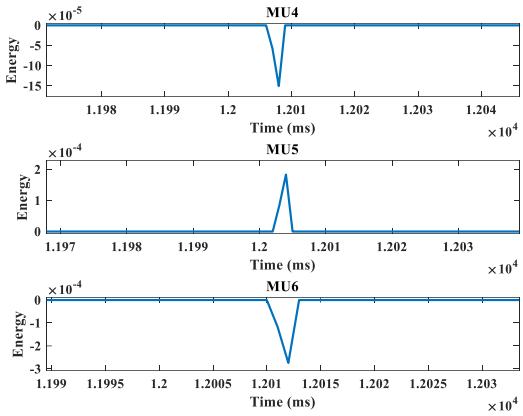

Fig. 9. Performance of the directional protection scheme under a three-phase fault on bus A during islanding mode operation.

towards the source. Under such conditions, the energy polarity of relay 5 is positive, implying a fault outside the protected line. Furthermore, the negative polarity of relay 6 confirms that the fault is located outside the protection zone. Fig. 10 illustrates the operational performance of the proposed directional scheme in response to an external fault occurring on line 8.

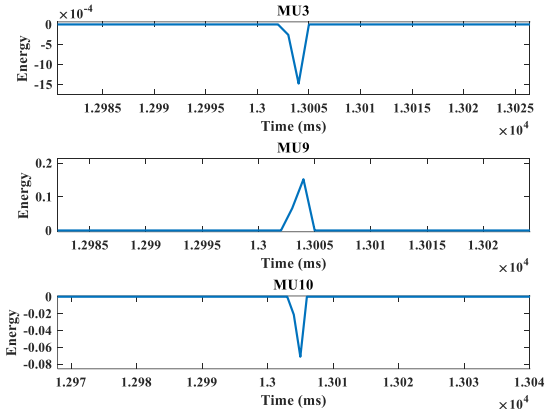

Fig. 10. Performance of the proposed directional scheme under single-phase fault conditions (A-G) in grid-connected mode on line 8.

As illustrated in Fig. 10, it can be observed that in the case of a fault occurring on line 8, relay number 3, which operates with negative polarity, is able to identify the fault occurring behind it. Therefore, should a fault arise at any location within the network, all relays will react in a positive or negative manner depending on the fault's position. This capability is particularly beneficial for accurately locating the fault. Furthermore, on line 7, the first relay exhibiting positive polarity and the last relay exhibiting negative polarity indicate the existence of a fault external to the line. Based on the results obtained from the execution of the directed protection scheme under fault conditions within the microgrid, it is evident that the proposed approach is adequately equipped to detect faults and differentiate between internal and external faults in the designated protection zone. The assessment was conducted with a fault impedance of 20 ohms, and the fault identification time was 5 milliseconds post-occurrence.

B. Current Differential Protection Scheme

In this section, the performance of the proposed differential protection scheme is evaluated for detecting and discriminating faults both inside and outside the protection zone, while considering network loading conditions.

Case 1: Internal Faults: Fig. 11 demonstrates the operation of the proposed design when faults occur within the protected region.

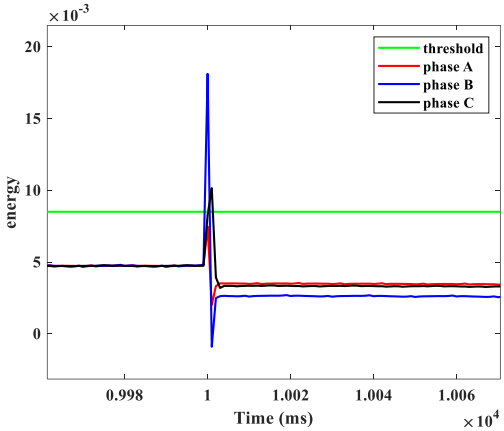

Fig. 11. Performance of the proposed scheme under three-phase fault conditions on Line 4 in grid-connected mode.

While noise in transmitted data is commonly considered in transmission lines, its impact is often overlooked in distribution networks where line lengths are shorter. Specifically, when a differential scheme is employed for short lines, susceptibility to noise can become a significant drawback of the proposed design. Fig. 12 illustrates the performance of the proposed scheme under fault conditions in islanded mode. When a fault occurs at 10 seconds, the difference in energy of the current signals exceeds the threshold, which can serve as a suitable criterion for determining a fault within the protection zone. The results clearly indicate that, following a fault within the protected zone, the difference in energy of the current signals entering and exiting the protected zone can serve as a reliable criterion for fault detection.

Case 2: External faults and load switching: One of the advantages of the proposed method is its immunity to external faults and load switching operations outside the protection zone. Fig. 13 illustrates the performance of the proposed scheme under fault conditions, both inside and

outside the protection zone. Fig. 14. depicts the performance of the proposed scheme under fault conditions on busbar F in islanded mode. The results clearly demonstrate the proposed scheme's ability to discriminate between faults inside and outside the protection zone.

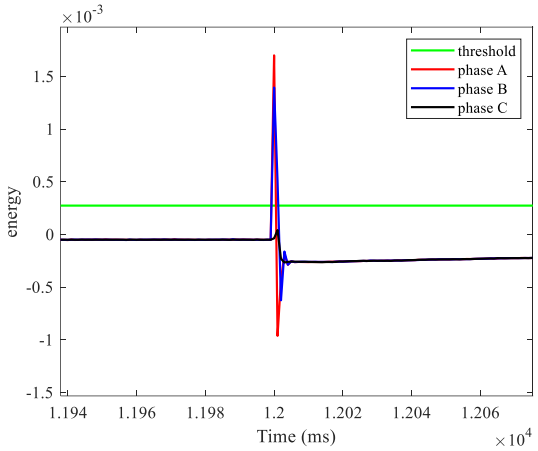

Fig. 12. Performance of the proposed scheme under an AB-G phase-to-ground fault condition on Line 4 in island mode.

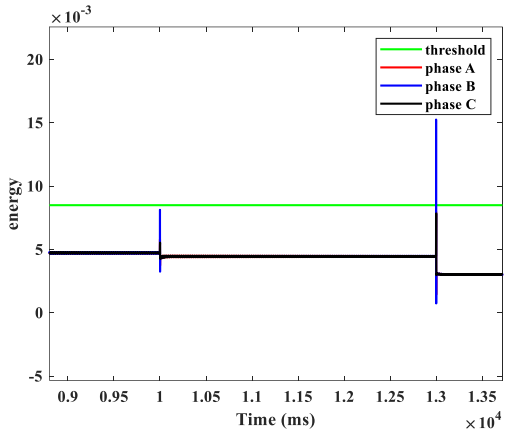

Fig. 13. Performance of the proposed scheme under a three-phase fault with an impedance of 0.1 ohms on line 5 at the 10th second, and a three-phase fault with an impedance of 20 ohms on line 4 at the 13th second in grid-connected mode.

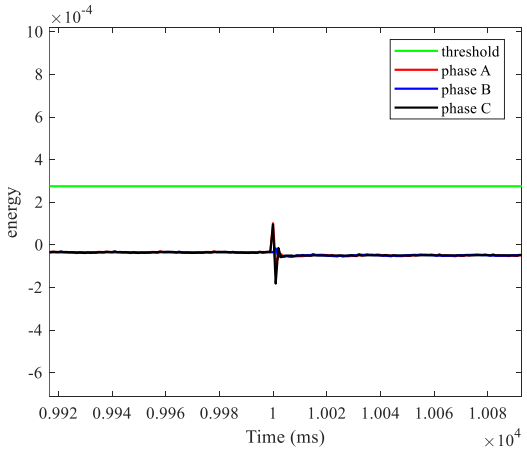

Fig. 14. Performance of the proposed scheme under three-phase fault condition on busbar F in islanded mode.

Fig. 15. illustrates the performance of the differential protection scheme under a single-phase fault outside the protection zone.

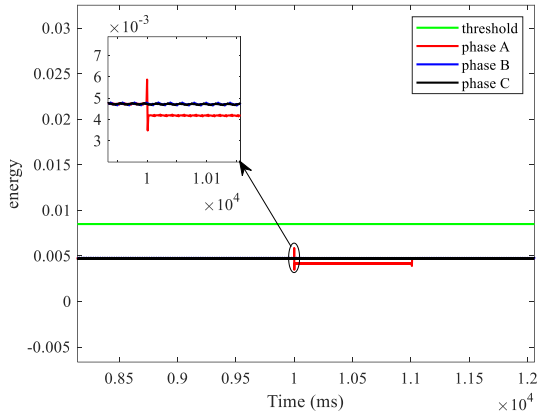

Fig. 15. The performance of the proposed scheme under single-phase (A-G) fault conditions on Line 5 in grid-connected mode.

As seen in the figure, when a fault occurs at the 10th second, the energy difference between the current signals becomes greater than under normal conditions. However, this difference is not sufficient to cause the proposed scheme to operate. The performance of the proposed scheme has been evaluated for internal faults within the protection zone with a fault impedance of 20 ohm and for external faults outside the protection zone with an impedance of 0.1 ohm.

Given that the algorithm employed to calculate the energy of current signals passing through the protection zones exhibits high accuracy and speed in tracking sinusoidal signals, the transit time resulting from the difference between the signal energy and the defined threshold is extremely short. Since this scheme is a sub-algorithm to complement the directional algorithm, it is reliable. The fault detection time for this algorithm is 3 milliseconds. Therefore, in addition to ease of calculation, the high speed and accuracy of the method used are confirmed by the obtained results.

Given that the proposed directional fault current algorithm is highly sensitive to variations in active power flow, it is imperative that the suggested sub-algorithm remains unaffected by such changes. As evident from Fig. 16, load switching results in a difference in the energy of current signals that deviates from the normal state. However, by defining a threshold and allowable load levels (10% of the load level both outside and inside the protected zone), the proposed scheme can effectively differentiate between loading conditions.

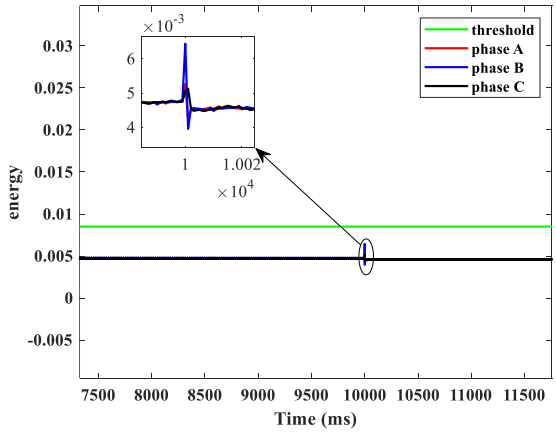

Fig. 16. Performance of the proposed scheme under increased load at bus F in grid-connected mode.

Fig. 17 illustrates the proposed scheme's ability to differentiate between load switching and fault occurrences within the protected zone during islanded operation. The results indicate that the proposed scheme, by determining an appropriate threshold in both grid-connected and islanded operation modes, can distinguish between faults within the protection zone and loads outside the protection zone.

While directional protection schemes offer superior speed, accuracy, and reliability for safeguarding areas containing distributed generation and loads, results have shown that the energy differential of current signals is effective only for internal faults. Given the proposed directional protection scheme's high sensitivity to active power variations, the energy-based differential algorithm can be employed as a supplementary method for external faults and load-switching conditions within the network.

A similar adaptive differential protection and direction-finding algorithm was employed in [10], but it exhibited limitations in identifying the fault current direction under single-phase fault conditions and had a detection capability for faults with an impedance of 0.1 ohms. Based on the obtained results, the proposed schemes have proven suitable for identifying various fault types under different microgrid operating conditions and have improved the impedance detection capability to 20 ohms compared to the similar method.

III. Conclusions

This paper presents a novel fault direction-finding scheme for the protection of lines and zones, leveraging incremental changes in active power flow. To prevent false operations during external faults and load switching events, a complementary differential protection scheme based on the energy of current signals is utilized. The Teager-Kaiser Energy Operator (TKEO) is employed to extract the energy from current signals at both ends of the line, and fault detection is accomplished by evaluating the energy difference between these signals. The results confirm that the proposed directional scheme accurately determines fault current direction under a variety of fault conditions, enabling rapid and precise discrimination between internal and external faults within the protected zone or line in diverse microgrid configurations. Additionally, the proposed methods demonstrate superior performance in handling higher fault impedances compared to existing directional schemes. Future work should investigate the impact of harmonics within microgrids on the proposed methodology.

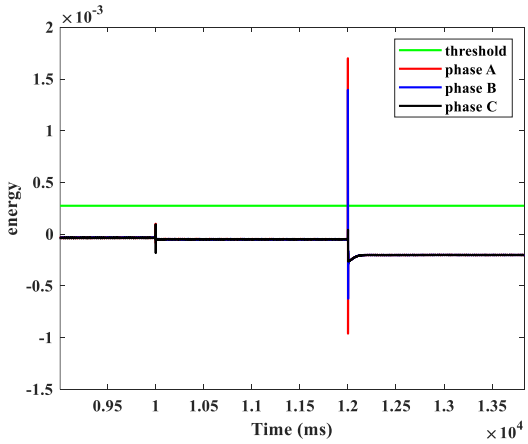

Fig. 17. Performance of the proposed scheme during a load increase at bus F at seconds10 and a three-phase fault at bus E at seconds12 under islanded operation.

References

[1] X. Kang, C. E. Nuworklo, B. S. Tekpeti, and M. Kheshti, "Protection of micro - grid systems: a comprehensive survey," The Journal of Engineering, vol. 2017, no. 13, pp. 1515-1518, 2017.

[2] S. Alzahrani, K. Sinjari, and J. Mitra, "An advanced control and protection integration scheme for microgrids," Sustainable Energy, Grids and Networks, vol. 32, p. 100940, 2022

[3] H. J. Laaksonen, "Protection principles for future microgrids," IEEE Transactions on power electronics, vol. 25, no. 12, pp. 2910-2918, 2010.

[4] M. R. Miveh, M. Gandomkar, S. Mirsaeidi, and M. R. Gharibdoost, "A review on protection challenges in microgrids," in 2012 Proceedings of 17th Conference on Electrical Power Distribution, 2012: IEEE, pp. 1-5.

[5] H. Nikkhajoei and R. H. Lasseter, "Microgrid protection," in 2007 IEEE Power Engineering Society General Meeting, 2007: IEEE, pp. 1-6.

[6] H. Hooshyar, M. Baran, S. R. Firouzi, and L. Vanfretti, "PMU-assisted overcurrent protection for distribution feeders employing Solid State Transformers," Sustainable Energy, Grids and Networks, vol. 10, pp. 26-34, 2017

[7] A. Salam, A. Mohamed, and M. Hannan, "Technical challenges on microgrids," ARPN Journal of engineering and applied sciences, vol. 3, no. 6, pp. 64-69, 2008.

[8] E. Sortomme, S. Venkata, and J. Mitra, "Microgrid protection using communication-assisted digital relays," IEEE Transactions on Power Delivery, vol. 25, no. 4, pp. 2789-2796, 2009.

[9] A. Hooshyar and R. Iravani, "Microgrid protection," Proceedings of the IEEE, vol. 105, no. 7, pp. 1332-1353, 2017.

[10] A. C. Adewole, A. D. Rajapakse, D. Ouellette, and P. Forsyth, "Protection of active distribution networks incorporating microgrids with multi-technology distributed energy resources," Electric Power Systems Research, vol. 202, p. 107575, 2022.

[11] A. Narimani and H. Hashemi-Dezaki, "Optimal stability-oriented protection coordination of smart grid's directional overcurrent relays based on optimized tripping characteristics in double-inverse model using high-set relay," International Journal of Electrical Power & Energy Systems, vol. 133, p. 107249, 2021.

[12] A. Reda, A. F. Abdelgawad, and M. Ibrahim, "Effect of non standard characteristics of overcurrent relay on protection coordination and maximizing overcurrent protection level in distribution network," Alexandria Engineering Journal, vol. 61, no. 9, pp. 6851-6867, 2022.

[13] P. Thararak and P. Jirapong, "Implementation of optimal protection coordination for microgrids with distributed generations using quaternary protection scheme," Journal of Electrical and Computer Engineering, vol. 2020, pp. 1-13, 2020.

[14] A. Dagar, P. Gupta, and V. Niranjan, "Microgrid protection: A comprehensive review," Renewable and Sustainable Energy Reviews, vol. 149, p. 111401, 2021.

[15] A. Hatata, A. Ebeid, and M. El-Saadawi, "Application of resistive super conductor fault current limiter for protection of grid-connected DGs," Alexandria engineering journal, vol. 57, no. 4, pp. 4229-4241, 2018.

[16] D. S. Kumar and D. Srinivasan, "A numerical protection strategy for medium-voltage distribution systems," in 2018 IEEE Innovative Smart Grid Technologies-Asia (ISGT Asia), 2018: IEEE, pp. 1056-1061.

[17] F. B. dos Reis, J. O. C. Pinto, F. S. dos Reis, D. Issicaba, and J. G. Rolim, "Multi-agent dual strategy based adaptive protection for microgrids," Sustainable Energy, Grids and Networks, vol. 27, p. 100501, 2021.

[18] E. C. Piesciorovsky and N. N. Schulz, "Comparison of Programmable Logic and Setting Group Methods for adaptive overcurrent protection in microgrids," Electric Power Systems Research, vol. 151, pp. 273-282, 2017.

[19] S. D. Saldarriaga-Zuluaga, J. M. Lopez-Lezama, and N. Munoz-Galeano, "Optimal coordination of over-current relays in microgrids considering multiple characteristic curves," Alexandria Engineering Journal, vol. 60, no. 2, pp. 2093-2113, 2021.

[20] R. Sitharthan, M. Geethanjali, and T. K. S. Pandy, "Adaptive protection scheme for smart microgrid with electronically coupled distributed generations," Alexandria Engineering Journal, vol. 55, no. 3, pp. 2539-2550, 2016.

[21] Q. Jia, X. Dong, and S. Mirsaeidi, "A traveling-wave-based line protection strategy against single-line-to-ground faults in active distribution networks," International Journal of Electrical Power & Energy Systems, vol. 107, pp. 403-411, 2019.

[22] M. Išlić, S. Sučić, J. Havelka, and A. Marušić, "Centralized radial feeder protection in electric power distribution using artificial neural networks," Sustainable energy, grids and networks, vol. 22, p. 100331, 2020.

[23] D. Orazgaliyev, A. Tleubayev, B. Zholdaskhan, H. K. Nunna, A. Dadlani, and S. Doolla, "Adaptive coordination mechanism of overcurrent relays using evolutionary optimization algorithms for distribution systems with DGs," in 2019 International Conference on Smart Energy Systems and Technologies (SEST), 2019: IEEE, pp. 1-6.

[24] S. D. Saldarriaga-Zuluaga, J. M. López-Lezama, and N. Muñoz-Galeano, "Adaptive protection coordination scheme in microgrids using directional over-current relays with non-standard characteristics," Heliyon, vol. 7, no. 4, 2021.

[25] H. Liang, H. Li, and G. Wang, "A Single-Phase-to-Ground Fault Detection Method Based on the Ratio Fluctuation Coefficient of the Zero-Sequence Current and Voltage Differential in a Distribution Network," IEEE Access, vol. 11, pp. 7297-7308, 2023.

[26] A. Ataee-Kachoee, H. Hashemi-Dezaki, and A. Ketabi, "Optimized adaptive protection coordination of microgrids by dual-setting directional overcurrent relays considering different topologies based on limited independent relays' setting groups," Electric Power Systems Research, vol. 214, p. 108879, 2023.

[27] P. Mahat, Z. Chen, B. Bak-Jensen, and C. L. Bak, "A simple adaptive overcurrent protection of distribution systems with distributed generation," IEEE Transactions on Smart Grid, vol. 2, no. 3, pp. 428-437, 2011.

[28] A. Hussain and H.-M. Kim, "A hybrid framework for adaptive protection of microgrids based on IEC 61850," International Journal of Smart Home, vol. 10, no. 5, pp. 285-296, 2016.

[29] H. Laaksonen, D. Ishchenko, and A. Oudalov, "Adaptive protection and microgrid control design for Hailuoto Island," IEEE Transactions on Smart Grid, vol. 5, no. 3, pp. 1486-1493, 2014.

[30] E. Dehghanpour, H. K. Karegar, R. Kheirollahi, and T. Soleymani, "Optimal coordination of directional overcurrent relays in microgrids by using cuckoo-linear

optimization algorithm and fault current limiter," IEEE Transactions on Smart Grid, vol. 9, no. 2, pp. 1365-1375, 2016.

[31] W. K. Najy, H. H. Zeineldin, and W. L. Woon, "Optimal protection coordination for microgrids with grid-connected and islanded capability," IEEE Transactions on industrial electronics, vol. 60, no. 4, pp. 1668-1677, 2012.

[32] M. H. Cintuglu, T. Ma, and O. A. Mohammed, "Protection of autonomous microgrids using agent-based distributed communication," IEEE Transactions on Power Delivery, vol. 32, no. 1, pp. 351-360, 2016.

[33] H. M. Sharaf, H. H. Zeineldin, and E. El-Saadany, "Protection coordination for microgrids with grid-connected and islanded capabilities using communication assisted dual setting directional overcurrent relays," IEEE Transactions on Smart Grid, vol. 9, no. 1, pp. 143-151, 2016.

[34] M. N. Alam, R. Gokaraju, and S. Chakrabarti, "Protection coordination for networked microgrids using single and dual setting overcurrent relays," IET Generation, Transmission & Distribution, vol. 14, no. 14, pp. 2818-2828, 2020.

[35] S. P. Ramli, H. Mokhlis, W. R. Wong, M. A. Muhammad, and N. N. Mansor, "Optimal coordination of directional overcurrent relay based on combination of Firefly Algorithm and Linear Programming," Ain Shams Engineering Journal, vol. 13, no. 6, p. 101777, 2022.

[36] A. Saber, H. Zeineldin, T. H. EL-Fouly, and A. Al-Durra, "A signed correlation index-based differential protection scheme for inverter-based islanded microgrids," International Journal of Electrical Power & Energy Systems, vol. 145, p. 108721, 2023.

[37] S. M. Nobakhti, A. Ketabi, and M. Shafie-khah, "A new impedance-based main and backup protection scheme for active distribution lines in ac microgrids," Energies, vol. 14, no. 2, p. 274, 2021.

[38] A. Chandra, G. Singh, and V. Pant, "A novel protection strategy for microgrid based on estimated differential energy of fault currents," Electric Power Systems Research, vol. 214, p. 108824, 2023.

[39] A. H. Ataee-Kachoee, H. Hashemi Dezaki, and A. Ketabi, "Optimized Microgrid Protection Considering Different Topologies Based on N-1 Contingency by Dual Setting Directional Overcurrent Relays," International Journal of Industrial Electronics Control and Optimization, vol. 5, no. 3, pp. 205-213, 2022.

[40] F. Özveren and Ö. Usta, "A power based integrated protection scheme for active distribution networks against asymmetrical faults," Electric Power Systems Research, vol. 218, p. 109223, 2023.

[41] Q. Lai, Z. Zhang, K. Xu, and X. Yin, "A new method of fault direction identification for different types of renewable energy source integrations," IEEE Transactions on Power Delivery, vol. 37, no. 4, pp. 2932-2941, 2021.

[42] L. KANDASAMY and K. Jaganathan, "Intelligent protection scheme using combined Stockwell-Transform and deep learning-based fault diagnosis for the active distribution system," Turkish Journal of Electrical Engineering and Computer Sciences, vol. 32, no. 2, pp. 234-250, 2024.

[43] A. R. Adly and M. E. Rezk, "Optimal Protection Scheme for Distribution Systems Integrated with Distributed Generator," Arab Journal of Nuclear Sciences and Applications, vol. 57, no. 1, pp. 100-106, 2024.

[44] L. Wang, X. Song, and W. Jiang, "Differential protection scheme for distribution network with distributed generation based on improved feature mode decomposition and derivative dynamic time warping," Frontiers in Energy Research, vol. 12, p. 1369880, 2024.

[45] K. Dubey and P. Jena, "Novel Fault detection & classification index for active distribution network using differential components," IEEE Transactions on Industry Applications, 2024.

[46] Z. Moravej, A. Ebrahimi, and M. Barati, "A new differential protection scheme based on Synchro-squeezing transform applied to AC Micro-Grid," Electric Power Systems Research, vol. 231, p. 110336, 2024.

[47] L. S. Czarnecki, "Comparison of power definitions for circuits with nonsinusoidal waveforms," IEEE Tutorial Course 90EH0327-7-PWR, pp. 43-50, 1990.

[48] J. F. Kaiser, "On a simple algorithm to calculate the'energy'of a signal," in International conference on acoustics, speech, and signal processing, 1990: IEEE, pp. 381-384.

[49] W. Huang, T. Nengling, X. Zheng, C. Fan, X. Yang, and B. J. Kirby, "An impedance protection scheme for feeders of active distribution networks," IEEE transactions on power delivery, vol. 29, no. 4, pp. 1591-1602, 2014.

[50] H. J. Laaksonen, "Protection principles for future microgrids," IEEE Transactions on power electronics, vol. 25, no. 12, pp. 2910-2918, 2010.

[51] G. Benmouyal et al., "IEEE standard inverse-time characteristic equations for overcurrent relays," IEEE Transactions on Power Delivery, vol. 14, no. 3, pp. 868-872, 1999.

Reza Karimi was born in Esfahan**,** Iran**.** He received his B.S.c degree in Electrical Engineering from Shahid Rajaee Kashan National University of Skill and his M.S.c degree in Power Electrical Engineering from University of Kashan in 2021 and 2024, respectively. He has been a lecturer at National University of Skill since 2022. His research interests include microgrid protection and power electronics.

Abbas Ketabi received his B.Sc. and M.Sc. degrees in electrical engineering from the Department of Electrical Engineering, Sharif University of Technology, Tehran, Iran, in 1994 and 1996, respectively. He received his Ph.D. degree in electrical engineering jointly from Sharif University of Technology and the Institute National Polytechnique de Grenoble (INPG), Grenoble, France, in 2001. Since 2001, he has been at the University of Kashan, Department of Electrical Engineering. He is currently a Full Professor. He has published more than 130 technical papers and 6 books. He is the Director-in-Charge and editor of the "Energy Engineering and Management" journal. Dr. Ketabi was the recipient the University of Kashan Award for Distinguished Teaching and research. His research interests include power system restoration, power system protection, smart grids, renewable energy, optimization of electric machines, power electronics, and evolutionary computation.

Seyyed Mohammad Nobakti was born in Kashan, Iran, in 1985. He received his M.S. degree from the Faculty of Engineering at Shahed University, Tehran, Iran, in 2011. He obtained his Ph.D. in Electrical Engineering from the Department of Electrical and Computer Engineering at the University of Kashan, Kashan, Iran, in 2021. He is an instructor in the Department of Electrical Engineering at the National University of Skills (NUS) in Tehran, Iran. His current research interests include power electronics and protection in power systems.

International Journal Of
Industrial Electronics Control and Optimization
Print ISSN: 3517-2645
Online ISSN: 3568-2645
Homepage: https://ieco.usb.ac.ir/

Novel Modeling and Nonlinear Control of the Siwakoti-H Inverter Considering Flying Capacitor Voltage Balance for Photovoltaic Applications

A. M. Mohammadi[1] | N. R. Abjadi[2] | G. R. Arab Markadeh[3]

Faculty of Engineering, Shahrekord University, Shahrekord, Iran. [1,2]
Department of Electrical Engineering, Faculty of Engineering, Ferdowsi University of Mashhad, Mashhad, Iran. [3]
Corresponding author's email: abjadi.navidreza@sku.ac.ir

Article Info

Article type:
Research Article

Article history:
Received: 31-January-2025
Received in revised form: 16-March-2025
Accepted: 03-April-2025
Published online: 23-Sep-2025

Keywords:
feedback linearization,
flying capacitor,
photovoltaic,
Siwakoti-H inverter.

ABSTRACT

The Siwakoti-H inverter (SHI) with a flying capacitor is a recent addition to the transformerless inverter family, suitable for grid-connected single-phase photovoltaic systems. It offers a promising alternative to traditional topologies without the need for transformers, due to its minimal power electronic components. However, one of the key challenges in managing flying capacitor (FC) inverters is ensuring that the voltage of the FC remains within the desired range. Materials and Methods: To tackle this issue, first, a novel nonlinear model of the SHI is obtained defining two control inputs and two control outputs, and then a nonlinear feedback linearization (FBL) control design is proposed for the SHI when connected to a single-phase grid. This article introduces a novel approach to the modeling and control of the SHI enabling simultaneous control of both the injected current to the grid and the flying capacitor voltage. The proposed modeling and the designed control method play a crucial role in maintaining the capacitor voltage within the specified range and in tracking a sinusoidal reference for the injected current into the single-phase network. A PWM implementation of the proposed control is also suggested which is useful in the practical setup. The obtained model can be extended for the SHI with other line filters and it can be used to design more sophisticated controllers for SHI. The simulation and practical results presented in this study demonstrate the effectiveness of the proposed modeling and control approach.

I. Introduction

Power electronics converters play a crucial role in converting and regulating electric power in grid-connected renewable energy systems through the switching patterns [1]. The focus on renewable energy systems, such as wind turbines and photovoltaic systems has been on achieving high efficiency over the past decade [2-4]. In [3], a microgrid with renewable energy sources is investigated and complicated controllers are designed. In [4], a power system with some distributed wind resources is considered and some sophisticated nonlinear controllers are designed for the system.

To minimize losses within the system, utilizing converter topologies with fewer switching elements is essential. In addition, there is a growing tendency in photovoltaic systems towards not using transformers in converters [5-6]. Transformerless inverter has higher efficiency, less weight and lower cost compared to inverter with transformer; however, conventional single-phase grid-connected photovoltaic systems suffer from leakage current [7]. Besides safety issue, the leakage current increases grid current ripples, photovoltaic system losses and electromagnetic interference (EMI) [8]. The leakage current is more investigated in [9]. In [10-12], three multi-level switched-capacitor inverters are proposed which are not suitable for grid-connected transformerless photovoltaic application due to the issue of leakage current. In [13], a fifteen-level inverter which has several DC sources and suffers from leakage current.

Copyright © N. R. Abjadi(s).
Publisher: University of Sistan and Baluchestan

There are various transformerless single-phase inverters which eliminate or reduce leakage current such as HERIC, H5, H6 [14, 8]; however, compared to conventional H-bridge inverter, these inverters have additional switches; some of them need special modulations or can't inject reactive power to the grid. In [15], an H-bridge less grid-tied multilevel inverter is proposed which reduce the leakage current significantly; however, it cannot be built with the available conventional H-bridges.

Some of the configurations use common ground to omit the leakage current. In these configurations the negative end of the solar panel is connected to the grid neutral directly. In [16] and [17] two common ground transformerless inverters are proposed which have simple configurations. They have an additional capacitor compared to conventional H bridge inverter. This capacitor is called the flying capacitor (FC). The inverter in [17] is called Siwakoti H inverter (SHI). There are three types of single-phase inverters with FC for photovoltaic grid-connected applications: Type-I, which has two switches in series during positive cycle [18]. This type can be implemented using two half-bridges and an additional diode. Type-II, which has a single switch in series during the positive cycle [18]. The components of this type are the same as those of type-I. Type-III or SHI which is discussed in this paper. Other types of single-phase inverters for photovoltaic grid-connected applications are reviewed in [19].

The SHI is a notable transformerless inverter topology that has gained attention [18]. This innovative design, which consists of only four switches, operates based on the flying capacitor principle [17]. What sets this topology apart is its ability to meet the needs of both positive and negative voltage sources using a single flying capacitor. Consequently, the number of the input voltage sources is reduced in comparison to the three-level neutral point clamp converter. Compared to the conventional H-bridge inverter, the SHI eliminates leakage current while using the same number of switches and a very similar topology. Compared to the HERIC, the SHI has less components and it can also inject reactive power to the grid without any special modulation technique. For a single-phase photovoltaic system, it is noteworthy that the nominal power is limited to 5KVA and given the relatively high costs of the solar power system, it is usually preferred to inject only active power into the grid. In the past, the operation of the grid-connected SHI was analyzed using a state feedback controller [20]. While the controller demonstrated satisfactory steady-state performance for the mentioned converter, it exhibited a noticeable deviation near the zero crossing of injected current to the grid. Besides, the FC voltage is decreased during the discharge state. This phenomenon can be attributed to the abrupt transition of the power from the input source to the floating capacitor. To address this issue and enhance the dynamic response, an alternative approach, utilizing direct/indirect model predictive control (MPC) strategy for a grid-connected SHI has been suggested in [21-22]. Both papers address the unbalancing issue of the FC voltage; however, the presented controls are not perfect. Considering a cost function to control the injected current and the FC voltage simultaneously is not enough to achieve perfect tracking and selection of the weights in the cost function is also difficult. In addition, despite the offline computation, the computation in the controllers is still high, which consumes DSP time.

Nonlinear control methods address complex challenges by analyzing and designing systems with nonlinear components [23-24]. They offer diverse and powerful techniques, established in industrial applications. Feedback linearization methods, such as input-output feedback linearization (IOFL), solve the tracking problem in many systems and provide the stability of the closed-loop system [25]. In this paper, first a suitable model is obtained for SHI, then using this model an IOFL control is designed to achieve injected current reference tracking and the FC voltage balancing.

The organization of the paper is as follows: In section II the SHI is described and its operation is discussed. A new modeling of SHI is obtained in section III. A nonlinear controller is designed for SHI in section IV. Simulation and practical results are shown in sections IV and V respectively. Finally the conclusions are provided in section VI.

II. SHI description and operation

The circuit diagram of the SHI connected to a single-phase grid is depicted in Fig. 1. The SHI consists of four power switches and a capacitor, as shown in Fig. 1. Among these switches, S1 and S4 function as bipolar voltage blocking switches, while S2 and S3 serve as unipolar voltage blocking switches [17]. Consequently, switches S2 and S3 are implemented using MOSFETs or IGBTs, whereas switches S1 and S4 are implemented using a reverse blocking IGBTs (RB-IGBTs) or MOSFETS with blocking diodes. C_F is the FC. Since the polarity of the voltage across the FC does not change and it must be large enough to store energy to generate the negative voltage, a polarized electrolytic capacitor can be used as the FC. There is no need for an AC capacitor to serve as the FC. The inductance L is used as a filter to connect the inverter to the grid. As it is seen, the negative end of the input source is connected to the neutral of the grid and the DC and AC sections have a common ground.

TABLE I THE STATES OF THE SHI SWITCHES FOR THE OPERATIONAL MODES

Mode	S1	S2	S3	S4
P	0	0	1	0
Z	1	0	0	1
N	0	1	0	0

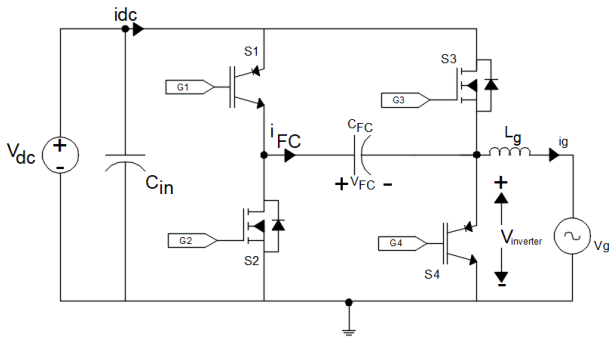

Fig. 1. The SHI connected to a single-phase grid

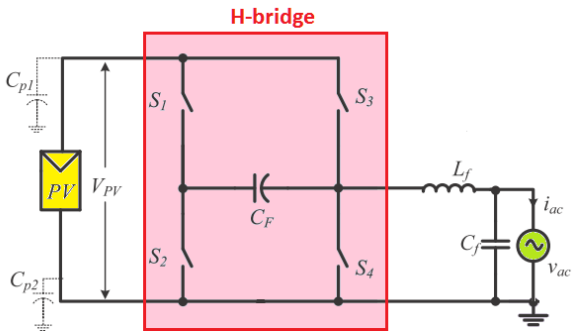

Fig. 2. The SHI fed from a photovoltaic panel and the parasitic capacitors

In Fig. 2, it is shown when the source is a photovoltaic panel, using the common ground, the parasitic capacitors of the panel cannot generate leakage current. In fact, the parasitic capacitor connected to the negative end is short circuited and the parasitic capacitor connected to the positive end has a constant voltage and its current equals zero.

A notable characteristic of this configuration is the utilization of the input DC source to fulfill the negative voltage required for the negative mode. This is accomplished by cyclically charging and discharging the FC, resulting in a virtual negative forward link, as illustrated in Figure 3.

The operation of the SHI can be described in three modes: positive (P) mode, negative (N) mode, and zero (Z) mode, as depicted in Fig. 4. During the P and N modes, switches S3 and S2 are activated, respectively. In the Z mode, switches S1 and S4 are activated to provide the zero voltage at the output and to charge the FC.

III. Modeling of the SHI

The three operational modes of the SHI are summarized in Table I. For each of these modes, an equivalent circuit can be obtained which are shown in Fig. 5. In the following, considering the FC voltage (x_1) and the inductor current (x_2) as state variables, the state-space equations of each mode is obtained; then these equations are combined to achieve the average model of the SHI.

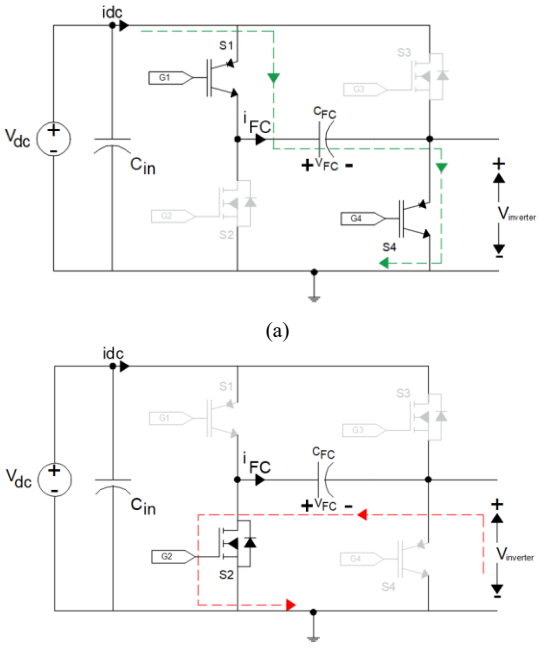

(a)

(b)

Fig. 3. Illustration of the charging and discharging of the FC, a) charging mode b) discharging mode wherein the capacitor uses as a virtual negative DC-link.

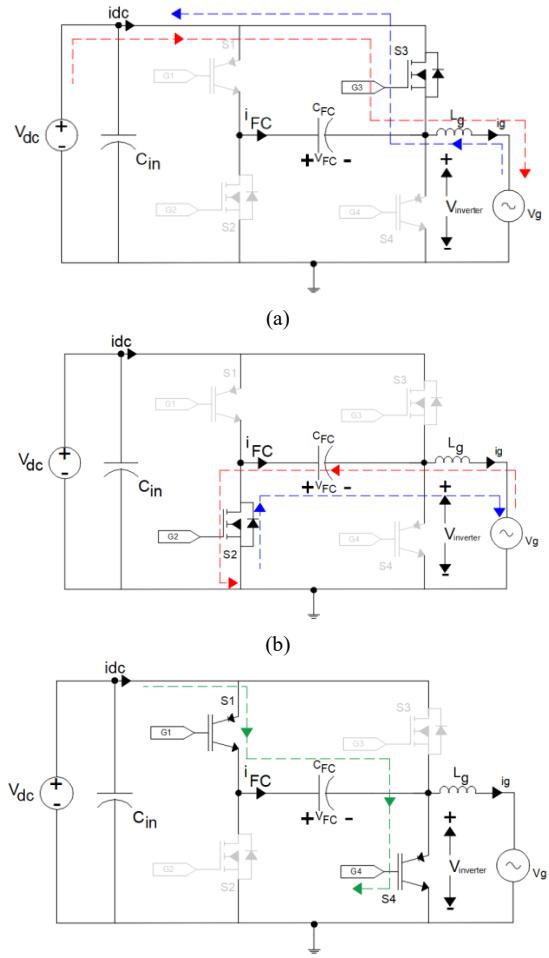

(a)

(b)

(c)

Fig. 4. The three operational modes of the SHI: a) P mode b) N mode c) Z mode

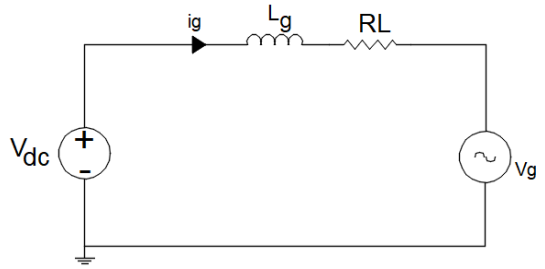

(a)

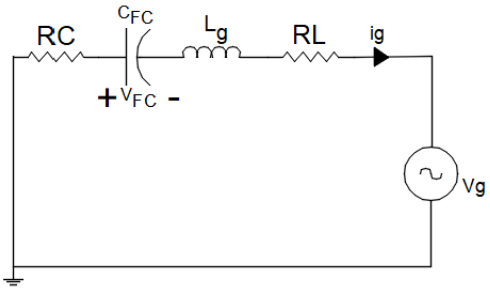

(b)

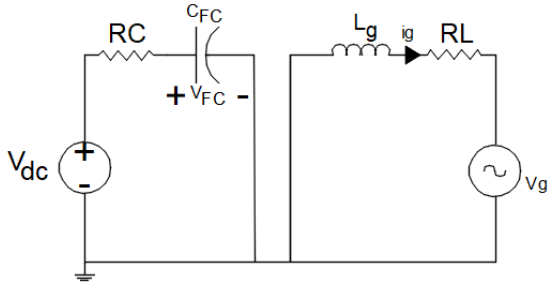

(c)

Fig. 5. The equivalent circuits of the SHI: a) P mode b) N mode c) Z mode

A. P mode

Referring to Fig. 5.a and using Kirchhoff voltage/current laws, one can obtain

$$i_{C_{FC}} = 0 \tag{1}$$

$$V_{dc} = Lg\frac{di_L}{dt} + R_L i_g + V_g \tag{2}$$

where R_L is the equivalent series resistance (ESR) of the inductor.

These equations can be rewritten as

$$\dot{x}_1 = 0 \tag{3}$$

$$\dot{x}_2 = \frac{V_{dc} - V_g - R_L x_2}{Lg} \tag{4}$$

B. N mode

Referring to Fig. 5.b and using Kirchhoff voltage/current laws, one can obtain

$$i_{C_{FC}} = i_g \tag{5}$$

$$V_{C_{FC}} + V_L + V_{Lg} + (R_C + R_L)i_g = 0 \tag{6}$$

where R_C is the ESR of the FC.

These equations can be rewritten as

$$\dot{x}_1 = \frac{x_2}{C_{FC}} \tag{7}$$

$$\dot{x}_2 = \frac{-V_g - x_1 - (R_C + R_L)x_2}{Lg} \tag{8}$$

C. Z mode

Referring to Fig. 5.c and using Kirchhoff voltage/current laws, one can obtain

$$-V_{dc} + V_{C_{FC}} + R_C i_{C_{FC}} = 0 \tag{9}$$

$$R_L i_L + V_L + V_g = 0 \tag{10}$$

These equations can be rewritten as

$$\dot{x}_1 = \frac{V_{dc} - x_1}{R_C C_{FC}} \tag{11}$$

$$\dot{x}_2 = \frac{-V_g - R_L x_2}{Lg} \tag{12}$$

D. Average model

To obtain the average model, the following duty-cycles are defined for P, N and Z modes:

$$u^+ = \frac{t^+}{T} \tag{13}$$

$$u^- = \frac{t^-}{T} \tag{14}$$

$$u^0 = \frac{t^0}{T} \tag{15}$$

where t^+, t^- and t^0 are the time intervals of P, N and Z modes respectively; T is the switching period.

It is notable that

$$u^+ + u^- + u^0 = 1 \tag{16}$$

Multiply (3)-(4), (7)-(8) and (11)-(12) by (13), (14) and (15) respectively. From the sum of the results and using (16), it is concluded that:

$$\dot{x} = A + BW \tag{17}$$

where

$$A = \begin{bmatrix} \frac{V_{dc} - x_1}{R_C C_{FC}} \\ \frac{-V_g - R_L x_2}{Lg} \end{bmatrix} \tag{18}$$

$$B=\begin{bmatrix} \frac{x_1-V_{dc}}{C_{FC}R_C} & \frac{x_1-V_{dc}}{C_{FC}R_C}+\frac{x_2}{C_{FC}} \\ \frac{V_{dc}}{Lg} & \frac{-x_1-R_Cx_2}{Lg} \end{bmatrix} \quad (19)$$

$$x^T=\begin{bmatrix} V_{C_{FC}} & i_g \end{bmatrix} \quad (20)$$

$$W^T=\begin{bmatrix} u^+ & u^- \end{bmatrix} \quad (21)$$

where W is the control input vector.

It is notable that (17) is a nonlinear system.

IV. FBL control

The SHI exhibits nonlinear behavior due to the product of the state and input variables. In this section, using the new model obtained in (17), a FBL controller is designed for SHI. The FBL controller is designed based on the input-output linearization. The basic approach of input-output linearization is simply to differentiate the outputs functions repeatedly until the inputs appear and then design the inputs to cancel the nonlinearity and the coupling.

A. FBL controller design

Define the following tracking errors:

$$e_1 = x_1 - x_1^*$$

$$e_2 = x_2 - x_2^*$$

where x_1^* and x_2^* are reference values. One can consider e_1 and e_2 as new outputs and their desired values are 0.

Differentiating (22) and (23) with respect to time and substituting from (17), one can obtain:

$$\dot{e}_1 = \dot{x}_1 - \dot{x}_1^* = a_1 + b_{11}u^+ + b_{12}u^- - \dot{x}_1^* \quad (22)$$

$$\dot{e}_2 = \dot{x}_2 - \dot{x}_2^* = a_2 + b_{21}u^+ + b_{22}u^- - \dot{x}_2^* \quad (23)$$

where a_i and b_{ij} are the elements of (18) and (19) respectively.

By equating (22) with $-k_1e_1$ and (23) with $-k_2e_2$, the result is:

$$\dot{e}_1 + k_1e_1 = 0 \quad (24)$$

$$\dot{e}_2 + k_2e_2 = 0 \quad (25)$$

By choosing positive coefficients k_1 and k_2, the errors converge to zero exponentially.

By comparing (22) with (24) and (23) with (25), it is concluded that:

$$u = \begin{bmatrix} u^+ \\ u^- \end{bmatrix} = B^{-1}\left(\begin{bmatrix} \dot{x}_1^* \\ \dot{x}_2^* \end{bmatrix} - A - \begin{bmatrix} k_1e_1 \\ k_2e_2 \end{bmatrix}\right) \quad (26)$$

Eq. (26) is the FBL control law. Selecting k_is large enough, the errors converge to zero rapidly.

B. Stability analysis

The system described by (17) or (22)-(23) is a multi-input multi-output (MIMO) square system with two inputs (u^-, u^+) and two outputs (e_1, e_2). The system order n is 2. The number r_i of differentiations required for one of the inputs (u^-, u^+) to appear in the derivatives of output e_i is called the relative degree of the corresponding subsystem. For the MIMO system the relative degree is $(r_1, r_2) = (1,1)$. The total relative degree is $r = r_1 + r_2 = 2$ which is equal to the system order n=2. In this case, there is no internal dynamics. The control law (26) guarantees the exponential convergence of errors to 0 without any need to worry about the stability of the internal dynamics or zero dynamics. Based on the fact that there is no zero dynamic, the system is also a minimum phase system [23].

To check the singularity of the proposed controller, the determinant of matrix B in (19) is obtained:

$$\det(B) = \frac{1}{L_gC_{FC}R_C}(2V_{dc}x_1 + 2V_{dc}R_Cx_2 - x_1^2 - R_Cx_1x_2 + V_{dc}^2) \quad (27)$$

This determinant rarely becomes zero.

Assuming $x_1 \approx V_{dc}$ one can obtain:

$$\det(B) \approx \frac{1}{L_gC_{FC}R_C}(2V_{dc}^2 + V_{dc}R_Cx_2) \quad (28)$$

Moreover, assuming $|R_Cx_2| \ll V_{dc}$ it is concluded that:

$$\det(B) \approx \frac{1}{L_gC_{FC}R_C}(2V_{dc}^2) > 0 \quad (29)$$

C. Implementation Dwell times with PWMS

To implement this control law using PWM technique, one can consider the following procedure. The gates pulses based on t^+, t^- and t^0 are shown in Fig. 6.a. Comparing the pulses in Fig. 6.a and the PWM signals in Fig. 6.b, one can obtain the gates pulses as:

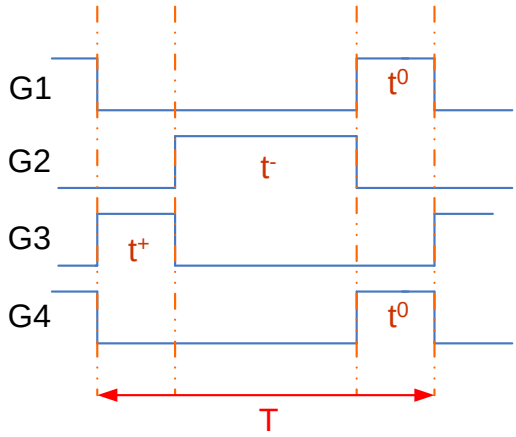

(a)

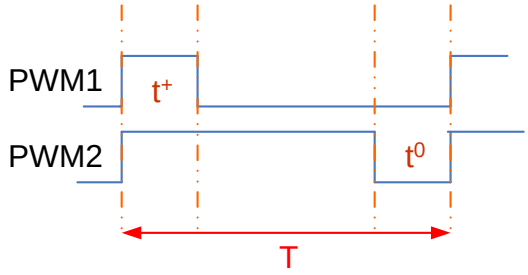

(b)

Fig. 6. Dwell times and PWM pulses, a) gates pulses, b) PWM signals

$$G_1 = G_4 = \overline{PWM_2} \quad (30)$$

$$G_2 = \overline{PWM_1} \bigwedge PWM_2 \quad (31)$$

$$G_3 = PWM_1 \quad (32)$$

V. Simulation results

To show the validity and the effectiveness of the proposed model and the proposed controller, some simulation results are obtained using PSIM software. Details of the parameters used in all simulation runs are provided in Table II.

In Fig. 7 the simulation results of PI control without controlling the FC voltage is presented. It is seen that the FC voltage changes a lot, which can cause problems for the inverter. Even the overall closed-loop system may become unstable.

In Fig. 8 the simulation results of FBL control are presented. It is seen that the injected current to the grid tracks its reference perfectly. The FC voltage is also near its reference; however it has pulsations. This phenomenon is due to the instantaneous power at the single-phase ac port, which pulsates at twice the AC voltage frequency, generating the second harmonic current at the DC bus.

FBL does not inherently account for the uncertainties, making it less robust in practical scenarios where exact

TABLE II SHI AND CONTROLLER PARAMETERS VALUES

Parameter	Value
DC input voltage	20 v
Switching frequency	2 KHz
Line frequency	50 Hz
FC	1000 µF-35v
Filter inductor	20 mH
r_L	1Ω
r_C	1 Ω
k_1	250
k_2	9500

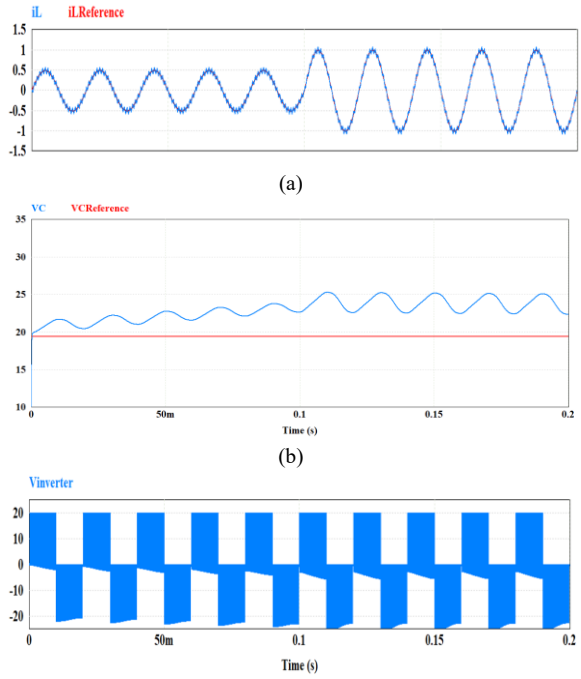

Fig. 7. The simulation results of PI control without FC voltage control, a) the injected current and its reference, b) the FC voltage and its reference, c) the inverter voltage

system parameters are unknown or subject to variation. To demonstrate the resilience of the designed control, an additional simulation test has been added, considering a 20% error in the values of the FC and the inductor. The results of this test are presented in Fig. 9. It is seen with small inaccuracy in the parameters, small deviations are appeared between the responses and their references. To achieve a robust control, the designed FBL control should be combined with sliding mode control or adaptive control techniques.

VI. Experimental results

Fig. 10 shows the experimental setup. To implement the proposed controller a Discovery board is used. It has a 32 bit STM32F407 microcontroller. This microcontroller has 1 MB of Flash memory, 192 KB of RAM, 17 timers, 3 ADCs and 2 DACs. This device provides a 168 MHz/210 DMIPS

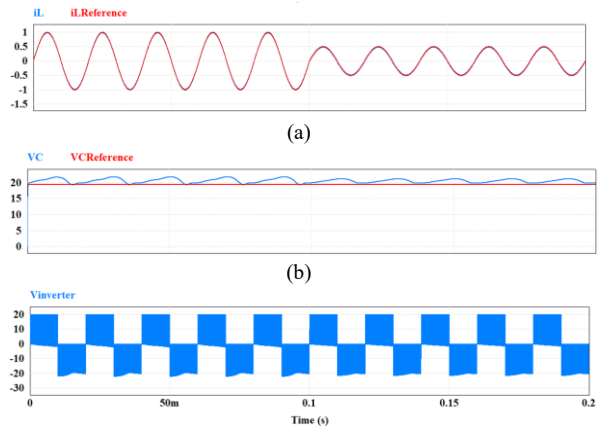

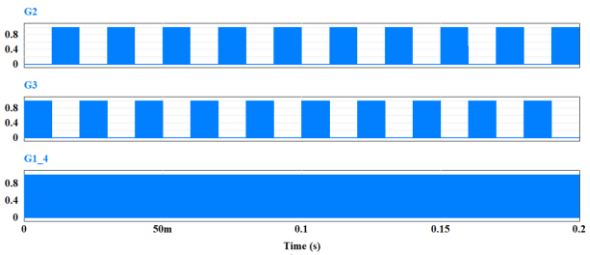

(c)

(d)

Fig. 8. The simulation results of FBL control, a) the injected current and its reference, b) the FC voltage and its reference, c) the inverter voltage, d) the pulses of gates

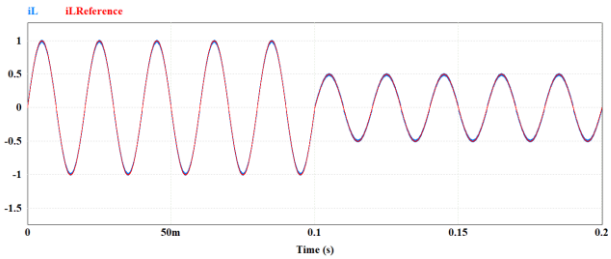

(a)

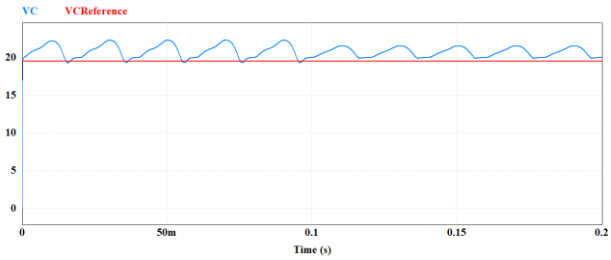

(b)

Fig. 9. The simulation results of FBL control with 20% error in some parameters, a) the injected current and its reference, b) the FC voltage and its reference

Cortex-M4 with single cycle DSP MAC and floating point unit suitable to measure the required variables and to implement the nonlinear controller.

Two signals are measured and fed back to the control system: the FC voltage (x_1) and the inductor current (x_2). The advantage of feeding back of these two variables is the simultaneous control of the FC voltage and the injected current into the grid.

In Fig. 11 the obtained practical results using the proposed FBL control are shown. In Figs. 11.a and 11.b, the injected current and its reference are shown in both increase and decrease of the injected current. In both case, the injected current tracks its reference. In Fig. 11.c the FC voltage is shown during the increase of the injected current. The ripple on FC voltage is from second order harmonics in single-phase system and it is increased when the injected current is increased as seen in the Fig. 11.c. Using the proposed FBL control, the FC voltage does not deviate. The DC voltage input is also shown in Fig. 11.d

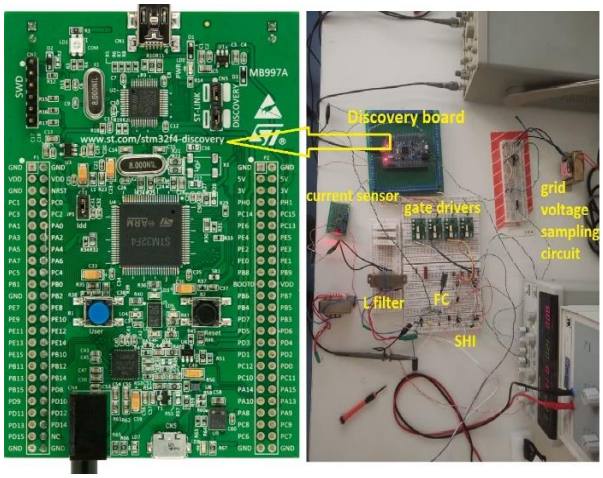

Fig. 10. The experimental setup

VII. Conclusions

In this paper, a new model is developed for the SHI. A novel controller for the SHI is proposed based on the FBL control. The deviation of the FC voltage is investigated and it is demonstrated that such deviations can be avoided using the proposed control. The proposed control is compared with conventional PI control and it is shown that the proposed controller can control the injected current and the FC voltage simultaneously. To implement the proposed control using PWM techniques, particularly in practical setups, an innovative method is suggested. Simulation and practical results are obtained and the superiority and effectiveness of the proposed modeling and control are verified. It is observed that although the experimental results are slightly less accurate than the simulation results, the overall patterns of the outcomes remain consistent. The innovative obtained model of the SHI can be used to design more sophisticated controllers. To improve robustness, the FBL control can be combined with robust control techniques such as adaptive control or sliding mode control techniques in future research works.

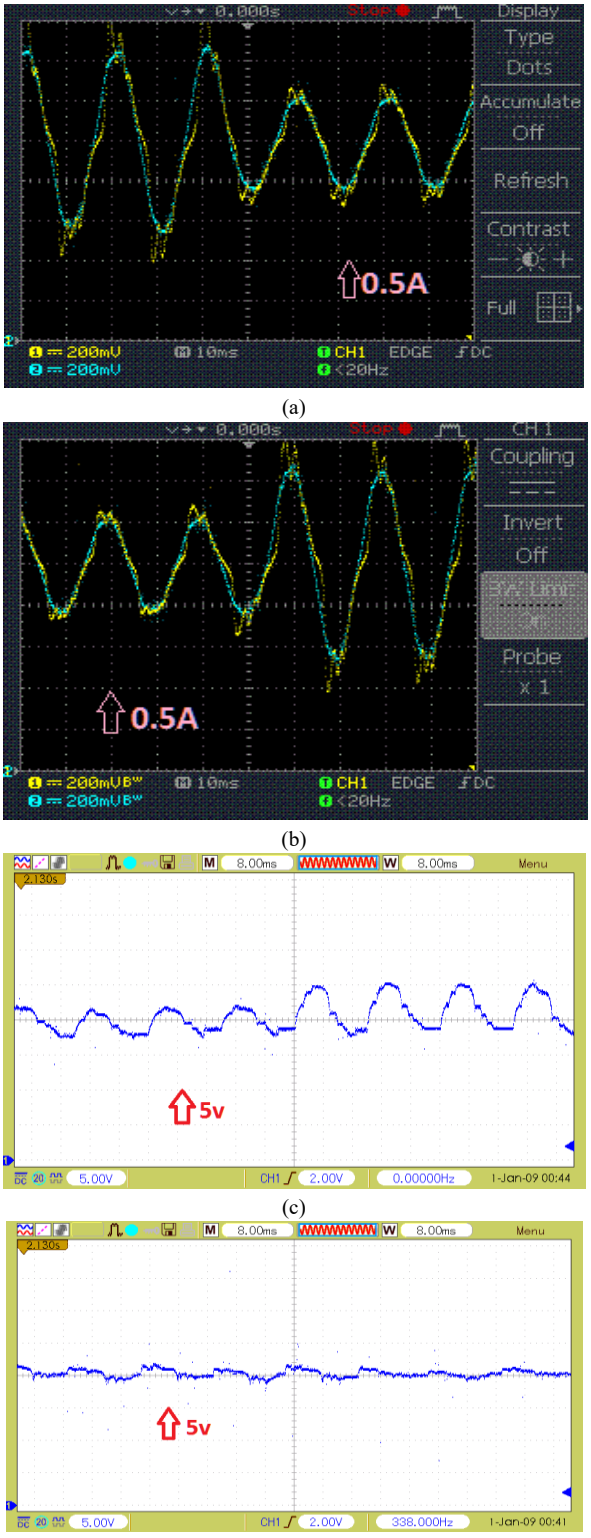

(a)

(b)

(c)

(d)

Fig. 11. The practical results, a) increasing current, b) decreasing current, c) FC voltage, d) input DC voltage

REFERENCES

[1] L. A. Kumar, S. A. Alexander, M. Rajendran, Power Electronic Converters for Solar Photovoltaic Systems, Academic Press, 2020, doi: 10.1016/C2019-0-04270-7.

[2] I. Dincer, M. Temiz, Renewable Energy Options for Power Generation and Desalination, Springer, 2024, doi: 10.1007/978-3-031-53437-9.

[3] N. R. Abjadi, "Adaptive Input-Output Feedback Linearization Control for Islanded Inverter-Based Microgrids," International Journal of Industrial Electronics, Control and Optimization (IECO), Vol. 6, No. 3, 2023, doi: 10.22111/ieco.2023.44787.1465.

[4] S. Abazari, "Novel Non-linear Control of DFIG and SSSC for Stability Increment of Power System," International Journal of Industrial Electronics, Control and Optimization (IECO), Vol. 7, No. 1, 2024, 10.22111/ieco.2023.45795.1485.

[5] H. Xiao, X. Wang, Transformerless Photovoltaic Grid-Connected Inverters, Springer, 2021, doi: 10.1007/978-981-15-8525-8.

[6] M. Farhadi-Kangarlu, F. Mohammadi, "Performance Improvement of Single-Phase Transformer less Grid-Connected PV Inverters Regarding the CMV and LVRT," Journal of Operation and Automation in Power Engineering, Vol. 7, No. 1, 2019, doi: 10.22098/JOAPE.2019.4366.1344.

[7] Md. F. Kibria, A. Elsanabary, K. S. Tey, M. Mubin, S. Mekhilef, "A Comparative Review on Single Phase Transformerless Inverter Topologies for Grid-Connected Photovoltaic Systems," Energies, Vol. 16, No. 1362, 2023, doi: 10.3390/en16031363.

[8] T. K. S. Freddy, N. A. Rahim, W.-P. Hew, H. S. Che, "Comparison and Analysis of Single-Phase Transformerless Grid-Connected PV Inverters," IEEE Transactions on Power Electronics, Vol. 29, No. 10, 2014, doi: 10.1109/TPEL.2013.2294953.

[9] H. Xiao, S. Xie, "Leakage Current Analytical Model and Application in Single-Phase Transformerless Photovoltaic Grid-Connected Inverter," IEEE Transaction on Electromagnetic Compability, Vol. 52, No. 4, 2010, doi: 10.1109/TEMC.2010.2064169.

[10] M. Derakhshandeh, M. Hosseinpour, A. Seifi, M. Shahparasti, "An enhanced 13-level triple voltage gain switched capacitor inverter with lower power electronics devices," IET Power Electronics, 2024, doi: 10.1049/pel2.12748.

[11] A. Vijayakumar, A. A. Stonier, G. Peter, E. Vignesh, V. Ganji, "Machine learning based model predictive control for grid connected enhanced switched capacitor cross-connected switched multi-level inverter (ESC3SMLI)," IET Power Electronics, 2023, doi: 10.1049/pel2.12546.

[12] M. Noori, M. Hosseinpour, S. R. Mousavi-Aghdam, "Single Source Switched Capacitor Multilevel inverter with Voltage Boosting Capability and Low Switch Count," Journal of Iranian Association of Electrical and Electronics Engineers (JIAEEE), No. 2, 2024, doi: 10.61186/jiaeee.21.2.47.

[13] Y. Joshi, S. S. Letha, F. I. Bakhsh, G. L. Jaat, S. Tilak, "Harmonic elimination of a fifteen-level inverter with reduced number of switches using genetic algorithm," IET Power Electronics, 2023, doi: 10.1049/pel2.12622.

[14] T. K. S. Freddy, J.-H. Lee, H.-C. Moon, K.-B. Lee, N. A. Rahim, "Modulation Technique for Single-Phase Transformerless Photovoltaic Inverters With Reactive Power Capability," IEEE Transaction on Industrial Electronics, Vol. 64, No. 9, 2017, doi: 10.1109/TIE.2017.2686366.

[15] T. Debela, J. Singh, V. K. Sood, "An assessment of H-bridge less grid-tied multilevel inverter with minimum

device count and lesser total standing voltage," IET Power Electronics, 2023, doi: 10.1049/pel2.12566.
[16] Y. P. Siwakoti, F. Blaabjerg, "A Novel Flying Capacitor Transformerless Inverter for Single-Phase Grid Connected Solar Photovoltaic System," 2016 IEEE 7th International Symposium on Power Electronics for Distributed Generation Systems (PEDG), Canada, 2016, doi: 10.1109/PEDG.2016.7527086.
[17] Y. P. Siwakoti, F. Blaabjerg, "H-Bridge Transformerless Inverter with Common Ground for Single-Phase Solar-Photovoltaic System," 2017 IEEE Applied Power Electronics Conference and Exposition (APEC), USA, 2017, doi: 10.1109/APEC.2017.7931066.
[18] Y. P. Siwakoti, F. Blaabjerg, "Common-Ground-Type Transformerless Inverters for Single-Phase Solar Photovoltaic Systems," IEEE Transactions on Industrial Electronics, Vol. 65, No. 3, 2018, doi: 10.1109/TIE.2017.2740821.
[19] M. N. H. Khan, M. Forouzesh, Y. P. Siwakoti, L. Li, T. Kerekes, F. Blaabjerg, "Transformerless Inverter Topologies for Single-Phase Photovoltaic Systems: A Comparative Review," IEEE Journal of Emerging and Selected Topics in Power Electronics, Vol. 8, No.1, 2020, doi: 10.1109/JESTPE.2019.2908672.
[20] M. A. W. Begh, E. Liegmann, A. Mahajan, A. Palanisamy, Y. P. Siwakoti, P. Karamanakos, M. Abdelrahem, R. Kennel, "Design of State-Feedback Controller for a Single-Phase Grid-Connected Siwakoti-H Inverter with LCL filter," PCIM Europe 2019; International Exhibition and Conference for Power Electronics, Intelligent Motion, Renewable Energy and Energy Management, Germany, 2019.
[21] M. A. W. Begh, E. Liegmann, P. Karamanakos, R. Kennel, "Direct Model Predictive Control of a Single-Phase Grid-Connected Siwakoti-H Inverter," IECON 2020 The 46th Annual Conference of the IEEE Industrial Electronics Society, Singapore, 2020, doi: 10.1109/IECON43393.2020.9255091.
[22] M. A. W. Begh, E. Liegmann, P. Karamanakos, A. Mahajan, Y. P. Siwakoti, R. Kennel, "Indirect Model Predictive Control of a Three-Phase Grid-Connected Siwakoti-H Inverter," IECON 2019 - 45th Annual Conference of the IEEE Industrial Electronics Society, Portugal, 2019, doi: 10.1109/IECON.2019.8927830.
[23] J. Slotine, W. Li, Applied Nonlinear Control, Pearson, 1991.
[24] W. M. Haddad, V. S. Chellaboina, Nonlinear Dynamical Systems and Control: A Lyapunov-Based Approach, Princeton University Press, 2008, doi: 10.2307/j.ctvcm4hws.
[25] C. M. Kellett, P. Braun, Introduction to Nonlinear Control: Stability, Control Design, and Estimation, Princeton University Press, 2023.

Amir Mohamad Mohamadi received his B.S. degrees in Electrical Engineering from Islamic Azad University of Najafabad, Isfahan, Iran, in 2002. He received his M.S. degree in electrical engineering from Iran University of Science and Technology, Tehran, Iran, in 2007. He is currently pursuing a Ph.D. in Electrical Engineering at Shahrekord University, Shahrekord, Iran. His current research interests include power electronics and photovoltaic systems. His research aims to contribute to advancements in photovoltaic systems through energy efficiency and innovative control strategies.

Navid Reza Abjadi received the B.S., M.S., and Ph.D. degrees in electrical engineering from Isfahan University of Technology, Isfahan, Iran in 1999, 2001, and 2010 respectively. He is a lecturer at Shahrekord University. His research interests include motor drives, control theory applications, and power electronics.

Gholamreza Arab Markadeh was born in Shahrekord, Iran, in 1974. He received the B.Sc., M.Sc., and Ph.D. degrees in Electrical Engineering from Isfahan University of Technology, Iran, in 1996, 1998, and 2005, respectively. He is currently a Professor in the Department of Electrical Engineering, Faculty of Engineering, Ferdowsi University of Mashhad, Mashhad. His fields of research include nonlinear control, power electronics, and variable-speed drives. He is the Editor-in-chief of Journal of Dam and Hydroelectric Power plant. Dr. Arab Markadeh was the recipient of the IEEE Industrial Electronics Society IECON'04 best paper presentation award in 2004.